Structure and Dynamics of Intramembrane Protease Substrates by NMR Spectroscopy

Zur Erlangung des akademischen Grades einer

Doktorin der Naturwissenschaften

(Dr. rer nat.)

von der KIT-Fakultät für Chemie und Biowissenschaften
des Karlsruher Instituts für Technologie (KIT)

genehmigte
Dissertation

von

M. Sc. Mara Silber

Ich versichere wahrheitsgemäß, die Arbeit selbstständig angefertigt, alle benutzten Hilfsmittel vollständig und genau angegeben und alles kenntlich gemacht zu haben, was aus Arbeiten anderer unverändert oder mit Änderungen entnommen wurde. Weiterhin versichere ich, dass der Inhalt dieser Arbeit bis auf die unten angegebenen Teilpublikationen noch nicht veröffentlicht wurde und dass ich eine solche Veröffentlichung nicht vor Abschluss des Promotionsverfahrens vornehmen werde.

Karlsruhe, 03.03.2021

....
Mara Silber

Publications

1. M. Silber, M. Hitzenberger, M. Zacharias, C. Muhle-Goll, "Altered Hinge Conformations in APP Transmembrane Helix Mutants May Enzyme-Substrate Interactions of γ-Secretase". In: *ACS Chemical Neuroscience* 11.24 (2020).

2. A. Götz, N. Mylonas, P. Högel, M. Silber, H. Heinel, S. Menig, A. Vogel, H. Feyrer, D. Huster, B. Luy, D. Langosch, C. Scharnagl, C. Muhle-Goll, F. Kamp, H. Steiner, "Modulating Hinge Flexibility in the APP Transmembrane Domain Alters γ-Secretase Cleavage". In: *Biophysical Journal* 116.11 (2019).

3. A. Götz, P. Högel, M. Silber, I. Chaitoglou, B. Luy, C. Muhle-Goll, C. Scharnagl, D. Langosch, "Increased H-Bond Stability Relates to Altered ε-Cleavage Efficiency and Aβ Levels in the I45T Familial Alzheimer's Disease Mutant of APP". In: *Scientific Reports* 9.1 (2019).

4. N. Altincekic et al., "Large-scale recombinant production of the SARS-CoV-2 proteome for high-throughput and structural biology applications". In: *Frontiers in Molecular Biosciences* published online (2021).
The topic of this publication is not part of this thesis.

Abstract

In this thesis, the substrates of two intramembrane proteases were investigated. The transmembrane domain of the amyloid precursor protein (APP) is a substrate of γ-secretase that is related to Alzheimer's disease. The other substrate was the transmembrane domain of the serine/threonine-protein phosphatase PGAM5, which is cleaved by the Rhomboid PARL that is associated with Parkinson's disease.

Intramembrane proteases cleave their substrates at the membrane level. These unusual enzymes are involved in a large variety of biological processes. The cleavage mechanism of these proteases has not been studied on the structural level so far, however, the structure and dynamics of their substrates are thought to be decisive features. Unlike soluble proteases, intramembrane proteases do not recognise a consensus sequence, but are nevertheless sensitive to point mutations in the substrate sequence.

APP, the first substrate studied, is cut by γ-secretase at the ε-cleavage site and then successively processed until a short fragment is released, called Aβ. Different processing routes are possible, leading to different products. The two main products are Aβ40 and Aβ42, the latter forming the amyloid plaques that are found in the brains of patients with Alzheimer's disease. In the two FAD mutations studied in this thesis, the level of Aβ42 was found to increase compared to Aβ40. Since both mutations were found in patients with familial Alzheimer's disease, the shift of this ratio is suspected to be one of the reasons for the early onset and lethality of the disease.

With nuclear magnetic resonance spectroscopy, the wild type of the APP transmembrane domain and four single-point mutations were thoroughly investigated. These were the two FAD mutants near the ε-cleavage site (V44M and I45T) and two mutations at the central $G_{37}G_{38}$-motif. The proline mutant (G38P) was introduced to destabilise the transmembrane domain at this site. For stabilisation, the same glycine was exchanged for leucine (G38L). A set of NMR spectra was recorded from which structural parameters were derived. Secondary chemical shifts were determined that report on the secondary structure at each amino acid site. Based on restraints derived from NMR data, three-dimensional structures were calculated. In addition, the hydrogen-deuterium exchange was measured, which reports on the structural flexibility of the peptide.

The peptides were analysed in TFE/H_2O, as this solvent mimics the properties of the water-filled cavity at the active site of the enzymes. The four mutants showed only slight deviations from the wild type. No structural differences were observed at the ε-cleavage site that could explain the altered processing. All peptides, wild type and mutants, consisted of two α-helical regions separated by the $G_{37}G_{38}$-motif. Strikingly, the overall structures were not straight but bent. The $G_{37}G_{38}$-motif acted as a hinge, with the angle between the two parts limited to a certain range. Furthermore, the relative rotation of the two regions with respect to each other was also restricted. Both the strength of the kink and the preferred directions were affected differently by each mutation.

Based on MD simulations of substrate entry into γ-secretase by M. Hitzenberger, it was postulated that the substrate must kink at this $G_{37}G_{38}$-hinge in order to enter into the active site of γ-secretase. The WT structure fitted nicely into this model whereas mutant structures collided with the TMDs of the enzyme.

PARL, a rhomboid protease, does not recognise a consensus sequence either. Thus, it is assumed that it selects its substrates based on their structure and dynamics as well. The transmembrane domain of the PARL substrate PGAM5 WT and four single-point mutations were also analysed with NMR spectroscopy. Here, three residues were mutated that are conserved between different organisms, as these were assumed to fulfil essential functions. All three amino acids were exchanged for leucine (C12L, G17L, G18L) and additionally a serine mutant was investigated (C12S).

As for APP TMD, secondary chemical shifts were determined and the three-dimensional structures calculated. Furthermore, hydrogen-deuterium exchange was measured. This showed that the TMD of PGAM5, like that of APP, consisted of two helical regions. In PGAM5, however, they were connected by a longer unstructured stretch of amino acids. Therefore, in contrast to APP, the comparison of the five peptides did not result in a clearly defined preferred direction of the WT. However, tendencies were visible. By means of X-ray structural analysis, it had been shown for another rhomboid, GlpG, that the region around the scissile bond must be highly dynamic as soon as it leaves the membrane. The model postulated in literature suggests that the region around the scissile bond must completely unwind before it can enter the active site. The calculated structures of PGAM5 suggest that substrate selection is based on a similar mechanism.

In summary, the transmembrane domains of both APP as a substrate of γ-secretase and PGAM5, consisted of two segments. In the case of APP TMD, their relative orientation was comparatively strongly restricted, whereas no clear preference emerged for PGAM5. Based on these results, a hypothesis for γ-secretase substrates could be proposed using the NMR data: Only the structure of the wild type can bend in the direction adopted in the MD simulation, whereas the structures of the four mutants have to be rotated to interact with the enzyme. This rotation could then lead to altered substrate processing.

Zusammenfassung

In dieser Arbeit wurden die Substrate zweier Intramembranproteasen untersucht. Beim ersten Substrat handelte es sich um die Transmembrandomäne des Amyloid Precursor Protein (APP), ein Substrat der γ-Sekretase. Es ist im Zusammenhang mit Morbus Alzheimer bekannt. Das zweite Substrat war die Transmembrandomäne der Serin/Threonin-Protein Phosphatase PGAM5, die von PARL prozessiert und mit Morbus Parkinson in Verbindung gebracht wird.

Intramembranproteasen, die an einer Vielzahl biologischer Prozesse beteiligt sind, schneiden ihre Substrate in der Ebene der Membran. Bisher wurden die Spaltungsprozesse selbst noch nicht auf struktureller Ebene untersucht, aber man geht davon aus, dass die Struktur und die Dynamik ihrer Substrate von entscheidender Bedeutung sind. Im Gegensatz zu löslichen Proteasen wird in Intramembranproteasen keine Konsensussequenz erkannt, trotzdem reagieren sie empfindlich auf Punktmutationen in der Substratsequenz.

APP, das erste untersuchte Substrat, wird von der γ-Sekretase zunächst an der ε-Schnittstelle geschnitten und dann in mehreren Schritten weiter verkürzt, bis ein kurzes Fragment entsteht, das Aβ genannt wird. Dabei sind verschiedene Prozessierungswege möglich, die zu unterschiedlichen Produkten führen. Die zwei Hauptprodukte sind Aβ40 und Aβ42, wobei letzteres die im Zusammenhang mit Morbus Alzheimer bekannten Amyloid-Plaques im Gehirn bildet. Bei den beiden in dieser Arbeit untersuchten FAD Mutationen wurde festgestellt, dass der Anteil von Aβ42 im Vergleich zu Aβ40 zunimmt. Da beide Mutationen bei Patienten mit erblichem Morbus Alzheimer gefunden wurden, wird die Veränderung dieses Gleichgewichts als einer der Gründe für die früh einsetzende und schnell zum Tod führende Krankheit vermutet.

Mit hochaufgelöster Kernresonanzspektroskopie wurden der Wildtyp der APP Transmembrandomäne sowie vier Punktmutationen intensiv untersucht. Dabei handelte es sich einerseits um die zwei FAD Mutanten nahe der ε-Schnittstelle (V44M und I45T), andererseits um zwei Mutationen am zentralen $G_{37}G_{38}$-Motiv. Eine Prolinmutante (G38P) wurde eingeführt, um die Transmembrandomäne an dieser Stelle zu destabilisieren. Zur Stabilisierung wurde das gleiche Glycin gegen Leucin (G38L) ausgetauscht. Es wurden verschiedene NMR Spektren aufgenommen, aus denen Strukturparameter abgeleitet werden konnten. Zum einen waren dies sekundäre chemische Verschiebungen, die die Sekundärstruktur beschreiben. Zum anderen konnten dreidimensionale Strukturen auf Basis der NMR Daten errechnet werden. Zusätzlich wurde der Wasserstoff-Deuterium Austausch gemessen, der Rückschlüsse auf die Stabilität von Wasserstoffbrücken zulässt.

Die Analysen wurden in TFE/H_2O durchgeführt, da das aktive Zentrum des Enzyms mit Wasser gefüllt ist. TFE/H_2O ist deshalb besonders gut geeignet, um die Bedingungen im Inneren des Enzyms abzubilden. Die vier Mutanten unterscheiden sich in ihrer Struktur kaum vom Wildtyp. An der ε-Schnittstelle waren keine Unterschiede zu erkennen, die die unterschiedliche Spaltung erklären könnten. Auffällig war, dass es sich zwar in allen

Fällen um durchgehende α-Helices handelte, diese aber aus zwei Bereichen bestanden. Dabei bildete das $G_{37}G_{38}$-Motiv eine Art Scharnier zwischen beiden Abschnitten, sodass die Gesamtstruktur nicht gerade, sondern geknickt war. Der Winkel zwischen den beiden Segmenten war dabei auf einen bestimmten Bereich beschränkt. Auch die relative Orientierung, also die Richtung des Knicks, war eingeschränkt. Sowohl die Stärke des Knicks, als auch die Vorzugsrichtungen wurden von jeder Mutation anders beeinflusst. Auf der Grundlage von MD-Simulationen von M. Hitzenberger wurde daraufhin postuliert, dass das Substrat an diesem $G_{37}G_{38}$-Scharnier knicken muss, um das aktive Zentrum der γ-Sekretase erreichen zu können. Hitzenberger hatte den initialen Komplex von Enzymen und Substrat untersucht. Die NMR Strukturen des APP TMD Wildtyp passten gut zu diesem Modell, wohingegen die Strukturen der Mutanten mit den TMDs der γ-Sekretase kollidierten.

Für PARL, eine Rhomboid Protease, wird angenommen, dass es Substrate ebenfalls anhand ihrer Struktur und Dynamik erkennt, da hier ebenfalls keine Konsensussequenz erkannt wird. Die Transmembrandomäne des PARL Substrats PGAM5 WT und vier Punktmutationen wurden ebenfalls mittels NMR untersucht. Im Falle von PGAM5 wurden drei Reste mutiert, die zwischen verschiedenen Organismen konserviert sind, da angenommen wurde, dass diese eine essentielle Funktion erfüllen. Alle drei Aminosäuren wurden gegen Leucin ausgetauscht (C12L, G17L, G18L). Als vierte Mutation wurde eine Serin-Mutante untersucht (C12S).

Auch hier wurden verschiedene sekundäre chemische Verschiebungen ermittelt und die dreidimensionalen Strukturen berechnet. Zusätzlich wurde ebenfalls der Wasserstoff-Deuterium Austausch gemessen. Dabei zeigte sich, dass die TMD von PGAM5 genauso wie die von APP aus zwei helikalen Bereichen bestand. Bei PGAM5 waren diese allerdings durch einen unstrukturierten Bereich verbunden. Deshalb ergab sich aus dem Vergleich der fünf Peptide, anders als bei APP, keine klar definierte Vorzugsrichtung. Allerdings waren Präferenzen zu erkennen. Mittels Röntgenstrukturanalyse war für ein anderes Rhomboid, GlpG gezeigt worden, dass der Bereich um die Schnittstelle hoch dynamisch sein muss, sobald er die Membran verlässt. Das in der Literatur postulierte Modell geht davon aus, dass sich der entsprechende Bereich der Helix vollständig entwinden muss, bevor er ins aktive Zentrum gelangen kann. Die berechneten Strukturen von PGAM5 lassen vermuten, dass in diesem Falle ein ähnlicher Mechanismus zugrunde liegt.

Zusammenfassend lässt sich sagen, dass die Transmembrandomänen sowohl von APP als Substrat der γ-Sekretase als auch von PGAM5 aus zwei Segmenten bestanden. Im Falle von APP TMD war deren relative Anordnung vergleichsweise stark eingeschränkt, während sich für PGAM5 hingegen keine klare Präferenz ergab. Basierend auf diesen Ergebnissen konnte anhand der NMR Daten eine Hypothese für Substrate der γ-Sekretase formuliert werden: Nur die Struktur des kann in die von der MD Simulation vorgegebene Richtung abknicken, wohingegen die Strukturen der vier Mutanten gedreht werden müssen, um mit dem Enzym interagieren zu können. Diese Drehung könnte dann dazu führen, dass das Substrat anders prozessiert wird.

Contents

Acronyms

Aβ Amyloid-β

AD Alzheimer's Disease

APH1 anterior pharynx-defective 1

APP Amyloid Precursor Protein

CF Cell-free

cryo-EM cryo-electron microscopy

CSI Chemical Shift Index

CSP Chemical Shift Perturbation

CTF C-terminal fragment

DPC n-Dodecylphosphocholine

ER Endoplasmic Reticulum

FAD Familial Alzheimer's Disease

FM Feeding Mix

GSI γ-secretase inhibitor

GSM γ-secretase modulator

HDX Hydrogen/Deuterium Exchange

HSQC Heteronuclear Single Quantum Coherence Spectroscopy

ICD Intracellular Domain

IMM Inner Mitochondrial Membrane

LC–MS/MS liquid chromatography-tandem mass spectrometry

LMPG 1-myristoyl-2-hydroxy-sn-glycero-3-phospho-1'-rac-glycerol

MD molecular dynamics

MSP Membrane Scaffold Protein

NMR Nuclear Magnetic Resonance

NOE Nuclear Overhauser Effect

NOESY Nuclear Overhauser Enhancement SpectroscopY

NTF N-terminal fragment

OMM Outer Mitochondrial Membrane

PARL presenilin-associated rhomboid-like

PCR Polymerase Chain Reaction

PDB Protein Data Bank

PEN-2 presenilin enhancer 2

PGAM5 phosphoglycerate mutase family member 5

PINK1 Phosphatase and tensin (PTEN)-induced putative kinase 1

POPC 1-palmitoyl-2-oleoyl-sn-glycero-3-phosphocholine

PSEN presenilin

PSH presenilin homolog

RDC Residual Dipolar Coupling

RM Reaction Mix

SA Simluated Annealing

TFE Trifluoroethanol

TMD Transmembrane Domain

TOCSY TOtal COrrelaction SpectroscopY

WT Wild Type

1. Introduction

1.1. Intramembrane Proteolysis

In this thesis, substrates of two intramembrane proteases were investigated.

Intramembrane proteases cleave their substrates within the hydrophobic core of a membrane [1]. These versatile enzymes, which were first discovered in the 1990s, occur in all kingdoms of life.

In eukaryotic cells, intramembrane proteases are even found in all cellular compartments except peroxisomes. They fulfil two main functions. First, intramembrane proteolytic cleavage events can be part of signalling cascades. The activation of transcription factors containing a transmembrane domain or the secretion of growth factors after cleavage of their membrane anchor belong to this category. Second, intramembrane proteases assist regulated protein degradation when substrate fragments are metastable and can be successively degraded by the proteasome. Malfunctions in these important enzymes were linked to severe diseases such as Alzheimer's or Parkinson's disease. [2, 3] Due to their involvement in many essential processes on the one hand and severe diseases on the other, intramembrane proteases are intriguing subjects of investigation.

Four families of these diverse enzymes have been identified based on their transmembrane topologies and catalytic residues: Aspartyl proteases, serine proteases, one glutamyl protease and zinc metalloproteases. All of them are polytopic membrane proteins, but differ in structure and active site residues [4]. Aspartyl proteases are characterised by the GxGD motif with two catalytic aspartates in their active site. They include, most prominently, presenilin (PSEN), the catalytic subunit of γ-secretase, but also signal peptide peptidase (SPP) and SPP-like proteases (SPPLs) [2, 5–7]. Serine proteases, in turn, consist of a conserved six transmembrane domain core that opens to the periplasmic site, similar to zinc metalloproteases[8, 9]. They were found to harbour a catalytic serine-histidine diad [10, 11]. The only known glutamyl protease is Ras-converting enzyme 1 (RCE1) with its catalytic Glu-His in the active site [12]. And finally, Zinc-metalloproteases, such as site-2-protease (S2P), harbour a catalytic zinc atom in the centre of a six transmembrane helix bundle. Water, which is important for the cleavage step, can enter the catalytic cleft through a channel-like opening to the cytosolic site [13, 14].

Some of these intramembrane proteases mentioned are specialized on single-span transmembrane helices as substrates, while others also process polytopic transmembrane proteins [15]. They are generally not specialized on a single substrate but process a variety of different substrates. Whether ectodomain shedding is required prior to intramembrane cleavage or full length proteins are recognised depends on the specific protease [16].

Intramembrane proteases even differ in their topology within one family. SPP and SPPL exhibit a N_{out} topology, this means their N-termini are located on the extracellular side,

in contrast to presenilin whose N-termius is situated in the cytosol (N_{in}). Moreover, the former do not require cofactors for their activity, whereas PSEN, the catalytic subunit of γ-secretase forms a complex with nicastrin, APH-1 and PEN-2 [2, 17, 18].

Intramembrane proteases are found in a variety of cell-types and cellular compartments. γ-Secretase, which exists in up to six different complexes as two PSEN and two APH-1 isoforms are known, is found in various subcellular locations. PSEN2 complexes that are associated with Alzheimer's Disease are mainly situated in endosomes and lysosomes in neurons and brain tissue [19]. The only intramembrane protease known in mitochondria, PARL, a serine protease, is located at the inner mitochondrial membrane [20]. Its malfunction is associated with familial Parkinson's disease [21, 22]. The endoplasmic reticulum (ER) and the inner nuclear membrane in contrast, harbour a variety of intramembrane proteases of all four families. As the ER is the cellular compartment where translocated proteins mature and begin to fold, it is crucial to remove misfolded proteins prior to their release to the cytosol [23, 24]. The function of these proteases is to clear out transmembrane peptide remainders in the membrane or, as in the case of ZMPSTE24, to remove peptides stuck in translocon channels [6, 25, 26]. Additionally, intramembrane proteases in the ER are part of pathways themselves by creating peptide fragments that trigger for example the ER-associated degradation pathway [23]. Three other intramembrane proteases are located at the Golgi apparatus: S2P, the first intramembrane protease ever identified, that is part of the secretory pathway regulation, the aspartyl protease SPPL3 and the serine protease RHBDL1 [9, 27–29].

Intramembrane proteolysis is a multi-step process. The membrane-incorporated substrate must bind to the exosite of the enzyme, a secondary binding site remote from the active site, and enter the water-filled catalytic cavity. Two principle mechanisms describing the migration of the substrate from the initial exosite to the active site are discussed in the community. The first, simpler model proposes that after detachment from the exosite the substrate slides laterally into the enzyme towards the catalytic cleft, where it unfolds and exposes its scissile bond to the catalytic residues [30–32]. The second, more complicated theory states that the substrate does not fully enter the enzyme but remains partially bound to the exosite. By bending at a hinge motif within the transmembrane domain of the substrate, the amino acid stretch harbouring the scissile bond can approach the catalytic residues where it unfolds [10, 33–37].

1.2. Scope of this Thesis

Although intramembrane proteases have been studied intensively in the last decades, neither the full repertoire of substrates and their functions nor the prerequisites that define a substrate as such are known. Essentially, the only certainty is, at least in the case of aspartyl proteases and rhomboids, that there is no consensus sequence. The known substrates are enormously diverse in terms of their amino acid sequence and their only commonality is their α-helical structure. Seemingly, in contrast, these unusual enzymes also react very sensitively to point mutations. Thus, substrates are most likely selected based on criteria other than sequence. Structure and dynamics of their transmembrane domains have been extensively discussed as decisive discriminators without final proof.

Structural investigations of the possible substrates, if they have been investigated, have so far mostly been limited to analysis in membrane or membrane mimetics, which resembles their natural environment before they enter the enzyme. It is assumed that the migration from the membrane into the enzyme is one of the decisive steps that determines whether a peptide is recognised as a substrate or not.

In order to shed more light on the structural properties that make up a substrate, the transmembrane domains of substrates of two intramembrane proteases were investigated in this work. The main focus were their structure and dynamics which were examined by liquid-state NMR and complementary CD spectroscopy. The first substrate was the transmembrane domain of the amyloid precursor protein, the most widely known substrate of γ-secretase. The second substrate studied was the transmembrane domain of PGAM5, a substrate of the rhomboid PARL.

In order to understand the conditions in the enzyme and the transition from the membrane to the enzyme when the restrictions of the lipid environment no longer apply, a mixture of TFE and water was chosen as a solvent, which is considered a good approximation of the conditions in the enzyme.

Because both enzymes are known to be very sensitive to the exchange of single amino acids, four single point mutants of the corresponding transmembrane domains were examined comparatively in addition to the respective wild types. Based on the NMR data, three-dimensional structures of all ten peptides could be calculated. In the case of γ-secretase, of which various structures exist, among others of the enzyme with bound substrates, a hypothesis could thus be formulated which properties distinguish a good substrate from a bad one.

In order to reconstruct the discrepancies between the known structures of the transmembrane domain of the amyloid precursor protein determined in lipid mimetics, a longer APP construct was produced by cell-free protein expression. This was incorporated into DPC micelles and analysed by liquid-state NMR spectroscopy.

2. Biomolecular NMR Spectroscopy

The fundamental observations, based on which nuclear magnetic resonance spectroscopy (NMR) could be developed, were made about 100 years ago, by Zeeman in 1897 and by Gerlach & Stern in 1922 [38, 39]. Several Nobel Prizes honoured the developments that led to nowadays modern NMR spectroscopy. Otto Stern received the Nobel Prize in Physics in 1943. Rabi, who with his co-workers observed the resonance effect for the first time in 1938 [40] was awarded the Nobel Prize in Physics in 1944. In 1946 nuclear magnetic resonance of ^{1}H was discovered by two groups independently: Felix Bloch and colleagues and Edward Purcell and co-workers [41, 42]. Their contributions were honoured with the Nobel Prize in Physics 1952. Few years later the chemical shift was observed for the first time [43]. The introduction of Fourier transform by Ernst & Anderson in 1966 was the priming event for modern NMR spectroscopy [44]. The first NMR spectrometer, developed in the following years by Varian, had a resonance frequency of 30 MHz [45]. Only some years later, the first spectra of a protein, Ribonuclease A, were acquired by Martin Saunders at 40 MHz [46]. After the introduction of two-dimensional NMR by Jeener in 1971, and the first 2D spectrum by Richard Ernst and co-workers in 1975, a NMR-derived protein structure was first published in 1984 by Kurt Wüthrich and colleagues [47–49]. Richard Ernst and Kurt Wüthrich were each awarded Nobel Prizes in Chemistry: Ernst 1991 for his contributions to the development of high resolution NMR and Wüthrich in 2002 for the application of NMR to the structure determination of proteins in solution.

In the following years many methodological and technical improvements followed, that nowadays allow the elaborate analysis of proteins by NMR spectroscopy. The most important point on the spectrometer side were increasing magnetic fields strengths to as high as 1.2 GHz in 2020, which dramatically enhanced sensitivity and resolution and the development of cryoprobes that allow further noise reduction. Electronics were improved and computers became faster. On the methodological side, further parameters such as residual dipolar couplings (RDCs) were discovered [50, 51]. Size limitations could be overcome by new experiments like TROSY (Transverse Relaxation Optimized Spectroscopy) that allows to access proteins larger than 100 kDa [52]. Development of three-dimensional experiments and the introduction of ^{13}C and ^{15}N-labelling allowed to overcome limitations due to peak overlap in two-dimensional spectra and provided a variety of new techniques to study protein dynamics [53].

Initially suspiciously regarded by the X-ray crystallographic community, acceptance was increased when the NMR derived structure of metallothionein-2 suggested that the corresponding X-ray structure needed to be revised [54]. The great benefit of NMR compared to crystallography is that NMR spectra can be acquired under (almost) native conditions, thus no crystals have to be prepared. The other huge advantage is that not only structures but also protein dynamics, conformational changes, folding and chemical reactions can be explored. Moreover, apart from proteins alone, protein-protein or protein-

ligand interactions can be studied. [55] Despite these advantages, NMR structures still account for a rather small share of published three-dimensional protein and nucleic acid assemblies, since NMR is limited to rather small proteins up to 100 kDa, whereas by means of X-ray crystallography proteins larger than 200 kDa can be analysed. To date, more than 153 000 X-ray (88.3%), 13 000 NMR (7.6%) and almost 7000 cryo-EM structures (4%) have been deposited in the Protein Data Bank (PDB) (www.rcsb.org/stats/summary) [56]).

2.1. NMR Observables

The General Principle of NMR Spectroscopy

Like all spectroscopy techniques, NMR is based on energy transitions between two or more states that differ in their individual energy levels. Interactions of a nuclear magnetic dipole moment with an external magnetic field induce the energies of these states in NMR.

The magnetic momentum μ is defined by the nuclear spin angular momentum I and the gyromagnetic ratio γ as

$$\mu = \gamma I \ and \ \mu_z = \gamma I_z \tag{2.1}$$

μ_z and I_z are the z-components of μ and I, respectively, as the external magnetic field is defined along z.

Nuclei with $I = \frac{1}{2}$ have two spin quantum numbers $m = +1/2$ and $m = -1/2$, corresponding to two spin states. This holds true for the nuclei usually observed in biomolecular NMR: ^1H, ^{13}C, ^{15}N and ^{31}P.

When the spins are exposed to an external magnetic field B_0, applied along the z-axis, their interaction with the magnetic field results in the so-called Zeeman effect. The energy levels (α for $m = +1/2$ and β for $m = -1/2$), the so-called Zeeman levels, are

$$E_m = -\gamma I_z B_0 = -m\hbar\gamma B_0 \tag{2.2}$$

with the reduced Planck constant $\hbar$. The energy required for a transition between the two states, $\alpha \rightarrow \beta$ and $\beta \rightarrow \alpha$ is given by

$$\Delta E = \hbar\gamma B_0 \tag{2.3}$$

The so-called Larmor frequency ν_0 or ω_0 describes the precession of the spin angular momentum around the magnetic field B_0. This frequency is equal to the frequency of radiation required to induce transitions between the states and is, according to Planck's Law, defined as

$$\omega_0 = \Delta E/\hbar = -\gamma B_0 \tag{2.4}$$

in rad s^{-1} and

$$\nu_0 = -\omega_0/2\pi = -\gamma B_0/2\pi \tag{2.5}$$

in Hz.

The number of nuclei in each state is given by the Boltzmann distribution. As the energy difference between the two states is very small, the population difference between the spin states is small as well. This makes NMR a very insensitive method. [57, 58]

Chemical Shifts

The resonance frequency of each nucleus is dependent on the local environment that induces the effective magnetic field at that nucleus (B_{loc}). This is the sum of the external magnetic field B_0 and the secondary fields induced by its environment, which is described by the local shielding tensor σ_{kk}. Thus, the local field depends on B_0 and the local shielding tensor σ_{kk}

$$B_{loc} = (1 - \sigma_{kk}B_0) \tag{2.6}$$

In isotropic solution, molecular tumbling leads to rapid reorientations of the shielding tensor, which is averaged to a scalar value σ. The average isotropic shielding constant reduces to

$$\omega = -\gamma(1 - \sigma)B_0 \tag{2.7}$$

Chemical shifts are defined as the resonance frequency of the given nucleus with respect to a reference frequency

$$\delta[ppm] = 10^6 \frac{\nu - \nu_0}{\nu_0} \tag{2.8}$$

where ν is the Larmor frequency in Hz and ν_0 that of a reference compound. Using chemical shifts instead of frequencies has the great advantage that chemical shifts are independent of B_0. That makes them easily comparable between spectra acquired at different external field strengths. [58]

While chemical shift ranges are well known for small molecules, the correlation between chemical shifts and protein structure was unravelled over the past 25 years. In contrast to small molecules, proteins, although relatively uniform in their covalent structure due to neighbouring effects, exhibit not a few but hundreds of chemical shifts. Based on chemical shifts, the secondary structure of proteins can be identified, torsion angles can be calculated, the flexibility of proteins can be estimated and structural models can be established. [59–63]

Chemical shifts of proteins are very sensitive to the protein structure. The first spectrum acquired of a protein sample is usually a ^{1}H-^{15}N-HSQC as shown in Figure 2.1. In this spectrum, ^{1}H and directly bound ^{15}N are correlated. This results in one signal per residue due to the chemical nature of amino acids. The signal dispersion in this spectrum already indicates whether the molecule is more structured or unstructured. In structured proteins, the chemical shifts are influenced by ring currents and dipolar interactions that lead to a wide range of resonances, while these effects are averaged out in random coil-like structures. Thus, in the folded state, backbone amide resonances are usually distributed over a range of 3 ppm. Also H$_\alpha$ chemical shifts report on the secondary structure. In α-helices their chemical shifts are usually located between 3.4 and 4.1 ppm, while in β-sheets they are between 4.9 and 6.0 ppm. In random coil structures they are found in-between the two regions [64–66].

Based on these initial observations, it was discovered that H$_\alpha$, C$_\alpha$ and C$_\beta$ chemical shifts in peptides and proteins can predict secondary structure. So-called secondary chemical shifts, $\Delta\delta$ were defined as the difference between measured, δ_{obs}, and random coil shifts,

δ_{rc}, thus the part of chemical shifts that is influenced by the three-dimensional protein structure [67–71]:

$$\Delta\delta = \delta_{obs} - \delta_{rc} \tag{2.9}$$

As neighbouring amino acids can also impact chemical shifts, for example prolines strongly affect the preceding residue, nearest neighbour correction factors were introduced to compensate for these effects [70].
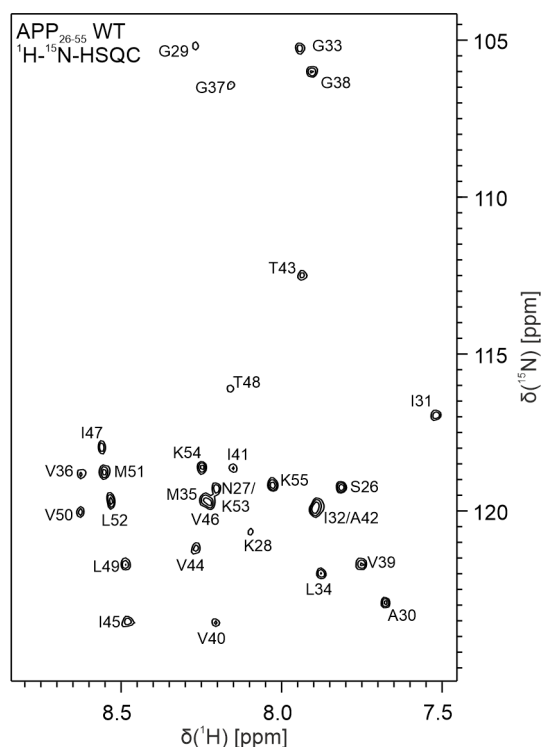
Figure 2.1. Exemplary ^{1}H-^{15}N-spectrum of APP$_{26\text{-}55}$: On the x-axis ^{1}H chemical shifts are shown, on the y-axis ^{15}N chemical shifts. Each signal correpends to the H$_N$-N-pair of a specific amino acid.

Dihedral angles derived from chemical shifts are of great importance for structure calculation. Tools like TALOS+ compare the chemical shifts of an amino acid stretch with database values that are correlated with Φ and Ψ backbone dihedral angles. [72]

Chemical shift changes can report on subtle alterations around the respective residue. Especially resonances of the protein backbone (^{1}H$_N$ and ^{15}N, the two observables in the ^{1}H-^{15}N-HSQC, as shown above) are very sensitive to perturbations of their environment. The exchange of one amino acid within a peptide can, for example, influence numerous cross-peaks (see Figure 4.15, p. 60). The chemical shift changes in ^{1}H$_N$ and ^{15}N are caused by different effects and are therefore almost uncorrelated. ^{1}H chemical shift differences are mostly influenced by through-space interactions, while ^{15}N shifts are affected by both through-bond and through-space interactions such as hydrogen bonds. Combined chemical shift perturbations (CSP) are often used to summarize effects on both ^{1}H$_N$ and ^{15}N. The ^{15}N shift is weighted according to the relative shift ranges of ^{1}H and ^{15}N. The

weighing factor is always an approximation, however. The CSP of every single amino acid can be calculated for glycines as

$$\Delta\delta_{total} = \sqrt{(\Delta\delta_{H2})^2 + (0.2 * \Delta\delta_N)^2} \tag{2.10}$$

and as

$$\Delta\delta_{total} = \sqrt{(\Delta\delta_{H2})^2 + (0.14 * \Delta\delta_N)^2} \tag{2.11}$$

for all other amino acids. The CSP can be employed to follow changes upon ligand binding or to quantify differences between mutants. [73]

Scalar Couplings

The interaction of nuclear spins mediated by their connecting chemical bonds is called scalar coupling (or J-couplings). Scalar couplings are denoted as follows:

$$^n J_{AB}$$

This expression refers to the coupling constant between nuclei A and B connected through n bonds. The strength of J-couplings depends on various factors.

The magnitude of vicinal scalar couplings, ^3J, depends on the dihedral angle Φ according to Karplus:

$$^3J(\theta) = A\,cos^2(\Phi) + B\,cos(\Phi) + C \tag{2.12}$$

The constants A, B and C were determined empirically by correlating observed coupling constants with angles known, for example, from X-ray structures. On this basis, the dihedral angles in proteins (see Figure 2.2) can be estimated from $^3J_{HH}$ coupling constants. [58, 74]
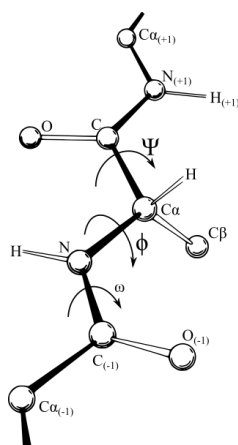

Figure 2.2. Backbone dihedral angles in proteins [75]

The Nuclear Overhauser Effect

Nuclear spins can be regarded as magnetic dipoles that generate a magnetic field around themselves. Another spin in the vicinity interacts with this field, while the first spin in turn experiences the field of the second spin. This so-called dipole-dipole coupling results from the interaction through space of these two spins, which can be oriented parallel or antiparallel to the external magnetic field. The interaction depends on their distance and the angle between the external magnetic field B_0 and the vector connecting the two spins.

The dipolar coupling D_{IS} between two spins, I and S, can be described as

$$D_{IS} = -\frac{\hbar \gamma_I \gamma_S \mu_0}{16\pi^2} \left\langle \frac{1}{r_{IS}^3}(3cos^2\theta - 1) \right\rangle \tag{2.13}$$

with the gyromagnetic ratio of the two nuclei I and S, γ_I and γ_S, the angle θ between their internuclear vector and B_0, their distance r_{ij} and the permeability of the vacuum μ_0. [76]

While scalar couplings are in the Hertz range ($^1\mathcal{J}_{CH} \approx 110 - 220\ Hz$), dipolar couplings can reach values of several thousand Hz. In solid-state NMR they lead to extremely large linewidths, but the dipolar couplings are averaged out due to molecular tumbling in solution. The distance between the two spins, r_{IS}, and the angle of their internuclear vector relative to the external magnetic field, θ, adopt all kinds of values and are therefore averaged with time, as indicated in Equation 2.13 by the angle brackets. Nevertheless, cross-relaxation, the transfer of z-magnetization between these two spins, remains. This effect is called the Nuclear Overhauser Effect (NOE).

For a pair of two isolated protons (I and S) in a rigid molecule the NOE is defined as

$$\sigma_{IS} = \frac{\hbar^2 \mu_0^2 \gamma_H^4 \tau_c}{160\pi^2 r_{IS}^6} \left(-1 + \frac{6}{1 + 4\omega_0^2\tau_c^2} \right) \tag{2.14}$$

with the permeability of the vacuum μ_0, the gyromagnetic ratio of the two nuclei γ_H, the larmor frequency of the nuclei ω_0, the rotational correlation time τ_c and the distance r_{IS} between the two protons observed . All the variables are properties of the single spins except for their distance r. Thus the NOE intensity between two protons within a given molecule is proportional to their distance:

$$I_{NOE} \sim k\frac{1}{r^6} \tag{2.15}$$

When the factor k is known, the distance of a pair of protons, up to 5Å, can be calculated from the NOE intensity. k can either be calibrated based on a known distance or calculated. [57, 58]

In proteins, different types of NOEs are observed. Intraresidual between nuclei of the same amino acid, sequential between the amino acid and the following or preceding, medium range between amino acids two to four residues apart and long range NOEs where the distance is five or more amino acids. Characteristic NOE patterns are observed for structural motifs like α-helices or β-sheets. NOEs are usually interpreted as upper

distance limits and not as absolute values, because the NOE intensity depends not only on distance but also on internal motions and exchange. [55]

Residual Dipolar Couplings

For the sake of completeness, residual dipolar couplings (RDCs) as structural parameters cannot be neglected here. RDCs could not be obtained for the peptides investigated in this thesis and incorporated into structure calculations, as mainly natural abundance peptides were used. Due to the low natural abundance of ^{15}N, about 0.3%, extremely high concentrations would have been required to measure RDCs and this was not achievable.

In liquid-state NMR dipolar couplings, orientation dependent interactions through space are averaged out due to molecular tumbling, as described above. Dipolar couplings can, to some extent, be reintroduced by partial alignment along the external magnetic field, this partially restricts the molecules in their isotropic tumbling and introduces a slight preference orientation. The dipolar couplings are in the kHz range, but if an alignment is induced for, e.g., 0.1% of the time, the dipolar coupling is accordingly reduced to a few Hz. [50, 51, 77]

Partial alignment can be achieved by anisotropic media like liquid crystals, stretched polyacrylamide gels, pf1 phages or poly-(ethylenglykol)-diacrylate (PEG-DA) gels. The latter can be used for a wide range of molecules, from small organic molecules to proteins, as their properties are adaptable. Besides, they tolerate a wide variety of solvents. [78–83]

The residual dipolar coupling is then proportional to the distance between the two respective nuclei and, more importantly, the angle between their connecting vector and B_0. In contrast to NOE restraints, which only report on close proton pairs, RDCs can define long-range orders. [51]

Dipolar couplings can be described by Equation 2.13, explained above. When RDCs are measured, the distance between the two nuclei is generally assumed constant. Thus, the coupling constant depends on the angle between the external magnetic field and internuclear vector only:

$$D_{ij} = -\frac{\hbar \gamma_I \gamma_S \mu_0}{16\pi^2 r_{IS}^3} \left(3 \left\langle cos^2 \theta \right\rangle - 1 \right) \tag{2.16}$$

This angle is averaged over time, but as the vectors are oriented for a small fraction of the time, as explained above, the mean value is not zero. D_{ij} cannot be measured directly, but as it adds to the scalar coupling, it can be derived from the difference of coupling constants obtained in an istotropic and an anisotropic spectrum. [58]

In labelled proteins especially, various [1]H-^{13}C and [1]H-^{15}N RDCs can be obtained. [1]H-^{15}N RDCs are usually measured with an alignment in the range of -20 Hz to +20 Hz. RDCs also report on dynamics, as motions in a picosecond to millisecond time range can alter the dipolar splitting. [84–90]

2.2. Protein Structure Determination by NMR

Structure determination by liquid-state NMR essentially follows the same principle. Restraints are derived from a set of NMR spectra, which are in most cases be NOEs from which distances between proton pairs are calculated. Additionally, dihedral angles can be estimated from backbone chemical shifts. Based on these restraints, the three-dimensional structure is calculated. The individual steps are explained more closely in the following sections.

Resonance Assignment

The first step on the path to three-dimensional structures is the assignment of resonances to the respective nuclei in the protein. Small, unlabelled proteins and peptides can be assigned using a combination of 2D-^{1}H-^{1}H-TOCSY (Total Correlation Spectroscopy) (or COSY (Correlated Spectroscopy)) and 2D-^{1}H-^{1}H-NOESY (Nuclear Overhauser Enhancement Spectroscopy) experiments. This is the oldest method used before isotope labelling was introduced. For isotope labelled proteins, a series of triple resonance experiments has been developed for easy and unambiguous assignment. [68, 91]

COSY and TOCSY rely on magnetization transfer via scalar couplings. In COSY spectra, only correlations between spins connected by two or three bonds (^2J and ^3J) are obtained, while in TOCSY experiments the magnetization is transferred over the entire spin system. In biomolecular NMR, each amino acid can generally be considered as an isolated spin system, as at least four bonds separate the protons of neighbouring amino acids. [92–94]
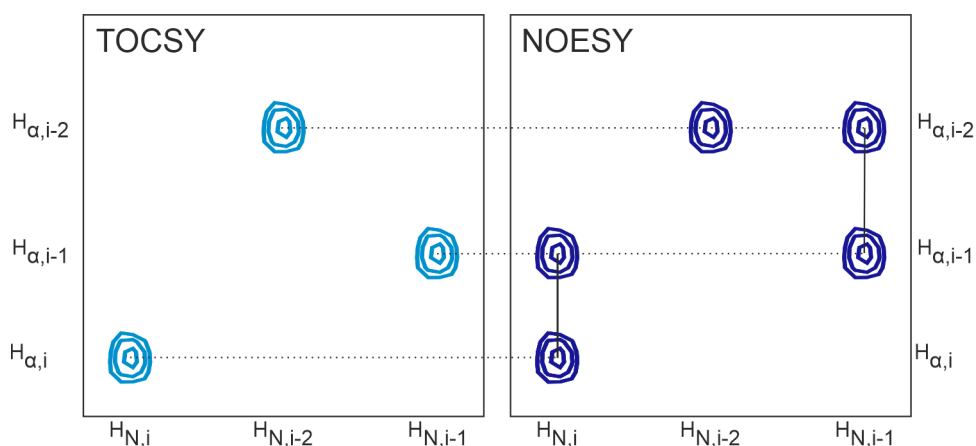
Figure 2.3. Assignment based on TOCSY and NOESY spectra: Resonances visible in the TOCSY (light blue) spectrum are present in the NOESY (dark blue) spectrum as well. The NOESY shows additional peaks corresponding to H_N of the current amino acid (i) and H_α of the preceding one (i-1). This connection is indicated by solid lines. By following this "sequential walk", the amino acid chain of a protein can be assigned one after the other.

These individual spin systems can be linked by NOESY spectra. Signals between $H_{\alpha,i}$ and the amide proton of the following residue ($H_{N,i+1}$) are generally close enough to experience a NOE. In Figure 2.3 the so called "sequential walk", initially described by Kurt Wüthrich, is shown. The corresponding ^{13}C and ^{15}N resonances can be identified in the respective

HSQC spectra. They cannot be directly linked by triple resonance experiments as the protein is unlabelled and concentrations of a few mM are generally too low.[68, 95, 96]

Triple Resonance Experiments

With increasing protein size, growing peak overlap progressively complicates unambiguous resonance assignment. To overcome this problem, triple resonance experiments are used that significantly reduce signal overlap by introducing a third dimension.
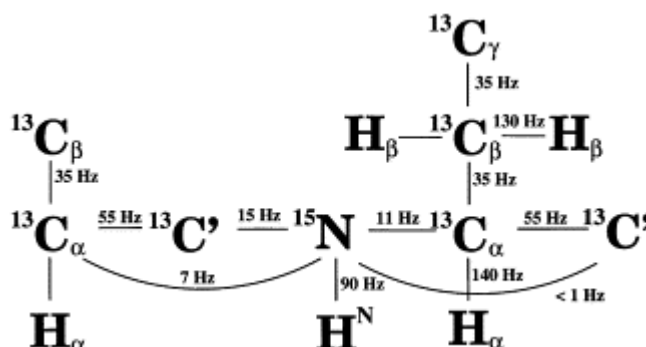
Figure 2.4. Average coupling constants between the different nuclei in the protein: Schematic representation of the protein backbone spin systems with the ^1J and ^2J coupling constants used in tripleresonance experiments. [97] Reprinted from Progress in Nuclear Magnetic Resonance Spectroscopy, 34, M. Sattler et al., Heteronuclear multidimensional NMR experiments for the structure determination of proteins in solution employing pulsed field gradients, pp. 93-158 (1999), with permission from Elsevier

In triple resonance experiments magnetization is transferred via ^1J and ^2J scalar couplings between ^1H, ^{13}C and ^{15}N. The respective coupling constants are shown in Figure 2.4. As the scalar couplings are usually larger than the linewidth, coherence transfer is efficient even for large molecules. Furthermore, as the coupling constants are quite different for different pairs of nuclei, magnetization can be transferred selectively between the respective types of nuclei. This principle was first applied in 1990 to calmodulin. [97–99]

One distinguishes between the experiments used for assignment and those needed to obtain structural data. The most basic experiments used for sequential protein backbone resonance assignment are HNCA, HN(CO)CA and HNCO. The HNCA-experiment allows to correlate ^1H_N, ^{15}N and $^{13}C_\alpha$ resonances of the same amino acid to its preceeding neighbour in a three-dimensional spectrum. Magnetization is transferred from ^1H to ^{15}N, then to $^{13}C_\alpha$, and back via ^{15}N to ^1H. This results in two $^{13}C_\alpha$ resonances, as the C_α-N J-coupling has a similar value for both cases, within the residue (~11 Hz) and to its preceding residue (~ 7 Hz) (see Figure 2.4). In the HN(CO)CA experiments, in contrast, magnetization is transferred via the carbonyl ^{13}C to the $^{13}C_\alpha$ of the preceding amino acid in an unambiguous way. By combining the two spectra, $C_{\alpha,i}$ and $C_{\alpha,i-1}$ can be clearly distinguished and the backbone residues can be sequentially assigned, as depicted in Figure 2.5. [99–103]

HNCACB and HN(CO)CACB experiments follow the same principle but correlate one further piece of information, the $^{13}C_\beta$ chemical shift. These experiments are generally less sensitive than HNCA and HN(CO)CA and require considerably longer acquisition times. Further experiments like HBHA(CO)HN (^1H_N-^{15}N correlated to $^1H_\alpha$ and $^1H_\beta$ of

2 Biomolecular NMR Spectroscopy
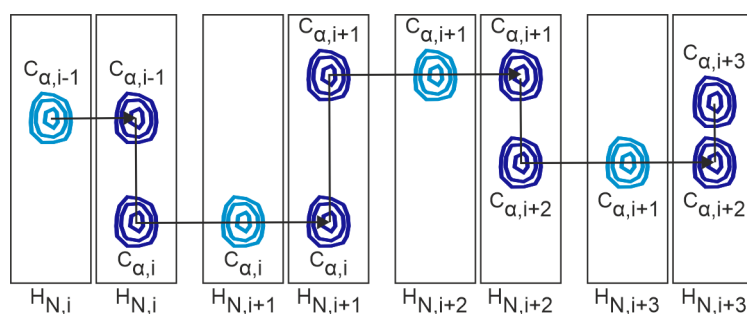
Figure 2.5. Resonance assignment path based on triple resonance experiments: Schematic representation of ^{15}N slices of 3D experiments. HNCA (dark blue) shows peaks at the H_N (and N) frequency of a given amino acid (i) for the C_α of the same residue (i) and the C_α of the preceding residue (i-1), while the HN(CO)CA (light blue) exclusively shows a cross peak to the preceding residue. The combination of these two spectra allows to follow a path along the backbone resonances.

the preceding residue) or CC(CO)NH (^1H_N-^{15}N correlated to all side chain carbons of the preceding amino acid) allow assignments of most of the remaining proton resonances. [101, 104, 105]

Distance restraints for structure calculation derived from three-dimensional ^{13}C and ^{15}N edited NOESY-HSQC spectra are the main source of structural information. [106–109] The 2D-NOESY is expanded by a third dimension to alleviate spectral overlap. This dimension (^{15}N or ^{13}C) correlates a proton with its attached heteroatom before it cross relaxes to a neighbouring proton and gives rise to a NOE.

Three-dimensional Structure Calculation

Simulated Annealing

For structure calculation based on NMR restraints simulated annealing (SA) [110, 111] can be used. Annealing in general refers to a physical process: a solid is heated until it reaches the liquid phase. In this state, all particles are randomly distributed. When the system is cooled down slowly, the particles arrange themselves in the state with the lowest energy. Simulated annealing adapts this principle to structure calculations: The starting structure is heated up slowly until it reaches liquid phase. In this state all particles are randomly distributed and each atom has a high velocity, respectively kinetic energy. At this stage the atoms can move almost freely, overcoming energy barriers due to bonds, dihedral angles, and interactions with neighbouring atoms. When the temperature is gradually diminished in many discrete cooling steps, the atoms slow down and interactions like Van der Waals forces and chemical bonds become more and more important. In these steps, gradually distance restraints come into play and exert their ordering influence. Multiple phases of successive heating and cooling allow to overcome local energy barriers and the structure to converge to the energetically favoured conformation. [112]

Due to the usually much larger number of adjustable variables compared to the number of atoms in the molecule, numerous local energy minima exist besides the global minimum

[113]. With SA, local energy barriers can be crossed. Thus, a greater share of the energy landscape can be explored, hopefully leading to the global energy minimum.

The target function E, with E being the equivalent of potential energy in the system is defined as

$$E = E_{chem} + E_{data} = \sum_i w_i E_i \tag{2.17}$$

where E_{chem} comprises empirical contributions of geometrical properties like covalent bonds, bond angles, dihedral angles and other bonded and non-bonded interactions, based on a molecular modelling force field [114]:

$$E_{chem} = w_{bond}E_{bond} + w_{angle}E_{angle} + w_{dihed}E_{dihed} + w_{imp}E_{imp} + w_{non-bonded}E_{non-bonded} \tag{2.18}$$

E_{data} in contrast contains energy contributions based on NMR data, like NOEs, dihedrals or RDCs

$$E_{data} = w_{NOE}E_{NOE} + w_{torsion}E_{torsion} + w_{RDC}E_{RDC} \tag{2.19}$$

To balance forces, each energy contribution is scaled with a weighting factor (w_i) that is determined by independent protocols [115]. The single energy contributions of the experimental parameters are defined as

$$E_{NOE} = k_{NOE} \sum_{NOE} (d - d_0)^2 \tag{2.20}$$

$$E_{torsion} = k_{torsion} \sum_{torsion} (\theta - \theta_0)^2 \tag{2.21}$$

with d and θ being the distance and torsion angle of the distances in the calculated structure while d_0 and θ_0 are the experimentally determined values. k_{NOE} and $k_{torsion}$ are the respective force constants. When $|(\theta - \theta_0)|$ and $|(d - d_0)|$ are smaller than the respective error margins in the case of flat bottom potential, the corresponding energy is set to 0. [58, 112, 113]

As the distances derived from NOE cross peak volumes are generally only approximations, an interval defined by upper and lower distance limits is used. The energy is then described as a harmonic potential with zero energy between the limits [68]. Dihedral angle and RDC restraints are treated accordingly.

Ambiguous Distance Restraints

Due to the large number of NOE contacts within a protein, peak overlap in the NOESY-spectra cannot be avoided. Thus, a single NOE can contain contributions of many interactions and the size of each is *a priori* not known. ARIA is a program to automatically assign NOESY peaks and calculate structures by simulated annealing [116–118]. To untangle

ambiguous distance restraints, an effective distance $\bar{D}$ is calculated as the sum of the inverse sixth power of all distances contributing to the signal volume:

$$\overline{D} = \left(\sum_{c=1}^{N_c} d_c^{-6} \right) \tag{2.22}$$

where N_c runs over all possible assignments with d_c, the corresponding distance. The resulting $\overline{D}$ is always smaller than the individual distance contributions as the reciprocal of the sixth power of the distances is used. In an iterative process, the assignments and distances are refined and a structural ensemble is calculated. The consistency of assignments is evaluated and the assignment ambiguity is accordingly reduced for the next iteration. [119]

Spin Diffusion

Long NOE mixing times theoretically result in higher peak intensities, but the signal intensities are adulterated by spin diffusion. Spin diffusion refers to the transfer of magnetization via indirect pathways, usually resulting in too elevated intensities.

Assuming a three-spin system in which spins I_1 and I_3 are too far apart to experience direct magnetization transfer via cross-relaxation, but cross-relaxation between I_1 and I_2 and between I_2 and I_3 takes place, spin diffusion can cause indirect magnetization transfer between spins I_1 and I_3 via I_2. That leads to a cross peak between I_1 and I_3 in the spectrum. In addition, back transfer can occur, for example $I_1 \rightarrow I_2 \rightarrow I_1$, which decreases the intensity of the cross peak between I_1 and I_2. Thus, spin diffusion leads to increased cross peak intensities of spins far apart and decreased cross peak intensity of spins close together, resulting in inaccurate distance restraints. Spin diffusion effects can be avoided by short mixing times, but this leads to overall low NOE intensities. [58]

The calculation of a relaxation matrix, as incorporated in ARIA, allows to compensate for cross-relaxation effects. This calculation requires information on the mixing time, the rotational correlation time and the spectrometer frequency. To account for errors in the assignment or miscalculated distances arising from conformational dynamics, restraints exceeding a certain difference between input distances and recalculated distance in a larger share of the calculated structure, are removed for further iterations [120, 121].

Structure Validation

Structures based on NMR restraints result in a bundle of conformations. These conformers all fulfil the input data, but reflect a certain uncertainty because soft restraints, namely upper and lower bounds are applied. Thus, deviations between the single structures of a bundle do not necessarily imply dynamics, but simply report on all conformations that are compatible with the distance restraints. A subset is selected from this structural ensemble to account for unphysiological structures within the structural bundle. This is based on an energy cut-off.

The total number of NOE restraints applied should not be used as a criterion for the quality of calculated structures. Many restraints are redundant, for example specific

interresidual distances that are always in a certain distance range, such as between H_α and H_N of the same residue. Additionally, the number of NOEs depends on the number of amino acids, the amino acid type and the secondary and tertiary structure of the protein. And lastly, due to conformational dynamics, NOEs that might be expected for a static model may not be observable. [120]

The uncertainty in the obtained molecular coordinates of a NMR-based structural ensemble can be described by the root mean square deviation (RMSD). One has to distinguish between precision and accuracy. Accuracy is the closeness of the obtained structures to the true structure, while precision describes the closeness of one single value to the mean of all values. In the context of structure calculation, this describes how well a given structure within the bundle superimposes with the mean structure. Presuming accuracy is quite good, precision describes how the experimental values are spread around the true values. There are three possible scenarios that all lead to different errors. When the experimental values are too precise, the true variance is underestimated. This might result in a bundle of perfectly overlaying structures that does not contain information on all accessible conformations. When the variance of physical errors is larger than the true variance, the structures are less precise and result in a bundle that probably envelopes the true structure in a too wide range. In the ideal case, the spread of experimental values resemble the true values. [120, 122]

The second quality parameter is the geometric quality, this means errors or abnormalities in the geometry have to be eliminated. There are different methods available. Bond lengths and dihedral angles, for example, can be compared with reference values to identify outliers. [123–125]

2.3. Protein Dynamics Accessible by Liquid-State NMR
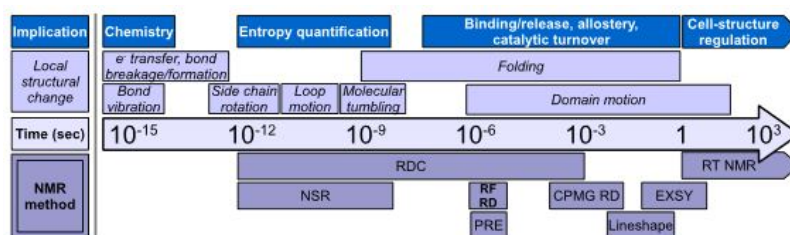
Figure 2.6. NMR accessible time scales of protein motion: By liquid-state NMR protein dynamics can be measured on a timescale of 18 orders of magnitude by a variety of experiments. [126] Reprinted from Biochimica et Biophysica Acta (BBA) - Proteins and Proteomics, 1814, I. Kleckner & M. Foster, An introduction to NMR-based approaches for measuring protein dynamics, pp. 942-968 (2011), with permission from Elsevier.

Dynamics play an important role regarding the biological function of proteins. Structural fluctuations occur in many processes like protein folding, enzymatic catalysis and protein regulation. A variety of NMR methods allow to access a broad range of motions on a timescale ranging from picoseconds to several seconds or even hours, as depicted in Figure 2.6. The great advantage of NMR as a tool to probe protein dynamics is that, in

contrast to methods such as fluorescence based methods, many nuclei can be observed simultaneously. [127]

Rotational Correlation Time τ_c

The time required for a molecule to tumble by one radian due to Brownian motion is called the rotational correlation time τ_c. It depends on the molecular mass and shape of the protein, the viscosity of the solvent η_W and the temperature T. τ_c can be approximated by Stoke's law presuming a globular protein with effective hydrodynamic radius r_H^3 as

$$\tau_c = \frac{4\pi\eta_W r_H^3}{3k_B T} \tag{2.23}$$

The peak linewidth strongly depends on τ_c, as longer correlation times usually lead to broader lines. T_1 and T_2 relaxation times are correlated to τ_c (see below). T_1 describes the recovery of z-magnetization to its equilibrium state and is due to interactions of spins with their environment. T_2 is the decay of magnetization orthogonal to the z-axis to its zero equilibrium value.

T_2 decreases almost linearly with τ_c, see Figure 2.7.
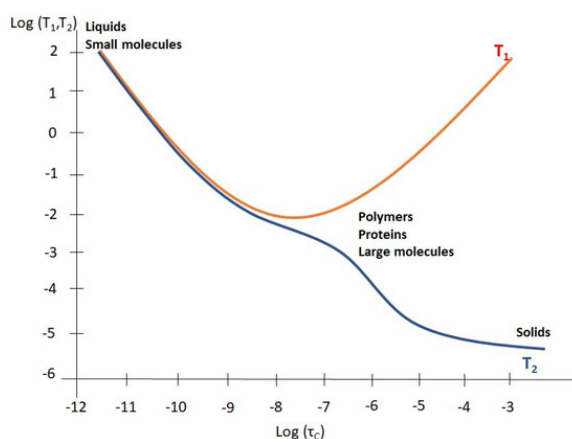
Figure 2.7. T$_1$ and T$_2$ relaxation times depend on the correlation time τ_c: Large, slowly tumbling molecules exhibit short T$_2$ times. Taken from [128].

The linewidth at half height ($\Delta v_{1/2}$) of a signal depends on T_2 as

$$\Delta v_{1/2} = \frac{1}{\pi T_2} \tag{2.24}$$

and T_2 in turn is small for large, slowly tumbling molecules with long τ_c. This results in very broad lines for large molecules like proteins. [55, 58]

Slow Exchange: $\tau_{ex} > 1s$

Chemical shifts depend on protein structure, as explained above. When a protein exists in two conformations, each is characterized by a distinct set of chemical shifts. For a given
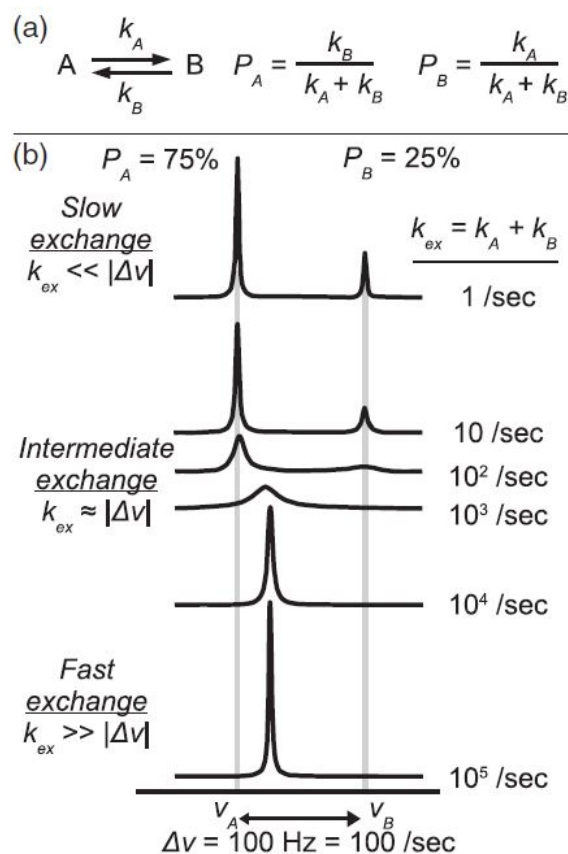
Figure 2.8. Chemical exchange processes and their influence on the NMR observables:
(a) The exchange of two states A and B can be described by the respective rate constants k_A
and k_B. The populations of both states depend on the ratio of the respective rate constant
and the sum of k_A and k_B. $P_A+P_B=1$. (b) The influence of various k_{ex} on spectra of two
differently populated states with Δv=100 Hz. In the slow exchange regime signals of
both states are sharp and separated by Δv. The peak intensities are corresponding to the
relative population of both states. In the intermediate exchange regime, depending on the
exchange rates, the two peaks approach each other and experience severe linebroadening
until eventually the two peaks merge in one signal. In the fast exchange regime this one
signal is sharp again, its position, intensity and linewidth are determined by the relative
populations of both states. [126] Reprinted from Biochimica et Biophysica Acta (BBA) - Proteins and Proteomics, 1814, I. Kleckner & M.

Foster, An introduction to NMR-based approaches for measuring protein dynamics, pp. 942-968 (2011), with permission from Elsevier.

nucleus these signals are separated by Δv and characterized by their intensities depending on the relative populations of both states. As long as Δv is much larger than the exchange rate k_{ex} between the two states, two separate, sharp peaks can be distinguished in the spectrum. This characterizes the slow exchange regime, as shown in Figure 2.8. Exchange is simulated here with the following parameters: States A and B are interchanging with the rates constants k_A and k_B. Their relative populations are $P_A = 75\%$ and $P_B = 25\%$. The exchange rate between the two states, $k_{ex} = 1\ Hz$ is much smaller than the frequency separation, $\Delta v = 100\ Hz$, of the signals corresponding to A and B. This results in signal intensities according to the relative populations. The signals of both states, A and B, are clearly visible, even though state B is only 25% populated. Processes in the slow exchange regime comprise protein folding and solvent-hydrogen exchange or slightly faster processes like domain movement or secondary structure interconversion [126, 129–131].

Slow exchange can be followed by real-time NMR by perturbation of the system. When a protein is titrated with a ligand and interactions are within the slow exchange regime, a second set of peaks in addition to the resonances of the unbound protein appears, those of the protein-ligand complex appears. With increasing ligand concentration, the peak intensities of the unbound protein decrease while those of the complex increase. This can be followed by a series of 2D-^{1}H-^{15}N-HSQC spectra. [58]

Fast Exchange: $\tau_{ex} < 1ms$

When two states are in the fast exchange regime, i. e. $k_{ex} >> \Delta v$, the two states are no longer distinguishable. As shown in Figure 2.8, only one sharp line at an average position can be observed. Its chemical shift depends on the relative populations of the two states. Applied to the example above, this means that titration of a protein with its ligand when the unbound protein is in rapid exchange with the complex does not noticeably change the linewidth or intensity of the protein resonances. As the ligand concentration increases, they observed signals slowly shift because the chemical shift depends on the relative populations of the free protein and the complex. Very fast dynamics in the picosecond to nanosecond range can be indirectly probed by measuring ^{15}N relaxation times and the heteronuclear Nuclear Overhauser Effect (hetNOE). ^{15}N relaxation is a method to probe peptide bonds in proteins that can report on conformational exchange. However, not every effect on ^{15}N relaxation must be due to conformational exchange. [127, 132, 133]

When global or internal motions induce the reorientation of the ^{1}H-^{15}N bond vector of a given spin pair, the local field fluctuates. This is to a first approximation due to dipolar interactions between ^{1}H and ^{15}N. This interaction is averaged out by molecular tumbling. But as these fluctuations are time-dependent and sensitive to external perturbations by radio-frequency pulses, their relaxation rates report on dynamic parameters. With ^{15}N relaxation experiments either spin-lattice relaxation, T_1, or spin-spin relaxation, T_2, can be monitored.

T_1 can be calculated by fitting an exponential function to the observed decay of the signal intensity $I(t)$. For small proteins the rate constant $R_1 = 1/T_1$ is between 0.5 and 5 Hz.

$$I(t) = I(0) \ (1 - exp(-R_1 t)) \tag{2.25}$$

Transverse relaxation or spin-spin relaxation, T_2 is the loss of phase coherence in the x-y-plane mainly caused by spin-spin interactions and field inhomogeneities. The rate constant $R_2 = 1/T_2$ typically ranges from 5 to 50 kHz.

$$I(t) = I(0) \ exp(R_2 t) \tag{2.26}$$

The main determinant of T_2 in proteins is the correlation time τ_c. This in turn depends on protein size and shape, as described above. Short rotational correlation times result in long T_2 times, while slow tumbling gives short T_2 times as shown in Figure 2.7.

The hetNOE is a method to quantify thermal fluctuations in the protein. It relies on magnetization transfer between ^1H_N and the directly bound ^{15}N. Unfolded or unstructured domains, due to their short correlation times, result in signals of opposite sign and can therefore be identified easily. The HetNOE depends on the gyromagnetic ratios of ^1H and ^{15}N, γ_H and γ_N, their NOE σ_{NH} and the T_1 rate constant R_1. [134]

$$HetNOE = 1 + \frac{\gamma_H}{\gamma_N} \frac{\sigma_{NH}}{R_1} \tag{2.27}$$

The combination of the three parameters, R_1, R_2 and hetNOE allows the fast motion of N-H bonds of each amino acid to be studied.

A spectral density function $j(\omega)$ of each bond vector is determined. The spectral density gives the amount of motion for a given frequency and is defined as the Fourier transform of the correlation function $C(\tau)$ that describes the time-dependence of bond reorientation. The correlation functions results from the bond vector orientation at t=0 and its value at another time point.

The "model-free" formalism, introduced by Lipari & Szabo, allows to discriminate the individual motion of the H-N vector from the contribution of overall molecular tumbling. It is a variant of the spectral density function

$$j(\omega) = \frac{2\tau_c}{1 + \omega_0^2 \tau_c^2} \tag{2.28}$$

extended by an order parameter S^2 that describes the amplitude of internal motions or the degree to which information on the orientation of the H-N bond vector is lost due to dynamics processes

$$j(\omega) = S^2 \frac{\tau_m}{1 + (\omega \tau_m)^2} + (1 - S^2) \frac{\tau}{1 + (\omega \tau)^2} \tag{2.29}$$

with $\tau^{-1} = \tau_m^{-1} + \tau_e^{-1}$. Thus, the relaxation rate depends on three paramters: τ_m, the overall correlation time, τ_e the ^1H-^{15}N internal correlation time and the order paramter S^2 that describes the amplitude of internal motions. When the internal motion is very fast, τ_e approaches 0 and when there is no internal motion at al, S^2 approaches 1. S^2 can adopt values between 1 and 0, while 1 refers to a completely rigid bond. With the increasing

amplitude of internal motion S^2 decreases. By ^{15}N relaxation, both, amplitude S^2 and timescale τ_e can be determined. S^2 allows to discriminate between rigid and mobile motifs within a protein, while τ_e reports on sites where local dynamics occur.

Intermediate to Fast Exchange

When k_{ex} approximates the difference between the two frequencies, $\Delta\nu$, signals approach each other and get broader and the lower populated state might not be observable any more, as indicated in Figure 2.6(b). This is called "intermediate exchange regime". With increasing exchange rate the two signals are shifted towards each other until they merge in one broad signal when $k_{ex}/\Delta\nu = 1$, this phenomenon is called coalescence. If the states are differently populated, it happens that one signal is not observable even before coalescence, as it is not distinguishable from the noise due to linebroadening. [126, 129] Employing the example of a protein that is titrated with a ligand once more, the processes can be described as follows: The signals of the free protein get broader with increasing ligand concentration. When the concentrations of free protein and the complex are almost equal, the protein signal disappears due to linebroadening. At some point, when ligand concentrations are even higher, the protein signal reappears, possible at another position. [58] The position of the intermediate signal can be predicted by the McConnell equations, which are an extension of the Bloch equations taking chemical exchange into account [135].

A popular method to measure intermediate to fast exchange is based on a principle already introduced in the 1950s by Erwin Hahn: the Spin Echo [136]. CPMG (Carr-Purcell Meiboom-Gill) relaxation dispersion uses the spin echo to gain information on relative populations of the states and exchange rates on a micro- to milliseconds timescale [137, 138]. During a fixed time interval a variable number of refocusing pulses is applied, the so-calle "spin echo" element that consists of two delays τ enclosing a 180° refocusing pulse. With every refocusing pulse, chemical shift evolution is inverted. When the rate of refocusing pulses (ν_{CPMG}) is slower than interconversion between the two different states, dephasing and thus linebroadening occurs, because chemical evolution is not fully refocused. When ν_{CPMG} is faster than the exchange the resulting signal can be even narrower as interconversion is reduced. The exchange parameters can then be deduced from the dependence of linewidth on ν_{CPMG}. [129, 139] The value determined is the exchange contribution (R_{ex}) to the transverse relaxation rate R_2^{obs}

$$R_2^{obs} = R_{ex} + R_2^0 \tag{2.30}$$

R_{ex} in turn depends on the population of states A and B, P_A and P_B, chemical shift difference $\Delta\nu$ or the difference in frequency $\Delta\omega_{AB}^2$, the exchange rate constant k_{ex} (or its reciprocal τ_{ex}) and pulse frequency $\nu_{CPMG} = 1/(4\tau)$ [140]:

$$R_{ex} = (1 - 4\nu_{CPMG}\tau_{ex})P_A P_B \Delta\omega_{AB}^2 \tau_{ex} \tag{2.31}$$

Over a series of spectra v_{CPMG} is varied during a constant total time T_{CPMG}. The observed signal intensity can be used to calculate R_2^{obs}:

$$R_2^{obs}(v_{CPMG}) = \frac{-ln\frac{I(v_{CPMG})}{I_0}}{T_{CPMG}} \qquad (2.32)$$

The obtained R_2^{obs} can then be used to determine R_2^0, k_{ex}, P_A and P_B and the frequency difference between the two states $\Delta\omega$. The Carver-Richards equations are applicable for any exchange regime while the simpler Ishima-Torchia equation can be used for skewed populations ($P_A << P_B$) and the fast exchange equation for the case when $k_e x > \Delta v$. [55, 58, 141]

Hydrogen-Deuterium Exchange

Hydrogen-deuterium exchange (HDX) is a long established method to monitor slow dynamics that are correlated to hydrogen bonds. Hydrogen-deuterium exchange can be measured by a series of spectra in real time. Fully protonated proteins are dissolved in deuterated solvent and a set of ^{1}H-^{15}N-HSQC or ^{1}H-^{1}H-TOCSY spectra is acquired. As in liquid-state NMR spectroscopy usually ^{1}H are observable whilst D are not, the successive exchange of hydrogen against deuterium leads to decreasing signal intensity with time. This can be approximated by an exponential function with the exchange rate constant k_{ex}:

$$I_t = I_0 e^{-k_{ex}t} \qquad (2.33)$$

The standard model states that every hydrogen bond can exist either in a closed $(N-H)_C$ or in an open $(N-H)_O$ state. Exchange can only occur in the open state with the exchange rate k_{int}. The scheme then is as follows:

$$(N-H)_C \underset{k_{cl}}{\overset{k_{op}}{\rightleftharpoons}} (N-H)_O \xrightarrow{k_{int}} (N-D)_O$$
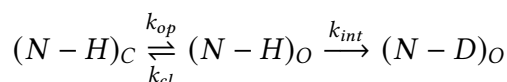
When the structure is relatively stable, $k_{cl} > k_{op}$ and reclosing is faster than exchange ($k_{cl} > k_{int}$), the exchange rate depends on the fraction of time the open form exists:

$$k_{ex} = \frac{K_{op}}{1 + K_{op}k_{ch}}$$

with the opening equilibrium constant K_{op} [142].

The underlying mechanism, admittedly, remains unclear and data should be interpreted with caution. Exchange is catalysed by hydroxide ions under most conditions. The rate depends on steric effects of secondary structure and side-chains of neighbouring residues [143]. Exchange rates are fast for unstructured, completely solvent-exposed amide protons. In the base catalysed regime the exchange rate is pD dependent in a simple manner. Increase of pD by one unit enhances exchange approximately by a factor of ten. Thus, a broad range of exchange rates can be covered by measurements at different pD values [144].

3. Materials and Methods

3.1. Peptides

Synthetic Peptides

Synthetic peptides were purchased from Core Unit Peptid - Technologien, Leipzig. THe sequences are given below:

```
                      30         40         50
APP₂₆₋₅₅       SNKGA IIGLMVGGVV IATVIVITLV MLKKK
APP₂₆₋₅₅, ₈lab  SNKGA IIGLMVGGVV IATVIVITLV MLKKK
G38L          SNKGA IIGLMVGLVV IATVIVITLV MLKKK
G38P          SNKGA IIGLMVGPVV IATVIVITLV MLKKK
V44M          SNKGA IIGLMVGGVV IATMIVITLV MLKKK
I45T          SNKGA IIGLMVGGVV IATVTVITLV MLKKK


                      10         20         30
PGAM5 WT₂₋₃₆  AFRQALQLA ACGLAGGSAA VLFSAVAVGK PRAGGD
PGAM5 C12S    AFRQALQLA ASGLAGGSAA VLFSAVAVGK PRAGGD
PGAM5 C12L    AFRQALQLA ALGLAGGSAA VLFSAVAVGK PRAGGD
PGAM5 G17L    AFRQALQLA ACGLAGLSAA VLFSAVAVGK PRAGGD
PGAM5 S18L    AFRQALQLA ACGLAGGLAA VLFSAVAVGK PRAGGD
```

Cell-Free Expression Construct

APP$_{0-55}$ WT was inserted in the Pivex2.3d vector that was kindly provided by Daniel Huster's Lab, Leipzig. Pivex2.3d (Biotechrabbit, Hennigsdorf, Germany) is a plasmid designed for cell-free expression and yields a C-terminal His-tag, T7 promotor and terminator, ampicillin resistance and various restriction enzyme cleavage sites. The vector map is given in the appendix (p. 151).

The APP$_{0-55}$ expression construct:

```
            0         10         20         30         40
APP₀₋₅₅, cf  M DAEFRHDSGY EVHHQKLVFF AEDVGSNKGA IIGLMVGGVV
                      50         60
            IATVIVITLV MLKKKPGGGS HHHHHH
```

3.2. Sample Preparation

Synthetic Peptides in TFE/H$_2$O

The lyophilized peptide was dissolved in 500 µL 80% TFE-d2 and 20% H$_2$O (V/V) by gentle vortexing and supersonication. The sample concentration was set to 500 µM and pH values were adjusted with HCl and NaOH. The sample was transferred to a 5 mm NMR tubes and measured. APP WT TMD and mutants in TFE/H$_2$O were measured at pH 7. PGAM5 WT TMD and mutants in TFE/H$_2$O were measured at pH 5.

For hydrogen deuterium exchange experiments the peptide was dissolved in 80% TFE-d3 and 20% D$_2$O to a final concentration of 500 µM. pD values were adjusted with DCl and NaOD to 4.0, 5.0 and 6.5 respectively.

APP$_{0-55, \text{cf}}$ in DPC micelles

Following cell free expression and purification the lyophilized peptide and deuterated dodecylphosphocholine (DPC-d38) were mixed, 180 µL NMR-buffer (see p. 153) was added. The detergent to peptide ratio was set to 70:1.

Sample homogeneity was achieved by several freeze-thaw cycles (15 minutes at -20 °C, 15 minutes at 37 °C in the ultrasonic bath). The sample was transferred to 3 mm NMR tubes (Norell® Select Series™ 3 mm high-throughput NMR tube) and measured.

3.3. NMR Data Acquisition and Resonance Assignment

Spectrometer

All spectra were acquired on a 600 MHz Bruker Avance III spectrometer, equipped with a CPTCI cryogenically cooled probehead (Bruker BioSpin GmbH, Rheinstetten, Germany).

Pulse Sequences

The following pulse sequences were used:

zggpw5	^{1}H	1D	[145]
dipsi2gpphpr	^{1}H-^{1}H-TOCSY	2D	
noesygpphpr	^{1}H-^{1}H-NOESY	2D	[146, 147]
hsqcetgp	^{1}H-^{13}C-HSQC	2D	
clipcosy19.mk	^{1}H-^{1}H-CLIP COSY	2D	[148]
hsqcetf3gpsi	^{1}H-^{15}N-HSQC	2D	[149–151]
hsqcctetgpsisp	constant time ^{1}H-^{13}C-HSQC	2D	
b_hncogp3d	HNCO	3D	[152, 153]
b_hncocagp3d	HN(CO)CA	3D	[153]
b_hncagp3d	HNCA	3D	[152, 153]
b_hncocacbgp3d	HN(CO)CACAB	3D	[153]
b_hncacbgp3d.2	HNCACB	3D	[152, 153]
noesyhsqcf3gpsi3d	NOESY-HSQC	3D	[149–151]
dipsihsqcf3gpsi3d	TOCSY-HSQC	3D	[149–151]

Assignment of Unlabelled APP TMD in TFE/H$_2$O

^{1}H-^{15}N-HSQC, ^{1}H-^{13}C-HSQC, ^{1}H-^{1}H-TOCSY and ^{1}H-^{1}H NOESY spectra were acquired at 300 K. For structure calculation longer ^{1}H-^{1}H-NOESY spectra with 1000 increments in the indirect dimension and 200 ms mixing time were acquired.

Spectra were processed using TopSpin (Bruker BioSpin, Rheinstetten, Germany). For peak assignment and integration CCPN was used [154].

Assignment of labelled APP $_{0\text{-}55,\, cf}$ in DPC

Besides ^{1}H-^{15}N-HSQC and real-time ^{1}H-^{13}C-HSQC experiments, a set of 3D experiments at 320 K was acquired: HNCO, HNCA, HN(CO)CA, HNCACB and HN(CO)CACB.

Spectra were processed using TopSpin (Bruker BioSpin, Rheinstetten, Germany). For peak assignment and integration CCPN was used [154].

3.4. Structure Calculation Based on NMR Restraints

Three-dimensional structures were calculated based on NOE constraints and dihedral angles. Dihedral angles were obtained from TALOS+ [72]. NOESY peaks were integrated and exported for structure calculation with CCPN [154]. Structures were then calculated with ARIA2/CNS [118, 155, 156].

Peaks were assigned manually, no automated assignment was used. Seven iterations with 200 structures each were calculated, the last iteration comprised 400 structures of which the 20 best (lowest energy) were chosen. Spin diffusion correction was applied to all calculations. Graphical representations of structures were created with PyMol (The PyMOL Molecular Graphics System, ver. 2.3.4, Schrödinger, LLC, 2015).

Determination of Kink and Swivel Angles

Kink θ and swivel angle ϕ were calculated using a script written in python by C. Muhle-Goll. The kink angle was defined as the angle between the axis of the C-terminal and the N-terminal helices. The swivel angle was calculated as the relative rotation of the N-terminal helix around the C-terminal part. The axis through the C-terminal helix was aligned along the z-axis and the x-axis was defined by the V_{46} H_α-C_α bond vector. The swivel angle was caluclated as the projection of the N-terminal helix axis onto the x-y-plane [157].

3.5. Cell-Free Protein Expression

For cell-free protein expression $APP_{0\text{-}55}$ gene sequence was transferred into the Pivex 2.3d vector. pQE60 vector containing the full C99-sequence was obtained from Harald Steiner (DZNE, Munich) and Pivex2.3d from Ulrike Krug (AK Prof. Huster, University of Leipzig).

Polymerase Chain Reaction

PCR standard mix and standard conditions are given in the appendix (p. 152). Primers (sequences p. 151) were purchased from Eurofins Genomics, Ebersberg, Germany; Pfu-Polymerase was purchased from New England Biolabs (Ipswich, MA, USA). After PCR DNA was purified using the peqGold CyclePure Kit (VWR Peqlab), then PCR fragments were separated from residual primers and template DNA by agarose gel electrophoresis (2% low melt agarose, TAE-buffer (p. 153) and SybrGreen) and subsequent gel extraction with the QIAquick Gel Extraction Kit (Quiagen, Hilden, Germany). Afterwards followed a second purification step using the peqGold CyclePure Kit to remove EDTA from TAE-buffer.

Restriction Enzyme Digestion

The used restriction enzymes, *NcoI* and *SmaI*, were purchased from New England Biolabs (Ipswich, MA, USA). Digest of empty Pivex2.3d and PCR product was carried out at 37 ℃ for two hours (digestion mix see p. 152). CutSmart®Buffer recommended by NEB for both enzymes was used. Afterwards Antarctic Phosphatase (New England Biolabs,Ipswich, MA, USA) was added to the plasmid containing batch and the mixture was incubated further 30 minutes. Both batches, PCR product and plasmid were purified, again using the peqGold CyclePure Kit.

Ligation

Ligation with T4 DNA-Ligase from New England Biolabs (Ipswich, MA, USA) was carried out for 45 minutes at room temperature (see p. A.1).

Transformation

For transformation 50 µL NEB®5-alpha Competent *E.coli* were thawed on ice for 10 minutes and then incubated with 1 µL purified vector on ice for 30 minutes. Heat shock was carried out in a water bath at 42 °C for 45 s, the mixture was cooled down on ice for five more minutes. 800 µL SOC medium (see appendix p. 153) were added and the batch was incubated with gently shaking at 37 °C for 60 min. 200 µL of the mixture were spread onto a selection plate with ampicillin (1:1000) and incubated at 37 °C over night.

Colony PCR

To preselect colonies carrying the desired vector colony PCR was performed prior to plasmid preparation and sequencing. The components and conditions are given in the appendix (see p. A.1). To ensure cell disruption the initial denaturation step was extended to ten minutes. PCR products were analysed by agarose gel electrophoresis, as above. Positive colonies were picked.

Over Night Culture

Two or more flasks containing 10 ml LB medium (see standard recipe on p. 153) with Ampicillin (1:1000) were inoculated with one colony each and incubated over night at 37 °C.

Small Scale Plasmid Preparation

Plasmid extraction and preparation was done with the PeqGold Plasmid Miniprep Kit (VWR, Darmstadt, Germany). For final elution 50 µL sterile H_2O was used.

Sequencing

Samples were sent to Eurofins Genomics (Eurofins Genomics, Ebersberg, Germany) for sequencing.

Large Scale Plasmid Preparation for Cell-Free Protein Expression

For cell-free protein expression lare quantities of vector are needed. Therefore large scale plasmid preparation was done. Transformation with the validated vector was done as described above. 200 mL LB medium (see p. 153) with Ampicillin (1:1000) were inoculated with the respective cells and incubated over night at 37 °C. Plasmid were isolated with the PeqGold Plasmid Maxiprep Kit (VWR, Darmstadt, Germany). Final elution was done with 500 µL sterile H_2O.

Solutions and Reagents for Cell-Free Protein Expression

S21 extracts were prepared following a protocol of Daniel Huster's group in Leipzig, Germany with the help of Ulrike Krug at their facilities.

Solutions and reagents are given on pages 154 and 155 in the appendix. If not stated otherwise all compounds are dissolved in H_2O. Amino acid stocks were set to pH 7.4 with KOH.

Amino Acid Mixtures

The individual compositions of the amino acid mixtures are next displayed next to the respective CF-scheme.

Cell-Free Protein Expression

Cell-free protein expression was established from scratch to overcome problems emerging with recombinant protein expression. It is a considerably faster, less labor-intensive and easy to apply once alternative. As all amino acids are added separately special sample requirements, for example ^{15}N, ^{13}C and/or $_2D$ labelling can be achieved easily. Furthermore the incorporation of unnatural amino acids is feasible.

APP_{0-55} was expressed using continuous exchange, precipitation based cell-free synthesis.

Hydrophobic proteins like APP_{0-55} simply precipitate and can, at least in most cases, remain correctly folded or will fold correctly upon solubilization.

Cell-Free Containers

Three different RM containers were used. For analytical scale expression 150 μL RM were used. For preparative scale expressions one first a 650 μL container was used but for even higher yield a 1 mL container was developed with the highest surface to volume ratio achievable.

Cell-Free Setup

First the amino acid mix adjusted for the respective peptide was prepared. Then the master mix (MM) was generated, this was used to prepare feeding mix (FM) and reaction mix (RM). RM was prepared immediately before start of the expression and was kept cool. Volumes were adjusted depending on the desired FM:RM ratio and the RM volume. Reaction conditions varied from 30 to 34 °C in temperature and 20 to 22 h in duration. Both cell extracts (P- and R-extract) were tried. One exemplary batch is given on the next page. The others can be found in the appendix (pp. 158, 159, 160).

The membrane used had a molecular weight cutoff of 12 - 14 kDa (ZelluTrans/ROTH T3). As precipitation based cell-free expression was used, diffusion of the peptide with MW of about 4 kDa out of the RM did not occur despite the high MWCO.

An examplary setup is given on the next page. APP_{0-55} was expressed in precipitation mode. Mg^{2+} was 14 mM, K^+ was 240 mM. FM:RM was 12:1 and 1 mL RM was used. The reaction was carried out for 21 h at 34 °C.

APP MDAE P-CF 07.01.20, markiert			FM:RM 12:1		
Compound	**Stock Concentration**	**Final Concentration**	**MM (µL)**	**FM (µL)**	**RM (µL)**
ddH2O					
HEPES (pH 8.4)	2510 mM	100.00 mM	518		
Mg(OAc)2	2021 mM	5.63 mM	36		
KOAc	4002 mM	94.78 mM	308		
PEG 8000	40.03 % m/V	2.00 % m/V	649		
NaN3	10.25 % m/V	0.05 % m/V	63		
Folinic acid	20.00 mg/mL	0.10 mg/mL	65		
DTT	515 mM	2.00 mM	50		
NTP	75.00 x	1.00 x	173		
Complete	50.00 x	1.00 x	260		
PEP	1016 mM	20.00 mM	256		
AcP	1000 mM	20.00 mM	260		
aa-Mix	4.00 mM	1.00 mM	1625	1625	
Mastermix				4028	237
S30 C buffer	1.00 x	0.35 x		4200	
PK	2.40 mg/mL	0.04 mg/mL			17
tRNA	40.00 mg/mL	0.50 mg/mL			12.5
T7RNAP	200.00 U/µL	6.00 U/µL			30
RiboLock	40.00 U/µL	0.30 U/µL			7.5
DNA	749.00 µg/mL	26.00 µg/mL			35
S30-Extract	100.00 %	40.00 %			400
ND (MSP-buffer)	0.35 mM	0.00 mM			0
ddH2O				2147	262
		Total (µL)	4265	12000	1000

AA Mix ges 3.3 mL

AA	Stock c.	Final c.	AA µL
Ala	4.0 mM	1.00 mM	130
Arg	2.0 mM	0.50 mM	65
Asn	1.0 mM	0.25 mM	33
Asp	6.0 mM	1.50 mM	195
Cys	0.0 mM	0.00 mM	0
Gln	1.0 mM	0.25 mM	33
Glu	6.0 mM	1.50 mM	195
Gly	8.0 mM	2.00 mM	260
His	8.0 mM	2.00 mM	260
Ile	4.0 mM	1.00 mM	130
Leu	4.0 mM	1.00 mM	130
Lys	4.0 mM	1.00 mM	130
Met	6.0 mM	1.50 mM	195
Phe	3.0 mM	0.75 mM	98
Pro	1.0 mM	0.25 mM	33
Ser	3.0 mM	0.75 mM	98
Thr	2.0 mM	0.50 mM	65
Trp	0.0 mM	0.00 mM	0
Tyr	1.0 mM	0.25 mM	163
Val	8.0 mM	2.00 mM	260
H2O			780
		Total (µL)	3250

Mg2+	14 mM	
K+	280 mM	
Plasmid	749 µg/mL	

P-Extrakt, Nov 18	**Cond.**	34 °C, 100 rpm
Pivex+APP, 02.05.2019	**Start**	15:00
	End	12:00

Reaction Mix to Feeding Mix Ratios

Different reaction mix (RM) to feeding mix (FM) ratios were tested to find the best compromise between high yields at reasonable consumption of expensive compounds like labelled amino acids in the FM. FM:RM 8:1, 12:1, 17:1 and 20:1. As 8:1 resulted in significantly lower amounts of peptide whereas 12:1, 17:1 and 20:1 did not lead to notably different yields. Thus for large scale expressions FM:RM ratio of 12:1 was used.

Magnesia Concentrations

Cell-free expression is largely influenced by Mg^{2+} (and to a lesser extent K^+) concentrations. Mg^{2+} can be adjusted by the amount of $Mg(OAc)_2$ solution added while it has to be taken into account that S30 C buffer and S30 extract already contain Mg^{2+}. For this reason total concentrations of 14 mM, 16 mM and 18 mM were tested. The best results were obtained when using 14 mM Mg^{2+}.

P- and R-Extract

Both cell extracts were tried. In the case of APP higher yields were obtained using P-extract. Interestingly, within the scope of a Master's Thesis [158] , cell-free expression of TNR12 was tried where R-extract lead to better results. Thus it seems to be dependent from the construct which cell extract works better.

Detergent Based Cell-free Expression

In the context of the Master's Thesis mentioned above detergent based cell-free expression was tested as TNR12 did not provide as high yields as APP and seemed to form aggregates that could not be dissolved.

Hein et al. suggest, amongst others, Brij-98 as detergent to use in cell-free expression [159]. To improve protein folding Brij-98 was added in a final concentration of 1.7 mM to the reaction mix for TNR12 expression. TNR12 was successfully incorporated into the micelles but detergent exchange with detergents established for NMR spectroscopy, DPC for example, was not easily achieved.

Disulphide Bond Formation

To prevent aggregation due to formation of unintentional disulphide bonds glutathione can be added during cell-free expression [160]. The addition of oxidized and reduced glutathione keeps newly forming disulphide bonds in equilibrium and promotes correct folding. 1 mM oxidized and 4 mM reduced glutathione were added to the reaction mix [158]. This seemed a promising approach for proteins with disulphide bonds but was not applied to APP that does not contain cysteines.

Purification

Due to the hydrophobic nature of the expressed peptides they precipitated in the RM, what made purification easy. Peptides were harvested by centrifugation (10000 xg, 30 min, 4°C). Supernatant was discarded and the pellet was incubated with 500 μL CF wash buffer (pp. 153) at 30 °C for 30 min. After a second centrifugation step the pellet was again dissolved in 500 μL CF wash buffer (pp. 153), incubated again. Then a third centrifugation step followed. The supernatant was discarded, the pellet resuspended in 200 μL H_2O and lyophilised.

Nanodisc Preparation and Assembly

MSP Expression and Purification

MSP1D1ΔH5 expression was done according to the protocol published by Hagn et al. in 2017 [161]. pet28a-MSP1D1ΔH5 plasmid was purchased from addgene (addgene, Watertown, MA 02472,USA [162]).

Nanodisc Assembly

Nanodiscs were prepared following the protocol of Hagn et al. [161]. MSP1D1ΔH5 was concentrated to a final concentration of 500 μM. A 50 mM DMPC stock solution was prepared in 100 mM cholate buffer. For nanodisc assembly the compounds were mixed as follows:

Volume	component	final concentration
1.2 mL	MSP-buffer	
0.6 mL	DMPC stock	10 mM
1.2 mL	MSP1D1ΔH5	200 μM

The mixture was incubated at room temperature for one hour. To remove detergents Bio-Beads (Bio-Rad, Hercules, California) were added, incubated for one hour, then the same amount of Bio-Beads was added and incubated for another two hours. After Bio-Bead removal the solution was dialysed against MSP-buffer.

Cell-Free Protein Expression into Nanodiscs

Cell free expression of TNR12 into nanodiscs was tried (pipetting scheme p. 160). Nanodiscs were assembled according to the procedure described above and dialysed against MSP buffer without EDTA because EDTA might impair cell-free expression. Nanodiscs were supplied at a final concentration of 0.05 mM.

After expression the RM was purified via Ni-NTA affinity chromatography following the procedure described above. Buffer was exchanged against NMR buffer.

3.6. Circular Dichroism Spectroscopy

CD spectra were acquired on a JASCO J-810 spectrometer (*Jasco, Pfrungstadt, Germany*) of IBG-2, KIT. Scanning mode was 10 nm/min, scanning speed 8s, data pitch 1 nm and

three spectra were accumulated. Measured was circular dichroism (CD), voltage (HT) and absorbance (Abs) from 180 to 250 nm. Sample concentratation was set to 50 μM and pathlength was 1 mm.

Data was analysed using the BestSel online tool [163] [164].

4. Amyloid Precursor Protein

4.1. Introduction

4.1.1. Alzheimer's Disease

General Overview

Alzheimer's disease (AD), that contributes to 60% to 80% of dementia cases [165] was first described by Alois Alzheimer in 1906 [166]. In 2013, the G8 held the first dementia summit, addressing dementia as a global health problem. One of the aims defined there was to find a cure or therapy by 2025.

While dementia describes the loss of mental ability due to the damage or destruction of neurons that interferes with daily life in general, Alzheimer's is a specific brain disease and thus a type of dementia. Common symptoms of AD are, at early stages, difficulties remembering recent information, apathy and depression. With progression of the disease, symptoms become more severe, such as problems with speaking, walking and swallowing. In 2013, the diagnostic criteria of AD were updated to include alterations in the brain before symptoms appear [167–170].

The main risk factor for dementia, and therefore AD, is age [171], with 15% of patients being between 65 and 74 years old and 44% between 75 and 84. AD is relatively rare in people who are younger than 65 [172]. While 1.9% of the German population suffered from dementia in 2018, the number of AD patients is expected to reach almost 3.5% of the total population in Germany within the next 30 years [172]. In the United States more than 25% of deaths are due to AD [173]. The second risk factor is family history [174], as people with relatives suffering from Alzheimer's are more likely to develop the disease [175]. Whether this is due to genetic or rather environmental and lifestyle factors is unclear. Another factor is the ε4 form of the *APOE* gene that increases risk of AD compared to its other variants, especially at a younger age [176–179].

Indicators of AD in the Brain

In 1984, Glenner et al. isolated Amyloid beta (Aβ) peptides from the cerebrovascular amyloid of a patient and unravelled their amino acid sequence [180]. One year later, Masters et al. linked them to amyloid plaques when they determined the amino acid sequence of Aβ in these plaques [181], which led to the identification of the gene encoding for the β-amyloid precursor protein (APP) [182–185].

The two indicators of AD are the accumulation of Aβ fragments outside neurons in the brain and tau protein tangles inside neurons, which ultimately lead to neuronal damage and death [165]. Aβ plaques are believed to impair neuron-to-neuron communication and

tau tangles to prevent the transport of metabolites into neurons [165]. Amyloid plaques result from the accumulation of Aβ peptides. These are the product of subsequent cleavage of the β-amyloid precursor protein (APP), first by β-secretase and then by γ-secretase [186].

The amyloid hypothesis dominated AD research in the last decades [187–190]: Normally, Aβ is released from the cell and rapidly degraded. Under pathological conditions, however, the Aβ fragments cannot be degraded but accumulate. The two main components of these agglomerates are Aβ40, which is 40 amino acids long, and the more hydrophobic Aβ42, which is two amino acids longer. Amyloid fibrils that mature into plaques are formed when Aβ42 levels increase. These clusters then induce tau pathology and subsequently neuronal cell death and neurodegeneration.

Early Onset Familial Alzheimer's Disease

The vast majority (more than 90%) of AD cases are sporadic at older age [191]. Early onset familial Alzheimer's disease (FAD) leads to AD symptoms at unusually young age. This form accounts for 1% to 6% of all AD cases. It is generally hereditary, and patients carrying one of these mutations are not only more likely to develop AD, but literally guaranteed to [192]. Mutations within three genes are known to cause FAD: *APP*, *PSEN1* or *PSEN2* genes. Most mutations are found in the *PSEN1* gene, which encodes for the catalytic subunit of γ-secretase, presenilin (PSEN) [193].

AD Drug Development

Drug development concentrated on blocking Aβ formation. The inhibition of β-secretase BACE1, which performs the first step of APP processing, alters APP cleavage and results in peptide fragments other than Aβ [194]. The second promising drug target is γ-secretase, so several so-called γ-secretase modulators (GSM) or inhibitors (GSI) are being investigated. Two potential drug candidates, Semagacestat, which blocks APP and Notch cleavage [195], and Avagacestat, which selectively prevents APP processing over Notch, have been investigated in clinical trials [196]. Furthermore, allosteric GSIs were intended to impair Aβ42 production [197]. The second large branch are anti-amyloid agents as, for example, monoclonal antibodies targeting Aβ [198]. More recent developments concentrated on targeting plaque formation in the early stages of the disease.

4.1.2. Amyloid Precursor Protein

The amyloid precursor protein, a central feature of Alzheimer's disease [199], is the most widely studied γ-secretase substrate on the basis of which proteolytic processing was assessed.

APP is expressed in various tissues but is concentrated in the synapses of neurons [200]. Its precise function is not yet clear, but it has been shown to be involved in neural plasticity [201] and regulation of synapse formation [202]. After synthesis in the endoplasmic reticulum (ER), it is transported to the Golgi apparatus where it is modified. Subsequently, it is transported to the cell surface via the secretory pathway [203]. It is also endocytosed

from the cell surface and processed in the endosomal-lysosomal pathway [204]. APP and Aβ have been found in mitochondria and have been implicated in mitochondrial dysfunction [205, 206].
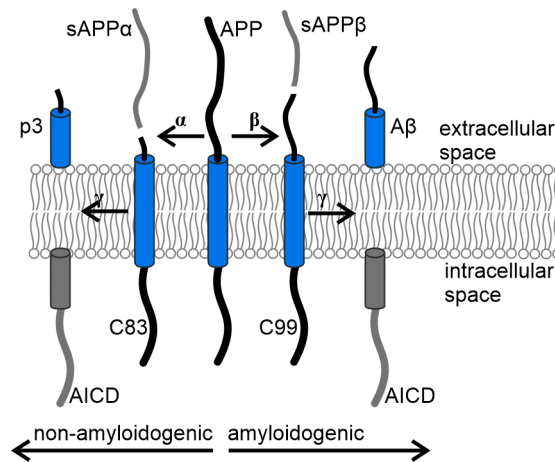
Figure 4.1. Summary of the different processing routes of APP: Full length APP is incorporated into the cell membrane. It can be processed following two principal routes. First, it is cleaved by either α-secretase or β-secretase, resulting in the formation of sAPPα and C83 or sAPPβ and C99, respectively. C83 and C99 are then further processed by γ-secretase, leading to the generation of p3 and AICD or Aβ and AICD. The AICD is released into the cell, while p3 and Aβ are released to the extracellular space.

In neuronal cells, there are two major APP proteolysis pathways: The more prevalent non-amyloidogenic pathway leading to small p3 peptides [207] and the amyloidogenic pathway resulting in Aβ generation. Both pathways follow the same principle as depicted in Figure 4.1. Following the non-amyloidogenic pathway, α-secretases initiate cleavage by the ADAM-family metalloproteases ADAM10 or ADAM17 at or near the cell surface, resulting in soluble sAPPα and membrane anchored C83 [208]. α-Secretase mediated cleavage of APP has been observed in the *trans*-Golgi network, at the plasma membrane and in endocytic compartments [209, 210]. The N-terminal fragment is released into the intracellular space and the remaining membrane-anchored C83 is further cleaved twice by γ-secretase, resulting in the release of APP intracellular domain (AICD) and the small p3 peptide ($A\beta_{17-42}$) [211–215]. The p3 peptide might be neurotoxic as it has been shown to induce apoptosis in cell cultures [216] and modulate inflammatory response [217]. sAPPα was assumed to represent the primary physiological function of APP based on multiple studies [218–220]. Its effect on neurons is generally assumed to be positive [221, 222]. C83 is a poorer substrate for γ-secretase than C99, which is generated via the amyloidogenic pathway [223]. Therefore, the generation of C83 indirectly prevents Aβ production [224].

The amyloidogenic route shown in Figure 4.1 initiates with cleavage of APP by β-secretase (BACE), releasing soluble sAPPβ and leaving membrane-anchored C99 [225–228]. C99 is subsequently cleaved by γ-secretase at various cleavage sites, again following multiple pathways. The first cleavage occurs at the so-called ε-cleavage site [229], which is buried three or four residues inside the lipid bilayer on the cytosolic side. This generates AICD, that is released into the cytosol, and a remaining membrane-anchored Aβ peptide.

sAPPβ has been shown to exhibit neuroprotective effects like sAPPα but is less effective [221]. C99 has been found to be toxic and to induce symptoms of AD [230, 231].

The AICD, which is the same in both pathways, assembles in a complex with the adaptor proteins Fe65 and Tip60, translocates to the nucleus, and regulates apoptosis and the transcription of genes such as *KAI1, glycogen kinas-3β, neprilysin* and *p53* [213, 215, 232, 233].

Multiple pathways of C99 processing exist (Figure 4.2). Initial ε-cleavage can occur after either residue L_{49} or T_{48}, leading to Aβ49 and AICD49 or Aβ48 and AICD50 [229, 234, 235]. Subsequent tripeptide and to a lesser extent tetra- and pentapeptide cleavage result in different Aβ species [236, 237]. Under normal conditions less than 10% of total Aβ is the more aggregation-prone Aβ42 and about 90% of Aβ is Aβ40 [238–240].
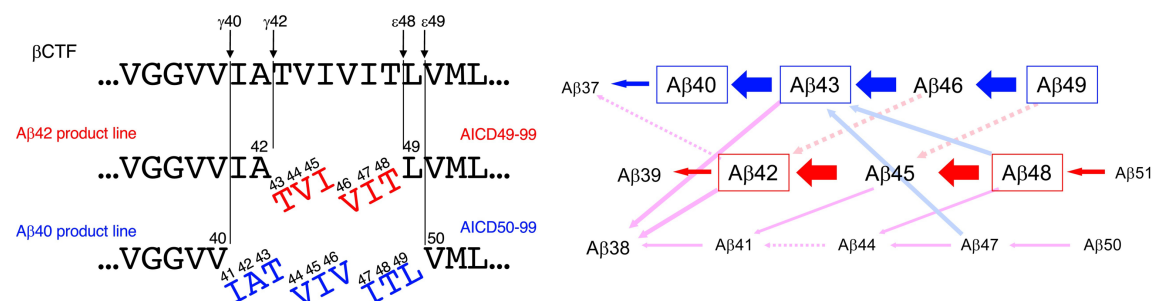
Figure 4.2. Successive processing of C99 by γ-secretase: Left: The processing of C99 starts at the ε-cleavage site at either L_{49} or T_{48}. Then, two or three tripeptide fragments are removed, resulting in Aβ42 or Aβ40. Right: In addition to these two main routes, alternative routes are possible. Aβ43 and Aβ42 can be further processed to Aβ38 or pathway transitions may occur [241]. Reprinted from Seminars in Cell & Developmental Biology, 105, Funamoto et al., Successive cleavage of β-amyloid precursor protein by γ-secretase, pp. 64-72 (2020), with permission from Elsevier.

Apart from these two major routes, interconversion between pathways is possible as depicted in Figure 4.2. Thus, the final Aβ length is not strictly determined by the initial ε-cleavage site, but a variety of paths are possible, resulting in all kinds of Aβ. In most cases, C99 processing follows the main routes. [241, 242].

There is evidence that this tripeptide cleavage scheme holds true for other γ-secretase substrates as well. Investigation of C83 processing showed that five different tripeptides were released, also suggesting two product lines (unpublished observation in [243]). γ-Secretase processing of APLP1 was found to produce three different, Aβ-like peptides and the collocation of cleavage sites in the transmembrane domain (TMD) suggested a tripeptide cleavage mechanism [244]. Accordingly, Notch1 proteolysis was found to generate three or four amino acid long fragments [245] and Nβ fragments of varying lengths (Nβ21, Nβ25) [246]. Cleavage site location resembled those of APP as well [247]. And, last but not least, PSEN autoproteolysis was also found to follow a tripeptide scheme [248].

APP TMD Structure

Four experimentally determined structures of APP TMD in membrane mimetics, shown in Figure 4.3, were published.
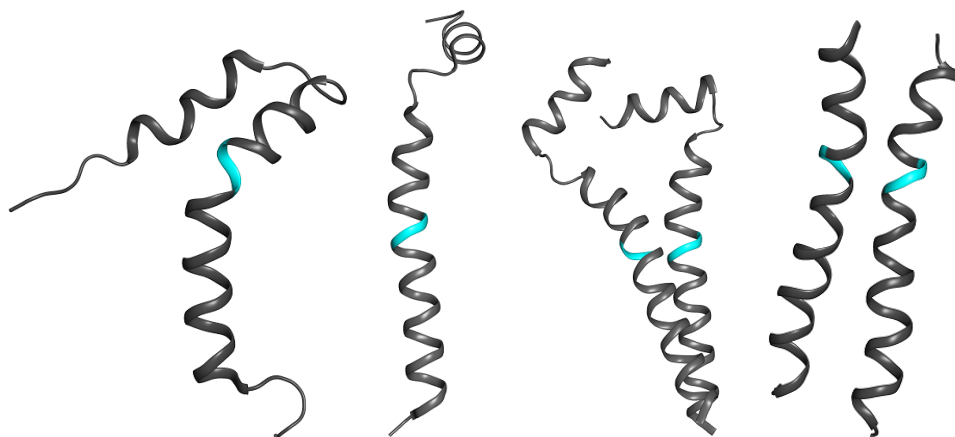
Figure 4.3. APP TMD structures in micelles: From left to right: APP TMD monomer in LPMG micelles (PDB: 2LP1; Barrett et al. [249]), APP TMD monomer in DPC micelles (PDB: 2LLM; Nadezhdin et al. [250]), left-handed APP TMD dimer in DPC micelles (PDB: 2LOH; Nadezhdin et al. [251]), right-handed APP TMD dimer in DPC micelles (PDC: 2LZ3; Chen et al. [252])

Barrett et al. observed a monomeric, highly curved structure in lyso-myristoyl phosphatidylglycerol (LMPG) micelles (PDB: 2LP1) with the apex of curvature at the GlyGly-motif in the middle of the TMD. For structure determination, they used a combination of NMR restraints such as NOE distances, RDC values and distances derived from paramagnetic relaxation enhancement experiments. [249] Nadezhdin et al. observed APP TMD as monomer and as dimer in n-dodecylphosphocholine (DPC) micelles, depending on the detergent to peptide ratio they used. When they used 50 DPC molecules per APP TMD they observed two sets of signals in a ^{1}H-^{15}N-HSQC spectrum, from which they assumed that monomeric and dimeric APP TMD were present in the sample. When they increased the detergent to peptide ratio to 70:1 only one set of signals was visible in the corresponding spectrum. Therefore, they concluded that the monomer dimer equilibrium could be shifted to the respective side by means of the detergent concentration. Structures calculated based on NOE restraints derived from filtered NMR experiments resulted in a left-handed parallel dimer, with the dimerization motif basically along the whole TMD (PDB: 2LOH). The monomer structure they had published one year before (PDB: 2LLM) only deviates slightly from the structures of the two molecules forming the dimer. [250, 251] Chen et al. published a further dimer structure, also in DPC micelles. In contrast to the structure of Nadezhdin et al. they observed a right handed dimer with the interface mainly at $G_{38}XXXA_{42}$. However, similar to Nadezhdin et al. they detected hydrophobic side chain contacts almost along the whole APP TMD. [253] These structures will be analysed further in the context of experimental data obtained in this thesis.

4.1.3. γ-Secretase

γ-Secretase is considered the "proteasome of the membrane" [254], due to the large number of substrates. Güner & Lichtenthaler recently described 149 γ-secretase substrates [255, 256]. Its supposed function is to clear out protein stubs in the membrane that cannot be degraded by the proteasome. However, when cleaved by γ-secretase, intracellular and extracellular domains can emerge from the membrane to be degraded by the proteasome [255]. Contradicting this theory, γ-secretase was found not to cleave all protein stubs and γ-secretase inhibited cells did not accumulate large amounts in their membranes [257, 258].

γ-Secretase substrates

γ-Secretase substrates and their cleavage products cover a broad range of physiological functions as many γ-secretase substrates are, for example, involved in regulatory processes. APP was shown to be crucial for synapse formation and function [202], axonal transport [259], neurite extension [260] or cell adhesion [261, 262]. Furthermore, numerous key signalling pathways were found to depend on γ-secretase processing [263–265]. In AD related neurodegeneration some of these processes are disturbed [204, 266].

Besides APP, some of the best studied γ-secretase substrates are Notch1, cadherin, ErbB4, p75NTR, TREM2 and BCMA [255].

Notch receptors (Notch1, Notch2, Notch3 and Notch4) are part of signalling pathways in many aspects of animal development [267, 268]. γ-Secretase plays an important role in the Notch1 pathway during development [269–272], as the intracellular cleavage product (Notch intracellular domain, NICD) enters the nucleus where it regulates expression of genes involved in cell differentiation [245]. The importance of balanced Notch1 expression and processing can be deducted from the finding that the inhibition of Notch1 signalling by γ-secretase knockouts was shown to be lethal in embryonic cells [269, 270] and lead to severe toxic effects like gastrointestinal bleeding, immunosuppression, and skin lesion in clinical trials [273, 274]. On the other hand, tumour growth (for example leukaemia) is induced when Notch signalling is hyperactivated [275–277].

N-cadherin, a cell adhesion molecule, is involved in regulation of transcription factors after γ-secretase cleavage, which in turn are involved in various processes like cell growth, differentiation and apoptosis [264].

γ-Secretase Substrate Features

γ-Secretase substrates share no obvious common features, such as a consensus sequence at or near the cleavage site that would allow to distinguish substrate from non-substrate. Most γ-secretase substrates are α-helical type I transmembrane proteins, i.e. single-pass peptides with cytosolic C-termini and extracellular N-termini harbouring large ectodomains [255, 256]. Because the enzyme prefers short ectodomains [257], a shedding step takes place before γ-secretase cleavage [278, 279]. BCMA is the only known substrate whose ectodomain is inherently short enough to be processed directly [280]. More precisely, it has been shown that exceedingly long ectodomains impair γ-secretase cleavage and that the TMD of the substrate is sufficient for high-affinity binding [278, 281], as APP,

for example, could be cleaved when only the TMD and few additional N-terminal amino acids were provided (E_{22} to K_{55}) [282]. Therefore, ectodomain shedding could be the first step of substrate selection. Few non-substrates are known, which further complicates the narrowing of substrate requirements. One non-substrate is integrin β1 [257], whose amino acid sequence, however, does not reveal any noticeable features that could explain why it is not cleaved by γ-secretase. As a consequence, it was hypothesised that the TMD topology, conformation and flexibility of the substrate determined the cleavability [283].

As explained above, APP is not always processed following the same pathway, but two ε-cleavage sites and several ζ- and γ-sites have been identified. To further complicate matters, transitions between the two major pathways are possible, as shown in Figure 4.2 [237, 284]. Therefore, it was assumed that ε-cleavage preference and the other processing steps were uncoupled and possibly dependent on different substrate properties [243].

Three major models have been proposed to explain how enzymes select their substrates. The first theory was proposed by Emil Fischer in 1894, the lock-and-key hypothesis [285]. A few decades later, the induced fit hypothesis was suggested by Dan Koshland, accounting for conformational plasticity of enzymes [286]. Another 50 years after that Ruth Nussinov introduced the conformational selection hypothesis, which recognises that enzymes (and their substrates) are ensembles of many differentially populated states [287]. In the case of γ-secretase, it seems unlikely that there is a fixed enzyme conformation in which the substrate, presumably also stationary, may or may not fit. It is more likely that the complex formation is based on induced-fit or the selection of a suitable substrate conformer from a structural ensemble, as has been described for other systems [288, 289]. Both cases require conformational ductility of substrate and/or enzyme. This fits with the finding that proteases generally need their substrates to unfold around the cleavage site [290] and that cleavage efficiency is related to the TMD stability of the substrate [33, 35–37, 291–293]. Various conformational transformations of membrane proteins have been described [294–296]. Many deviate from α-helical conformation and exhibit bends, curved axes or π- or 3_{10}-helical regions [297, 298]. In addition to the helix backbone, the side chains are also flexible and can switch between rotameric states [299] and intrahelical hydrogen bonds can open and close. All these local fluctuations taken together can result in global conformational changes such as helix bending or twisting [300].

For APP, in particular, flexibility at a double glycine motif in the middle of its TMD has been proposed to be required for substrate entry into the enzyme. It was assumed that this motif acts as a hinge, facilitating the necessary bending motion during translocation to the catalytic cleft [249, 301].

γ-Secretase Structure

γ-Secretase is a complex of four integral membrane proteins: Nicastrin, anterior pharynx-defective 1 (APH1), presenilin enhancer 2 (PEN-2) and the catalytic subunit presenilin (PSEN) [302]. Structures obtained by cryo-electron microscopy (cryo-EM) confirmed that the γ-secretase complex consists of one entity of each subunit [303–305]. γ-Secretase compositions vary between cell types and tissues [306]. Between four and six different γ-secretase complexes exist, since two APH1 isoforms have been described in humans (APH1a and APH1b) [306] and two PSEN variants (PSEN1 and PSEN2) have been found [307, 308].

The complexes containing PSEN1 were found in the secretory pathway compartments, especially at the plasma membrane whereas PSEN2 is rather localized in endosomes and lysosomes [309, 310].
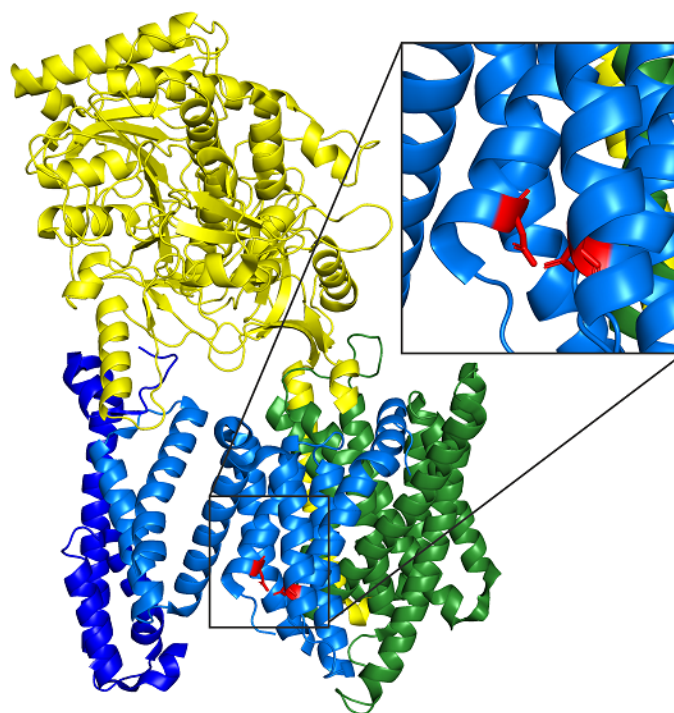
Figure 4.4. γ-Secretase structure (PDB: 5A63 [311]): The four subunits are shown in different colours: nicastrin (yellow), APH1a (green), PEN2 (dark blue) and PSEN1 (light blue). The catalytic aspartates of PSEN are depicted in red.

The catalytic subunit PSEN is an aspartyl protease, as mentioned above. In TMD 6 (D_{257}) and TMD 7 (D_{385}) of PSEN, there are two aspartates, marked in red in Figure 4.4, which are located near the border between membrane and intracellular side. They have been shown to be crucial for cleavage as their mutation completely prevented APP processing [213, 312, 313]. The active site is therefore most likely located between these two TMDs. During assembly of the γ-secretase, PSEN undergoes autoproteolysis within the loop connecting TMD 6 and TMD 7 [314, 315]. The two catalytic aspartates of PSEN are involved in this step as well [312, 313].

The bulky nicastrin ectodomain governs entry and retains the substrate in the complex [278, 316]. This was shown as reducing disulphide bonds in nicastrin allowed cleavage of substrates with longer ectodomains that previously could not be processed with intact nicastrin [278, 279]. PEN-2, which stabilises the two PSEN fragments after autoproteolysis [317], consists of a single-pass TMD (TMD 2) and another TMD that enters the membrane but does not traverse (TMD 1). TMD 1 forms a reentrant loop that turns back within the membrane [318]. PEN-2 interacts directly with TMD 4 of PSEN1 [319, 320]. The catalytic pore itself was found to be constantly accessible to water molecules that are required for proteolysis [30].

Enzyme-Substrate Complex
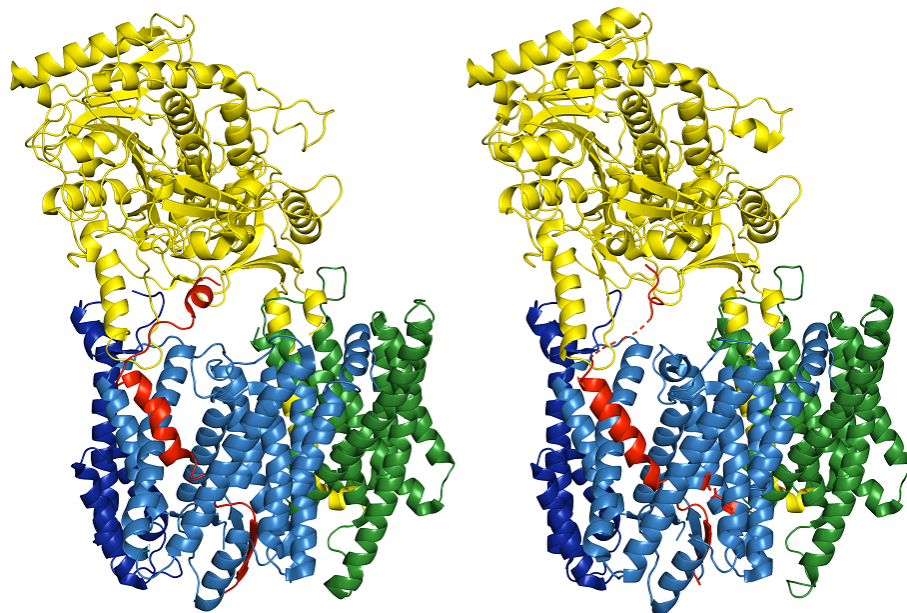
Figure 4.5. cryo-EM structures of the γ-secretase-substrate complex: The substrates were covalently bound to PSEN at their N-termini by a disulphide bond. Furthermore, D_{385} was mutated to alanine to deactivate the enzyme. Left: Notch-100 (PDB: 6IDF [304]). Right: C83 (PCB: 6IYC [305]) Nicastrin (yellow), APH1a (green), PEN2 (dark blue) and PSEN1 (light blue). APP and Notch are depicted in red.

PSEN1, APH1 and PEN-2 are arranged in a horseshoe-like shape in the membrane, covered by nicastrin, as it could be confirmed by the first cryo-EM structure without substrate [311]. Recently, cryo-EM structures of the γ-secretase-substrate complex have been published and are shown in Figure 4.5. Zhou & Yang et al. introduced a cysteine residue into loop 1 of PSEN1 and another one within the N-terminus of each substrate shortly before the beginning of their TMDs. In addition, to prevent cleavag one of the catalytic residues, D_{385}, was mutated to alanine. The substrate was located in a cavity formed by TMD 2, TMD 3, TMD 5, TMD 6, and TMD7 of PSEN1. They found that APP TMD unwound at its C-terminus and formed a hybrid β-sheet, from M_{51} to K_{55}, with two β-strands on loop 2 of PSEN1. The preceding residues, T_{48}, L_{49} and V_{50} adopted a completely extended conformation that enabled access to the scissile bond, by the catalytic residues. For Notch1, they observed a similar conformation as it likewise formed a hybrid β-sheet with loop 2 of PSEN1. [304, 305] In the case of APP, the positioning of the substrate TMD between PSEN NTF and PSEN CTF was revealed earlier when Fukumori et al. found amino acids A_{42}, V_{44}, I_{45} and L_{49} to interact with PSEN NTF and M_{51} and L_{52} with PSEN CTF via photoreactive labelling assays [321]. Furthermore, the cryo-EM structures showed that the N-terminal domain of the substrate is in contact with PSEN1 and that both substrates, which are supposed to bend upon entry into the enzyme, appeared straightened again [304, 305].

Dynamics of γ-Secretase

The two structures of the γ-secretase-substrate complexes provide valuable insights into the substrate positioning within the catalytic cleft [304, 305]. However, like all cryo-EM structures, they represent only static snapshots of what are most likely dynamic events.

γ-Secretase domain motions were studied under different conditions. Nicastrin has been shown to be the most mobile subunit, with its ectodomain moving up and down and rotating [322–324]. In addition, the small and large lobe of nicastrin were found to move independently [325] but this mobility appears to be uncoupled from the TMD movement around the active site [322, 324, 325]. Since interactions between APP, PSEN2 and nicastrin have been observed in photo-affinity studies [321], nicastrin might play a role in substrate adaption or stabilisation of the enzyme-substrate complex.

TMD 2, TMD 3 and the cytosolic fragment of TMD 6 of PSEN1 were found to be highly mobile in molecular dynamics (MD) simulations based on the cryo-EM structure of γ-secretase with the γ-secretase inhibitor DAPT (PDB: 5FN2) [311]. Transitions from the active to the inactive state required motions of TMD 1, TMD 6, TMD 7, TMD 8 and TMD 9 (for TMD numbering see Figure 4.6) [322, 325].

The general mechanism of aspartic proteases suggests that one aspartate acts as an acid and attacks the peptide bond [326, 327], which was confirmed by MD simulations showing that one of the aspartates has to be protonated to form the active site [322]. In the absence of substrate, the active site was stabilised by either a water-bridged structure or a hydrogen bond between the two catalytic aspartates [325].

Substrate Recognition by γ-Secretase

It has been suggested that the initial contact between the substrate and the nicastrin exosite occurs prior to contact with the active site [321]. Moreover, it has been shown that conformational changes in PSEN1 TMDs, PEN-2, and the hydrophilic loop 1 were necessary to enable the interaction. In particular, loop 1 connecting TMD 1 and TMD 2 of PSEN, interacted with charged residues of APP, whereas the $G_{29}XXXG_{33}XXXG_{37}$-motif of APP TMD interacted with PSEN TMD 2. Consequently, the ε-site was exposed to the lipid interface. [311, 323]

Substrate entry into γ-secretase

Substrate entry to the catalytic site of γ-secretase was not unravelled yet. Three main scenarios are discussed that are shown in Figure 4.6: Entry could occur through an opening between TMD 2 and TMD 6 [328–330]. This would require the N-terminus of the substrate to wiggle underneath the loop connecting TMD 1 and TMD 2 (loop 1), which in turn would have to be highly mobile to act as a gatekeeper at all. Bolduc et al. showed that nicastrin was the limiting factor for the size of the substrate ectodomain. They used a construct of C83 bound to ubiquitin to introduce a very bulky ectodomain. This fusion protein was not cleaved under native conditions. When they reduced the disulphide bonds of nicastrin, however, they observed that ubiquitin-bound C83 was efficiently processed. They concluded that if loop 1 were the gatekeeper, the reduction of disulphide bonds should not have enabled processing of ubiquitin-bound C83. Thus, nicastrin must have been the

size limiting factor [278]. Entry between TMD 2 and TMD 3 on the other hand would avoid this obstacle but there is another steric barrier. TMD 2 and TMD 3 are connected by a relatively short cytosolic loop (loop 2), that the C-terminus of the substrate would have to overcome [325]. And the third pathway would be through the cleft between TMD 6 and TMD 9. Hitzenberger & Zacharias tested all three possible entry routes by MD simulations. They found the substrate in the catalytic cleft only in the case when the path through TMD 2 and TMD 3 was chosen as entry route. It has to be noted that they pulled the substrate into the enzyme much faster than it enters naturally and that they used a shorter fragment (V_{12} to Y_{57}), neither including the whole N-terminal nor the whole C-terminal domains. Their starting structure was based on the kinked structure determined in LMPG micelles, described above (PDB: 2LP1) [249]. Interestingly, they observed that H-bonding at the catalytic cleft with the substrate at its ε-site was already possible before the whole C-terminus had entered the enzyme. Additionally, they found TMD 2 and the N-terminal part of TMD 3 of PSEN to be quite flexible, allowing a wider opening for substrate entry than expected [325].
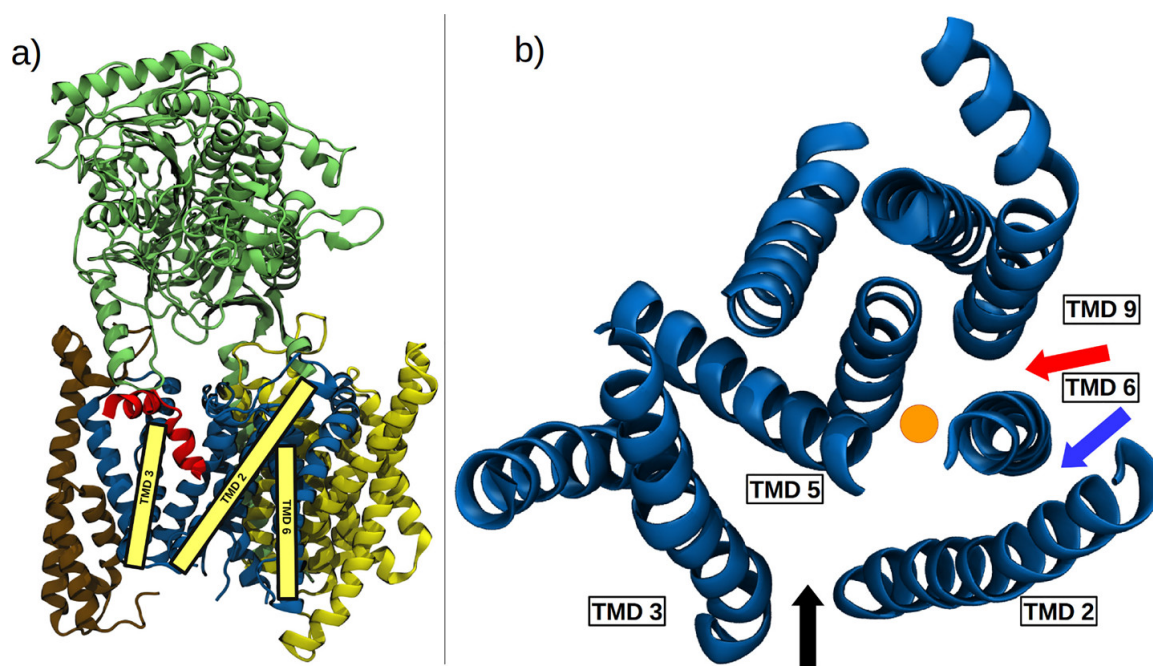
Figure 4.6. Possible substrate entry pathways into γ-secretase: a) Three-dimensional structure of γ-secretase b) Substrate entry was proposed via three different entry ways: Through the opening between TMD 2 and TMD 6 (blue arrow), which would require the N-terminus of the substrate to wiggle underneath loop 1 connecting TMD 1 and TMD 2; Between TMD 2 and TMD 3 (black arrow), which requires the C-terminus of the substrate to overcome loop 2 connecting TMD 2 and TMD 3; And between TMD 6 and TMD 9 (red arrow). The orange dot indicates the catalytic residues. [325] Reprinted with permission from ACS Chem. Neurosci. 2019, 10, 3, 1826-1840

During substrate entry, Hitzenberger & Zacharias observed a kink at $G_{37}G_{38}$ when the N-terminus of APP had already reached its final position and its C-terminus bypassed loop 2. It was proposed earlier that the N-terminal substrate domain might remain bound

to the exosite, while the C-terminal domain could move into the active site by hinging at the double-glycine motif [249, 300, 301, 331]. When the C-terminus had reached its destination, the kink disappeared and APP adopted a straight conformation similar to the one observed in the cryo-EM structures [304, 325].

Substrate Unwinding and Cleavage

Once the substrate has reached its final position within the catalytic cleft, three more steps are required to finalize processing. The scissile bond of the substrate must be exposed to the catalytic residues to enable the actual hydrolysis and subsequently the products are released.

Upon final docking the C-terminal helix of the substrate is weakened [311, 332, 333]. One full helical turn is unwound (T_{48}, L_{49} and V_{50}) while the residues further towards the C-terminus form a β-sheet with two domains of PSEN1 [304]. Similar observations were made in the case of Notch [305].

γ-Secretase processing was found to be quite slow compared to soluble proteases as cleavage rate constants are about one per hour, for both Notch and APP [278, 334]. This was dramatically slower than cleavage rates observed in soluble proteases, which were about 40 per minute [335]. Thus, hydrolysis itself is unlikely to be the rate-limiting factor. Substrate unwinding, nevertheless, requires a high transition step energy, so this was proposed to be the rate-limiting step [289, 336].
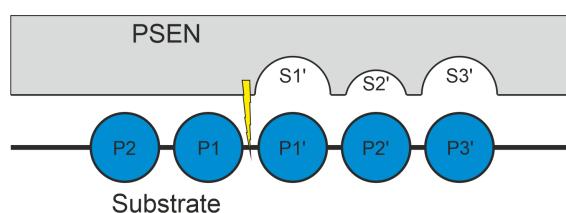
Figure 4.7. PSEN has three substrate binding pockets: Two large ones, S1' and S3', which can accommodate bulky amino acids and one small one, S2', that is limited to small amino acids with short side chains.

Three S' pockets were identified in the active site, schematically shown in Figure 4.7. Mutation assays suggested that the S1' and S3' pockets were large enough to accompany bulky amino acids, whereas S2' was considerably smaller and therefore limited to amino acids with short side chains [278, 325, 337]. Bolduc et al. also showed that cleavage pathways could be conducted (see Figure 4.2) by mutating V_{50} or M_{51}. The exchange of V50 with phenylalanine, tryptophan, or tyrosine, i.e. bulky amino acids at P2', led to initial ε49-cleavage resulting in Aβ40 mainly. In contrast, replacement of M51 with phenylalanine, tryptophan or tyrosine prevented ε49 cleavage, as the bulky amino acid would then be in S2', and shifted the cleavage line to ε48-cleavage, resulting in a predominant Aβ42. Additionally, they could show that not only ε-cleavage was affected but also ζ-cleavage. Furthermore, bulky amino acids at position 40 almost completely inhibited Aβ38 generation. [278] Thus, product line preferences appear to be mainly controlled by the amino acid that has to fit into S2'. Moreover, the product lines can also be shifted after ε-cleavage.

To enable successive cleavage steps along a substrate TMD helix, the distance between the two catalytic aspartates might fluctuate in a way that is facilitated by the glycine residues in the GXGD active site motif of TMD7 of PSEN. γ-Secretase was observed in three distinct states: closed, semi-open and open. They were discriminated by varying distances between TMD 2, TMD 3 and TMD 6 [325, 330]. MD simulations suggested that due to the different TMD distances, the size of the catalytic cleft changed and thus influenced the stability of the enzyme-substrate complex [330]. When APP TMD was bound, not only the closed, but also the semi-open and open states could be observed in MD simulations [328]. The semi-open state was determined as the most active, leading to shortest cleavage products while in the open state longer peptides arouse from shorter residence times [330]. Experimental results of Szaruga et al. substantiated these observations. They found that the enzyme-substrate complex was destabilised by the shortening of the substrate and that mutations of both PSEN and C99 destabilised the complex, resulting in longer cleavage products. However, when the complex was stabilised, processing continued and shorter fragments were produced [338].

4.1.4. Familial Alzheimer's Disease Mutations
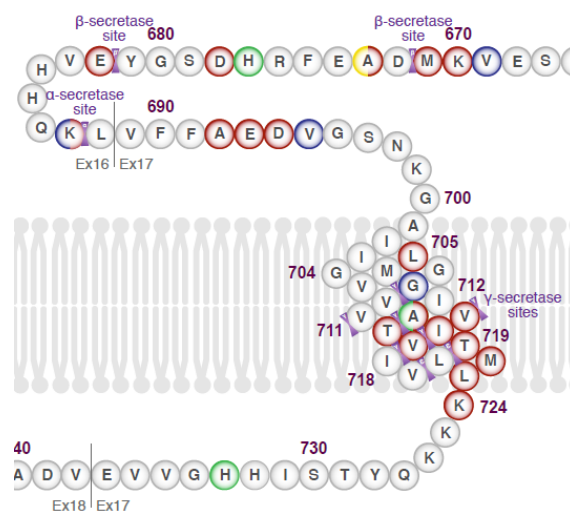
Figure 4.8. Known FAD mutations of APP: FAD mutations detected within the APP sequence. Marked red are positions where mutations were pathogenic, green indicates non-pathogenic mutation sites, yellow protective and blue mutations with unclear impact. (www.alzforum.org) [339]

Most FAD mutations of APP are located around the γ-secretase cleavage sites, as shown in Figure 4.8 [339] and generally result in a change of APP cleavage preferences, usually increasing the ratio of more toxic Aβ42 over Aβ40. Different mutations have different modes of action and affect ε-cleavage, processivity in general, or promote transitions between product lines. [2, 340–343]

In vitro experiments showed that the most abundant Aβ peptide generated by the processing of the C99 wild type (WT) was Aβ40, and to a lesser extent Aβ42, Aβ39 Aβ38 and Aβ37 [344, 345].

The so-called French mutation, V44M, was first described in 1999 [346]. It has been shown to lead to elevated Aβ42/Aβ40 ratios and to shift ε-cleavage preference from L_{49} to T_{48}, as could be revealed by double mutation essays [278, 347]. Pathway switching between initial ε- and γ-cleavage was excluded, as blocking ε-cleavage at T_{48} (V50F mutation) led to Aβ42/Aβ40 ratios comparable to WT levels [278]. Compared to WT, Aβ40 levels decreased and Aβ42 increased, leading to almost equal amounts [347]. Moreover, V44M was the only mutation in the study of Xu et al. that led to slightly increased protease activity compared to C99 WT, whereas all other FAD mutations investigated within the C-terminal part of C99 TMD diminished cleavage activity [347].

The other FAD mutant investigated in this thesis, I45T, was detected only once. The patient developed AD at the age of 36 and died seven years later [348]. I45T was found to even further increase Aβ42/Aβ40 ratios. The impairment of ε-cleavage at T_{48} (V50F mutation) did not significantly impact the Aβ42/Aβ40 ratio. Thus, the cleavage pathway probably shifted after the initial ε-cleavage step [278, 347]. Xu et al. detected dramatically higher amounts of Aβ42 compared to C99 WT, while Aβ40 levels were decreased for I45T. However, overall processing was significantly reduced [347]. Another study had led to similar results, as it was observed that AICD levels did not change compared to C99 WT, but Aβ40 decreased, while Aβ42 and more dramatically Aβ38 increased. This was interpreted as a shift in cleavage line preference towards ε48-cleavage [349].

Besides FAD mutants, numerous designed constructs have been studied. In most cases, a specific amino acid was exchanged for another, thereby specifically changing the properties of the protein. This allows hypotheses to be verified or falsified. Glycines are a frequent target, as they provide flexibility on the one hand and can be part of dimerization motifs on the other. Exchange of G_{33} with all other 19 amino acids did not decrease Aβ levels compared to WT (except for H, P, D and N). The exchange of G33L with isoleucine, valine, methionine or phenylalanine promoted processing to shorter Aβ species like Aβ38 and Aβ37, whereas hydrophilic amino acids at this position led to Aβ42 and Aβ40 production [350]. Exchange of hydrophilic threonines with hydrophobic valines led to dramatically increased Aβ42 levels and almost disappeared Aβ40 levels in the case of T43V, leading to ε48-cleavage. Similar effects were observed for T43I [350–352], while T48V had the opposite effect, as Aβ levels decreased while Aβ40 levels increased [350].

G38 was targeted in this work. Two G38 mutants of C99 were designed and analysed in collaboration with the Langosch Lab (TUM, Munich), the Scharnagl Lab (TUM, Munich), the Steiner Lab (DZNE & LMU, Munich) and the Huster Lab (Leipzig University). Our collaborators showed that processing of G38L by γ-secretase resulted in extremely high amounts of Aβ37 and no detectable levels of Aβ42. In contrast, G38P processing led to very high Aβ40 levels and no Aβ42. Intriguingly, the overall ε-cleavage was apparently impaired, as the total amount of the G38L AICD was reduced to about 38% and Aβ to 47% compared to C99 WT. In the case of G38P, AICD and Aβ were further reduced to 8% and 16%, respectively [344]. These observations suggest that the overall processivity was reduced for both G38 mutants, but once positioned in the catalytic cleft of γ-secretase, they are processed more efficiently than C99 WT. ε-Cleavage preference cannot be easily deducted from these findings, as Aβ38 can result from both pathways (see Figure 4.2).

Fernandez et al. exchanged I_{47} and T_{48} against GG (or GA). This resulted in almost 4-fold higher AICD levels due to helix destabilisation in this region, while replacement

with LL reduced AICD levels by almost 4-fold compared to WT. Additionally, V$_{max}$ and k$_{cat}$ were increased for the GG and GA mutants and decreased for the LL mutant. In the case of the GG mutation, γ-secretase almost exclusively favoured ε49-cleavage. Mutations of V$_{44}$ and I$_{45}$ to GG, GA and LL did not considerably affect ε-cleavage while the I$_{41}$ and A$_{42}$ with GG and GA led to the complete impairment of γ-secretase cleavage. The I41G/A42G mutant was found to form a stable dimer, both mutations added another GxxxG or GxxxA motif to the TMD. This suggests that too strong dimerization of the substrate prevents γ-secretase cleavage. Besides, all V$_{44}$I$_{45}$ and I$_{41}$A$_{42}$ to LL mutations primarily led to AICD49 resulting from ε48-cleavage [353]. Thus, they showed that destabilisation of the helix around the ε-cleavage site promotes processing by γ-secretase while stabilisation of the helix impairs cleavage. Mutations in the middle of the C-terminal helix, in contrast, did not exert dramatic effects. β-Branched amino acids near the ε-site (I47, T48) are known to destabilise helices due to their bulky side chains [354]. Mutation of I47 and T48, the residues close to the scissile bond, increased and sped up AICD production [353]. On the other hand, the replacement of V46 with glycine or leucine decreased cleavage efficiency [347].

The only FAD mutation known at the GlyGly-motif, G38S, was found to decrease Aβ40 and to increase Aβ39 levels and, to a lesser extent, Aβ37 [345].

Considering all these observations, it can be concluded that it is not clear in which way mutations influence the interactions of enzyme and substrate and thus the cutting. One possibility is that the movement of the flexible GlyGly-hinge could be affected. Local effects do not necessarily cause this, as the flexibility of the TMD is based on an ensemble of factors and a complex network of hydrogen bonds. Since it has been shown that mutations of both threonines, which can form an additional hydrogen bond via their hydroxyl group, are associated with FAD [355], the loss of this additional hydrogen bond could affect the entire network of interactions and thus alter the mobility at the hinge [300].

4.2. Analysis of APP WT TMD in TFE/H$_2$O

The best known and thus most intensively studied γ-secretase substrate is the C99 fragment of the Amyloid Precursor Protein. A wide variety of mutations within APP TMD were identified that have very different effects on processing by γ-secretase and thus on the course of the progress of Alzheimer's Disease in patients. Thus APP TMD is commonly used as a model to access discriminating substrate properties.

APP TMD was studied in different environments and with a variety of liquid-state NMR-based methods. Furthermore, four single point APP TMD mutants were investigated, two associated with familial early-onset Alzheimer's Disease and two designed to alter the TMD structure in a predictable way. Special attention was paid to the GlyGly-hinge within the TMD that is supposed to be required for substrate entry into γ-secretase, as explained in the introduction to this chapter.

The peptides were analysed in a mixture of Trifluroethanol (TFE) and water, as special interest was on the migration of the substrate from the membrane into the enzyme. As soon as APP TMD, for example, migrates from the membrane to the active site of γ-secretase, its environment changes. Its conformation and motions are no longer restricted by the lipids
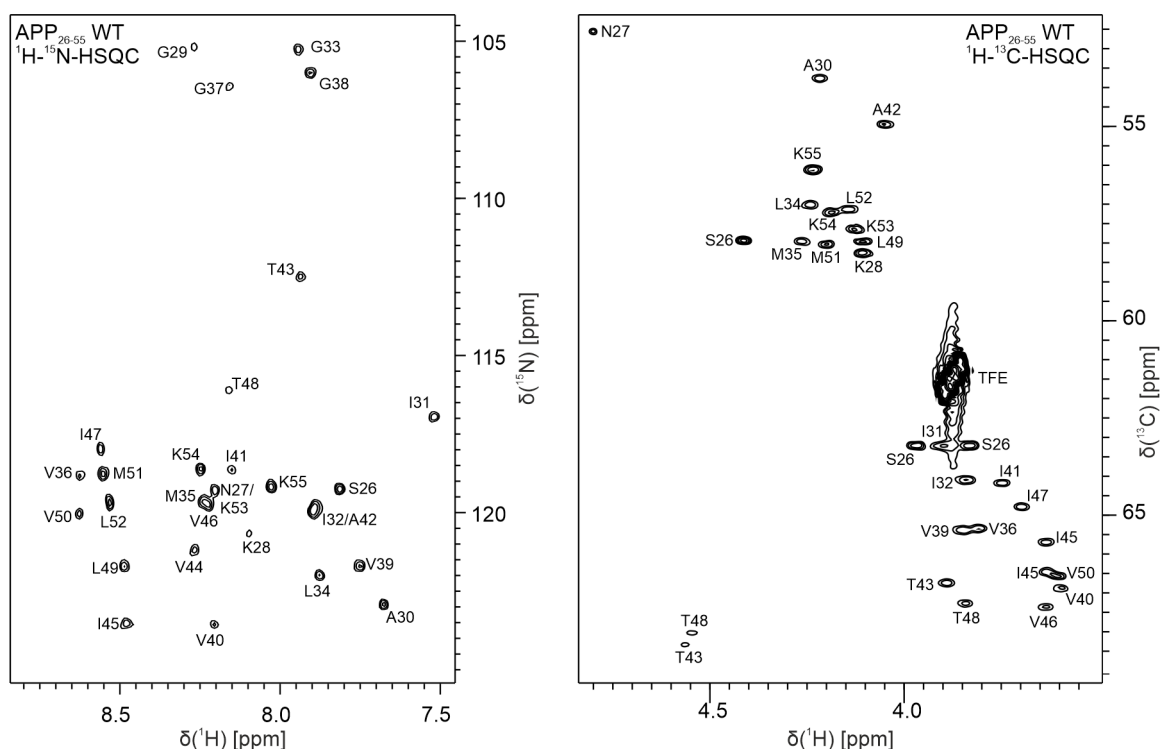
Figure 4.9. HSQC-spectra of synthetic APP$_{26\text{-}55}$ WT in TFE/H$_2$O at pH 7: In both spectra, all peaks could be assigned. The broad signal dispersion observable in the ^{1}H-^{15}N-HSQC indicates a structured peptide, while the chemical shift range, in which the H$_\alpha$-C$_\alpha$ resonances in the ^{1}H-^{13}C-HSQC are found implies an α-helical structure.

and thus cannot be sampled in membrane mimetics. TFE is a long established cosolvent for peptides and proteins. It is widely approved as mimic of the interior of proteins in general and in particular for the water filled cavity at the active site of γ-secretase, close to the cytosolic border. Therefore, TFE/H$_2$O can be considered a reasonable approach to assess substrate dynamics and its conformation upon migration to and within the catalytic cleft and as a good compromise to study hydrophobic peptides in solution. [300, 301, 344, 356–358] Furthermore, membrane mimetics, like micelles, bicelles, vesicles or nanodiscs, in this case DPC micelles, were used to sample the substrate properties in the membrane.

The amyloid precursor protein transmembrane domain (APP$_{26\text{-}55}$, see sequence below) was measured in a mixture of TFE-d2 and H$_2$O (80/20 V/V) at pH 7.0 and 300 K. The pH value of 7.0 was chosen as it has been shown that γ-secretase activity is highest at pH 7.0 [359].

```
                  30          40          50
APP₂₆₋₅₅ WT   SNKGA IIGLMVGGVV IATVIVITLV MLKKK
```

4.2.1. Chemical Shift Information

The first indicators of proper protein folding and sample purity are usually obtained from ^{1}H-^{15}N-HSQC spectra. Figure 4.9 shows the ^{1}H-^{15}N- and ^{1}H-^{13}C-HSQC spectra of the

synthetic $APP_{26\text{-}55}$ WT peptide. The number of cross peaks in the ^1H-^{15}N-HSQC spectrum coincides with the number of amino acids of $APP_{26\text{-}55}$ WT. This and the rather sharp peaks indicates that no by-products, like shorter fragments that might have been generated during peptide synthesis, are present in significant amounts. Moreover, broad background signals that would suggest larger aggregates are also not detectable.

Both backbone H_N and H_α exhibit large chemical shift dispersion. H_N resonances are spread between 7.5 ppm and 8.5 ppm whereas H_α resonances can be found between 3.6 ppm and 4.3 ppm. This indicates a folded, α-helical structure as explained in Section 2.1 (p. 7).

Secondary chemical shifts, the difference between observed and random coil values, were calculated for H_α, C_α and C_β. The results are shown in Figure 4.10A. Average secondary chemical shifts observed for α-helices are $\Delta\delta(^1H_\alpha) \approx 0.3$ ppm and $\Delta\delta(^{13}C_\alpha) \approx 2.6$ ppm that are marked by a red line in the bar diagrams. To take into account effects of neighbouring amino acids, nearest neighbour corrections were applied. Random coil chemical shift and nearest neighbour correction values were taken from D. Wishart [360].

The secondary chemical shifts determined for all three types of nuclei show two apparently helical regions separated by an unstructured motif. One, spanning from V_{39} to M_{51} is hereafter referred to as the C-terminal helix, while the other, the N-terminal helix ranges from G_{29} to V_{36}. The N-terminal helix appears less α-helical than its C-terminal counterpart because the secondary chemical shifts of (H_α and C_β) are less negative, while (C_α) values are less positive. At the double glycine motif, $G_{37}G_{38}$, the secondary chemical shifts indicate a random-coil like structure. It must be pointed out that in contrast to the other 19 amino acids, glycines do not exhibit such strong and consistent chemical shift trends and their secondary chemical shifts need to be interpreted more carefully.

Besides the simple secondary chemical shift calculations, CSI (Chemical Shift Index) 3.0 was used. CSI 3.0 is the combination of four previously published programs. CSI 2.0 that identifies the secondary structure type based on chemical shifts and sequence information, TALOS-N that calculates torsion angles from the same input data, RCI (Random Coil Index) that calculates order parameters to distinguish between ordered and disordered parts and analogous side-chain RCI. The combination of the parameters obtained is used to identify the secondary structure of a protein. [61, 361–364] The result of the calculation is shown in Figure 4.10B. The grey bars with positive value from G_{38} to K_{54} confirm the strong α-helical structure whereas the N-terminal domain is interpreted as unstructured. This is consistent with the information obtained from the secondary chemical shift values alone, where the values of the N-terminal helix were below the average values. Tthe CSI only distinguished between clearly separated secondary structure categories like β-sheet or α-helices based on a set of criteria. Regions, such as the N-terminal domain here that appear helical but do not meet all the requirements such as a specific chemical shift difference are not considered helical but unstructured. Nevertheless, the secondary chemical shift trends obtained for the N-terminal region clearly indicate an α-helical structure, only slightly less pronounced than the C-terminal part.

The observed i-(i+4) periodicity of the calculated secondary chemical shifts points towards a periodic variation of the lengths of the hydrogen bonds along the TM helix. This might indicate a moderately bent structure with longer H-bonds on one side of the helix.

Characteristic interresidual NOE patterns also report on secondary structure, since the NOE intensity depends on the distance between the two respective protons, as described
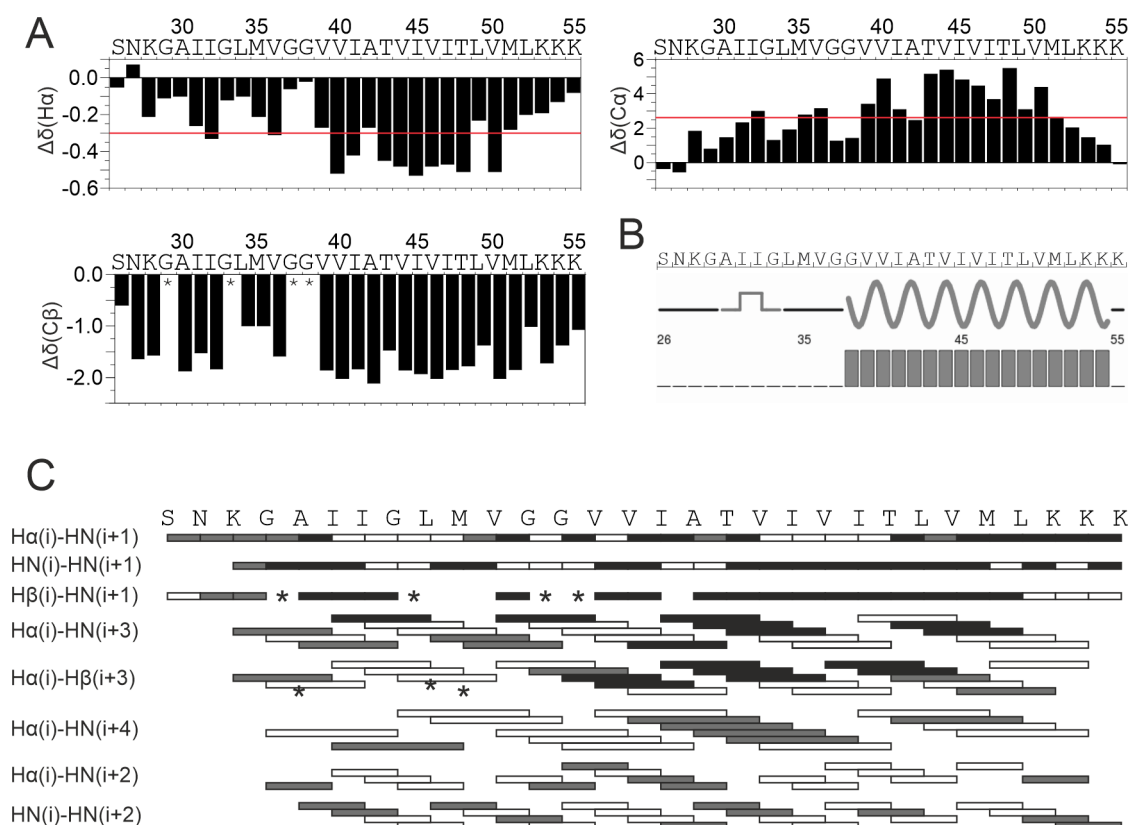
Figure 4.10. Secondary chemical shifts and NOE contacts of APP WT TMD in TFE/H$_2$O: A) H$_\alpha$, C$_\alpha$ and C$_\beta$ secondary chemical shifts of APP$_{26-55}$ WT in TFE/H$_2$O at pH 7.0 indicate an α-helical peptide consisting of two helix segments separated by the apparently less structured G$_{37}$G$_{38}$-motif. The average secondary chemical shift values usually observed for α-helices are shown by the red lines. B) CSI 3.0 output. The region identified as α-helical is represented by the red bars and the wavy line. C) Characteristic interproton NOEs. Strong NOE contacts are represented by black bars, weak NOEs by grey bars and white bars represent signals that could not be unambiguously assigned due to peak overlap. Positions marked with an asterisk indicate where the characteristic NOE or chemical shift cannot be observed due to the chemical nature of the respective amino acid.

in Section 2.1 (p. 10) and these distances in turn depend on the protein conformation. Relative NOESY cross peak intensities of APP WT TMD are shown in Figure 4.10C, they largely confirm the picture gained from chemical shifts. The cross peak intensities were categorised in strong NOEs (black bars) and weak NOEs (grey bars). Furthermore, white bars indicate NOEs that could not be unambiguously assigned due to peak overlap. In helices characteristic NOE contacts are $H_{\alpha,i}$-$H_{N,i+3}$, $H_{N,i}$-$H_{N,i+2}$ and $H_{\alpha,i}$-$H_{\beta,\,i+3}$. Additionally, $H_{\alpha,i}$-$H_{N,i+4}$ occur only in α-helices and $H_{\alpha,i}$-$H_{N,i+2}$ only in 3$_{10}$-helices. $H_{N,i}$-$H_{N,i+1}$ and $H_{\alpha,i}$-$H_{N,i+1}$ can be expected in both helix types. [365, 366] All cross peaks typical for α-helices could be observed over the entire TMD, but more pronounced in the C-terminal helix. Especially within the C-terminal helix, the characteristic $H_{\alpha,i}$-$H_{N,i+3}$ and $H_{\alpha,i}$-$H_{\beta,\,i+3}$ signals were clearly pronounced. Due to peak overlaps, many cross peaks could not be unambiguously assigned, hence conclusions drawn from NOE signals alone are limited. However, the conclusion based on the secondary chemical shifts that both parts are helical could be confirmed.

From chemical shift data alone, the structural framework can be deduced. APP$_{26-55}$ TMD is α-helical in TFE/H$_2$O, composed of two helical domains separated by the less structured G$_{37}$G$_{38}$-motif.

4.2.2. Three-Dimensional Structure of APP WT TMD in TFE/H$_2$O

Three dimensional structures were calculated with ARIA2/CNS [118, 155] based on a set of NOE restraints derived from ^{1}H-^{1}H-2D-NOESY experiments at pH 7 and 300 K. Additionally dihedral angle restraints, determined based on ^{1}H, ^{13}C and ^{15}N chemical shifts with TALOS+ [72], were incorporated in the structure calculation.

In accordance with secondary chemical shifts, the C-terminal helix appeared well defined. The N-terminal domain was α-helical as well. Interestingly, the more random coil-like structure indicated by secondary chemical shifts at the G$_{37}$G$_{38}$-motif did not lead to a break within the helix. Instead, the N-terminal domains fanned out at this motif and adopt several conformations relative to the C-terminal part. Strikingly, the relative orientation of N- and C-terminal helices were not fully arbitrary, but was restricted to a defined cone, as shown in Figure 4.11A, which was defined by two angles, the kink θ and the swivel angle φ. The kink angle was defined as the angle between the axis of the C-terminal and the N-terminal helices. The swivel angle was calculated as the relative rotation of the N-terminal helix around the C-terminal part. The axis through the C-terminal helix was aligned along the z-axis and the x-axis was defined by the V$_{46}$ H$_\alpha$-C$_\alpha$ bond vector. The swivel angle was then calculated as the projection of the N-terminal helix axis onto the x-y-plane. These calculations were performed using a python script written by C. Muhle-Goll. A graphical representation of the two angles is displayed in Figure 4.11B. The swivel angle φ was determined on the basis of 14 of these 20 structures, as θ was too small in the other cases to reliably determine φ. The kink angle θ of APP$_{26-55}$ WT in TFE/H$_2$O is 38.2° ± 18.5°, thus an entirely straight conformation could not be observed. Swivel angles are restricted to a cone with 29.7° ± 19.1°. A closer examination of backbone and side-chain conformations showed that the N-terminal helix kinked into the cavity formed by the missing glycine side chains, accompanied by presumably longer H-bonds at the other side of the helix.
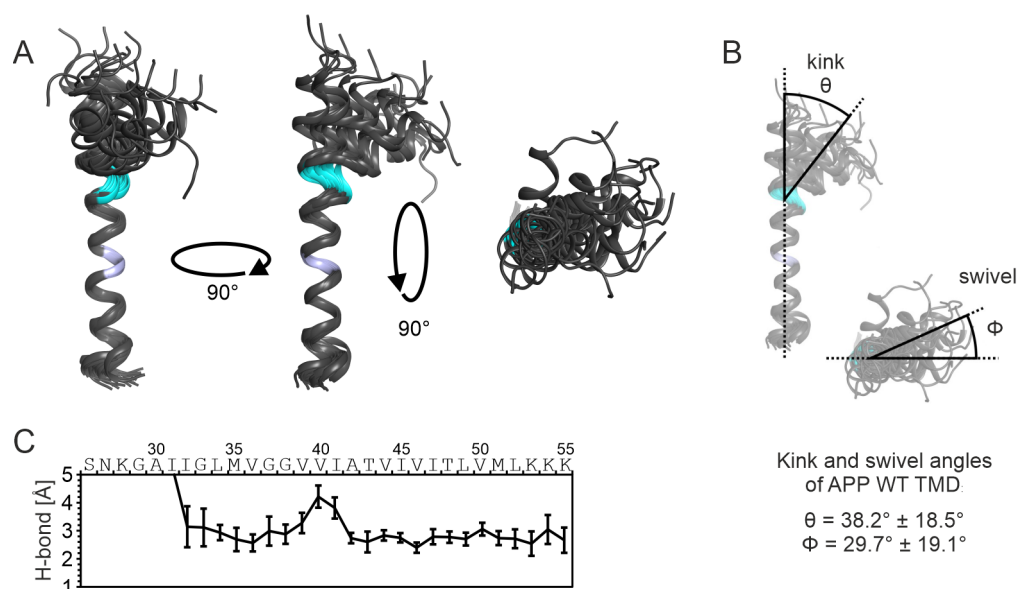
Figure 4.11. The three-dimensional structure of APP WT TMD in TFE/H$_2$O: A) Front view, side view and top view of the APP$_{26-55}$ WT structural bundle, the structures were superimposed on their C-terminal helices. G$_{37}$G$_{38}$ are coloured cyan, V$_{46}$, the reference for the swivel angle determination is highlighted in grey. The structural bundle shows that APP WT TMD consists of two α-helical regions which, emanating from the GlyGly-motif, can adopt different relative orientations. However, these are not arbitrary but confined. B) Graphic representation of kink, θ, and swivel angles, ϕ. θ is defined as the angle between N-terminal and C-terminal helix axes. ϕ is the angle of the C-terminal helix axis aligned along the z-axis and projection of the N-terminal helix onto the x-y-plane with the x-axis. The direction of the V$_{46}$ H$_\alpha$-C$_\alpha$ bond vector was defined as the x-axis. C) The H-bond lengths in Å derived from the calculated structures between the indicated amide proton and the oxygen four residues earlier confirm the rigid appearance of the C-terminal helix, since the H-bonds in this region are short and deviate only slightly. Around the helix centre, there is a clear elongation of H-bonds, which corresponds to the kink observed in the structures. The N-terminal helix has longer and more varied H-bonds than the C-terminal helix, indicating a less tightly defined region.

It must be emphasised here that these structures do not indicate dynamics, but represent the possible conformations the constraints used. The "true" structure may be a single one within the space defined by this bundle, but APP$_{26-55}$ WT might just as well adopt several conformations.

Distances of hypothetical H-bonds that were derived from the calculated structures between HN$_i$ and C=O$_{i-4}$ are shown in Figure 4.11C. This calculation strengthened the finding that the C-terminal helix was almost straight, because H-bond lengths from A$_{42}$ to M$_{51}$ were between 2.4 and 3 Å. The H-bonds that span over the hinge, i.e. I$_{41}$H$_N$-G$_{37}$H$_{C=O}$, V$_{40}$H$_N$-V$_{36}$H$_{C=O}$ and V$_{39}$H$_N$-M$_{35}$H$_{C=O}$ were considerably longer. The hydrogen bonds at the N-terminal helix were slightly longer and exhibit broader ranges than those of the C-terminal helix, again confirming the picture of a more rigid C-terminal and a slightly less structured N-terminal region. Hydrogen bonds between the two threonines in the C-terminal helix back to the peptide backbone are probable, as NOE signals between T$_{48}$H$_\gamma$ and V$_{44}$H$_\alpha$ and likewise between T$_{43}$H$_\gamma$ and V$_{40}$H$_\alpha$ could be observed.

Transitions between α- and 3$_{10}$-helices are supposed to be essential for twisting motions. NOE contacts between H$_{\alpha,i}$ and H$_{N,i+4}$ are characteristic for α-helices and between H$_{\alpha,i}$ and H$_{N,i+2}$ for 3$_{10}$-helices. [365, 366] However, neither from the NOE pattern shown before in Figure 4.10C nor from the calculated structures, was it possible to distinguish between α- or 3$_{10}$-helical conformations.

4.2.3. Hydrogen-Deuterium Exchange

The exchange rates of H$_N$ against solvent deuterium allow to indirectly access the hydrogen bond stability between a given amide proton and the carboxyl oxygen four (or three) residues earlier. Fully protonated peptides were dissolved in deuterated solvent, in this case TFE-d3/D$_2$O (80/20 V/V). Due to the excess of ^{2}D over ^{1}H exchangeable protons will be gradually replaced by deuterium. The principle is explained in Section 2.3 (pp. 23 ff.).

Hydrogen-deuterium exchange rates were measured at various pD values for APP$_{26-55}$ WT and APP$_{26-55,8lb}$ WT. Fast ^{1}H-^{1}H-TOCSY and ^{1}H-^{1}H-CLIP-COSY [148] experiments with an experimental time of approximately 3.5 h were acquired, and altogether a time span of about 38 hours was sampled. The parameters of the ^{1}H-^{1}H-TOCSY experiment were chosen as the best compromise between experimental time, signal intensity and resolution. Supplementary, using the partially isotope labelled APP$_{26-55,8lb}$ peptide, a series of ^{1}H-^{15}N-HSQC experiments could be acquired. By measuring at different pD values, it was possible to exploit the fact that the exchange rate depends on the pH or pD value, in a way that an increase in the pH value by one unit leads to an acceleration of exchange by approximately a factor of ten [367].

The combination of data obtained at various pD values therefore allows to cover several orders of magnitude in exchange rates. The peak volumes were integrated and the observed intensity decay was fitted to an exponential function (see Section 2.3, pp.23). In Figure 4.12A the signal decay of four signals (I$_{41}$, V$_{44}$, M$_{51}$ and L$_{52}$) based on a series of twelve ^{1}H-^{15}N-HSQC experiments of APP$_{26-55,8lb}$ at pD 5 is shown. All other spectra were superimposed on the spectrum of the first time point and shifted in such a way that the change in signal intensity could be observed. No signal shifts were actually observed between the spectra.
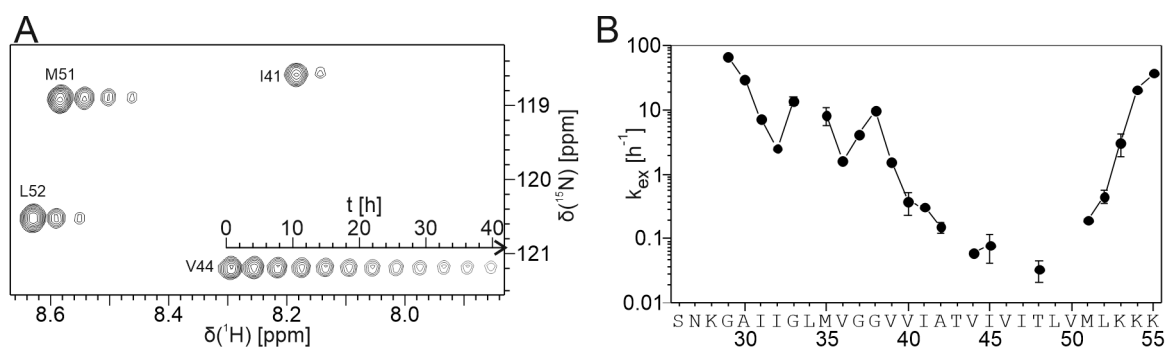
Figure 4.12. Hydrogen-deuterium exchange of APP WT TMD in TFE/H$_2$O: A) ^{1}H-^{15}N cross peak intensities decrease with time. All twelve spectra acquired at pD 5 are superimposed, but the spectra other than the first time point were shifted to show the changes in signal intensity. The comparison of the spectra already shows that V$_{44}$H$_N$ exchanges much more slowly than the other three H$_N$ shown. B) Hydrogen-deuterium exchange rates of APP$_{26-55}$ WT measured in TFE/H$_2$O. The exchange rates were obtained at various pD values and scaled to pD 5. The exchange rates at the very N-terminus could not be determined as the respective rate constants were too fast. The other missing values are due to signal overlap and, in the case of the C-terminal helix to slow exchange rates. The residues at the N-terminal helix experience faster exchange, indicating longer or less stable H-bonds, while the C-terminal helix appears more rigid, as suggested by slow exchange rates. The exchange rates of G$_{37}$H$_N$ and G$_{38N}$ are significantly faster than those of the surrounding residues. These findings are consistent with the impression gained from secondary chemical shifts and the calculated three-dimensional structures.

The measured HDX rates constants for APP$_{26-55}$ WT at pD 5 are shown in Figure 4.12B. Exchange rates span from more than one per minute to as slow as one per six weeks. G$_{29}$, G$_{33}$, G$_{37}$, G$_{38}$, I$_{41}$, V$_{44}$, M$_{51}$ and L$_{52}$ were ^{15}N-labelled and therefore ^{1}H-^{15}N-HSQC spectra could be acquired using this peptide.

Remarkably, in accordance with the chemical shift data and the calculated three-dimensional structures, the C-terminal residues exhibit very slow exchange whereas N-terminal amide protons show a lot faster exchange. Strikingly, the amide protons of G$_{37}$ and especially G$_{38}$ exchange faster than the neighbouring residues. As explained in Section 2.3 (pp. 23 ff.), amide protons can only exchange when they are not part of a hydrogen bond. Thus, transient unfolding enables an exchange, which in turn indicates conformational flexibility at the respective amino acid. The C-terminal helix is stabilised by H-bonds ranging from L$_{52}$H$_N$-T$_{48}$ to V$_{44}$H$_N$-V$_{40}$, those residues are apparently rigid in their secondary structure. Going further to the N-terminus conformational flexibility increases, as secondary chemical shifts already indicated. This profile is in accordance with hydrogen bond lengths derived from the calculated structures (see Figure 4.11). The slowly exchanging amide protons at the C-terminal domain are in concordance with short hydrogen bonds and small ranges. Fast exchange within the N-terminal helix corresponds to longer H-bonds and larger deviations.

Some imprecision of the method must be taken into account, although it has been shown that TFE does not significantly alters the exchange rates (50% TFE compared to pure water) [358, 368, 369]. However, not all exchange rate constants could be sampled for various

reasons. Residues exchanging significantly faster or more slowly than those measured could not be assessed because the correlation of exchange rate and pH is limited to a certain pH range. In the TOCSY-spectra, the H_N-H_α region was used, the disadvantage here is the partial signal overlap which makes fitting more difficult. On the other hand, there was still a remaining solvent signal that was within or close to the H_α frequency and which had to be suppressed. This solvent suppression could lead to undefined signal loss of some H_N-H_α resonances. The latter can be avoided using ^{1}H-^{15}N-HSQC experiments. Here, this was only possible for the eight labelled amino acids of APP$_{26\text{-}55,8\text{lb}}$, whose exchange rates therefore were the most reliable.

Nevertheless, hydrogen-deuterium exchange confirmed the overall observation of a stable C-terminal helix, stabilised by rigid H-bonds and a less stable N-terminal helix. The $G_{37}G_{38}$-motif apparently forms comparably weak hydrogen bonds, which is in accordance with secondary chemical shift date and the three-dimensional structures.

The exchange rate profiles were in good agreement with the values published by Cao et al. They measured hydrogen-deuterium exchange of APP TMD in LMPG micelles and observed, that especially $G_{38}H_N$ exchanged considerably faster than the surrounding amino acids [370]. This suggests that the apparent increased flexibility or destabilisation of APP TMD at the GlyGly-motif is at least partially retained in LMPG micelles.

4.2.4. Is APP TMD in TFE/H₂O a Monomer or a Dimer?
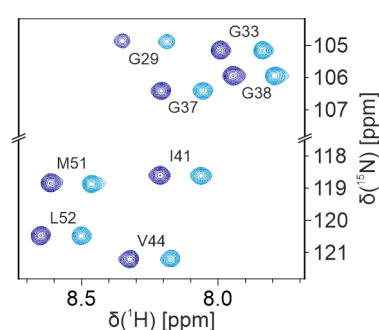
Figure 4.13. ^{1}**H-**^{15}**N-HSQC spectra of APP WT TMD acquired at different peptide concentrations:** APP$_{26\text{-}55,8\text{lb}}$ was measure in TFE/H₂O at two concentrations, the corresponding spectra were superimposed. The concentrated sample, 500 μM, was measured with 2 scans (dark blue) and the ten-fold diluted with 200 scans (light blue). The signals of the diluted samples were shifted for sake of clarity. As the signal intensities are similar in both spectra, APP TMD is most likely monomeric under the conditions used.

APP TMD most likely dimerises in membranes, although it is not clear under which conditions and how exactly. This is described in more detail in the discussion.

To investigate whether APP$_{26\text{-}55}$ WT forms a dimer or remains monomeric in TFE/H₂O, two concentrations were compared. First ^{1}H-^{15}N-HSQC spectra of a 500 μM sample were acquired, then the sample was diluted ten fold and was measured again. If a dimer were present at high concentration it should, at least partially, dissociate upon dilution according to Le Chatelier's principle. As signal-to-noise ratio is proportional to the number of scans squared [58], the number of scans was increased 100 fold when concentration was reduced

to 10%. In Figure 4.13 the two spectra are shown. Neither peak shifts nor changes of Peak intensities are visible, thus it can be assumed that APP is monomeric under the conditions used.

4.3. APP TMD WT and Mutants in TFE/H$_2$O

In addition to APP WT TMD, four single point mutants were investigated. The glycine at position 38 was exchanged for proline or leucine (G38P and G38L) to restrict the movement of the G$_{37}$G$_{38}$-hinge. Introducing leucine at the hinge was expected to straighten the helix and to restrict movements whereas proline should induce a kink and limit domain movement as well. The other two are Familial Alzheimer's Disease (FAD) mutants (I45T and V44M), that are known to impair and alter γ-secretase processivity. All mutations were investigated under two main aspects: Whether they affect the GlyGly-hinge motif and, whether they influence the ε-cleavage site in a way that could explain the product line shifts.

```
                    30          40          50
APP WT TMD   SNKGA  IIGLMVGGVV  IATVIVITLV  MLKKK
G38L TMD     SNKGA  IIGLMVGLVV  IATVIVITLV  MLKKK
G38P TMD     SNKGA  IIGLMVGPVV  IATVIVITLV  MLKKK
V44M TMD     SNKGA  IIGLMVGGVV  IATMIVITLV  MLKKK
I45T TMD     SNKGA  IIGLMVGGVV  IATVTVITLV  MLKKK
```

4.3.1. Circular Dichroism Spectroscopy of APP WT and Mutants

CD spectra APP$_{26-55}$ WT and the four APP mutant TMDs were acquired at 50 μM concentration and pH 5. As shown in Figure 4.14A APP$_{26-55}$ exhibits a high α-helical content. The two minima at 222 nm and 208 nm and the maximum 193 nm clearly indicate a mostly α-helical structure. The secondary structure fractions estimated with BeStSel [163, 164] are shown in Figure 4.14. The apparently low α-helix content, however, corresponds to the NMR results. These revealed the α-helix from G$_{29}$ to M$_{51}$, excluding the first and last three residues. Furthermore, the N-terminal part was less helical than the C-terminal section. Thus, probably about 50% overall helical content seem reasonable. According to the CD results shown in Figure 4.14, G38L has the highest α-helical content, followed by I45T and V44M, while G38P is less helical compared to the others. This gives a first glimpse on the effects the mutations induce on secondary structure.

4.3.2. Chemical Shift Information

Again, initial information on structural changes can be derived from ^{1}H-^{15}N-spectra. In Figure 4.15 the ^{1}H-^{15}N-spectra of the four mutants superimposed on the ^{1}H-^{15}N-spectrum of APP WT TMD, all acquired in TFE/H$_2$O at pH 7.0 are shown. Combined chemical shift perturbations (CSP) and the chemical shift differences of H$_N$ of the mutants compared to the WT are depicted below the spectra to better visualise the effects induced by the single point mutations. CSP were calculated as a combination of ^{1}H$_N$ and ^{15}N chemical shift differences as explained in Section 2.1 (p. 9).
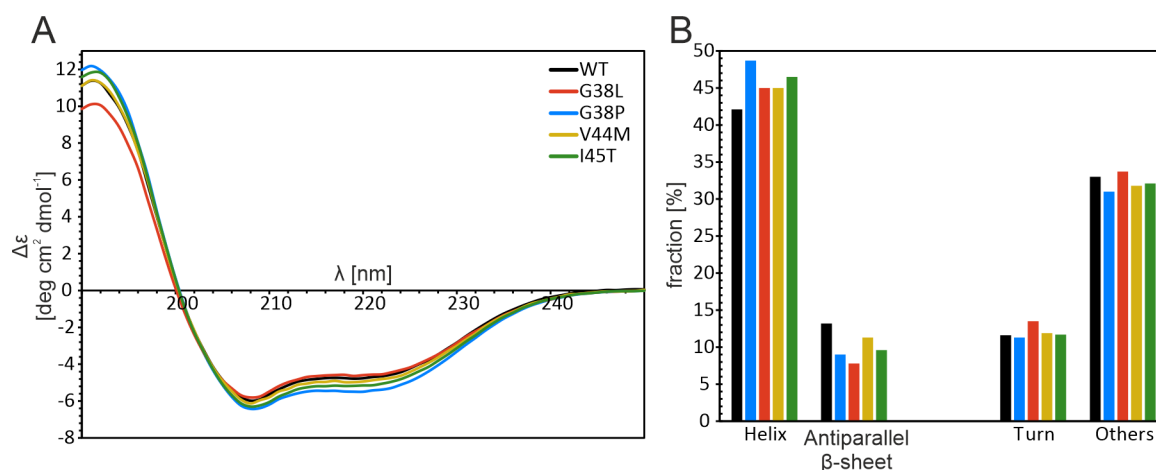
Figure 4.14. CD spectroscopy of APP WT TMD and the four mutants in TFE/H₂O: The spectra were acquired at 50 μM concentration and pH 5.0. A) CD spectra of APP WT TMD and the four mutants overlayed and B) the relative fractions of secondary structure motifs as calculated with BestSel [163, 164]. All five peptides are α-helical, as the two minima at 222 nm and 208 nm indicate. G38P appears less helical compared to APP WT TMD, while the other three mutants seem to be more helical. The secondary structure fractions confirm this expression with the exception of G38P, which has a higher α-helical content than the WT. However, these differences are marginal.

The largest chemical shift changes occur around the respective mutation sites, as expected. V44M causes only very small alterations compared to the other three mutants, mainly V_{40} to M_{44} and T_{48} are affected. As $T_{48}H_N$ forms a hydrogen bond with residue V_{44}, this could indicate changes in the H-bond network there. As V44M was preferably cleaved at T_{48} and not at L_{49} like the WT, weakening of the respective hydrogen bonds could explain this shift in ε-cleavage. The other perturbations caused by V44M are located within the C-terminal domain, but N-terminally from the mutation site. The other FAD mutant, I45T, affects mainly the C-terminal half, as well, but considerably stronger than V44M. In particular residues A_{42}, V_{44} and, as expected, T_{45} are changed. G38L causes large CSP at residue L_{38} by force of the large ^{15}N chemical shift difference between glycine and leucine. Furthermore the regions from G_{33} to G_{37} as well as V_{39}, V_{40} and A_{42} are affected. Interestingly the effect on I_{41} is smaller than on the surrounding residues. The largest deviation is around the mutation site but more towards the N-terminus than the C-terminus. A_{42} is the only residue in the C-terminal helix that is strongly changed, probably due to the H-bond between $L_{38}CO$ and $A_{42}H_N$. G38P causes different changes even though the same residue was mutated. The largest effects, considerably larger than in the case of G38L, are here at residues L_{34} to G_{37}, V_{39} and I_{41}. A_{42} does not change, although $A_{42}CO$ cannot form a H-bond with P_{38} due to its lack of H_N. The effect on I_{41} can be explained by the altered H-bond to G_{37}.

Amide proton chemical shifts are among the most sensitive reporters of hydrogen bond geometries, together with torsion angles between the observed and the preceding residue, ring currents, local changes and others [371]. Thus changes of H_N chemical shifts between WT and mutants can be used as indicators of alterations of the hydrogen bonding
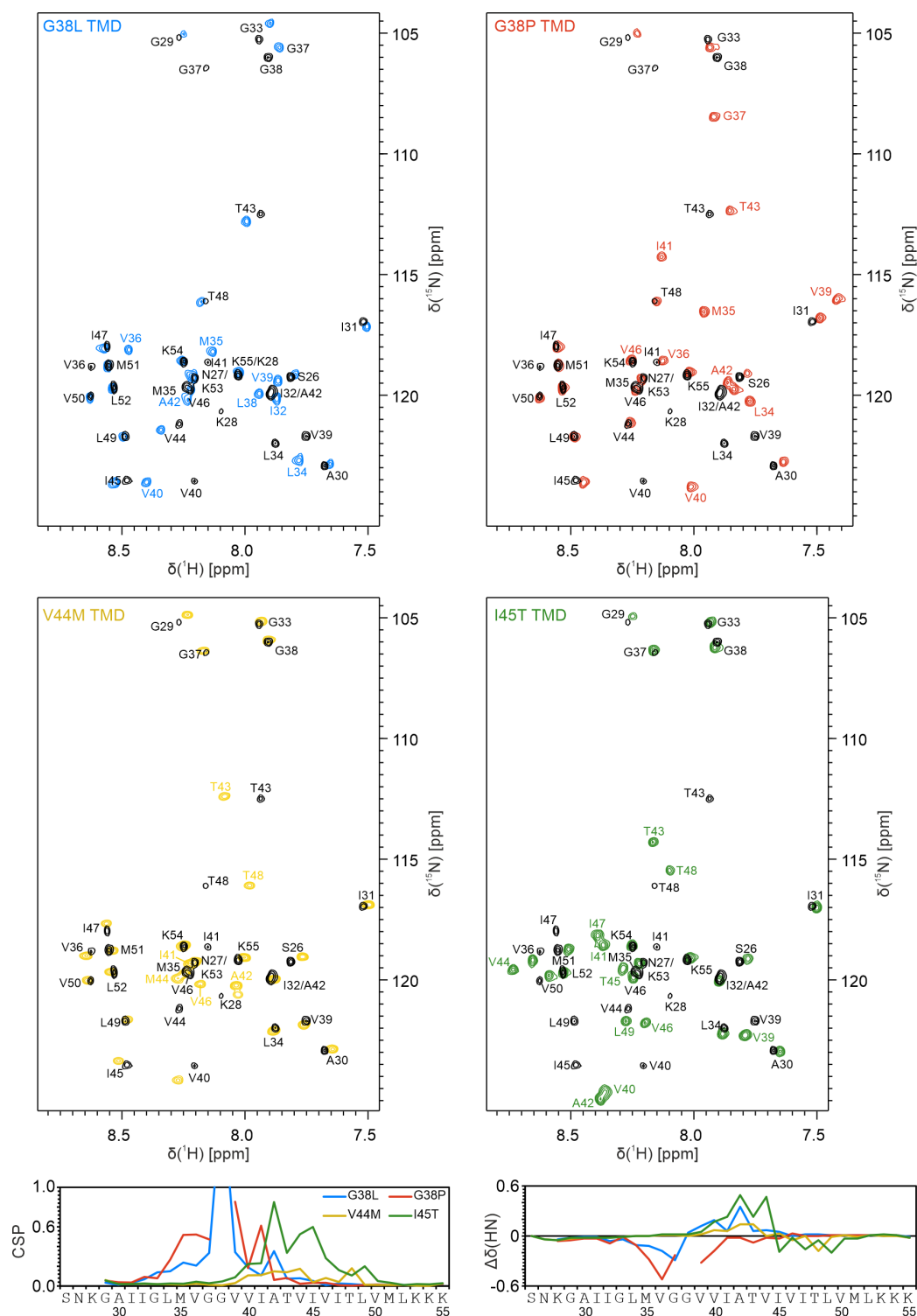
Figure 4.15. **^{1}H-^{15}N-HSQC spectra of all four single point mutants compared with APP$_{26-55}$ WT:** The spectra of APP WT TMD (black) and the respective mutant are superimposed and signals of the mutants significantly deviating from APP WT TMD chemical shifts are labelled in the corresponding colour. Below, the CSP derived from ^{1}H-^{15}N-HSQC spectra (left) and $\Delta\delta H_N$ of mutants compared to APP$_{26-55}$ WT are shown. The effects of the mutants are very diverse. All strongly affect the mutated residue, as could be expected. While V44M and I45T mainly alter chemical shifts within the C-terminus, the largest changes caused by G38L and G38P are N-terminal from the mutation site.

network. While G38L and G38P mostly affect the region around the hinge in general, V44M and I45T induce more pronounced effects at single residues. V44M influences hydrogen bonds at residues N-terminally from the mutation site but not at M$_{44}$ itself. And, most interestingly, the chemical shift of T$_{48}$H$_N$ changes. I45T has even larger effects at amino acids N-terminally from the mutation site, A$_{42}$, T$_{43}$ and V$_{44}$ while I$_{47}$H$_N$ and L$_{49}$H$_N$ are influenced to a lesser extent.

^{1}H$_\alpha$, ^{13}C$_\alpha$ and ^{13}C$_\beta$ secondary chemical shifts of all four mutants are widely similar but not completely alike as visible in Figure 4.16. The finding that the C-terminal helix is strongly α-helical holds true for all four mutants, there are slight deviations though. FAD mutants V44M and I45T decrease helicity locally at the mutation site compared to WT otherwise secondary chemical shifts are similar to the WT. The G38 mutants apparently do not affect helicity of the C-terminal domain. G38L leads to increased helicity around the mutation site (V$_{36}$, L$_{38}$, V$_{39}$) whereas G38P has the largest effect on secondary chemical shifts. This mutation apparently slightly increases helicity at P$_{38}$ but reduces it very strongly at V$_{36}$, M$_{35}$ and L$_{34}$.

Chemical shift derived S^2 order parameters of APP$_{26\text{-}55}$ WT and the four mutants are shown in Figure 4.16. S^2 model free order parameters describe the degree of motion and therefore the extent to which orientational information of the N-H bond vector is lost on the ps to ns timescale [372]. For all five peptides the N-terminal helix exhibits slightly smaller S^2 values than the C-terminal helix. This means there is more internal motion of the N-H vectors of the N-terminal helix whereas the C-terminal domain appears rigid. This is in accordance with secondary chemical shift data that suggested a less helical and therefore less rigid N-terminal half. Only the proline mutant experiences a break in S^2 at residues G$_{33}$ to V$_{36}$, suggesting more flexibility in this part of the molecule. For the same residues secondary chemical shifts indicate a loss of helicity. The other three mutants do not show significant deviations from APP WT TMD. The helix probability derived from TALOS+ (Figure 4.16) suggests again a perfectly strong helix at the C-terminal domain and is clearly reduced for residues G$_{37}$ and G$_{38}$ of APP TMD WT. G38L TMD in contrast almost reaches a helix probability of 1 for all residues while G38P TMD shows a break again for residues M$_{35}$ to G$_{37}$, as indicated by chemical shift data already. Both FAD mutants, V44M and I45T, apparently stabilise the helix at the GlyGly-motif, although the mutation sites are several residues apart.

The strong effects indicated by ^{1}H$_N$ and ^{15}N chemical shift perturbations are not reflected in secondary chemical shift, S^2 order parameters or helix probability to the same extent. Especially the large perturbations at the C-terminal helix induced by the two FAD mutants are not reflected in the other chemical shifts. Neither of the mutations shows an effect on the ε-cleavage sites at L$_{49}$ or T$_{48}$ in secondary chemical shifts, S^2 order parameters and helix probability. Nevertheless, helix probability hints at alterations regarding the hinge motif.

4.3.3. Three-Dimensional Structures

Analogue to APP$_{26\text{-}55}$ WT three-dimensional structures of the four mutant peptides in TFE/H$_2$O were calculated. Figure 4.17 shows the 20 lowest energy structures of all five peptides superimposed on their C-termini from V$_{40}$ to V$_{50}$.
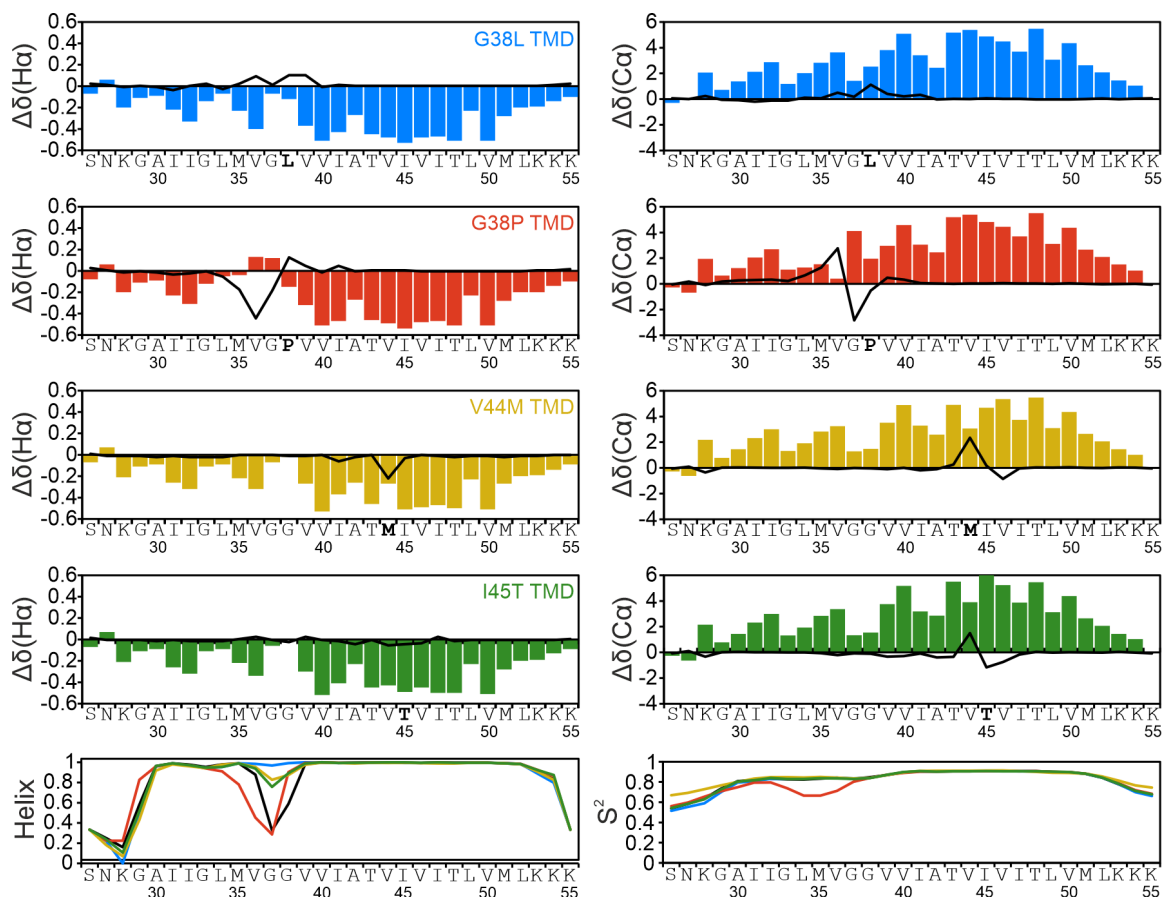
Figure 4.16. Secondary chemical shifts of the four mutants compared to APP TMD WT in TFE/H2O: The bars represent the secondary chemical shift values, calculated as difference between observed chemical shift and random coil values. The black lines indicate the difference between secondary chemical shifts of the respective mutant and APP WT TMD. For example, for H_α, a positive value of this difference indicates that the mutant is more helical than the WT a negative difference indicates that the mutant is less helical. Below the S^2 order parameters and the helical content, both estimated with TALOS+ are shown. These data suggest that G38L is more helical than APP TMD WT and stabilises especially the $G_{37}L_{38}$-motif. G38P decreases helicity, mainly at the residues N-terminally from the mutation site and leads, according to S^2 order parameters to dynamics at the respective residues. The two FAD mutants show only minor alterations of secondary chemical shifts compared to APP WT TMD and only locally around the mutation site. However, according to the estimated helix content, they appear to stabilise the GlyGly-hinge.

Aligned on the - in all cases well-defined - C-terminal domains and equally arranged, commonalities and differences are revealed. The N-terminal α-helical regions are marginally less consistent between the 20 conformations in each case. The difference in rigidity is less pronounced than could be expected based on chemical shift data. This can be due to the fact that this domain is less stable and the NOE contacts used for the structure calculation overestimate the structured part. Similar to the WT all four mutants show variations of the N-terminal helix that, emanating from residues G$_{37}$ and G/L/P$_{38}$, fans out. Notably the cones in which the N-termini are found differ between the five peptides. Mean kink angles as well as their ranges vary just as swivel angles. The values are given in Table 4.1.
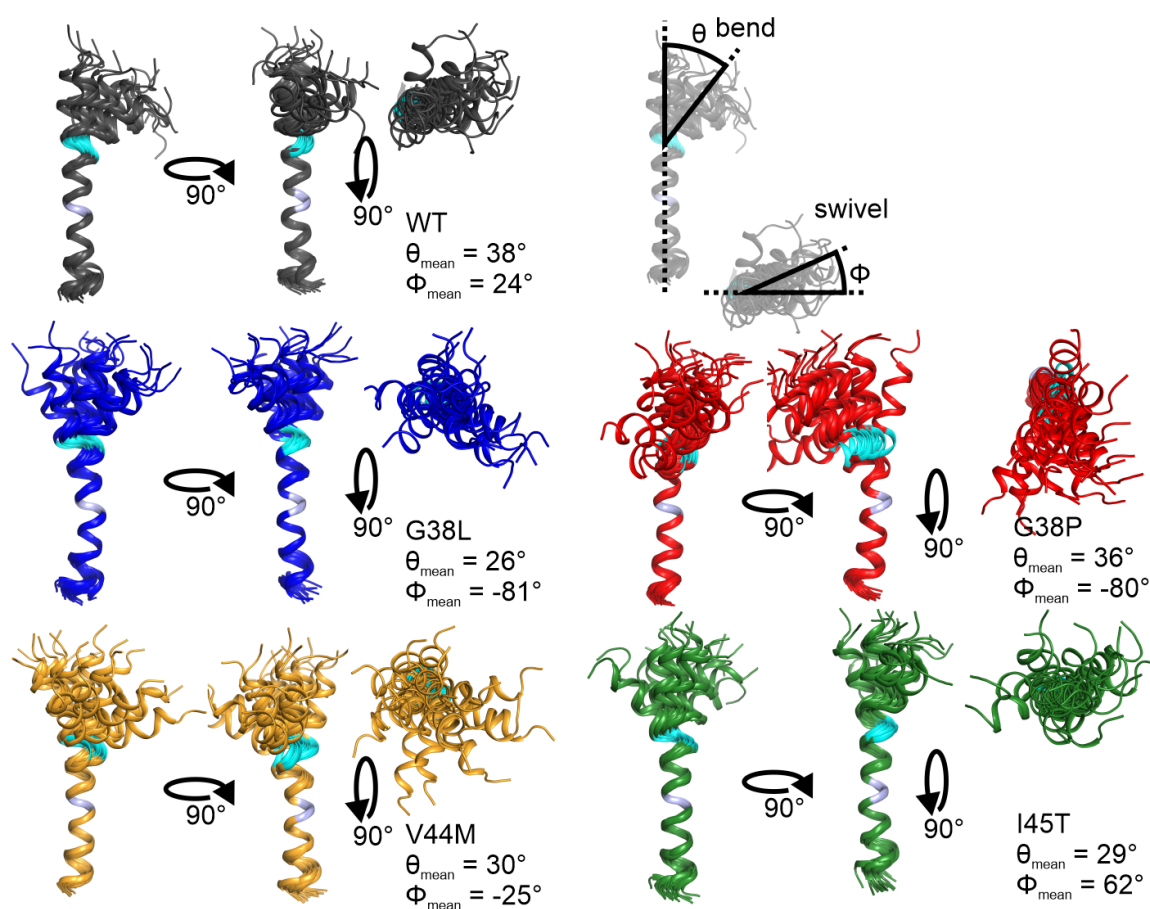
Figure 4.17. Structural bundles of APP WT TMD and mutant TMDs: Structural bundles are aligned on the C-termini from V$_{40}$ to V$_{50}$. Residues G$_{37}$ and G/L/P$_{38}$ are highlighted in cyan, V$_{46}$, the reference for swivel angle determination in grey. Mean kink and swivel angles are given as well.

All mutants are more restricted in their kink angles than the WT. G38L, I45T and V44M are straighter, whereas the mean kink angle of G38P is similar to WT, but comprises a slightly narrower range. Swivel angles differ more significantly. Both G38 mutants swivel in the same direction that is shifted by about 110° compared to APP TMD WT, but G38P exhibits a slightly larger range. Both FAD mutants are less restricted than APP WT TMD, but cover much broader ranges. Even though their mean swivel angles differ, their swivel

Table 4.1. Kink and swivel angles of APP TMD WT and the four mutants. Additionally kink and swivel angles of APP TMD structures available in the PDB were calculated by the same procedure used for APP TMDs in TFE/H2O. The Nadezhdin monomer (2LLM) and the Nadezhdin dimer (2LOH) were too straight to determine any swivel angle. The structures in micelles are described in the Section 4.1.2 (pp. 39)

		mean θ [deg]	mean ϕ [deg]
WT		38.2 ± 18.5	29.7 ± 19.1
G38L		25.8 ± 12.5	−81.4 ± 35.3
G38P		35.7 ± 15.4	−80.0 ± 41.9
V44M		30.1 ± 13.8	−24.9 ± 82.8
I45T		28.5 ± 11.9	61.5 ± 89.7
WT	LMPG monomer (2lpl)	75.2 ± 4.7	34.9 ± 10.0
WT	DPC dimer right-handed (2LZ3)	24.9 ± 1.6	153.2 ± 9.8
WT	DPC monomer (2LLM)	14.1 ± 0.7	
WT	DPC dimer left-handed (2LOH)	22.1 ± 3.7	
V44M	DPC dimer right-handed (2lz4)	23.7 ± 2.7	42.3 ± 6.5

angle ranges overlap in such a way, that both comprise the swivel angle range of the WT. This means that both FAD mutants can adopt all possible swivel angles of APP TMD WT.

Kink and swivel angles were calculated for the published APP WT TMD and APP V44M TMD structures that are described in Section 4.1.2 (pp. 4.1.2), as well. All these structures were determined in detergent micelles, either DPC or LMPG under various conditions. Two structures are monomers, the one determined in LMPG by Barett et al. (2LP1, [249]) is the only strongly kinked structure with a kink angle much larger than that observed for APP WT TMD in TFE/H_2O. Its swivel angle deviates significantly from that of APP WT TMD determined in TFE/H_2O. In contrast, the two structures determined by Nadezhdin et al, a monomer (2LLM, [250]) and a dimer (2LOH, [251]), exhibit significantly smaller kink angles, which are so small that the swivel angles could not be determined. The two dimer structures of APP TMD WT (2LZ3, [253]) and V44M (2lz4, [253]), published by Chen et al. in DPC micelles, are again straighter than both peptides in TFE/H_2O. Their kink and swivel angles are quite similar, the great discrepancy observed between APP WT TMD and V44M in TFE/H_2O cannot be observed. The restricted bend and swivel angles of the dimeric structures are probably caused by dimerization, as this forces the individual helices into a certain conformation and strongly restricts flexibility.

Helix flexibility, as bending and twisting motions, is not exclusively determined by a flexible motif, such as GlyGly, but by the whole network of fluctuating hydrogen bonds along the peptide backbone. Thus, mutations altering this network several residues distant from the flexible motif, like V44M or, more importantly I45T, can have a huge impact on helix conformation and dynamics. Upon bending hydrogen bonds on the opposite site of the hinge are weakened and therefore longer. Twisting motions in contrast require shifting between α- and 3_{10}-helices. Bending in a defined region has been proposed to be essential for the enzyme-substrate-complex by various studies. [249, 289, 300, 336, 356, 357, 373–376]
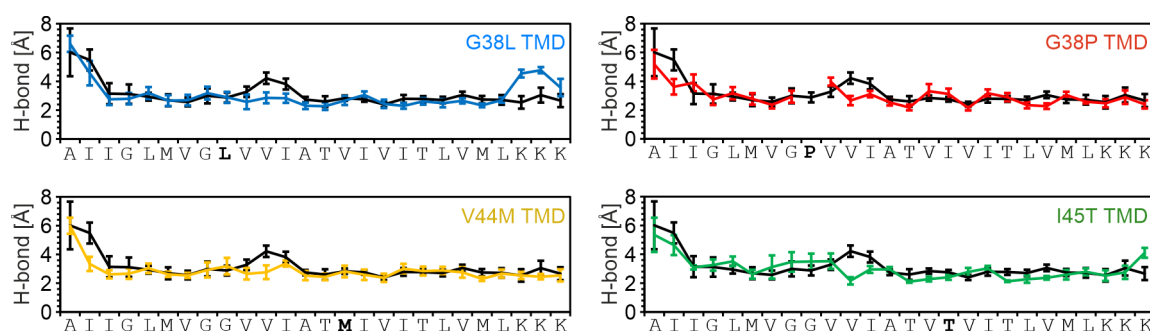
Figure 4.18. H-bond lengths of APP WT TMD and the four mutants derived from the calculated structures: The H-bonds lengths of APP WT TMD are shown in black those of the mutants in the respective colour. The H-bonds at the opposite site of the hinge motif are significantly elongated in APP WT TMD structures. G38L leads to significantly shorter distances between the respective residues. G38P also leads to shorter distances at the hinge motif but shows slight fluctuations at its C-terminus that might indicate an overall bent structure. Both FAD lead to shorter H-bonds at the hinge-motif, too.

In Figure 4.18 the theoretical H-bond lengths observed in the calculated structures of APP WT TMD and the four mutants are shown. Measured were H-bonds emanating from the given residues H_N to the O' atom four residues earlier. As shown before, H-bonds across the $G_{37}G_{38}$-hinge are significantly elongated in APP WT TMD, between $I_{41}H_N$ and $G_{37}O'$, between $V_{40}H_N$ and $V_{36}O'$ and between $G_{37}H_N$ and $G_{33}O'$. Otherwise the distances are more or less uniform, especially for the C-terminal helix. G38L exhibits no significant alteration of H-bond lengths over the hinge, again the H-bonds at the C-terminus are slightly shorter and in a narrower range than at the N-terminus. H-bonds directly C-terminally from the hinge are significantly shorter than observed for APP WT TMD, this fits the chemical shift differences in H_N as well as the smaller kink angle observed for this mutant and underlines the impression of a straighter helix. G38P has no H-bond between P_{38} and L_{34} due to the missing amide proton. The significant alterations of H_N chemical shifts of residues G_{37}, V_{36} and M_{35} are not reflected in the H-bond lengths of the calculated structures, though. Interestingly a pattern is visible at the C-terminus: $T_{43}H_N$-$V_{39}O'$ is very short, $T_{44}H_N$-$V_{40}O'$ and $T_{45}H_N$-$V_{41}O'$ are longer, $T_{46}H_N$-$V_{42}O'$ is very short again and $T_{47}H_N$-$V_{43}O'$ is longer. This pattern matches the bent visible in the C-terminal domain of G38P. Again, the deviations in H-bond length proposed from chemical shift data are not reflected in the calculated structures for V44M. Only I_{41}, V_{40} and V_{39} are shortened, but lengthening at e.g. T_{48} cannot be observed. I45T shows dramatically shortened H-bond at residue V_{40} and effects in the C-terminal helix that was, again, not directly reflected in chemical shift deviations. As T_{45} can form an additional H-bond between its carbonyl group and the carbonyl oxygen of I_{41}, the beginning of the C-terminal helix is stabilised and thus the hinge region.

In Figure 4.19 side chain packing is depicted. Bending is facilitated when, on the one hand, residues with short side chains provide free space and, on the other hand, hydrogen bonds at the opposite side of the helix are lengthened.

Residues G_{37} and G_{38} are coloured cyan. Dark blue coloured are the residues surrounding the hinge (V_{36} and V_{39}), turquoise the first half of the C-terminal helix (I_{41}, A_{42}, T_{43},
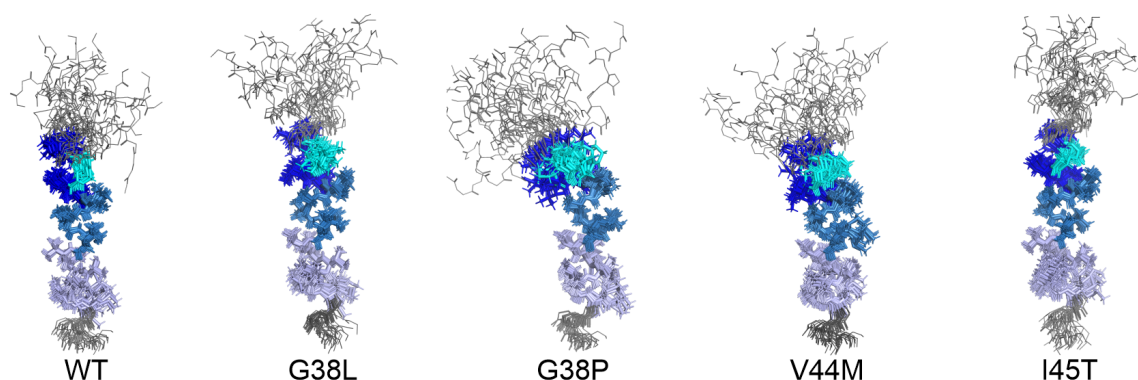
Figure 4.19. Side chain packing along the hinge region and the C-terminal helix of APP WT TMD and the four mutants in TFE/H$_2$O: Cyan: G37, G/P/L38; dark blue: V$_{36}$, V$_{39}$, V$_{40}$; turquoise: I$_{41}$, A$_{42}$, T$_{43}$, V/M$_{44}$, I/T$_{45}$; light blue: V$_{46}$-M$_{51}$. APP WT TMD structure shows that the N-terminal helix bends towards the hole created by the GlyGly-motif. The bulky leucine side chain of G38L at this position prevents bending and enforces helix straightening.

V$_{44}$/M$_{44}$, I$_{45}$/T$_{45}$), and light blue the second half of the C-terminal helix (V$_{46}$, I$_{47}$, T$_{48}$, L$_{49}$, V$_{50}$, M$_{51}$). It is noticeable that the glycine to leucine mutation forces the N-terminal helix to bend away from the bulkier leucine side-chain resulting in an overall straighter conformation. It was shown that a proline in an α-helix induces a kink in the helix and that this kinking is always away from the side with the proline [377–379]. In the case of G to P this can be observed as the N-terminal helix bends away from the proline. The V$_{44}$ to M mutation introduces a longer side chain at position 44 that pushed away the side chain of V$_{40}$, moving the N-terminal helix away. I$_{45}$ to threonine has no obvious effect on the side chain pattern but the additional H-bond between the T$_{45}$ side chain hydroxyl group and I$_{41}$ (indicated by an NOE between I$_{45}$ and A$_{42}$H$_\alpha$) stabilises the beginning of the C-terminal helix and thus changes local interactions.

The atomic coordinates and experimental data have been deposited in the Protein Data Bank (www.pdb.org) and BRMR (https://bmrb.io): WT: 6yhf,34506; G38L: 6yhi, 34570; G38P: 6yhO, 34508; V44M: 6yhp, 34509; I45T: 6yhx, 34510.

4.3.4. Hydrogen-Deuterium Exchange of APP G38L and G38P

Hydrogen-deuterium exchange was measured for G38L TMD and G38P TMD as well. The measured exchange rates are depicted in Figure 4.20 Even though not all amide protons could be sampled, the general picture already obtained from chemical shift data is evident, too. G38L exhibits slightly slower exchange around the mutation site while the exchange rates of G38P increase. For V44M and I45T, not enough data was measured to calculate exchange rates. As explained above, HDX had to be measured using only ^{1}H-^{1}H-TOCSY experiments because APP mutant peptides were not isotope labelled. Thus distances between measured time points were relatively long. Additionally, water suppression had to be used to eliminate residual solvent signals. This might have interfered with peak

volumes. And, because exchange rates are strongly pH dependent, small deviations from the measured pH value significantly alter the profile obtained. Nevertheless the observed effects are in accordance with the other data.
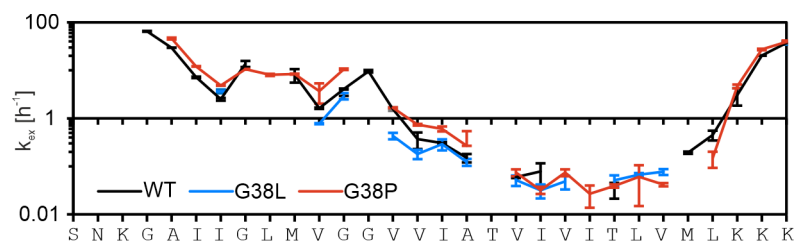
Figure 4.20. HDX exchange rates of APP WT, G38L and G38P: HDX around the residues 37 and 38 is slower for G38L and for G38P.

4.3.5. Interactions of APP WT TMD and the Four Mutants with γ-Secretase

The obtained structures of APP$_{26-55}$ WT and mutants were aligned on the substrate in the model of Hitzenberger & Zacharias [380], that is described in detail in Section 4.1.3 (pp. 44). This structure depicts the state directly after the substrate entering γ-secretase between TMDs 2 and 3. To reach its position in the catalytic cavity formed by TMD 2, TMD 3 and TMD 5, they observed that the substrate needed to kink at the GlyGly-motif to overcome the loop connecting TMD 2 and TMD 3.

Interestingly only APP WT TMD structures fitted the model, allowing the N-terminal helix to kink in the direction required. As can be seen in Figure 4.21A APP WT TMD structures can adopt the same kink as the modelled substrate. The three mutants that showed overall straightening (G38L, V44M and I45T) are not able to bend as required and collide with the PSEN TMD 5. G38P does not fit either due to its altered swivel angle, although its kink angle allows the required bending. Hitzenberger & Zacharias found that APP WT TMD kinked at the GlyGly-motif as it entered the active site through the opening between TMD 2 and TMD 3. When the C-terminal helix was positioned within the catalytic cleft, APP WT TMD adopted a straight conformation [325]. The RMSD values obtained for the overlaid structures are shown in Figure 4.21B. They corroborate the visual impression: APP WT TMD shows the smallest deviations from the structure obtained by MD simulations while G38P TMD differs the most.
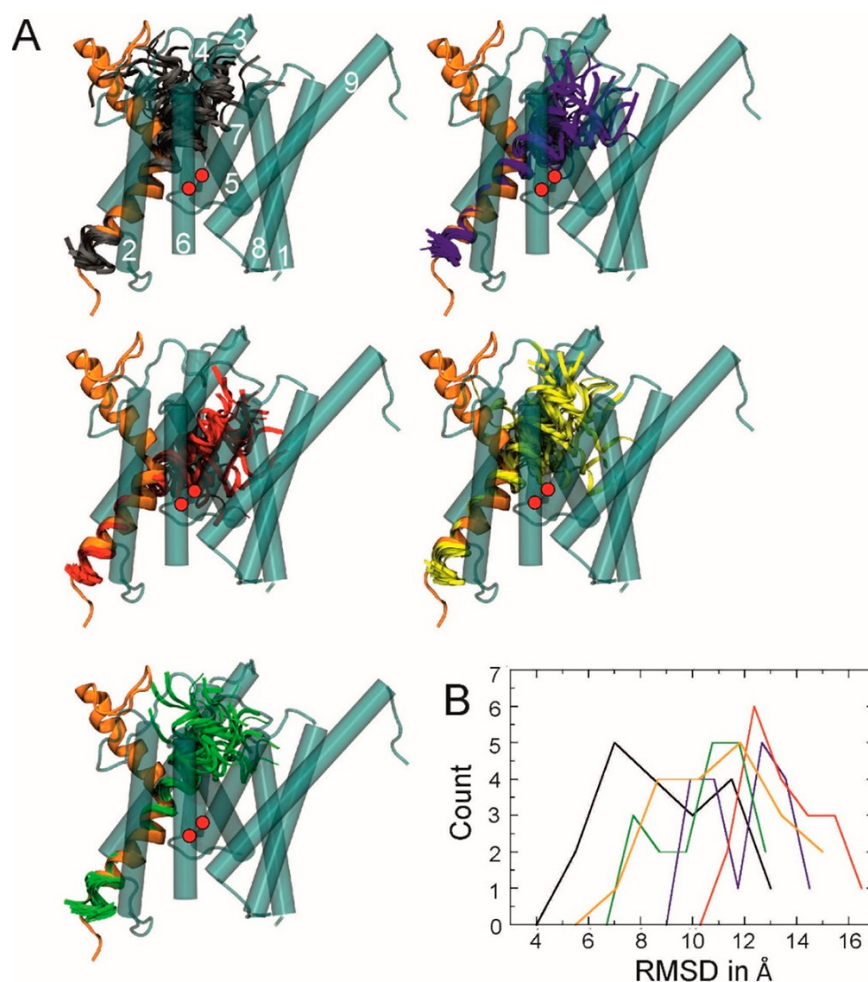
Figure 4.21. Interaction of APP WT TMD and the four mutants with γ-secretase: A) APP TMD structures calculated in TFE/H₂O aligned on a snapshot the substrate entry model provided by Manuel Hitzenberger. WT (gray), G38L (blue), G38P (red), V44M (yellow) and I45T (green) aligned on the theoretical model (orange). Only the WT model can adopt the required kink direction of the theoretical substrate while all other substrates clash with PSEN TMDS. B) C_α RMSD values of the WT and the four mutants compared to the theoretical model. The WT shows the lowest RMSD values. [157] Reprinted with permission from "Altered Hinge Conformations in APP Transmembrane Helix Mutants May Affect Enzyme–Substrate Interactions of γ-Secretase", Copyright 2020, American Chemical Society

4.4. APP$_{0-55}$ **in DPC Micelles**

APP$_{0-55}$ WT (see sequence below) was produced via cell-free protein expression and analysed in DPC micelles.

```
              0          10         20         30         40
APP₀₋₅₅, cf   M  DAEFRHDSGY  EVHHQKLVFF  AEDVGSNKGA  IIGLMVGGVV
                          50         60
                  IATVIVITLV  MLKKKPGGGS  HHHHHH
```

As other groups already published structures of APP TMD in micelles, that deviate strongly (see Section 4.1.2 p. 39), the aim to produce and measure ^{13}C^{15}N-labelled APP TMD in DPC micelles was to understand what led to these discrepancies. Furthermore, with regard to subsequent experiments, a fast and simple method of peptide expression and sample preparation that can be easily adapted to APP mutants or other γ-secretase substrates was to be established, as a prerequisite for the planned observation real-time of APP cleavage in the NMR tube.

4.4.1. **Cell-Free Protein Expression**

Cell-free protein expression was newly established in collaboration with the Huster Lab in Leipzig, Germany.

Cell-free protein production is an alternative to conventional protein expression techniques in bacterial or eukaryotic cells. It is especially useful when the protein of interest is toxic for the host cell. Difficult constructs like membrane proteins can be produced more easily by this method as well. And, in the NMR-context, selective ^{15}N-, ^{13}C and ^{2}D-labelling as well as the incorporation of unnatural amino acids is rather simple. The principle of cell-free expression is to break down the complex processes in cellular protein production to the essential actions. Besides, cell-free protein expression is usually considerably less time consuming. And, dependent on the amino acids used, it is not necessarily more expensive than recombinant protein production. [381–384]

Two principle expression modes were described: Continuous exchange cell-free expression (CECF) and batch mode (see 4.22). CECF usually leads to higher protein yields. Two reaction compartments are separated by a semipermeable membrane. The feeding mix (FM) in the larger container comprises low-molecular weight supplies like amino acids, NTPs and energy supplies, that are consumed during the reaction. The smaller chamber contains the cell-extract and other high molecular weight compounds like polymerase and template DNA, the so-called reaction mix (RM). This setting has two great advantages. First reaction can go on much longer than in batch mode as consumed educts are supplied by the FM. Second, side products that might impair expression will diffuse out of the RM into the FM. In batch mode consumed educts cannot be replenished and thus the reaction usually stops after few hours. [385–387]

Three principle modes to produce membrane proteins via cell-free protein expression are established, depicted in Figure 4.22. Precipitation based (P-CF) often leads to correctly folded proteins that can afterwards be resolubilized with detergents or lipids. When precipitation has to be prevented, addition of detergents to the RM (D-CF) allows proteins
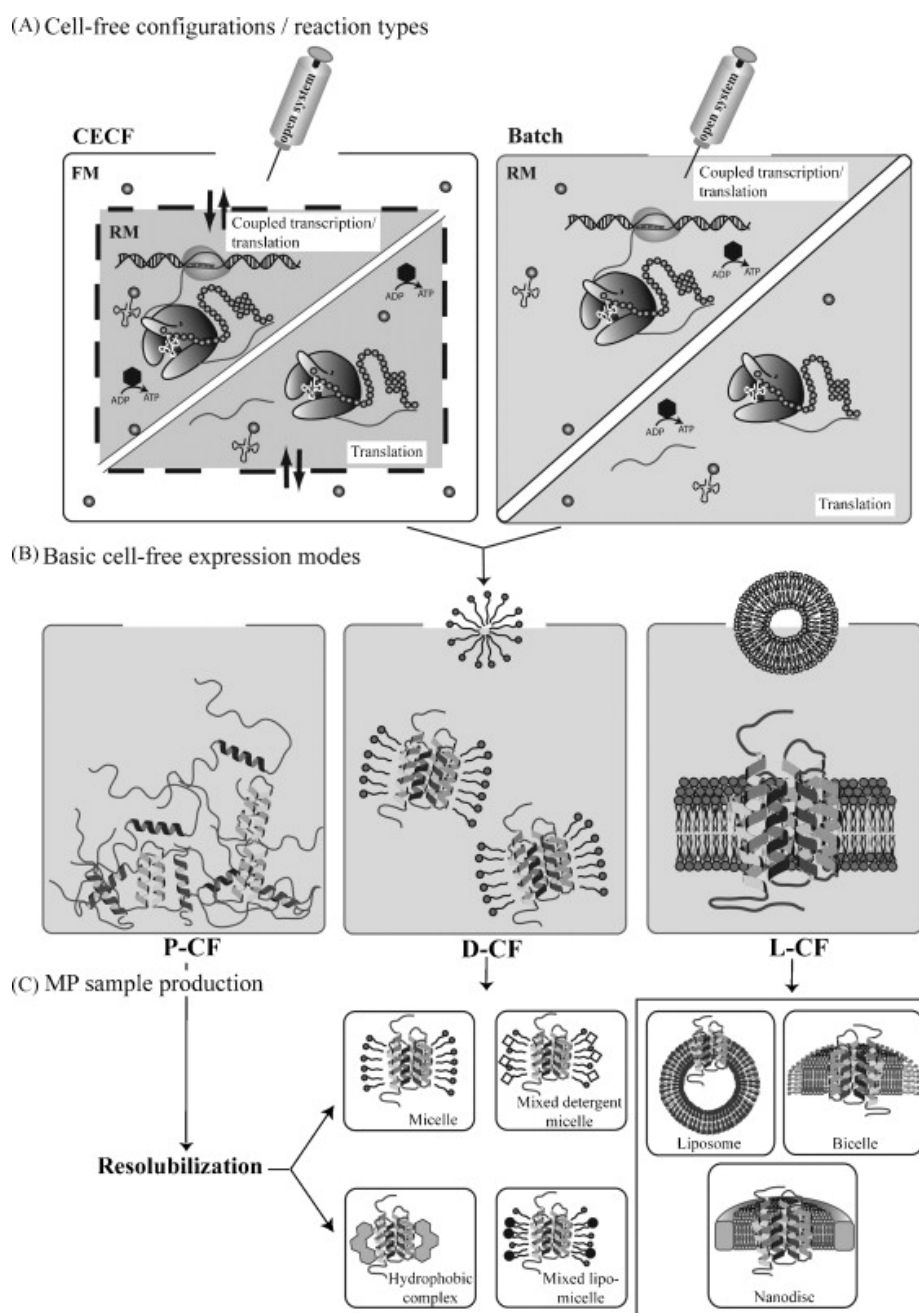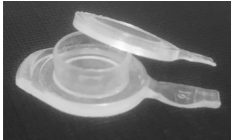
Figure 4.22. Cell-free protein expression modes: A) Continuous Exchange Cell-Free protein expression (CECF): FM and RM are separated by a semipermeable membrane that enables exchange of low molecular weight compounds. Transcription and translation take place in the RM, while the FM provides substances consumed during the reaction. Batch mode: No external FM, thus limited supply of reaction educts. The reaction will stop earlier than in CECF mode. B) CF expression modes: Precipitation based (P-CF), detergent based (D-CF), lipid based (L-CF). C) Membrane proteins are either expressed in P-CF mode and subsequently resolubilised in detergents or micelles or directly inserted during expression in D-CF or L-CF mode [387].

to be inserted into the micelles during expression. Especially in the context of NMR-based studies direct insertion into lipids is appealing when bicelles, liposomes or nanodiscs are provided in the RM. [388, 389]

APP$_{0-55}$ WT was expressed in the continuous exchange cell-free expression mode, using three different reaction containers, to optimise the protein yield. Furthermore, various parameters like Mg^{2+} concentrations, temperature and reaction time were adapted to the protein that was expressed.

The three reaction containers that were used are shown in Table 4.2. Initially 650 µL RM were put in the cap of a 5 mL Eppendorf-tube and covered with a dialysis membrane that was fixed by the flange. The RM-container was then placed in a 50 mL centrifuge tube containing the FM. This provided up to 1 mg protein per mL RM. For analytical approaches the lid of a 2 ml Eppendorf-tube was used in a similar manner. To enhance protein production a new device was developed, shown in Table 4.2. This disk shaped container can be covered with membrane on both sides, dramatically increasing the surface to volume ratio. As diffusion depends on the area through which substances can pass, efficiency increases with the surface area. As anticipated, the highest protein yields were achieved with the newly developed RM container.

Table 4.2. Containers used for analytical and preparative scale cell-free protein expression.

	Analytical scale	**Preparative scale**	
Container	2 mL Lid	5 mL Lid	custom
Volume	150 µL	650 µL	1 mL
Diameter	8 mm	12 mm	16 mm
Surface	0.5 cm^2	1.1 cm^2	4.0 cm^2
Surface/Volume	3.3 cm^2/mL	1.7 cm^2/mL	4.0 cm^2/mL

Since APP$_{0-55}$ could be produced and reconstituted easily, after all parameters were adjusted, the system was attempted to be applied to more complicated proteins. For this purpose, another γ-secretase substrate, TNR12, was produced by means of cell-free protein expression. This was investigated under my direction in the thesis of Celine Moser (2020) [158]. TNR12 was shown to be a γ-secretase substrate by G. Güner (Lichtenthaler Lab, DZNE, Munich; unpublished observation). The TNR12$_{28-129}$ construct was composed of the TMD, flanked by parts of the extracellular and intracellular domains. This makes it a challenging expression construct because, in addition to the transmembrane domain there is also a soluble domain that forms four disulphide bridges. As TNR12$_{28-129}$ could

not be resolubilised after precipitation, even if it was additionally denatured under harsh conditions, both detergent based and lipid based cell-free expression were applied. Brij-98, a detergent that had been described as good supplement for CECF [159] led to rather high TNR12$_{28-129}$ yields of up to 1.7 mg/mL. However, the exchange of Brij-98 against DPC for NMR measurements could not be achieved without a denaturation step that led to the insoluble aggregates as P-CF expression. Furthermore expression into nanodiscs was attempted as these are an interesting membrane mimetic for NMR measurements and, when TNR12$_{28-129}$ could be inserted directly. Nandodiscs were prepared following the protocol by Hagn et al. [161]. Size exclusion chromatography suggested that some peptides were indeed incorporated into nanodiscs but concentrations were too low to be detected by NMR spectroscopy.

Thus, cell-free protein expression is a versatile tool to produce transmembrane proteins, but is was shown that the parameters that led to high amounts of protein that could easily be reconstituted in organic solvent or detergent micelles do not necessarily translate to another protein.

4.4.2. Secondary Structure of APP$_{0-55}$ in DPC Micelles

APP$_{0-55}$ was expressed via cell-free protein expression and incorporated in DPC micelles. A set of homonuclear and heteronuclear two-dimensional and three-dimensional NMR spectra was acquired at 320 K.

Almost all ^{1}H-^{15}N-resonances could be assigned as shown in the ^{1}H-^{15}N-HSQC in Figure 4.23A as well as C$_\alpha$, C$_\beta$, C' and H$_\alpha$ chemical shifts (the full chemical shifts table can be found in the appendix).

^{1}H-^{15}N-HSQC spectra of APP$_{0-55}$ WT in DPC were acquired at two pH values, pH 7.0 and pH 5.0. Interestingly, the residues buried in the detergent micelles (A$_{30}$ to M$_{51}$) do not experience significant chemical shift differences between the two pH values, but the hydrophilic N-terminal region seems to be affected dramatically. The amides of the first twelve residues are affected by severe linebroadening and not visible. This could be due to conformational changes or hydrogen exchange with an unfavourable exchange rate in the intermediate exchange regime (see Section 2.3, pp. 22). Hence, the following experiments were acquired at pH 5.0.

The secondary chemical shifts of APP$_{0-55}$ WT TMD in DPC indicate a fully α-helical peptide from I$_{31}$ until V$_{50}$, as shown in Figure 4.23B. As observed in TFE/H$_2$O already, the C-terminal domain is more helical than the N-terminal part and there is a loss in helicity at G$_{37}$G$_{38}$, even though less pronounced. TALOS+ derived S^2 order parameters are similar between APP$_{0-55}$ in DPC micelles and APP$_{26-55}$ in TFE/H$_2$O at the C-terminal domain, but differ at the N-terminal helix where APP$_{0-55}$ in DPC is more structured than APP$_{26-55}$ in TFE/H$_2$O.

4.4.3. Hydrogen-Deuterium Exchange in DPC

Hydrogen-deuterium exchange measured with a series of ^{1}H-^{15}N-HSQC experiments at pH 5 and 310 K showed that the majority of amide protons exchanged relatively fast. Thus exchange rates could not be assessed quantitatively but only qualitatively. Figure 4.23C
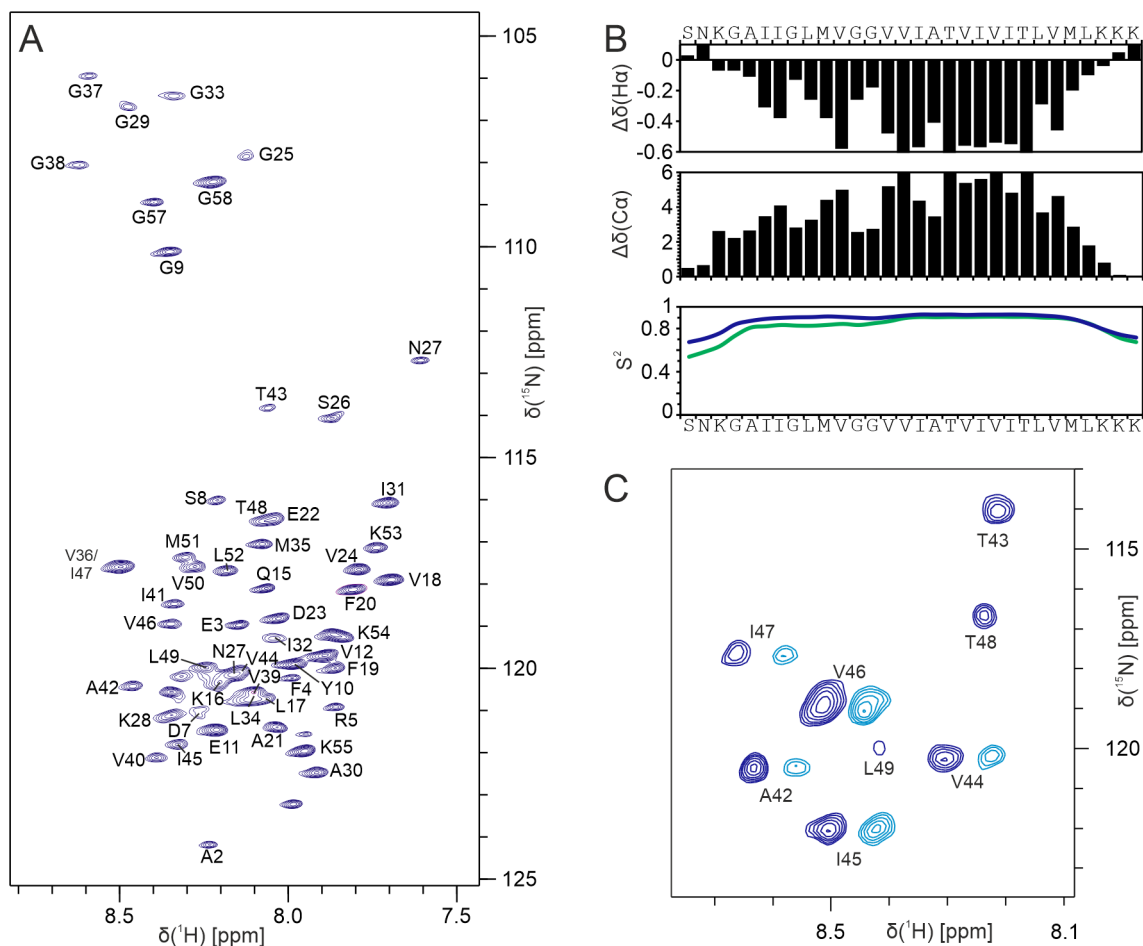
Figure 4.23. Chemical shift data and HDX of APP$_{0-55}$ in DPC micelles at pH 5.0: A) ^{1}H-^{15}N-HSQC of APP$_{0-55}$ in DPC at pH 5 and 320 K. B) H$_\alpha$ and C$_\alpha$ secondary chemical shifts of APP$_{0-55}$, below S^2 order parameters of APP$_{0-55}$ in DPC (dark blue) and APP$_{26-55}$ in TFE/H$_2$O (green). The secondary chemical shifts indicate a fully α-helical structure that is apparently marginally less helical at the G$_{37}$G$_{38}$-motif. C) Hydrogen-deuterium exchange: ^{1}H-^{15}N-HSQC of APP$_{0-55}$ in DPC and D$_2$O, acquired at 310 K. 2 h (dark blue) and 17.5 h (light blue) after resolubilisation. The light blue spectrum is shifted for better visibility. The H$_N$ within the C-terminal helix exchange significantly more slowly than those within the N-terminal region, as observed in TFE/H$_2$O.

shows in blue the protonated peptide and in red the remaining signals after 18 hours of exchange. Obviously the slow exchanging residues are located in the C-terminal transmembrane helix from I_{41} to V_{50} in which I_{45} and V_{46} experience the slowest exchange. This is in accordance with the finding that the N-terminal domain is less helical and probably less stable than the C-terminal helix. Chen et al. measured HD exchange rate constants of APP in DPC micelles at pH 7.2 and 298 K. They found that exchange is very fast for the N-terminal helix, medium for residues G_{37} to V_{40} and V_{50} and very slow for the C-terminal helix from I_{41} to L_{49} [253]. MD simulations of APP in DPC micelles showed that the number of water molecules close to each amino acid rapidly decreases when amino acids are buried deeper in the membrane. Very low water content was reached for almost the whole TM helix from residues G_{33} to V_{50} [373]. Therefore exchange rate deviations observed in DPC micelles are not simply due to low water accessibility but do report on conformational flexibility at the corresponding amino acids.

The results obtained in TFE/H_2O are quite close to those in DPC micelles. Thus TFE does not induce conformational or dynamic properties completely deviating from those in DPC.

It could be shown here that APP$_{0\text{-}55}$ can be expressed via cell-free protein expression and incorporated in DPC micelles and the structural and dynamical information obtained is in accordance with published data. Thus, further experiments to study the interaction of APP or other γ-secretase substrate TMDs can be designed and executed on this basis. Furthermore, cell-free protein expression was successfully implemented both precipitate-based and with the use of detergents. Even though the reconstitution of the TNR12 construct was not successful, it could be produced in sufficient quantities in both modes. Thus, for other constructs, such as other γ-secretase substrates, which have a similar amino acid sequence, cell-free protein expression can probably be adapted relatively well. In addition, attempts should be made to express the respective peptides directly into DPC micelles, which can then be measured by NMR spectroscopy without denaturing purification steps.

4.5. Discussion

γ-Secretase substrates such as APP TMD are challenging subjects for structural investigations as they relocate from hydrophobic membranes to the hydrophilic, water containing catalytic cavity of the enzyme.

Transmembrane proteins in general are largely influenced by their environment. Once inserted into the membrane, α-helical transmembrane domains are severely restricted concerning their possible conformations and dynamic processes such as domain motions. In structural biology membrane mimetics such as micelles, bicelles, vesicles or nanodiscs are used to study transmembrane protein properties in their native-like environment. Upon migration to the catalytic cleft, γ-secretase substrates leave the hydrophobic membrane and translocate into the water-filled cavity where their surroundings change severely. While strongly restricted by the lateral pressure of the lipids within the membrane, structural alterations of the substrates may occur upon entry into the catalytic site. The conditions

during this transition cannot be reproduced in membrane mimetics, but need to be investigated in a solvent allowing conformational flexibility. Besides, helix dynamics are strongly affected by solvent molecules, such as water in the catalytic cleft. Trifluoroethanol-water mixtures that were used in this thesis are a good compromise to monitor conformational and dynamic properties of the substrate in the catalytic cleft, as they do not strongly influence conformations, even though TFE is known to stabilise distorted helix structures [390].

For APP TMD it has been shown that at least the C-terminal domain, harbouring the scissile bonds, migrates from the lipid bilayer into the water-filled cavity within γ-secretase, but to date APP TMD has not been elaborately studied in TFE/H_2O, but only in membrane mimetics. For the reasons explained above, structural and dynamic information of APP TMD in an environment resembling the catalytic cavity of γ-secretase can provide valuable insights into substrate entry and processing.

APP$_{26-55}$ WT in TFE/H_2O adopts an entirely α-helical structure throughout its TMD as generally favoured by single pass transmembrane proteins. Two straight helical segments are connected by a flexible hinge at residues G_{37} and G_{38}. Bending and twisting at this hinge is restricted to a defined conformational space. APP TMD conformations observed upon substrate entry into γ-secretase by MD simulations lie within the scope of structures determined based on NMR derived restraints [325]. Apparently, the stabilising effect of TFE did not bias the structures, as the peptides in TFE/H_2O were less rigidly α-helical than in DPC micelles according to secondary chemical shifts.

Structural Properties of APP WT TMD and the Four Single Point Mutants

Although more than a hundred different γ-secretase substrates are known, with a variety of amino acid sequences in their transmembrane domains, γ-secretase is extremely sensitive to single point mutations. Thus, it is still unclear which properties discriminate between γ-secretase substrate and non-substrate or which feature leads to ε-cleavage at L_{49} or T_{48}. To address this question, five mutants were selected considering different aspects. The GlyGly-motif, which was assumed earlier to be a central feature facilitating substrate entry into the catalytic cleft [289, 373], was one starting point. However, it does not appear in all substrate sequences by far. Notch1 TMD and APLP2 TMD, for example, have none while ErbB4 TMD even contains one at approximately the same distance from the γ-secretase cleavage site as APP TMD. TNR12 also harbours a GlyGly-motif, but very close to the N-terminal end of its TMD. Therefore, the motif does not seem to be mandatory, but also not peculiar to APP. In cooperation with our collaborators in Munich and Leipzig, two single point mutants at this motif were designed. The glycine to leucine mutant was intended to straighten the helix and impair bending at this motif, whereas proline was expected to destabilise the helical structure. The other two variants, again single point mutations, are Familial Alzheimer's Disease (FAD) mutants, that were found in families with an accumulation of AD at young age [346, 348]. These mutations are not located near the ε-cleavage site but more in the middle of the very stable C-terminal helix. Nevertheless, they were shown to impact γ-secretase cleavage.

The results obtained in this thesis revealed similarities, but also differences between APP WT TMD, G38L, G38P, V44M and I45. As expected, the general structures of all five

peptides analysed in TFE/H$_2$O were similar. The four mutants altered kink and swivel angles of the N-terminal domain relative to its C-terminal counterpart compared to APP WT TMD. The proposed hinge at G$_{37}$X$_{38}$ was confirmed as bending occurred at this site. It has to be emphasised here, that exchange of one single amino acid, even some residues distant from the hinge motif, apparently led to drastic conformational alterations.

Both G38 mutations had the effect that was intended. Leucine with its large hydrophobic side chain was observed to straighten the transmembrane helix and to slightly stabilise the N-terminal part, reducing flexibility at the proposed hinge-motif. Proline in contrast, lacking an amide proton, was found to destabilise the N-terminal helix, as it cannot form the characteristic hydrogen bonds with carbonyl groups three or four residues towards the N-terminus. Furthermore, proline prevented a straight conformation of the TMD. The kink, usually not directly at the proline residue itself but located more N-terminally, is introduced by the steric clash between the proline ring and backbone carbonyl groups of preceding amino acids [377, 391–393]. Both G38 mutations mainly affected the swivel direction, changing the relative rotation of N- and C-terminal helix parts by about 110° compared to the WT. This corresponds to roughly one amino acid in an α-helix. Neither mutation affected the ε-cleavage site.

My results fit to MD simulations of our collaborators that showed that the overall helical conformation of G38L increased in POPC LUVs (large unilamellar vesicles) and decreased in the case of G38P. Furthermore, they could show that the kink angle of G38L greatly resembles values obtained for WT, whereas G38P structures simulated by MD resembled conformations obtained by NMR data in this work. Kink angles of G38P determined from MD simulations were considerably shifted towards more strongly bent conformations and angles smaller than 15° were almost non-existent. The changes in swivel angles compared to APP TMD WT observed in MD simulations were smaller than the ones derived from NMR data, with about 10° for G38L and about 40° for G38P [344]. Such discrepancies between MD simulations and NMR derived structures frequently occur as the two methods are based on differing principles. On the one hand, it has to be emphasised once again, that the structural bundle obtained from NOE restraints does not describe dynamic processes, but rather represents all the structures that are in accordance with the restraints used. Thus, the conformational space might be wider than the structures APP TMD can adopt in its natural environment. On the other hand, MD simulation times might be simply too short to observe energetically less favourable, more strongly kinked conformations.

The other two single point mutations investigated, V44M and I45T, impacted helicity as well as bending and twisting motions, even though the mutation sides were located in the middle of the very stable C-terminal helix. Götz et al. observed shifts in bend and swivel angles as well, when comparing APP WT TMD with V44M and I45T [357, 394]. Since calculations were not done concordantly (Götz et al. used G$_{33}$ as origin, C. Muhle-Goll used V$_{46}$) the absolute values cannot be compared. Nevertheless, both mutations resulted in a larger possible swivel angle range in the case of I45T compared to the WT and a slightly shifted kink angle of I45T with respect to the WT observed by the NMR data obtained here. This is in accordance with MD simulations by Scharnagl et al., that showed that I45T facilitated bending at the GlyGly-hinge [300].

Lengthening of hydrogen bonds around the ε-cleavage site is discussed as determinant of ε-cleavage site preference. Alterations of the hydrogen bond network were expected to
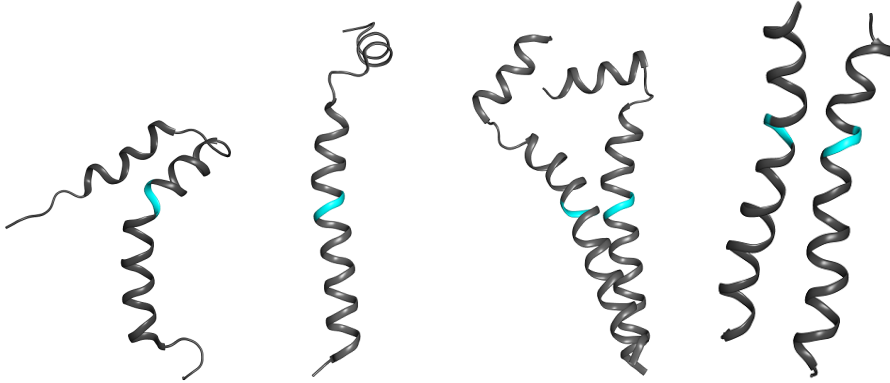
be caused by the mutations that could explain shifted ε-cleavage sites. Both G_{38} mutants did not impact the C-terminal helix but mainly the residues around the mutation site, according to the NMR data obtained. Alterations of the hydrogen bond network observed in MD simulations of our collaborators, the Scharnagl Lab, showed similar results. They observed no dramatic impact on the C-terminal domain but G38P led to a dramatic loss of H-bond occupancies at V_{39} and the surrounding residues [344]. Both C-terminal mutations, V44M and I45T, led to chemical shift perturbations at the ε-cleavage site, in the case of V44M at T_{48} and in the case of I45T at L_{49}. In DPC micelles, Chen et al. observed the same effect for V44M. The lengthening of H-bonds at residues T_{48} and L_{49} that they found in DPC micelles, however, is not seen for structures in TFE/H_2O. In contrary, NMR data even suggested strengthening of the H-bond network in this region as hydrogen bond lengths in the calculated structures were shortened compared to the WT. These findings were not reflected in the three-dimensional structures derived from NMR restraints, which indicated no weakening of H-bonds at this site. Likewise, the MD simulations by Scharnagl et al. showed no local unfolding around the ε-cleavage site of I45T [300]. These observations are in turn in accordance with cleavage assays done by two groups that clearly indicated no shift of the ε-cleavage site, but assumed that the product line is changed after the initial ε-cleavage [278, 347]. Again, MD simulations by Götz et al. showed lower H-bond occupancies for V44M within the C-terminal helix while I45T apparently stabilised the H-bond at T45 but destabilised H-bonds more towards the N-terminus [357].

Considering all these observations, it is very likely that more than one step of APP-γ-secretase interactions is affected by the four mutations. Impairment of overall processing may hint at disturbances upon initial substrate recognition while shift of ε-cleavage could be due to altered substrate positioning in the enzyme and changed interactions there. Shorter Aβ fragments may result from longer retention times within the enzyme and shift of cleavage line during processing might again be due to disfavoured positioning within the catalytic cleft.

Structural Properties of APP WT TMD in Membrane Mimetics

Even though already four APP TMD structures in micelles are published, summarized in Table 4.3, they raise more questions than they answer. Thus, a longer APP TMD construct, harbouring the entire N-terminal intracellular domain was analysed in DPC micelles in this work as well. All four structures were determined under quite similar conditions. One, the structure by Barett et al. (2LP1) was measured in LMPG micelles while the other three were determined in DPC micelles, two by Nadezhdin et al. (2LLM and 2LOH) and one by Chen et al. (2LZ3). Nevertheless, the structures differ in essential features.

The three structures determined in DPC micelles resemble rather straight helices without observable weakening of significant kink at the $G_{37}G_{38}$-motif. The structure of Barrett et al. (2LP1), however, that was determined in LMPG micelles was strongly kinked. This might be induced by the different detergent used, as Barrett et al. exchange G_{37} and G_{38} against two leucine residues which only moderately straightened the helix [249]. And Dominguez et al. compared the chemical shifts reported for the structure in LMPG with the α-helicity of APP$_{15-55}$ in DPC and POPC derived from MD simulations. They could show that the

Table 4.3. Published structures of APP TMD WT determined under different conditions. All structures were oriented alike. The GlyGly-motif is highlighted in cyan.

PDB code	2LP1 monomer	2LLM monomer	2LOH dimer left-handed	2LZ3 dimer right-handed
detergent	LMPG, pH 6.5	DPC, pH 5.0	DPC, pH 6.2	DPC, pH 7.2
D:P	700:1	70:1	50:1	250:1
Reference	[249]	[250]	[251]	[253]

N-terminal domain in LPMG was less helical than in POPC and DPC. Thus, the kinked conformation of the Barrett peptide probably was enforced by the LMPG micelles [373].

The three other structures, nevertheless, were obtained in DPC micelles. However, one monomer (Nadezhdin, 2LLM, [250]), one left-handed dimer (Nadezhdin, 2LOH, [251]) and one right-handed dimer (Chen, 2LZ3, [253]) were calculated. Furthermore, the dimers exhibit different dimerization interfaces. The most obvious differences in sample preparation are the pH values and the detergent to peptide ratios used. In this thesis, APP_{0-55} was measured at pH 7.0 and pH 5.0. When comparing the two ^1H-^{15}N-spectra the peaks corresponding to the residues embedded in the membrane were apparently not affected by pH values, as no chemical shift perturbations could be observed. Nadezhdin et al. observed the monomeric structure at a detergent to peptide (D:P) ratio of 70:1 and the dimer at a ratio of 50:1. They also reported two sets of signals in a $_1H$-$_{15}N$-HSQC of the putative dimeric peptide. From these observations, they concluded that dimerization is enforced at a D:P ratio smaller than 70:1 because they claim that a micelle consists of about 70 DPC molecules. Thus, statistically at a D:P ratio smaller than 70:1 two peptides should be at least embedded in some of the micelles [251]. In literature, DPC aggregation numbers are usually given as a range from 60 to 80 [395], which in turn would imply that even at D:L 70:1 the monomer is not necessarily obtained. Accordingly, it is also possible that the observed additional signals in the HSQC spectrum originate from oligomers. Further contradicting their conclusions is the fact that Chen et al. observed their dimer at a D:P ratio of 250:1 [253] what according to Nadezhdin should lead to monomeric structures.

The two groups observed different sets of interresidual NOE contacts. Nadezhdin et al. observed two sets of cross peaks in the ^1H-^{15}N-HSQC spectrum, which they claim, was

due to the presence of monomeric and dimeric APP in the sample. Furthermore, they based their dimeric structure on six intermonomeric NOEs obtained from ^{15}N- and ^{13}C-edited and ^{13}C- and ^{15}N-filtered NOESY experiments: $I_{32}H_\gamma$-$M_{35}H_\epsilon$, $L_{34}H_\delta$-$M_{35}H_\epsilon$, $L_{34}H_\delta$-$V_{39}H_\gamma$, $I_{41}H_\gamma$-$A_{42}H_\beta$, $I_{45}H_\delta$-$V_{46}H_\delta$ and $T_{48}H_\gamma$-$L_{49}H_\delta$ [251]. Chen et al. used chimera samples to obtain 13 intermolecular NOEs by ^{13}C- and ^{15}N-filtered NOESY experiments, for example: $V_{39}H_N$-$V_{39}H_\gamma$, $V_{46}H_{\gamma2}$-$V_{46}H_N$, $V_{40}H$-$V_{39}H_{\gamma1}$ and $M_{35}H_\epsilon$-$V_{36}H_{\gamma1}$. Furthermore they used RDCs for structure refinement. [253] Thus, both groups observed completely different inter-monomeric cross-peaks with basically the same experiments, resulting in diverging dimer interfaces. Furthermore, both groups that determined a monomer simply presumed that APP is present as monomer in their samples. They did not employ methods such as analytical ultracentrifugation to test this presumption.

As the question whether membrane bound APP forms dimers within its TMD or not is still under debate (APP TMD dimerization in general will be discussed later), APP_{0-55} was analysed in DPC at pH 5 in this work as well. The aim was to investigate under which conditions the monomeric or dimeric form could be observed and whether the kink observed by Barrett et al. in LMPG [249] could be reproduced in DPC micelles.
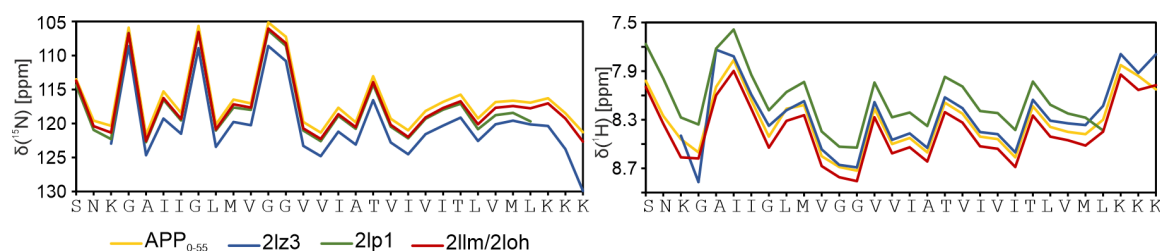
Figure 4.24. Chemical shift comparison of the published APP TMD structures and the data obtained in this work: ^{15}N (left) and ^{1}H$_N$ (right) chemical shifts of the four deposited structures compared with APP_{0-55} in DPC. The chemical shift profiles are almost perfectly overlapping and the differences are most likely due to diverse chemical shift referencing. For 2LLM and 2LOH deposited chemical shifts were identical.

Upon successful assignment of APP_{0-55} in DPC, the chemical shifts obtained were compared with those of the four structures available at the PDB. Indeed, one would expect ^{1}H$_N$ shifts in particular, which are very sensitive to small deviations in their environment, to be significantly perturbed. Instead, as shown in Figure 4.24 their profiles over the APP TMD sequence almost perfectly overlap. Differences are most likely due to variable reference frequencies.

The structural differences could be due to subtleties during sample preparation or, what seems more likely, APP can adopt a variety of structures with its TMD when embedded in the membrane or in micelles. All these studies may have sampled the same peptide but observed diverse snapshots. The comparison of the structures and the data used does not explain why different results were obtained by the three groups. APP TMD seems to constantly change its appearance like a chameleon, probably undergoing conformational exchange between most diverse structures.

Due to the large discrepancies the published structures do not clearly prove whether APP TMD is flexible or kinked in the lipid bilayer or not. Compared to TFE/H$_2$O, DPC induces straightening of the helix and stabilises the N-terminal domain. However, as shown in

this work based on chemical shifts, the transmembrane domain of $APP_{0\text{-}55}$ is more rigid in DPC micelles than APP TMD in TFE/H_2O, even though the N-terminal helix part appears less helical than the C-terminal part in both environments. Secondary chemical shifts hint at lower helicity and therefore possibly enhanced flexibility at the $G_{37}G_{38}$-motif in DPC and in TFE/H_2O. The structural information obtained is in accordance with published data, mainly from MD simulations. Calculations by Dominguez et al. had shown that APP TMD experiences a loss in helicity at residues G_{37} and G_{38}, both in POPC and DPC micelles and a higher helicity of the C-terminal helix with respect to the N-terminal domain [373]. This split structure was observed by MD in TFE/H_2O, too. Our collaborators at TUM (Scharnagl and co-workers and Langosch and co-workers) showed with MD simulations that H-bond occupancy decreases at residues G_{38} to I_{41} in TFE/H_2O and, less pronounced, in POPC [357]. Furthermore, the hydrogen-deuterium exchange profile observed in this work is in good agreement with deuterium-hydrogen exchange rates sampled by MD simulations [344]. Bending and twisting motions were observed by others as well. In micelles Dominguez et al. detected a kink of about 12° at the GlyGly-motif [373]. Furthermore, bend and swivel angles were determined by Götz et al., both in TFE/H_2O and POPC. They observed bending up to 30° with 12° mean value and the larger share between 0° and 20°. In TFE/H_2O this was shifted slightly, increasing the ratio of stronger bent structures. They observed restricted swivel angles as well, while APP WT TMD was limited to a range of about 60°. Due to differences in axis definition the absolute directions are not comparable, though [344].

This leads to the conclusion that the TMD flexibility is at least partially restricted in the lipid bilayer.

In the following sections, the specific interaction events and how they could possibly be influenced by the alterations observed, will be discussed.

Substrate Entry into γ-Secretase

As already described above, it is still under debate how substrates enter into γ-secretase. Cryo-EM structures of C83 bound to the enzyme's catalytic cleft were determined [304] (see Section 4.1.3 pp. 43) but initial binding or the entry event itself could not be investigated on a structural basis so far. Three entry pathways are discussed: The substrate could use an opening between TMD 2 and TMD 6, between TMD 2 and TMD 3 or, finally, between TMD 6 and TMD 9 [325, 328–330], explained more thoroughly in Section 4.1.3 (pp. 44).

The substrate initially binds to the N-terminal domain of PSEN1, according to cross-linking studies with C99 and CHAPSO-solubilized γ-secretase [321]. In collaboration with Manuel Hitzenberger and Martin Zacharias, the structures determined by NMR in this thesis were compared with their MD simulations. They assessed the entry of C99 (without extracellular domain) into γ-secretase via the three pathways described, by actively pulling residues L_{49} and V_{50} towards the catalytic centre. Entry through TMD 2 and TMD 3 was the most likely entry pathway according to their simulations. To reach its final position in a cavity formed by TMD 2, TMD 3 and TMD 5 they observed that the substrate needed to kink at the GlyGly-motif to overcome the loop connecting TMD 2 and 3 [325]. These observations were substantiated by the results obtained for APP TMD. The structure of APP TMD WT in TFE/H_2O permits the same kink angle and direction as observed by Hizenberger & Zacharias. The structures of the four mutants in TFE/H_2O, in

contrast, did not fit easily but clashed with TMDs of PSEN1. Hence, substrate entry might require specific bending and twisting motions of the TMD. When structures are too rigid or wrongly oriented, substrate entry may be impeded or entirely impaired. This seems to be the case for the two G38 mutants that were found to dramatically decrease AICD production to 38% in the case of G38L and only 8% in the case of G38P TMD compared to the WT [344]. These two mutants showed the greatest deviation in swivel angles compared to WT and, in contrast to V44M TMD and I45T TMD, do not cover the swivel angle range of APP WT TMD. As the swivel angles of the G38 mutants deviate from the WT by about 110°, they could be rotated by one amino acid. Then they would again fulfil the bending motion needed for entry. Within the active site they would end up turned by one amino acid, thus, not the bond between L_{49} and V_{50} but between T_{48} and L_{49} would be presented to the catalytic aspartates. As currently no data on the exact length of the AICD generated upon G38L TMD and G38P TMD cleavage is available, it is not known which ε-cleavage site is preferred to verify this proposal.

V44M in contrast was shown not to reduce overall processivity, but ε-cleavage preference was found to be shifted from L_{49} to T_{48} [278, 347]. What is speculated for G38P/L above could happen in this case as well. Even though V44M allowed a much broader range of swivel angles it is imaginable that, at least sometimes, the substrate entered the catalytic cleft rotated by one amino acid, with the result that T_{48} instead of L_{49} was positioned at the catalytic residues of γ-secretase. This fits to the finding that ε49-cleavage was not fully impaired but ε48-cleavage occurred more often than for APP WT TMD, shifting the ratio of the respective cleavage products.

I45T TMD on the other hand experiences much slower processivity. However, it was shown by Bolduc et al. that initial cleavage takes place at L_{49} [278]. This supports the first assumption, that substrate entry was impaired due to altered kink and swivel preferences. Initial positioning in the enzyme does not seem to be altered by the mutation.

The shift of cleavage line preference could be explained by the altered swivel angles, which could force the substrate to rotate by one residue to conduct the movement required to enter. This could lead to alternative positioning within the catalytic cleft and thus to altered processing. This theory could not be corroborated by MD simulations so far. Hitzenberger & Zacharias pulled residues L_{49} and V_{50} to the catalytic residues which corresponds to ε-cleavage at L_{49}. Thus, conclusions about how the entry of the substrate into the enzyme changes when ε-cleavage occurs at T_{48} cannot be drawn. Furthermore, they did not investigate how the single-point mutation within APP TMD considered in this work act in their simulation, but the structures determined in TFE/H_2O were only aligned to APP WT in the snapshot of their simulation.

Substrate Processing by γ-Secretase

After entering the active site, the scissile bond is presented to the catalytic residues and cleavage commences. The first cleavage step of C99 or C83 within its TMD, takes place at the ε-cleavage site. To make the scissile bond accessible to the catalytic residues the helix must unwind locally [332]. Zhou et al. showed in their cryo-EM structures that C83 adopted a β-sheet structure at its C-terminal domain in the catalytic cleft [304]. Hence, besides substrate recognition and entry this unwinding process could determine the cleavage

efficiency of γ-secretase. Helix unwinding after substrate entry might be impaired by the shorter hydrogen bonds observed around the ε-cleavage sites of G38L, G38P and I45T (see Figure 4.18) that promote structural rigidity. This could explain lowered processivity.

Val and Ile are considered helix destabilising residues in aqueous environment, Gly even helix breaking. The introduction of these residues around the scissile bond was shown to result in increased proteolysis [396]. In the membrane environment, however, β-branched amino acids like valine and isoleucine are helix promoters and glycine supports helicity as well [397] [398]. Val, Ile and Gly were indeed found to be below the five most abundant amino acids in single-span TM helices [399, 400]. These residues probably stabilise the cleavage sites when in the membrane but weaken the helix or even induce unfolding when C99 (or any other substrate) reaches the water filled cavity at the active side. However, these effects do not only depend on the naked amino acid sequence [380]. The introduction of three leucines at the ε-cleavage site to impair unravelling within the enzyme was shown not to be rate limiting for proteolysis. Nevertheless, cleavage line was shifted as Aβ42 generation was increased and Aβ40 decreased [293, 401]. Besides helical unwinding the substrate has to straighten upon arrival in the catalytic cleft [304, 325]. As G38P could not adopt an entirely straight structure according to the measurements in TFE/H$_2$O, this mutant might impair processing as it could not adopt an entirely straight conformation. Thus cleavage might be slowed down, as observed for G38P by our collaborators, although the substrate successfully reached the catalytic cleft [344].

After initial cleavage at the ε-cleavage site, γ-secretase substrate is processed further. Mostly consecutive tripeptide fragments are removed, resulting in the most abundant Aβ40 peptide or to a lesser extent Aβ42 and Aβ38 (see Section 4.1.2 pp. 36). As Aβ42 is the most aggregation prone product whose aggregates are commonly found in the brains of AD patients, most studies focus on substrate (or enzyme) properties that promote Aβ42 formation. It has been proposed that the time the substrate remains within the enzyme's catalytic cleft determines the number of γ-secretase cleavage steps [338]. This again could depend on the interactions of the substrate's N-terminal domain with γ-secretase [325]. This theory was substantiated by simulations detecting no conformational changes within the substrate's N-terminal helix inside the catalytic cleft [325, 338]. In the case of G38L the main cleavage product was Aβ37, indicating one cleavage step more than for G38P, that mainly led to Aβ40. In neither case Aβ42 was detected suggesting that only ε-49 cleavage occurs [344]. Successive trimming leads to Aβ46, Aβ43, Aβ40 and in the case of G38L even to Aβ37. Pathway shift of I45T could be due to the fact that helical instability facilitates subsequent trimming.

The observed helix stabilisation of G38L, especially at its N-terminus, might enable stronger interactions with γ-secretase that result in a longer retention time in the enzyme.

Monomer or Dimer?

Before its interaction with the enzyme, APP can either be present as dimer or as monomer in the lipid bilayer. APP TMD dimers, at least at higher concentrations, were reported by various groups [253, 282, 293, 373, 402–406]. However, it is disputed whether and when the dimer dissociates. Different models were proposed: The substrate might interact with γ-secretase as a dimer. Or, the dimer and the enzyme-substrate complex might be in

dynamic equilibrium, leading to dissociation upon interaction with γ-secretase [332, 407]. In this case dimer structure might influence substrate recognition. It was even proposed that APP TMD is processed as a dimer. However, the lately published cryo-EM structures substantiated other results, which stated that γ-secretase processes monomeric substrates [279, 304, 353, 408–410].

Presuming APP TMD dimerizes, various dimer interfaces are plausible. Three GXXXG dimerization motifs, for example, $G_{25}XXXG_{29}$, $G_{29}XXXG_{33}$ and $G_{33}XXXG_{37}$ are located within APP TMD. It is unknown which, if any, of these three motifs is relevant for dimerization. Interestingly, the two NMR derived dimeric structures are based on neither of these motifs but locate the dimer interface in the centre of the TMD. Nadezhdin observed a left-handed parallel dimer via $I_{31}XXXM_{35}XXG_{38}XXXA_{42}XXI_{45}XXXL_{49}XXL_{52}$, helices were maximally close at the $G_{38}XXXA_{42}$ interface [251]. Chen et al. in contrary obtained a right-handed dimer, and determined, consistent with Nadezhdin et al., the $G_{38}XXXA_{42}$ as the interface [411]. The structures are described in Section 4.1.2 (pp. 39) and Section 4.5 (pp. 77).

In a recent study, Perrin et al. investigated dimers at these three GXXXG motifs and showed that different dimer orientations determine the cleavage line preference. They enforced the formation of dimers at different interfaces. To achieve this, they designed fusion proteins of the left-handed leucine zipper coiled-coil of the transcription factor Put3 from *Saccharomyces cerevisiae* coupled to the extracellular domain of C99. Put3 was coupled at varying positions of APP, from residue 1 to residue 17. So they could create every possible left-handed APP dimer. They identified two GXXXG dimers that were processed differently by γ-secretase. Dimerization via the $G_{33}XXXG_{37}$ motif promoted Aβ42 generation while usage of the $G_{25}XXXG_{29}$ led to higher levels of Aβ43 and Aβ40. They did not investigate possible dimerization via $G_{29}XXXG_{33}$. Additionally, they found the two presenilins to prefer different dimerization motifs, as PSEN1, mostly located in the plasma membrane, preferred $G_{25}XXXG_{29}$ while PSEN2 that is rather found in endosomes and lysosomes favoured $G_{33}XXXG_{37}$ [309, 310, 410]. An earlier study had already shown that G33A, diminishing $G_{33}XXXG_{37}$ dimerization, led to reduced Aβ42 but almost unchanged Aβ40 levels [351]. Therefore dimerization at this motif might occur in the membrane. Perrin et al., however, only investigated dimerization at the N-terminal motifs and not within the TMD, especially not at the $G_{33}XXXG_{37}$ motif and neither the $G_{38}XXXA_{42}$-motif. The latter was identified as the main dimerization interface in previous studies [251, 411]. In accordance with the dimer proposed by Nadezhdin et al., Yan et al. identified the TVIV motif as essential for dimerization, especially the I_{45} side chain. They proposed a dimer where helices cross at TVIT with I_{45} and V_{46} in direct contact [282]. As Perrin et al. enforced dimerization, it is not clear whether the dimers they describe really occur under physiological conditions, especially with the context that previous studies always presumed dimerization motifs within APP TMD.

Based on all these observations, APP TMD seems to be able to form dimers in many different ways. Which variant is the physiologically relevant one, if a wide variety of conformations could not be present in exchange with each other anyway, still remains unclear.

Clemente et al. performed cleavage assays with the presenilin homologue (PSH) MCMJR1 and APP TMD. They monitored interactions of APP WT and PSH in DPC

by a series of ^{1}H-^{15}N-HSQC experiments and observed linebroadening of APP cross peaks and appearance of new peaks over time. From chemical shift perturbations they concluded that the initial contact between substrate and enzyme occurred at the N-terminal domain of APP TMD. They presumed APP TMD to be dimeric in the membrane, based on observations made in the same group [253]. As they did not observe chemical shift perturbations at the dimer interface they concluded, that APP TMD interacts with the enzyme as a dimer [332]. However, as discussed above, four different APP TMD structures in micelles exist that do not largely differ in their chemical shifts. Thus, presuming all these structures show snapshots of several conformations adopted by APP TMD in lipids, the work by Clemente et al. neither proves nor disproves that APP TMD interacts as a dimer with PSH.

Based on these observations, the results concerning the structures of APP TMD WT and mutants in TFE/H$_2$O must be put into the context of dimerization. Even though APP TMD is most likely monomeric in TFE/H$_2$O, the possible conformations found might hint at dimer formation. Swivel angles of G38L and G38P deviate by about 110° from the WT, this corresponds to approximately one amino acid turn of the α-helix. According to Perrin et al. this makes the difference between the two dimerization motifs they investigated [410]. Bend and swivel of the peptides certainly defines possible dimers and thus possible dimerization motifs. This could explain worse processivity observed for the G38 mutants, because dimerization occurs in a disadvantageous manner and recognition by γ-secretase is thereby impaired. V44M has a wider range of possible swivel angles, including the ones favoured by the WT but is more restricted regarding the kink angles. Thus this might shift dimerization preferences again. According to Perrin et al. Aβ42 processing occurs mainly upon G$_{33}$XXXG$_{37}$-dimerization. This seems possible when theoretical dimer conformations of the average structures of all five peptides are investigated. I45T has a as large range of possible swivel angles as V44M but its mean value is again shifted by 110°. From comparison of structures, G$_{33}$XXXG$_{37}$-dimerization seems sterically hindered while G$_{29}$XXXG$_{33}$ looks possible. Dimerization as proposed by Yan et al. is only slightly impaired by the I45T mutation, but significantly reduced for V44M [282].

Supposing APP adopts a dimeric structure, at least partially, under physiological conditions and the exact conformation of the dimer influences γ-secretase processing, alterations in bend and swivel angles can change the dimer formed. In accordance with Perrin et al. this could explain the altered cleavage line preferences observed for the WT and the four mutants.

Other γ-Secretase Substrate TMDs

Several other γ-secretase substrates were analysed in this thesis. APP WT and mutant TMDs strongly suggest that, on the one hand, some degree of bending and swivelling is required to allow substrate entry into γ-secretase. On the other hand, not only flexibility but the exact bending direction with respect to the TMD part harbouring the scissile bond, seems to affect processivity. Thus, the structures of APP TMD were compared to data obtained for other γ-secretase substrates and to other substrate structures deposited in the PDB.

Besides APP five other γ-secretase substrate TMDs were measured in the group: Tumor necrosis factor receptor superfamily member 12A (TNR12 or Fn14), Amyloid-like protein

2 (APLP2), Receptor tyrosine-protein kinase erbB-4 (ErbB4), N-Cadherin (or Cadherin-2) and Neurogenic locus notch homolog protein 1 (Notch1). Amino acid sequences are given in Table 4.4. All peptides were analysed in TFE/H_2O (80/20 V/V) at pH 7.

Figure 4.25 shows secondary chemical shifts, S^2 order parameters and helical content for APP WT and the five other γ-secretase substrates. Furthermore, the three-dimensional structures of APLP2 TMD, determined by Celine Moser, compared to APP WT TMD are shown. Three-dimensional structures were calculated and hydrogen-deuterium exchange rates were measured for TNR12 TMD, which was investigated under my direction in the thesis of Celine Moser (2020) [158].

Table 4.4. Sequences of the other γ-secretase substrate TMDs. TMDs are underlined, italic K are non-native amino acids added for MS analysis. γ-secretase cleavage sites are indicated by an asterisk. Lab members in sample preparation, NMR measurement and data analysis were Mara Silber (MS), Claudia Muhle-Goll (CMG), Celine Moser (CM) and Nadja Guschtschin-Schmidt (NGS)

Substrate	Sequence	Involved
APP	^{26}SNK<u>GAIIGLMVGGVVIATVIVITL</u>*VMLKKK^{55}	MS
TNR12	^{76}RLLWP<u>ILGGALSLTFVLGLLSGF</u>LVWRRCRRR^{107}	CM, MS
APLP2	^{689}SLSSS<u>ALIGLLVIAVAIATVIVISL</u>*VMLRKR^{719}	CM, CMG, NGS
ErbB4	*KKK*^{652}<u>LIAAGVIGGLFILVIVGLTFA</u>*VYVRRK^{678}	CMG, NGS
N-Cadherin	*K*^{723}<u>GAIIAILLCIIILLILVLMFVVWMK</u>^{747}*KK*	CMG, NGS
Notch1	*KKK*^{1734}<u>LHFMYVAAAAFVLLFFVGCG</u>*VLLS^{1757}*KKK*	CMG, NGS

Based on observations made for APP TMD, a hinge or at least a slightly flexible motif was expected, separating N-terminal and C-terminal domains, about ten residues N-terminally with regard to the γ-secretase cleavage site. The results obtained are summarized in Figure 4.25.

APLP2 TMD is highly homologous within its TMD to APP. Unlike APP TMD, neither secondary chemical shifts nor the three-dimensional structures or S^2 order parameters indicate two domains separated by a less structured motif. In contrast, H-bond lengths are fluctuating over the entire TMD. Thus, APLP2 TMD rather resembles the straighter and more constrained APP G38L mutant than APP WT TMD. As APLP2 harbours isoleucine and alanine at the positions corresponding to G_{37} and G_{38} of APP WT TMD, it is consequential that the long hydrophobic isoleucine has the same effect as L_{38} on APP TMD and leads to straightening.

TNR12 TMD on the other hand exhibits no obvious homology with APP TMD, except for a GlyGly-motif within its TMD. However, with regard to the residues spanning the TMD, it is located further N-terminally than found in APP TMD. As it is not clear where γ-secretase cleaves TNR12 TMD, it cannot be deduced whether this probable hinge could fulfil the same function as in APP TMD. TNR12 TMD deviates in its structure from APP TMD, too. It does not exhibit two distinct motifs, but shows more or less equal helicity over its entire TMD. HDX rates revealed a W-shaped profile of fast and slow exchange rates in its C-terminal domain that is reflected in hydrogen bond lengths derived from the
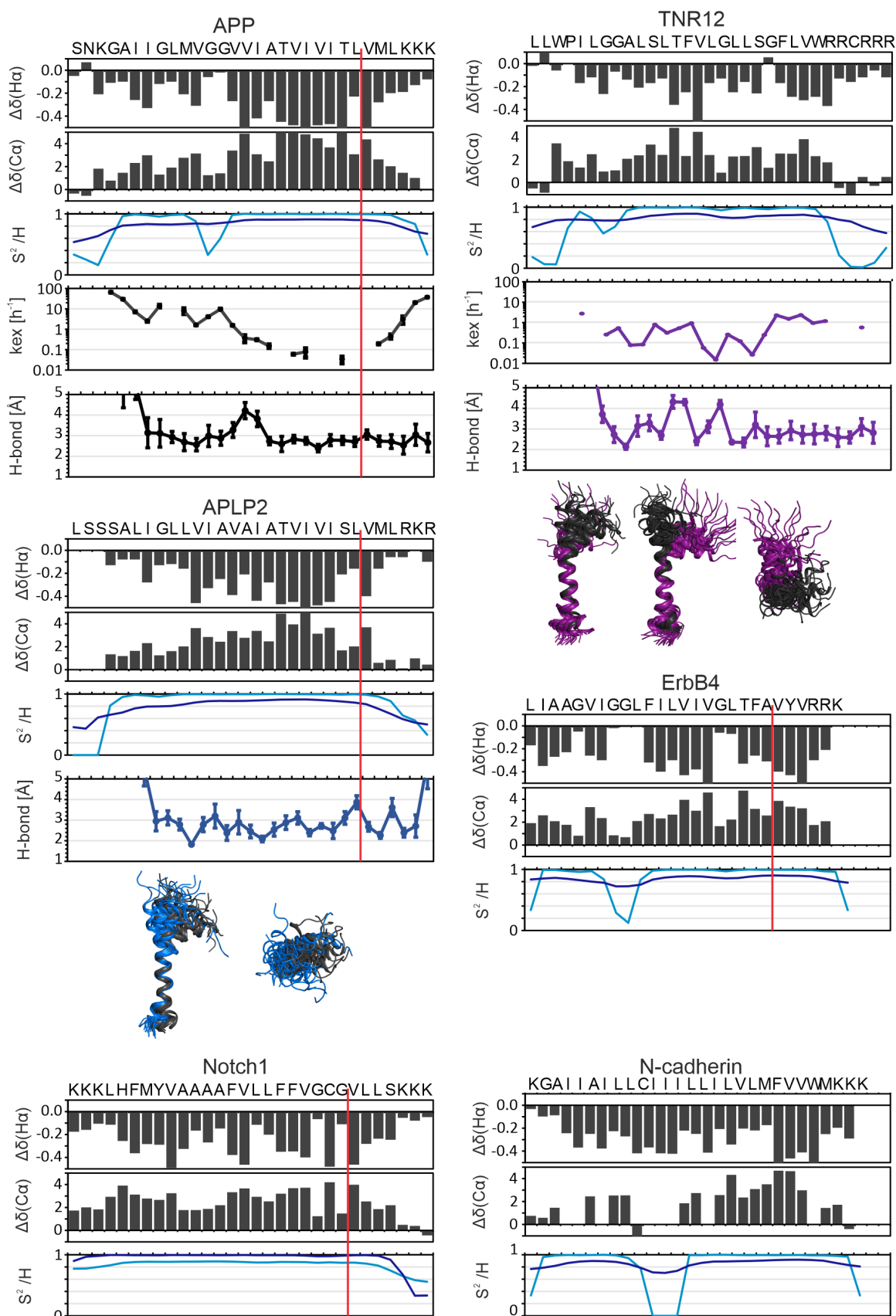
Figure 4.25. Comparison of APP, TNR12, APLP2, Notch1, ErbB4 and N-Cadherin TMDs in TFE/H2O: Secondary chemical shifts, S² order parameters, estimated helical content and, when available three-dimensional structures and HDX rates are shown. The red lines mark γ-secretase cleavage sites.

calculated structures. These observations suggest that TNR12 might form a dimer even in TFE/H_2O as the fluctuating H-bond lengths are in accordance with its GLLSG motif.

The other three substrates, N-Cadherin TMD, Notch1 TMD and ErbB4 TMD were not completely analysed in TFE/H_2O yet but only chemical shift data was available so far. ErbB4 contains a double glycine motif within the C-terminal part of its TMD and a GlyLeu motif further C-terminally. Interestingly, TALOS+ derived S^2 order parameters and helical content only advert a loss of structure at the GlyGly site. N-Cadherin TMD in TFE/H_2O apparently has no possible hinge locations. It has to be mentioned here, that ^{13}C chemical shifts were not fully assigned, thus the dip indicated by S^2 order parameter and helical content is most likely due to little chemical shift information. And, finally, Notch1, the apart from APP most thoroughly studied γ-secretase substrate, is the only substrate investigated here that shows no evidence for a flexible domain within its TMD. Instead the TMD appears well structured and α-helical.

Besides the peptides analysed in TFE/H_2O, three other γ-secretase substrate structures were obtained from the PDB: ErbB4 (PDB: 2LT2, [412]), CD4 (PDB: 2KLU, [413]) and Notch1 (PDB: 5KZO, [414]), were compared. The experimental details are given in Table 4.5. All these structures were determined in membrane mimetics, two in DMPC/DHPC bicelles and one in DPC micelles.

Table 4.5. Sequences of the γ-secretase substrates deposited in the PDB. γ-Secretase cleavage sites are indicated by an asterisk. Only the TMDs were analysed even though some of the published constructs comprised longer protein structures.

substrate	solvent	pH	Monomer/Dimer	
APP	DPC	5.0		MS
	^{26}SNKGAIIGLMVGGVV$\star$IATVIVITL$\star$VMLKKK^{55}			
Notch1	DMPC/DHPC	5.5	Monomer	PDB: 5KZO [245, 414, 415]
	^{1731}PAQLHFMYVAA$\star$AAFVLLFFVGCG$\star$VLLSRKR^{1760}			
CD4	DPC	6.2	Monomer	PDB: 2KLU [413]
	^{391}STPVQPMALI VLGGVAGLLL FIGLGIFFCV ^{420}			
ErbB4	DMPC/DHPC	5.0	Dimer	PDB: 2LT2 [412, 416]
	^{649}RTPLIAAGVIGGLFILVIVGLTFA$\star$VYVRRKS ^{679}			

As could be shown in this thesis, APP TMD is straightened when inserted into the membrane, but the weakening at the hinge motif could still be observed. Thus, secondary chemical shifts of these three TMDs were calculated based on the chemical shift values deposited in the PDB. Furthermore, S^2 order parameters and α-helical content were calculated with TALOS+ [72].

In Figure 4.26 secondary chemical shifts, S^2 order parameters and α-helical content of APP TM and the three other substrate TMDs are depicted. The corresponding three-dimensional structures are shown below.

ErbB4 TMD shows in both solvents similar secondary chemical shift patterns as APP TMD. As in TFE/H_2O, ErbB4 exhibits a considerable drop in S^2 order parameters and secondary chemical shifts at the GlyGly-motif. Thus, ErbB4 resembles APP TMD in both
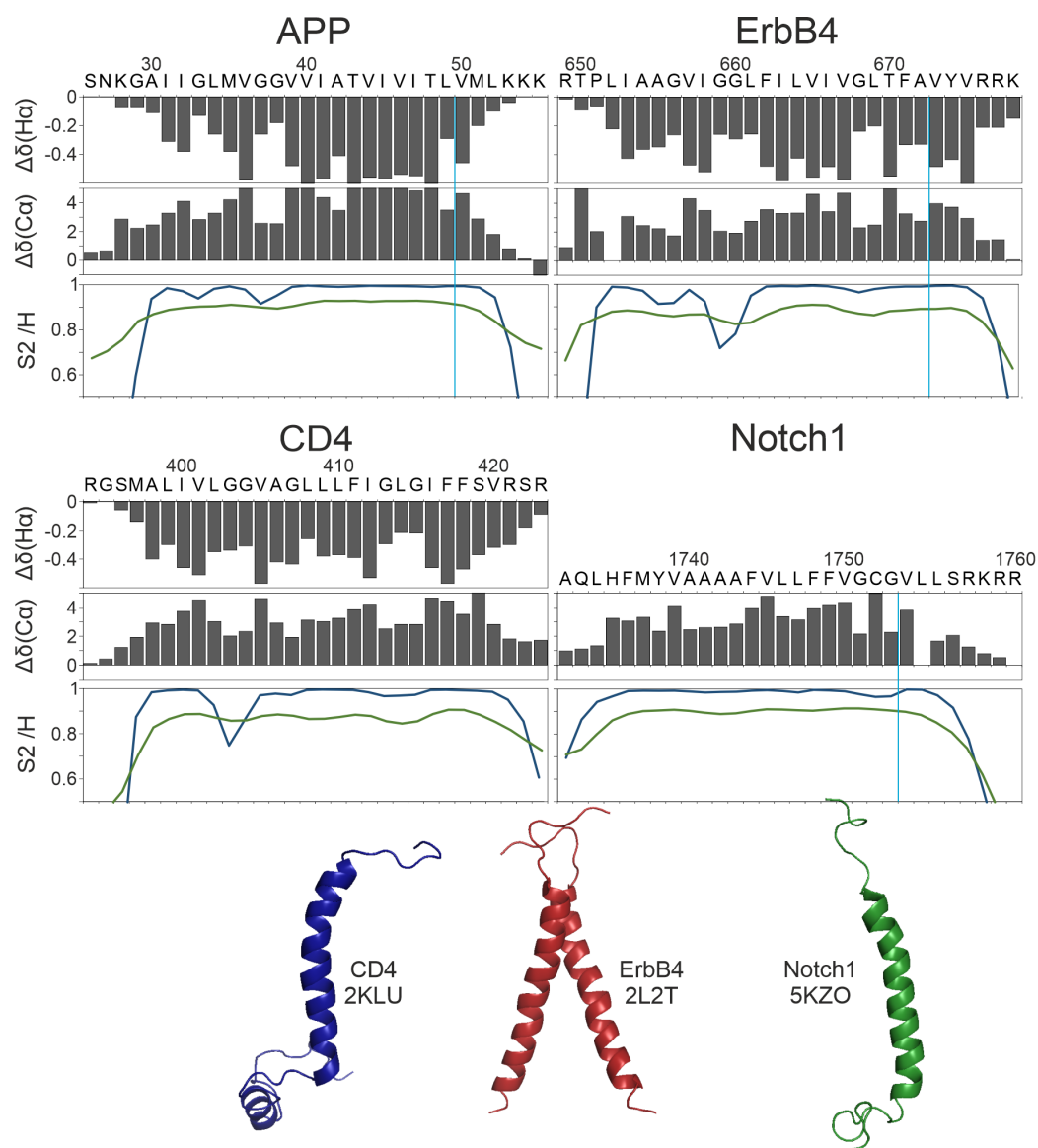
Figure 4.26. Comparison of APP ErbB4, CD4 and Notch1 structures in membrane mimetics: Secondary chemical shifts, S^2 order parameters (green) and helical content (blue) of APP, CD4, ErbB4, p75 and Notch1 TMDs in different membrane mimetics are shown (see Table 4.5). The blue vertical lines indicate the γ-secretase cleavage sites.

solvents, at least for the parameters analysed here. The structure derived from this data, however, is a dimer consisting of two very straight helices. As dimerization interface of ErbB4 TMD G_{656}XXGG$_{660}$ was proposed [412].

CD4 TMD again harbours a GlyGly-motif within its N-terminal domain. As observed for APP TMD and ErbB4 TMD S^2 order parameters drop at this site. In contrast to ErbB4 TMD, the structure of CD4 TMD was determined as monomeric (PDB: 5klu) and, very interestingly, appears kinked at the GlyGly-motif as observed for APP TMD in TFE/H$_2$O. As the γ-secretase cleavage site of CD4 TMD is not known, it cannot be deduced whether the distance to the GlyGly-motif is similar as for APP TMD. Nevertheless, it is probably within the C-terminal domain, close to the cytosolic border. Relating to the other substrates CD4 is probably cleaved around F_{392}.

Notch1 TMD, as already observed in TFE/H$_2$O, harbours a very straight helix according to chemical shift derived data. S^2 order parameters do only show slight deviations at the GlyGly-motif close to the C-terminal end. The corresponding structure in DMPC/DHP bicelles (PDB: 5kzo) shows a straight helix as well.

Notch1 cleavage by γ-secretase was studied in cell-based assays [247, 417, 418]. Similar to APP TMD, Notch TMD is cleaved at various sites within its TMD, experiencing initial cleavage close to the cyctosolic border at the so-called ε-like site. Subsequently one or two tripeptide fragments are removed until the remaining NECD is released. As neither AICD and NICD concentrations nor cleavage rate constants of γ-secretase processing of Notch1 TMD and APP TMD have been studied in comparative assays so far, it cannot be proven that Notch1 is cleaved more like APP G38L TMD, thus slower but probably more efficiently. The structure of the Notch1 TMD could also be bent like observed for APP G38P TMD. This conclusion seems likely based on the results obtained here for APP WT TMD and the four mutants.

The γ-secretase substrates compared resemble the findings for APP WT TMD and the four mutants. All peptides are known to be cleaved by γ-secretase despite their structural discrepancies. ErbB4 TMD and CD4 TMD seemingly resemble APP WT TMD regarding the flexible GlyGly-hinge. Others, APLP2 and N-Cadherin, are rather like APP G38L TMD, adopting straighter structures over the entire TMD in botstudio an membrane mimetics and TFE/H$_2$O. Strictly speaking this neither confirms nor contradicts assumptions drawn based on APP TMD structures but it still matches observations made for APP WT TMD and the four single point mutants.

5. PGAM5

5.1. Introduction

5.1.1. Rhomboid Proteases and PARL, the Mitochondrial Rhomboid

Rhomboid proteases are polytopic membrane proteins that are found in all kingdoms of life. The name rhomboid originates from studies on Drosophila with rhomboid shaped heads. The gene identified as responsible for this malformation was named "rhomboid" [419]. This class of intramembrane proteases comprise proteases and pseudoproteases: First, serine proteases that cleave transmembrane proteins within the lipid bilayer and second, catalytically inactive homologues that alter their substrates without cleaving them. Rhomboids regulate a wide range of biological processes and pathways, such as signal attenuation, proteolytic ligand activation [420, 421] or degradation of unstable membrane proteins [15]. Thus, they play an important role in quality control and trafficking of membrane proteins.
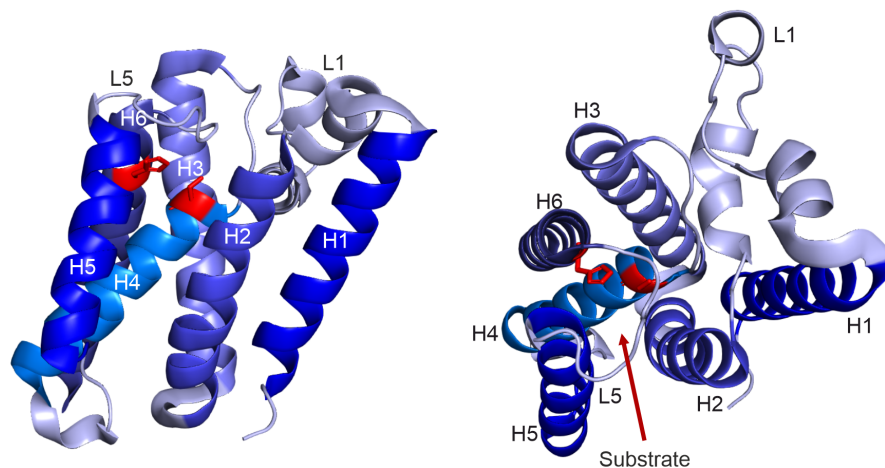
Figure 5.1. Three-dimensional structure of GlpG determined by X-ray crystallography: The front view of GlpG is shown on the left, the top view on the right. The catalytic residues, S_{201} on TM 4 and H_{254} on TM 6 are highlighted in red. The proposed substrate entry pathway through the opening between TMD 5 and TMD 2 ist indicated by the red arrow. (PDB: 4NJN [422]).

Moreover, they cover a wide range of functions and are not restricted to the release of a specific fragment, such as a signal peptide. In mammalian cells, for example, they

are found in all major cell organelles [419, 423, 424] and it is even possible that the same rhomboid is located in two different cellular compartments [420]. The basic structure of all rhomboids is similar. They consist of six transmembrane domains that are often complemented by additional TM segments and extended tails, either N- or C-terminally [9]. But while bacterial rhomboids contain only these six TMDs, a second form, usually found in eukaryotic cells, harbours an additional TM segment at the C-terminus, and a third variation accommodates the additional TM domain at the N-terminus [9]. This last variant is typically found in mitochondrial rhomboids [425]. The catalytic mechanism is conserved between rhomboids. A histidine-serine dyad has been identified by various mutagenesis studies and the catalytic centre is buried in the membrane [426–429].

The most widely studied rhomboid protease is the *E. coli* protease GlpG and its substrate LacY [430]. In addition, Rhomboid-1 of *D. melanogaster* and its substrates Gurken and Spitz have been extensively investigated [427, 429]. The three-dimensional structure of *E. coli* GlpG determined by X-ray crystallography is shown in Figure 5.1 [422]. The six TMDs are clearly distinguishable as is the catalytic dyad, serine S_{201} on TM 4 and histidine H_{254} on TM 6, that are highlighted in red. Both termini extend into the cytosol [8].

Currently, two models are being discussed to understand substrate entry into GlpG from the second binding site, the so-called exosite. The first proposes the gap between TMD 2 and TMD 5 as the entry pathway, as indicated by the red arrow in Figure 5.1, where TMD 5 acts as a lateral gate. To permit access to the catalytic core, TMD 5 and L5 would need to move [31]. The second model suggests that the flexible loop L5 may itself act as the gate and that the space between TMD 2 and TMD 5 opens only marginally [431, 432]. The latter model requires a more complex ensemble of actions, as the substrate TMD must unfold locally outside the membrane and subsequently the amino acid stretch harbouring the scissile bond migrates into the catalytic cleft [33, 433].

This theory was elaborated in more detail by the Urban lab. They proposed a model based on ecGlpG (*E. coli* GlpG) that covers the single steps from substrate recognition, through migration to the enzyme, to the final cut, based on a series of snapshots from time-resolved crystallography. The eight principal steps are shown in Figure 5.2. Their most astonishing finding was that L5 is apparently involved in all steps, seemingly guiding the substrate from stage to stage. As soon as L5 opens the gate, the substrate can dock to the recognition motif and the "interrogation complex" forms. The step prior to the actual transition to the active site had been proposed earlier by Strisovsky et al [33]. This "interrogation complex" represents the critical point at which substrate is distinguished from non-substrate, as only stretches of amino acids prone to unwinding can extend further into the enzyme to the catalytic dyad, while stable peptides are rejected. The substrate is fixed within the enzyme again by interactions between its N-terminus and L5, this leads to the formation of the so called "scission complex". Then the actual cleavage takes place, based on series of small structural rearrangements within the active site. Subsequently the C-terminal part of the cleaved substrate is released at which point L5 reopens the gate and liberates the N-terminal product [434, 435]. These findings confirmed what had been discussed as discriminatory substrate feature for more than a decade: helix destabilising residues around the scissile bond are essential to facilitate substrate unwinding and thus migration to the active site [32, 35].
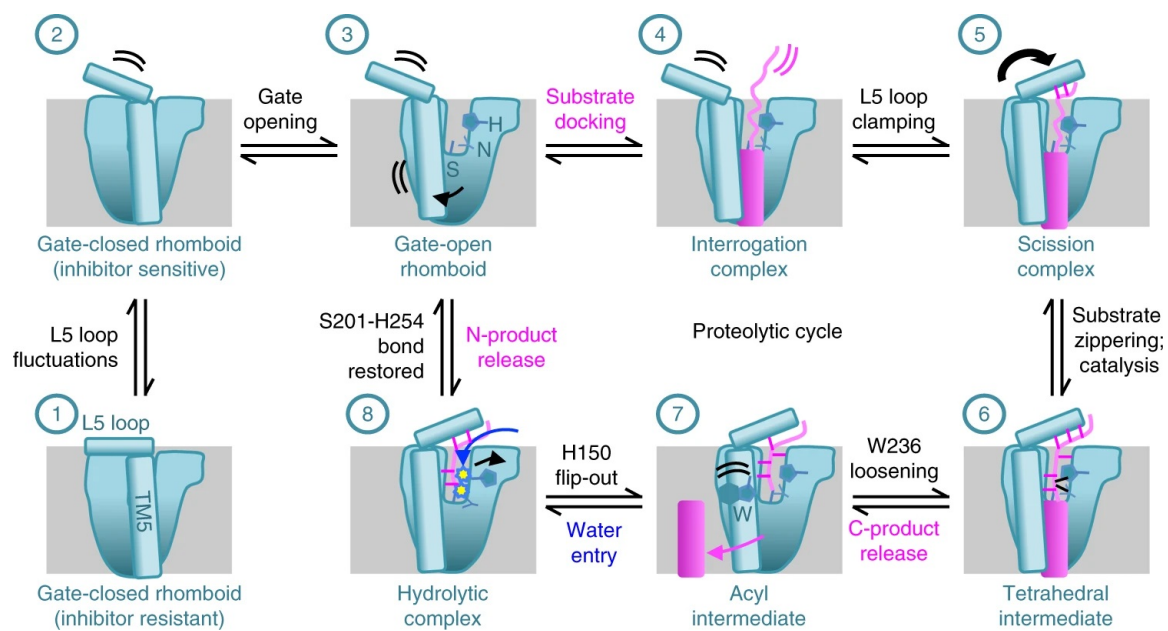
Figure 5.2. Model of the rhomboid proteolysis steps from gate opening to cleavage:
Proteolysis by rhomboids was found to comprise a preceding step, the so-called "interrogation complex" at which the actual selection of substrates takes place. [434]

Reprinted by permission from Springer Nature: Nat Struct Mol Biol, Ten catalytic snapshots of rhomboid intramembrane proteolysis from gate opening to peptide release., Cho, S., Baker, R.P., Ji, M. et al. (2019)

Although differences between the structures of hiGlpG (*Haemophilus influenza*), of which a crystal structure was determined as well, and ecGlpG (*E. coli*) were found, the cleavage mechanism of rhomboids seems to be strongly conserved. Especially TMD 5 and L5 seemed less structured in the HiGlpG compared to ecGLpG [436, 437].

Unlike other intramembrane proteases, γ-secretase for instance, rhomboids do not require a shedding step prior to intramembrane cleavage but can process full-length membrane proteins. Besides, they are not restricted to type I membrane proteins, but cleave type II and polytopic membrane proteins as well [15, 438, 439]. And, as observed for γ-secretase, rhomboid proteolysis is a quite slow process and can take minutes to hours [334, 422, 440].

One rhomboid protease is present in mitochondria of all eukaryotic cells, maintaining cellular integrity: PARL [22]. PARL is linked to mitochondrial dysfunction and this in turn is thought to play a role in diabetes, and in Parkinson's disease (PD) in association with mitochondrial dysfunction. Both of its two main substrates, PINK1 and PGAM5, may also be involved in PD due to their involvement in mitophagy [441–443].

Initially, the acronym PARL stood for Presenilin-Associated Rhomboid-Like protease [3, 21], but was recently renamed to PINK1/PGAM5 Associated Rhomboid-Like protease [22]. PARL is located at the inner mitochondrial membrane (IMM) [20]. In accordance with the general model of rhomboid topology, PARL was predicted to consist of six TM segments with a seventh TM segment at its N-terminus. The C-terminus was supposed to be located in the inner membrane space and the N-terminus in the mitochondrial matrix. The catalytic centre, buried in the membrane, consists of a serine (S_{277}) and a

histidine (H$_{335}$). The active site might face the mitochondrial matrix, shown in Figure 5.3, as suggested by topology predictions, but the orientation of PARL in the IMM has not yet been fully unravelled [9, 444, 445]. Since the mitochondrial matrix resembles the procaryotic cytosol, the predicted topology would be inverted compared to GlpG. Based on different processing in various tissues, several forms of PARL have been identified that differ in the length of the mitochondrial targeting sequence (MTS) that extends into the matrix. Besides full-length MTS two truncated forms are known: PARLΔ53, in which the MTS is almost completely removed that is considered the mature form that was found in spleen, kidney and lung [444]. The other variant, PARLΔ77, was shown to cleave substrates more efficiently than PARL harbouring full-length MTS [446]. PARLΔ77 and PARLΔ53 might have different functions, but all three variants are catalytically active [20, 446]. It has also been suggested that PARL is part of a larger multi-protein complex, which is not uncommon in the IMM. This protein hub might consist of PARL, YME1L and SLP2 [447]. It is not clear, however, to what extent PARL needs these possible partners and in which way they might interact and influence each other.
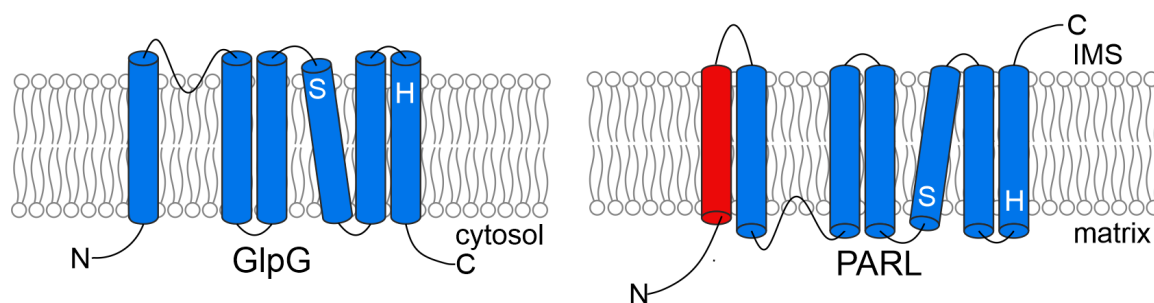
Figure 5.3. Schematic representation of GlpG and PARL: Both consist of six TMDs but PARL harbours an additional TMD at the N-terminus. The mitochondrial targeting sequence (MTS) extends into the mitochondrial matrix and can be removed partially or fully depending on the specific function and location of PARL [9, 20, 444].

Rhomboid substrate requirements are also still under debate. Bacterial rhomboids were shown to prefer small amino acids, like alanine, in the P1 position and bulky residues with hydrophobic side chains in the P4 position [33, 448]. These findings were questioned by two studies of the Urban lab, however, that showed substrate and rhomboid dynamics to be the main determinant of cleavage efficiency over specific recognition motifs as explained above [422, 435]. They could show in several studies that GlpG activity depends on substrate dynamics, more precisely on its instability. The introduction of helix-destabilising motifs as GlyGly-hinges that is a central feature of the APP TMD (see Chapter 4, pp. 35 ff.) or prolines induced the processing of former non-substrates such as APP TMD, whereas the insertion of helix-stabilising residues such as leucine had the opposite effect. When the substrate was already destabilised by its environment, for example in micelles, cleavage was also facilitated. Furthermore, shifts of the cleavage sites were observed depending on the substrate stability, as the introduction of prolines at specific positions could guide the cleavage site. Rhomboid proteolysis was a very slow process in their essays and they assumed that the "interrogation complex" might be the rate limiting step as it determines whether a substrate can be cleaved or not [37, 422, 435].

Lysyk at al. showed very recently, that PARL appears to prefer bulky amino acids in the P1 position, especially phenylalanine. Furthermore, they observed a preference for helix destabilising residues C-terminally from the cleavage site. Apart from that, they could show that PARL cleaves a quite broad range of substrates as they used a library of 228 peptides, many of which had been shown to be cleaved by bacterial rhomboids before [449]. 70 of these substrates were processed by PARL [446]. This is an interesting commonality between the two intramembrane proteases PARL and γ-secretase, as the latter is known to also process a variety of substrates as described in Chapter 4.1 (pp. 40 ff.)

5.1.2. PARL Substrates: PINK1 and PGAM5

Various PARL substrates have been identified so far, for example PGAM5 [450], PINK1 [451, 452], Smac [453], TTC19 [454] and STARD7 [455].

PGAM5 is one of the two best known PARL substrates. It is an atypical Ser/Thr phosphatase and regulates oxidative stress response [456], necroptosis in cancer cells [457, 458], apoptosis [459, 460], and probably mitophagy [303, 459, 461]. Furthermore PGAM5 was linked to immune responses and inflammatory diseases [462]. It is not fully clear yet whether PGAM5 is located at the outer and inner mitochondrial membrane or exclusively at the IMM [463]. PARL mediated PGAM5 cleavage is thought to serve as pro-apoptotic signal as cleaved PGAM5 in the cytosol is a substrate of apoptosis proteins [458]. Two mechanisms are known to be linked to PGAM5. First, it interacts with a mitophagy receptor [252, 459] and second it interacts with PINK1. Contrary to PINK1, PGAM5 processing increases when the inner membrane potential collapses [450]. PARL was found to preferentially cleave pink in healthy ("normal" membrane potential) mitochondria and to rather prefer PGAM5 as a substrate in damaged (low membrane potential) mitochondria (see Figure 5.4). Thus PINK1 and PGAM5 could be inversely correlated [303, 447, 464–466]. Loss of PGAM5 therefore leads to an accumulation of damaged mitochondria.

PINK1, a serine-threonine kinase, is the counterpart of PGAM5. It was found upon detection of a gene for early-onset Parkinson disease [467]. In healthy mitochondria with normal membrane potential PINK1 is imported by TOM (translocase of the outer membrane) and TIM (translocase of the inner membrane) complexes and inserted in the inner mitochondrial membrane with its transmembrane domain as depicted in Figure 5.4. Because the mitochondrial targeting sequence (MTS) is positively charged in its N-terminus, translocation through the TIM complex is energetically driven by the membrane potential across the IMM [468]. When inserted in the inner mitochondrial membrane the MTS is removed and PINK1 is cleaved by PARL at A_{103} in its transmembrane domain [469]. Then it is transported to the OMM and degraded in the cytosol (Figure 5.4) [470]. Upon mitochondrial damage the membrane potential drops and PINK1 accumulates at the outer mitochondrial membrane because transport through the TOM/TIM complex is no longer possible [471–474]. There it attracts parkin by phosphorylating ubiquitin, and parkin in turn ubiquitinates several mitochondrial proteins at the OMM [475–478]. PINK1 phosphorylates these polyubiquitin chains, inducing a positive feedback cycle that leads to mitochondria degradation [479–481]. Hence PINK1 cleavage by PARL functions as
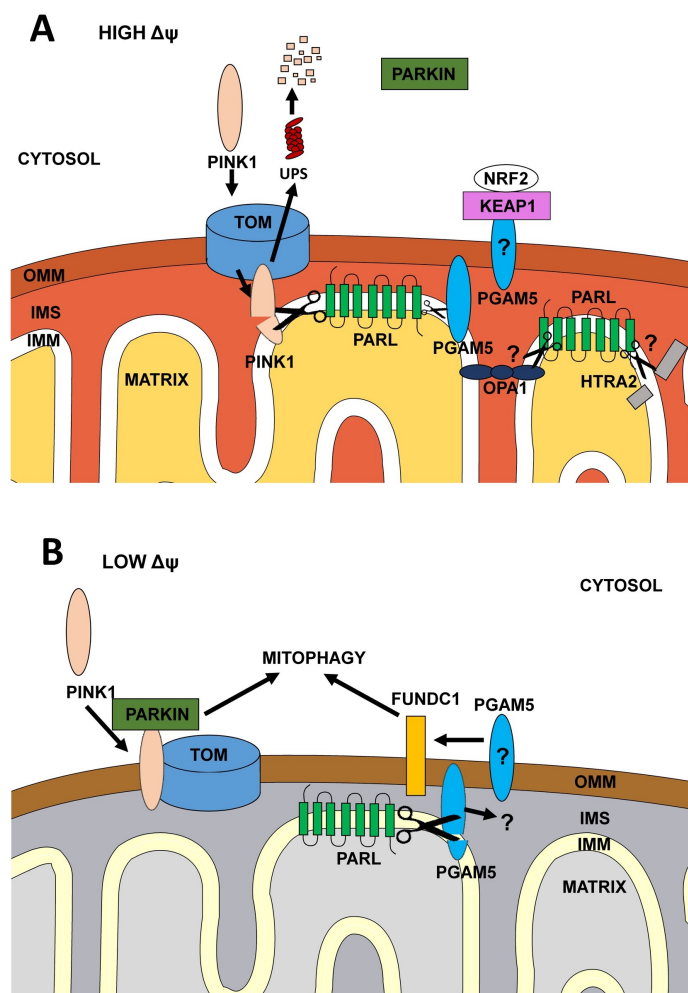
Figure 5.4. Substrate preferences of PARL depend on the mitochondrial membrane potential: A) At normal membrane potential PARL, located at the IMM, preferentially cleaves PINK1 and not PGAM5. PINK1 is transported to the IMM by the TOM/TIM complex and cleaved within its TMD by PARL. Then the PINK1 fragments are returned to the cytosol and degraded. B) At low membrane potential PINK1 is not imported to the IMM any more but remains in the OMM. Thus, PARKIN is recruited from the cytosol, this in turn triggers mitophagy. PARL then mostly cleaves PGAM5, the functions of both fragments are not known yet [22].

reporter of mitochondrial integrity [482]. PINK1 is to be analysed as part of a master's thesis by M. Himmelsbach , but this project failed due to experimental difficulties.

5.2. PGAM5 WT TMD in TFE/H$_2$O

The transmembrane domain of the PARL substrate PGAM5 was analysed by liquid-state NMR and CD spectroscopy. The synthetic peptide was dissolved in TFE-d2/H$_2$O (80/20 V/V) at pH 5.0 and a final concentration of 500 µM. A set of homo- and heteronuclear liquid-state NMR spectra, for resonance assignment and calculation of three-dimensional structures, was acquired at 300 K.

The peptide sequence analysed was

```
                            10        20        30
PGAM5₂₋₃₆ WT TMD:  AFRQALQLA ACGLAGGSAA VLFS/AVAVGK PRAGGD
```

5.2.1. Chemical Shifts Evaluation
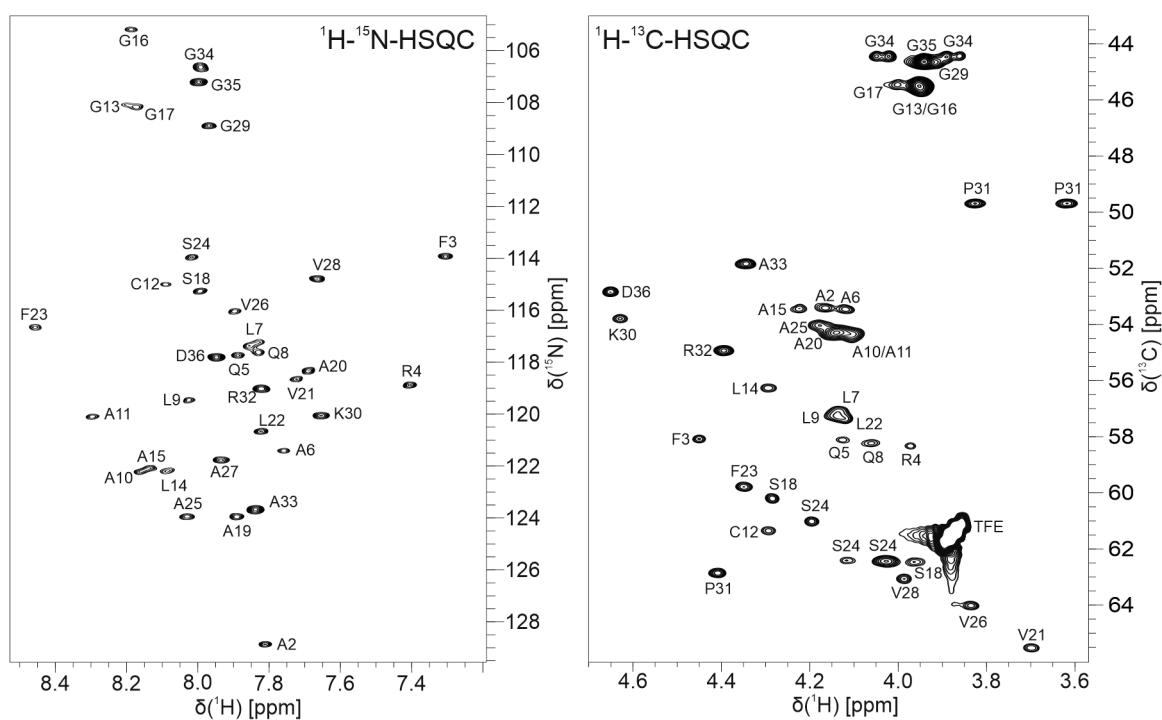
Figure 5.5. ^{1}H-^{15}N-HSQC and ^{1}H-^{13}C-HSQC spectra of PGAM5 WT TMD: The ranges of ^{1}H$_N$-^{15}N and ^{1}H$_\alpha$-^{13}C$_\alpha$ resonances are shown. The large resonance dispersion observed in the ^{1}H-^{15}N-HSQC indicates a structured conformation while the range of H$_\alpha$ resonances from 3.6 to 4.6 ppm in the ^{1}H-^{13}C-HSQC is characteristic for α-helices. All signals could be assigned, thus there seem to be no major side conformations.

All PGAM5 WT TMD backbone and side chain resonance could be assigned based on ^{1}H-^{15}N-HSQC, ^{1}H-^{13}C-HSQC, ^{1}H-^{1}H-TOCSY and ^{1}H-^{1}H-NOESY experiments. Figure 5.5 shows sections of both HSQC spectra. Amide proton resonances are spread between 7.2 and 8.3 ppm while H$_\alpha$ signals cover a range from 3.6 to 4.6 ppm. This indicates an α-helical, structured peptide. Since all ^{1}H-^{15}N and ^{1}H-^{13}C cross peaks could be assigned, there is no evidence of major side conformations or slow conformational exchange.

The secondary chemical shifts shown in Figure 5.6A also clearly indicate a predominantly α-helical structure. $\Delta\delta(H_\alpha)$ are mostly negative, just like $\Delta\delta(C_\beta)$, while $\Delta\delta(C_\alpha)$ are positive. The transmembrane helix apparently ranges from R_4 to A_{27}. However, there is a considerable break in helicity from G_{13} to G_{17}, indicated by both H_α and C_α secondary chemical shifts. The S^2 order parameter calculated with TALOS+ indicates to which degree information on the orientation of the H-N bond vector is lost and thus indicates dynamic processes at the respective position. This parameter does not show dramatic changes across the α-helical region, but a small reduction is observed at the central amino acid stretch, which is unstructured according to secondary chemical shifts. The α-helical content, again estimated with TALOS+ based on chemical shift data, resembles the probability to observe an α-helical structure at the respective residue. This also confirms the impression gained from the secondary chemical shifts, as it shows a severely reduced α-helical content in the central part of the peptide. In contrast to APP TMD, where the C-terminal part was more stable (see Section 4.2, pp. 50), both segments of PGAM5 WT TMD show a comparable degree of helicity. The PARL cleavage site between F_{23} and S_{24} is located within the C-terminal helix and is not marked by increased or decreased helicity. This in turn resembles the finding for APP TMD, where the cleavage site is also located within the very stable C-terminal helix. The very C-terminal end after G_{29} is unstructured, as could be expected due to the proline residue at position 31.
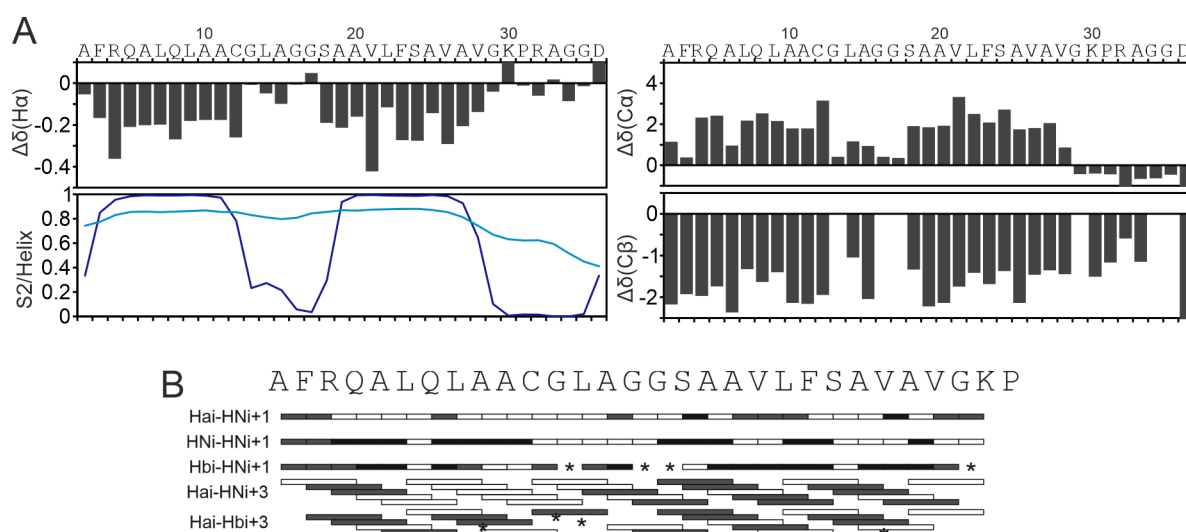
Figure 5.6. Structural and dynamic parameters obtained fo PGAM5 WT TMD: The peptide comprises two α-helical domains separated by a less structured region between G_{13} and G_{17}. A) H_α, C_α and C_β secondary chemical shifts of PGAM5 WT TMD. Random coil values were taken from Wishart 2011 [360]. Helical content (dark blue) and S2 order parameters (light blue) were obtained from TALOS+ [61, 72]. B) Characteristic interproton NOEs of PGAM5 WT TMD. Black boxes indicate strong NOEs, grey weak. White boxes show peak overlap hence NOE signals that could not be unambiguously assigned. Positions marked with an asterisk refer to missing NOE signals due to the chemical nature of the respective amino acid.

Characteristic NOE contacts between backbone and side chain protons are shown in Figure 5.6B. Both helix segments show comparable NOE contacts, whereas a few more cross

peaks could be observed in the C-terminal helix. The central less structured motif is not reflected in the NOE pattern. Admittedly, many NOE contacts could not be unambiguously assigned, as illustrated by white bars. The overall picture of an α-helix ranging from R_4 to A_{27} is largely reflected by the strong (black bars) and weak (grey bars) NOE contacts that could be identified. Even non-existent cross peaks would contain information, as this means that the respective protons were not sufficiently close for most of the time that magnetization could be transferred. However, such non-contacts could not be identified in the spectrum due to the severe peak overlap.

5.2.2. Hydrogen-Deuterium Exchange of PGAM5 WT TMD

Figure 5.7. Hydrogen deuterium exchange of PGAM5 WT TMD: Black dots indicate slow exchange, grey intermediate. Asterisks denote peak overlap that did not allow to estimate exchange rates.

Hydrogen-deuterium exchange was measured at pD 4.0 and pD 5.0. PGAM5 WT TMD showed slow exchange rates of the C-terminal helical domain and faster exchange rates at the N-terminal domain. Due to severe peak overlap some residues could not be assigned unambiguously and exchange rates could not be fitted but were estimated qualitatively. In contrast to APP TMD (see Section 4.2, pp. 55) exchange rates were much faster. The APP C-terminal domain was quite stable even at pD 7.0, while similar exchange rates of PGAM5 TMD at residues V_{21} to A_{27} were already observed at pD 5.0. Thus, the hydrogen-deuterium exchange of PGAM5 WT TMD is about 100 fold faster than observed for APP WT TMD. Furthermore, while APP TMD HDX clearly confirmed that the C-terminal helix is more stable than its N-terminal counterpart, PGAM5 TMD exchange rates within the N-terminal domain were only slightly faster compared to the C-terminal part. Unfortunately, G_{13}, G_{16} and G_{17} exchange rates were not accessible due to peak overlap in the TOCSY-spectrum used. Therefore, the presumably less stable region from G_{13} to G_{17} could not be confirmed by HDX.

5.2.3. CD Spectroscopy of PGAM5 WT TMD

The samples analysed by NMR were diluted tenfold and analysed by CD spectroscopy. The data obtained was evaluated with BestSel [163]. PGAM5 WT TMD shows the typical features of α-helices in the CD spectrum, shown in Figure 5.8. There is a maximum at 193 nm and two minima at 222 nm and 208 nm. However, the shape of the curve already indicates that the peptide is not fully helical, as the residual ellipticity at 222 nm is higher than at 208 nm. Estimation of the secondary structure content gives 47% helix, 9% antiparallel β-sheet, 6% turn and 38% other structural motifs. This confirms the information obtained from NMR chemical shifts, as the two separated helical domains identified by NMR comprise about half of the total sequence.
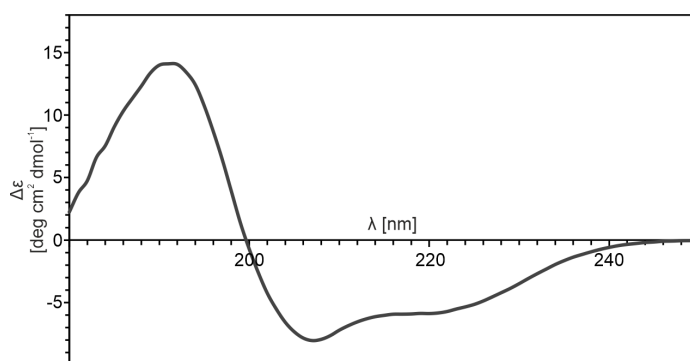
Figure 5.8. The CD spectrum of PGAM5 WT TMD indicates only a partially α-helical structure: This is in accordance with NMR data as about half of the sequence is suggested to be α-helical according to the secondary chemical shifts.

5.3. Comparison of PGAM5 WT TMD and Four Single Point Mutants

Four single point mutants were designed in collaboration with the Lemberg group (ZMBH, Heidelberg). Residues within the TMD that are conserved between different organisms were exchanged for leucine or serine (indicated in bold below). These residues were expected to alter the TMD structure in ways that might indicate PARL substrate specificity or its cleavage mechanism.

All PGAM5 TMD peptides were measured at 500 μM concentration, pH 5 and 300 K.

```
                       10        20        30
PGAM5 WT TMD     AFRQALQLAACGLAGGSAAVLFSAVAVGKPRAGGD
PGAM5 C12S TMD   AFRQALQLAASGLAGGSAAVLFSAVAVGKPRAGGD
PGAM5 C12L TMD   AFRQALQLAALGLAGGSAAVLFSAVAVGKPRAGGD
PGAM5 G17L TMD   AFRQALQLAACGLAGLSAAVLFSAVAVGKPRAGGD
PGAM5 S18L TMD   AFRQALQLAACGLAGGLAAVLFSAVAVGKPRAGGD
```

5.3.1. Chemical Shift Data of PGAM5 WT TMD and the Four Mutants

All four mutants exhibit only minor differences with regard to secondary chemical shifts compared to the PGAM5 WT TMD, mostly around the respective mutation sites. Both C12 mutants show only subtle effects, the greatest change is observed at residue L_{12} or S_{12}, which is expected. Smaller alterations occur N-terminally from the mutation site. The effect of C12L in this region is slightly more pronounced, as the estimated α-helical content suggests higher helicity at L_9 and A_{10}. C12S TMD, though, basically resembles the WT TMD. The greatest changes are observable for G17L TMD, where the central region from G_{13} to A_{15}, which appears disordered in the WT TMD, is clearly stabilised. The α-helical content is also estimated to be significantly higher than in all other four peptides. S18L TMD seems somewhat contradictory as its secondary chemical shifts show little difference from the WT TMD except for a small stabilisation around the mutated amino acid, while the calculated α-helical content is increased at residues G_{13}, L_{14} and A_{15}. The S^2 order parameter, however, shows a larger unstructured stretch.
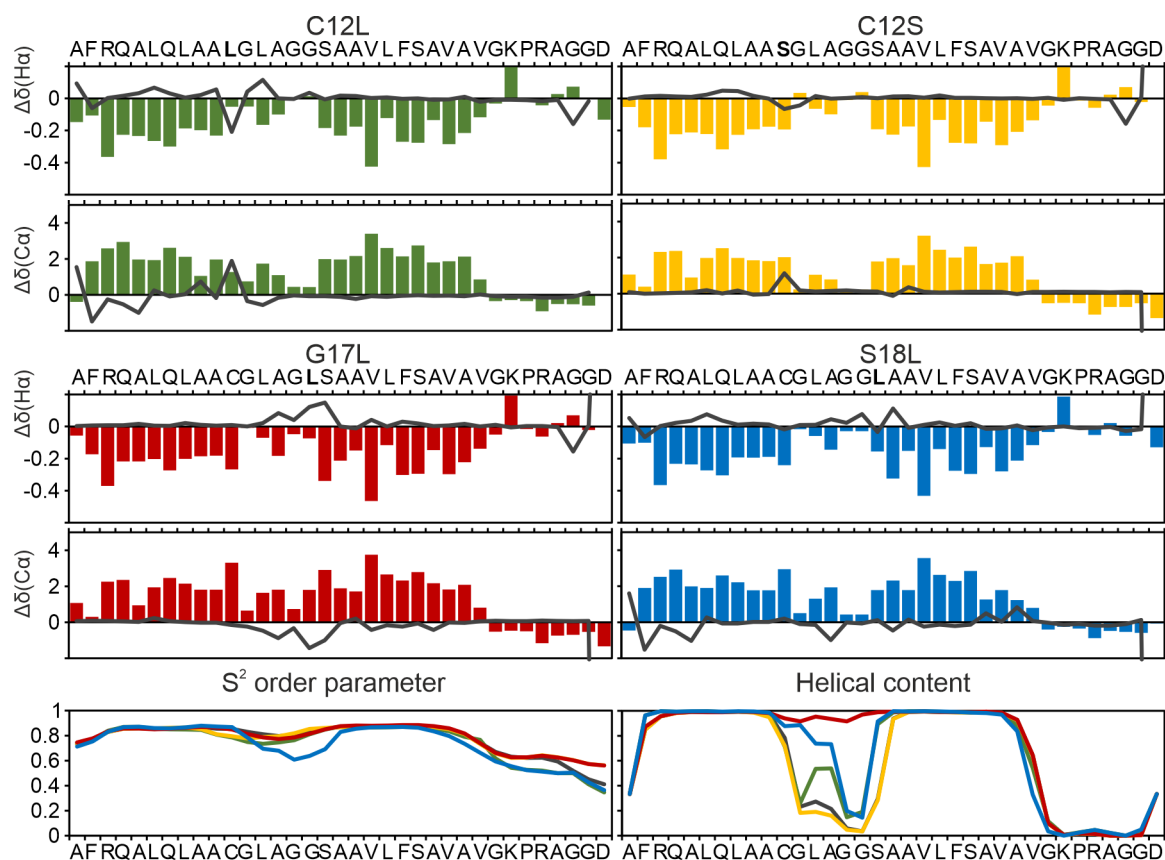
Figure 5.9. $^1H_\alpha$ and $^{13}C_\alpha$ secondary chemical shifts of all four PGAM5 TMD mutants compared to the WT: The bar charts show the absolute values determined for the respective PGAM5 mutant, while the black line indicates the difference between PGAM5 mutant and WT. Negative absolute values of $^1H_\alpha$ and positive of $^{13}C_\alpha$ indicate α-helical structure. Positive values of $^1H_\alpha$ compared to WT mean that the WT is less helical and vice versa for $^{13}C_\alpha$. S2 order parameters and helix probability are depicted in the bottom panel. Secondary chemical shifts, S^2 order parameter and α-helical content indicate only minor deviations for both C12 mutants, whereas G17L is considerably stabilised at the central amino acid stretch, while S18L seems to be destabilised.

5.3.2. CD Spectroscopy of PGAM5 WT TMD and the Four Mutants

CD measurements confirmed the impression gained from NMR data as shown in Figure 5.10. The helical content of the mutants is smaller than that of PGAM5 WT TMD, except for G17L TMD that was significantly more α-helical. The differences between C12L TMD, C12S TMD and S18L TMD are quite small, as expected. It is remarkable, though, that the exchange of one single amino causes that pronounced alterations of the secondary structure.
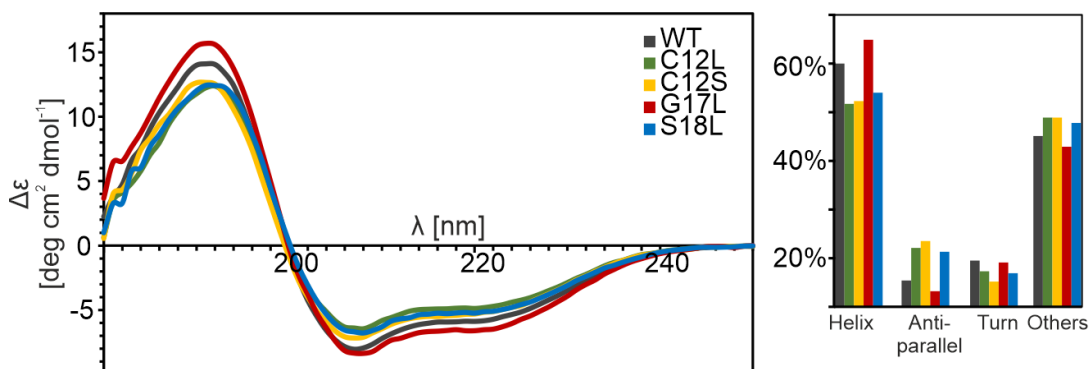
Figure 5.10. Results of CD spectroscopy of PGAM5 WT TMD and the four single point mutants: A) CD spectra of PGAM5 WT TMD and the four single point mutants and B) secondary structure content as estimated with BestSel [163]. Both graphs show that three mutants are less α-helical than PGAM5 WT TMD while G17L as the only variant appears more helical.

5.3.3. Structures of PGAM5 WT TMD and the Four Mutants

Three dimensional structures were calculated by ARIA2 based on distance restraints derived from NOESY spectra and dihedral angles derived from TALOS+ [72, 118]. The structural bundles depicted in Figure 5.11A confirm the overall impression gained from chemical shift data and CD spectroscopy. All five peptides comprise of two α-helical segments that are separated by an apparently short but quite flexible stretch of amino acids. In Figure 5.11A all structural bundles are shown superimposed on their C-terminal domains to visualize the relative orientations of both helical stretches. In contrast to APP TMD where the possible orientations were limited, PGAM5 TMD seems to be much less restricted. The histograms next to the structures show the abundances of all possible swivel angles summarised in 30° sections, while the mean bend angle and its standard deviation are given in the caption of the respective diagram. PGAM5 WT is seemingly not limited in its possible swivel angles, but exhibits the smallest kink angle with approximately 40°. The C12 mutants are more restricted in terms of swivel directions and do not allow as wide a range as the PGAM5 WT TMD, while their bend angles are generally larger and cover wider ranges. G17L TMD allows the largest bend angle and also does not show a clear preference for the swivel direction. Hydrogen bonds lengths derived from the structures, shown in Figure 5.11, confirm that H-bonds from A_{15} to C_{12} are elongated compared to the very uniform distances at the N-terminal and C-terminal domains. Interestingly, C12L

Figure 5.11. Comparison of NMR derived structures of PGAM5 WT TMD and the four single point mutants: A) Structural bundles of PGAM5 WT TMD and mutants, superimposed on residues A_{20} to A_{25}. Their C-termini are pointing downwards. Front view, side view and top view are shown. The histograms beside the structures show observed swivel angle ranges, grouped in 30° fractions. B) H-bond lengths derived from calculated structures between the amide proton given and the carbonyl oxygen four residues earlier.

TMD and S18L TMD significantly lengthen distances between C_{12} and A_{15}, indicating a more random coil-like structure in this region. The other two leucine mutants are close to the WT.

5.4. Discussion

Rhomboids and their substrates have not been investigated as extensively as other intramembrane proteases like γ-secretase. So far, GlpG is the only member of this enzyme family whose structure has been solved [8, 31], while the only structures of full-length substrate that were determined were that of *E.coli* TatA [483, 484]. However, neither PINK1 nor PGAM5 have been analysed on a structural basis, up to now. In this work PGAM5 TMD, a substrate of the human mitochondrial rhomboid PARL, was analysed by liquid state NMR spectroscopy. It is assumed that the active site of PARL is water-filled, as has been observed for GlpG, the *E. coli* rhomboid and other intramembrane proteases, such as γ-secretase [433]. Thus TFE/H_2O was chosen as solvent, as it is a good approximation of the conditions in the active site of the enzyme and provides unique insights into the substrate properties within the catalytic cavity.

The transmembrane domain of PGAM5 is generally presumed to be from L_9 to G_{29} [450]. The results obtained in this thesis contradict this assumption, as the two observed α-helical domains of PGAM5 WT span from R_4 to C_{12} and from S_{18} to A_{27}, connected by a flexible stretch of five amino acids. Structures of *E.coli* TatA, determined in DPC micelles, interestingly reflect this finding. Zhang et al. observed two α-helical domains, the N-terminal transmembrane domain, comprising 15 residues, and a second, amphipathic helix, 21 residues long, that is located at the cytosolic side of the *E.coli* cell membrane [484]. It seems unlikely that PGAM5 follows the same scheme and incorporates only one TMD in the membrane, as both peptides segments are significantly shorter than the TMD of TatA and do not show an amphiphilic pattern.

Analogous to the project of APP TMD, four single point mutants of PGAM5 TMD were designed in this thesis. Within the PGAM5 transmembrane domain three residues are conserved between different organisms: C_{12}, G_{17} and S_{18}. Based on this observation, the mutants were constructed in cooperation with Verena Siebert & Marius Lemberg (Lemberg Lab, ZMBH, Heidelberg). Leucine was introduced as helix stabilising residue at all three positions (C12L, G17L, S18L) complemented by a serine mutant (C12S). Cell-based assays showed that the C12 mutants (C12S, C12L) were cleaved more efficiently by PARL than the PGAM5 WT, whereas both mutations within the C-terminal helix (G17L, S18L) resulted in reduced processivity (Siebert & Lemberg, ZMBH Heidelberg, unpublished observation).

The most obvious structural alteration to affect cleavage would be expected around the scissile bond. The PARL cleavage site was assumed between S_{24} and A_{25} [450], while recent results strongly support the scissile bond one amino acid earlier, between F_{23} and S_{24}, though [446]. The structural differences induced by the four single point mutations were quite small, as NMR data revealed. G17L TMD was the only mutant that significantly increased the helicity at the flexible motif, while the other three induced only minor effects around their respective mutation sites and led to overall reduced helical content. However, the structures of both C12 mutants indicated longer hydrogen bonds between A_{25} and

V_{21}. This could be due to a slightly bent structure or general weakening of the helix in this region. It should be noted that the apparent weakening around the cleavage bond of C12S TMD and C12L TMD is not reflected in the chemical shift data, but appears only in theoretical H-bond lengths derived from the calculated structures. None of the five peptides showed any sign of helix destabilisation at the PARL cleavage site in terms of secondary chemical shifts and no obvious correlation between helix rigidity and cleavage efficiency can be deduced from the structural data obtained. Hence, no simple conclusion can be drawn here, but the four mutations apparently influence various aspects of substrate recognition and cleavage.

The three-dimensional structures should be regarded with some caution in this case, on the one hand. The absolute number of NOE contacts that would be theoretically possible is comparatively low due to the many glycines and alanines in the amino acid sequence. Since, naturally, amino acids with longer side chains can experience accordingly more NOE contacts with their neighbours, even if the side chains in helices are directed outwards and are therefore further apart, the PGAM5 sequence with its many glycines and alanines is not particularly favourable for structure determination. On the other hand, the signal overlap in the PGAM5 TMD NOESY spectra was significantly larger than in the APP TMD spectra. This resulted in a large number of ambiguously assigned peaks, in which the contributions of the involved contacts were possibly incorrectly weighted. Altogether, the lack of unambiguous NOEs could have led to an overestimation of conformational flexibility in the central GLAGG motif. However, as CD spectra confirmed the overall tendency and reflected the α-helical content of the calculated structure, the structures nevertheless seem to approximate the actual situation.

The question that arises from the cleavage assays of Verena Siebert & Marius Lemberg (Lemberg Lab, ZMBH, Heidelberg) is effect the mutations might have in the context of cleavage. The mutations could affect the structural stability around the cleavage site, even if it is not observed in the structures determined in TFE/H_2O. As helices are unfavourable protease substrates, generally destabilisation up to complete unwinding is required to permit processing [36, 291, 292]. For GlpG, it was shown that cleavage efficiency increased when the transmembrane helix of the substrate was already destabilised in the membrane [36, 37, 422]. Again similar to γ-secretase, small peptide-like inhibitors were observed to form an antiparallel β-sheet with loop 3 of GlpG that is stabilised by hydrogen bonds [448]. Thus, PGAM5 TMD in PARL most likely unwinds prior to cleavage. Helix-destabilising residues around the scissile bond facilitate this process. It is known that the preferences of amino acids to form an α-helix differ between non-polar (n-butanol) and aqueous media [485], so it is debated whether certain amino acids stabilise the helix in the hydrophobic membrane environments and destabilise it in aqueous media. The peptide would then retain the favourable α-helical structure in lipids but would unfold more easily in the catalytic cleft. The four mutants investigated are quite distant from the cleavage site, where unwinding must occur. However, the closest one, S18L, could impair unwinding as leucine has a much higher helix propensity than serine in both environments [485], which in turn could lead to the observed poor processivity. The other three mutants are unlikely to have a significant impact on α-helix stability within the C-terminal helix.

The second point of action could be substrate entry into the enzyme. APP TMD has been proposed to kink within its TMD upon entry to the catalytic cleft [325]. This finding is

strongly supported by the NMR derived structures of APP TMD in TFE/H$_2$O, as explained in Section 4.3.3 (pp. 61 ff.). In GlpG, a multi-step process was proposed, which has been explained in more detail in the introduction (pp. 93). In this model, it is suggested that the substrate first binds to the exosite of the enzyme and the so called "interrogation complex" is formed. At this point it is decided whether a possible substrate is processed. If the structure around the cleavage site is sufficiently unstable and unwinds, it can migrate further into the enzyme towards the catalytic cleft. If the peptide is too rigid it is released from the "interrogation complex" to the membrane [422, 434, 435]. It has been proposed earlier that the substrate might not enter the enzyme completely, but remains bound to the exosite, and only the stretch around the scissile bond migrates into the protease [10, 432]. This would mean that substrates that are cleaved more efficiently, such as C12S TMD and C12L TMD in this case, form a more stable or more favourable "interrogation complex" with the exosite of PARL. This could be related to smallest changes in the N-terminal helix, as it binds to the exosite and most likely remains bound during cleavage. Furthermore, the reduced swivel angle range of C12S TMD, similar to the observations in the case of APP TMD and γ-secretase, could lead to an improvement of the migration of the C-terminal substrate moiety into the catalytic centre by enforcing the "correct" direction. The increased helicity of G17L TMD at the centre could accordingly impede formation of the "interrogation complex" or substrate migration into the catalytic cleft. S18L TMD remains obscure. According to both, NMR and CD data, S18L TMD is less helical and more flexible at is centre. This could mean either that the "interrogation complex" is too unstable or that, as described above, the additional leucine leads to an increased stability of the C-terminal helix. However, the major drawback of these considerations is that, according to published models, PARL is inversely oriented in the membrane as shown in Figure 5.3 (Section 5.1, p. 94) [9, 444, 445]. This means that its catalytic residues are located close to the matrix border. PGAM5 migrates through the outer mitochondrial membrane in the inner mitochondrial membrane, so that its very N-terminal end reaches into the matrix. Consequently, the cleavage site within its C-terminal α-helical part is located on the other side of the membrane, close to the inter membrane space. This orientation of PARL, though, has been determined only based on topological comparisons and, at least to my knowledge, has not been confirmed with experimental data. If, however, the topology of the PARL was assumed wrong and it was actually oriented the other way around in the membrane, these considerations would make sense.

Thirdly, substrate dimerization within the membrane might play a role, as discussed for APP TMD. Full length PGAM5 is known to form dimers through its C-terminal tail that in turn form dodecameric rings, and PGAM5 phosphatase activity was shown to be dependent on dimerization [486, 487]. TatA TMD, in turn, could be detected as both monomer and dimer in DPC micelles, as the structures determined by Zhang et al. show. They demonstrated that TatA TMD was monomeric at a peptide to lipid ratio of larger than 1:200 and dimeric when P:L ratio was only 1:50 [484]. Dimerization of PGAM5 at its TMD has not been investigated yet. The observation that replacement of the cysteine residue within the TMD enhances processing may suggests that homodimers within the membrane could be stabilised by disulphide bonds. This suggests that PGAM5 forms dimers not only outside but within the membrane as well. For γ-secretase it was shown that even if substrates dimerize in the membrane, they are most likely cleaved as monomers [304, 305].

Transferred to PGAM5 and PARL this would mean that too stable dimers impair substrate processing. Thus, WT TMD, G17L TMD and S18L TMD are cleaved less efficiently than C12S TMD and C12L TMD since the former still harbour the cysteine. In the samples used for structure determination in this work, the cysteines were reduced, as their $C\alpha$ and $C\beta$ chemical shifts indicate: C_α (26 $\pm$ 1.1 in α-helices) was at 61 ppm (62.6 $\pm$ 1.7 ppm in α-helices) and C_β at 26 ppm [488]. Thus, dimerization via the disulphide bond could not be observed.

All these considerations illustrate that very little is known about PARL and its substrate preferences. Observations made for other rhomboids like GlpG cannot be simply transferred to PARL as long as its topology is not elucidated. The determination of the orientation, and even better the exact structure of PARL within the membrane, is the imperative first step to be able to investigate whether the model described for GlpG can also be applied to PARL. The substrate properties determined by liquid-state NMR in this work may contribute to the discussion, but require a much broader biological context to address in detail the observed differences and their influences on substrate processing by PARL.

6. Conclusion and Outlook

In this work, representative substrates of two intramembrane proteases were studied in terms of structure and dynamics by mainly liquid-state NMR-based methods. Intramembrane proteolysis is an unusual process in that the corresponding enzymes cut within the plane of the membrane. It has been the subject of intensive research, especially in the last decade. Intramembrane proteases are of particular interest because they are directly or indirectly associated with various diseases, some of them serious. While much has been understood at the biological level, the mechanism that distinguishes between substrates and non-substrates remains obscure. This is particularly surprising because, for example, γ-secretase cuts an enormous number of different substrates, but is extremely sensitive to small changes, such as single point mutations, within the amino acid sequence of its substrate. The only commonality in terms of substrates between the different enzymes is that, unlike many soluble proteases, intramembrane proteases do not recognise a given consensus sequence. Unfortunately, this complicates the understanding of their substrate processing, as structural and dynamic properties of the substrate itself must be the determining factors.

To investigate this discrepancy, two intramembrane proteases and their corresponding substrates were selected: γ-Secretase and the transmembrane domain of the amyloid precursor protein, which are directly linked to Alzheimer's disease. Second, PARL, a rhomboid protease found in the mitochondria of human cells, and its substrate, the transmembrane domain of PGAM5, that are associated with Parkinson's disease. The underlying assumption was that certain structural properties of the substrate transmembrane domain fundamentally influence whether a potential substrate is processed, and if so, how it is processed. Particularly in the case of γ-secretase, various processing pathways are known. The products of these pathways can, in the worst case, lead to the formation of plaques associated with Alzheimer's disease.

With this in mind, four point mutations in addition to the corresponding wild types were investigated. These mutants were selected primarily for their presumed effect on the stability of the substrate transmembrane domain. By comparing different properties derived from NMR measurements, a hypothesis could be phrased that represents a first approach to illuminate the relationship between substrate structure and processing. For this purpose, the peptides were studied in a TFE/H_2O mixture that approximates the conditions inside the enzyme, i.e. when the substrate has left the membrane plane and migrates into the active site of the enzyme.

The transmembrane domain of the amyloid precursor protein, probably the most intensively studied γ-secretase substrate, was found to be a continuous α-helix, but consisting of two stable regions separated by a GlyGly motif. Two interesting features emerge from three-dimensional structures derived from NMR data. First, the region around the first γ-secretase cleavage site is strikingly stable and second, perhaps the more interesting

detail, they revealed a structural bundle that, when superimposed on the C-terminus fans out starting from the GlyGly-hinge. However, the relative arrangement of the N-terminal and C-terminal helix is not completely free, but is restricted to a specific cone. Comparative analysis of four mutants, two associated with familial AD and two designed, showed that although only a single amino acid was exchanged, the relative arrangement of both helix segments changed significantly. With respect to the differential processing of the mutants by γ-secretase, the following hypothesis can be phrased: For the transition from the membrane into the enzyme, the substrate must briefly adopt a kinked conformation. This was also observed by MD simulations. However, to ensure correct positioning within the catalytic cleft, the kink direction must be restricted to a certain range so that the scissile bond is directed to the catalytic residues. The four mutations investigated influence the kink angle and the relative rotation of both helix segments, and thus the entry into the enzyme and the correct positioning within it. This could mean that a certain flexibility in the transmembrane domain is required.

The comparative analysis of other substrate transmembrane domains has so far only partially confirmed this model, as three-dimensional structures have not yet been determined from all of these peptides. The next step, on the basis of this work would be the comparative analysis of further substrate TMDs in TFE/H2O, in order to be able to narrow down the structural conditions even better. Furthermore, although structures in lipid mimetics have already been published for some substrates, the APP TMD, for which four fundamentally different conformations have been published, shows that further analyses are also necessary here [249–251, 253]. Since the basic question concerning these APP TMD structures is first whether it is present in the membrane as a monomer or dimer or possibly in an equilibrium of different conformations, the analysis of a covalently bridged dimer could help. In this work, in addition to the transmembrane domains in TFE/H2O, a longer APP TMD variant was also analysed in DPC micelles, so the basis has already been laid.

The second unresolved question regarding the APP TMD dimer is the actual dimerisation motif. Although APP contains several GXXXG motifs within its TMD that are generally considered dimerisation prone, the two published dimer structures are based on other interfaces in the centre of the TM region. Recent cleavage-essay-based studies have also shown that dimerisation at the N-terminal border of the transmembrane domain may have a crucial influence on substrate processing [410]. Thus, the elucidation of a possible dimer structure would be an important contribution to the understanding of this system.

First attempts to understand the processing of the APP TMD by the presenilin homologue (PSH), both incorporated in DPC micelles, with NMR spectroscopy have already been published [332]. The archaeal MCMJR1 (*Methanoculleus marisnigri* JR1) is established as a simpler system to study properties of γ-secretase, as it does not require complexation with other cofactor proteins. Even though its sequence homology with PSEN, the catalytic subunit of γ-secretase is quite low, cryo-EM structures resulted in quite similar structures, and PSH was shown to process APP TMD comparable to γ-secretase [30, 312, 332, 489, 490]. Possible further experiments in analogy to the ones of Clemente et al. could comprise studies of PSH with APP WT TMD and the four mutants investigated in TFE/H$_2$O in this thesis to examine whether the differences in kink and swivel angles affect interactions with PSH. The respective substrates could be produced via cell-free protein expression.

In the future, other substrates need to be compared. First, their structures should be determined in TFE/H$_2$O, detergents or lipids and subsequently their interaction with PSH should be investigated. Complementary, the only known non-substrate, ITGB1 [257], needs to be investigates. This could add valuable information on the substrate properties required by PSEN or PSH. Based on these results, the interactions of the APP WT TMD as well as those of the four mutants with the PSH should be investigated. Hopefully, this will allow the results from cell-based and in vitro cleavage assays to be directly replicated. Furthermore, as the substrate is known to unwind around the initial cleavage site it might even be possible to gain insights into this process.

APP TMD dimerisation could be investigated with a covalently linked dimer structure. Introduction of a cysteine residue into the N-terminal juxtamembrane region of APP allows crosslinking of two monomers via a disulphide bridge. This might enforce dimerisation.

Other structural parameters that could reveal more information about the GlyGly joint movement are RDCs. Possibly, the preferred direction could then be further defined. As already shown by T. Gloge, RDCs of APP could be obtained in PEG-DA gels and TFE/H$_2$O [82]. At the time of these experiments, no fully ^{15}N-^{13}C labelled APP TMD peptide was available. Now, however, it could easily be produced by cell-free protein expression. Accordingly, RDCs should be measurable. The most extensively studied γ-secretase substrate besides APP is Notch1. Initial results of the analysis of its TMD in TFE/H$_2$O showed, not quite fitting the model derived here from the APP TMD WT and mutant TMD structures, no evidence of a flexible region within its TMD. However, one of the analysed APP TMD mutants also showed a rather straight and less flexible structure, which led to a significantly reduced processing in cleavage assays. Since no comparative, neither *in-vivo* nor *in-vitro*, cleavage assays of Notch1 and APP have been done so far, it is not clear whether the cleavage efficiency of Notch1 is not as low as for the APP mutant, which would again support the model presented here. Accordingly, the corresponding experiments are essential for a further understanding of γ-secretase cleavage. Both, cleavage essays and the corresponding NMR interaction studies with PSH should be done urgently.

Another important subject would be the investigation of the only known non-substrate of γ-secretase: Integrin β1 (ITGB1) [257]. It should be analysed in TFE/H$_2$O that might already give further insights into substrate properties. Its interaction with PSH is highly interesting, as well, as this can be expected to be impaired in some way, probably preventing ITGB1 to enter the catalytic cleft at all.

To add another experiment to the long list of experiments to be executed upon successful interaction studies of APP TMD and PSH in the NMR tube, the short, generally three amino acids long, bi-products of γ-secretase cleavage are proposed to act as inhibitors of further processing steps, enforcing the release of the resulting Aβ fragment. Interactions with these tripeptides with PSH should be studied by NMR as well. However, this would not contribute to the understanding of substrate enzyme interactions directly but rather illuminate the basis of diverse substrate processing.

The second system investigated was the transmembrane domain of PGAM5, a substrate of the rhomboid PARL. In contrast to γ-secretase, much less is known about PARL, not even its topology within the membrane could be determined unambiguously. Accordingly, the results obtained in this work do not provide a clear picture. Nevertheless, principal

properties of the PGAM5 TMD could be elucidated: PGAM5 TMD comprises, similar to APP TMD, two α-helical segments. In contrast to APP TMD, however, they are separated by an unstructured five amino acid stretch. Thus, the relative arrangement of the N-terminal and C-terminal helices could not be narrowed down as well as for APP TMD. The PARL cleavage site, again similar to APP, lies within the strongly α-helical C-terminal domain. Accordingly, comparative analysis of the four single point mutants with PGAM5 WT TMD led to a less clear picture. Even though cell-based cleavage assays of our collaborators suggest that exchange of a cysteine within the N-terminal helix increases processivity, NMR derived structures only resulted in a local destabilization of the surrounding region. The other two mutants, located at the beginning of the C-terminal helix, were shown to decrease processivity. The results obtained by NMR analysis diverged, as one mutant was shown to destabilize the TMD around the central stretch of amino acids even more while the other increased helicity. The cystein within the N-terminal helix was reduced for the NMR analyses done so far, although it cannot be ruled out, that it might induce disulphide bridges and thus enforce a dimer under natural conditions. A comparative analysis of a dimer stabilized by a disulphide bond could be rather easily achieved by NMR analysis. If and how this adds to the general picture cannot be foreseen, though.

As explained before, the topology of PARL is predicted to be inverted compared to GlpG. Thus, the catalytic residues of PARL and the cleavage site of the substrate apparently reside at opposite sides of the membrane. Therefore, it is imperative that the topology of PARL is clarified. However, PARL has been shown to process its substrates when incorporated into micelles [446]. This sets the basis for interaction studies as described above for APP and PSH that might clarify this confusing fact. Thus, a lot more data is required to construct a satisfying picture of PARL and its substrates.

Bibliography

[1]   M. S. Brown et al. "Regulated Intramembrane Proteolysis". In: *Cell* 100.4 (2000), pp. 391–398.

[2]   S. F. Lichtenthaler, C. Haass, and H. Steiner. "Regulated intramembrane proteolysis–lessons from amyloid precursor protein processing". In: *Journal of Neurochemistry* 117.5 (2011), pp. 779–796.

[3]   E. Y. L. Chan and G. A. McQuibban. "The mitochondrial rhomboid protease: its rise from obscurity to the pinnacle of disease-relevant genes". In: *Biochimica et Biophysica Acta* 1828.12 (2013), pp. 2916–2925.

[4]   L. Sun, X. Li, and Y. Shi. "Structural biology of intramembrane proteases: mechanistic insights from rhomboid and S2P to g-secretase". In: *Current Opinion in Structural Biology* 37 (2016), pp. 97–107.

[5]   C. Haass and H. Steiner. "Alzheimer disease g-secretase: a complex story of GxGD-type presenilin proteases". In: *Trends in Cell Biology* 12.12 (2002), pp. 556–562.

[6]   A. Weihofen et al. "Identification of signal peptide peptidase, a presenilin-type aspartic protease". In: *Science* 296.5576 (2002), pp. 2215–2218.

[7]   M. S. Wolfe. "Processive proteolysis by g-secretase and the mechanism of Alzheimer's disease". In: *Biological Chemistry* 393.9 (2012), pp. 899–905.

[8]   Y. Wang, Y. Zhang, and Y. Ha. "Crystal structure of a rhomboid family intramembrane protease". In: *Nature* 444.7116 (2006), pp. 179–180.

[9]   M. K. Lemberg and M. Freeman. "Functional and evolutionary implications of enhanced genomic analysis of rhomboid intramembrane proteases". In: *Genome research* 17.11 (2007), pp. 1634–1646.

[10]   K. Strisovsky. "Structural and mechanistic principles of intramembrane proteolysis–lessons from rhomboids". In: *The FEBS journal* 280.7 (2013), pp. 1579–1603.

[11]   K. R. Vinothkumar and M. Freeman. "Intramembrane proteolysis by rhomboids: catalytic mechanisms and regulatory principles". In: *Current opinion in structural biology* 23.6 (2013), pp. 851–858.

[12]   I. Manolaridis et al. "Mechanism of farnesylated CAAX protein processing by the intramembrane protease Rce1". In: *Nature* (2013), pp. 301–305.

[13]   L. Kroos and Y. Akiyama. "Biochemical and structural insights into intramembrane metalloprotease mechanisms". In: *Biochimica et Biophysica Acta* 1828.12 (2013), pp. 2873–2885.

[14]   L. Feng et al. "Structure of a site-2 protease family intramembrane metalloprotease". In: *Science* 318.5856 (2007), pp. 1608–1612.

[15]   L. Fleig et al. "Ubiquitin-dependent intramembrane rhomboid protease promotes ERAD of membrane proteins". In: *Molecular Cell* 47.4 (2012), pp. 558–569.

[16]   S. F. Lichtenthaler, M. K. Lemberg, and R. Fluhrer. "Proteolytic ectodomain shedding of membrane proteins in mammals-hardware, concepts, and recent developments". In: *The EMBO Journal* 37.15 (2018).

[17]   M. Voss, B. Schröder, and R. Fluhrer. "Mechanism, specificity, and physiology of signal peptide peptidase (SPP) and SPP-like proteases". In: *Biochimica et Biophysica Acta* 1828.12 (2013), pp. 2828–2839.

[18]   B. de Strooper, T. Iwatsubo, and M. S. Wolfe. "Presenilins and g-secretase: structure, function, and role in Alzheimer Disease". In: *Cold Spring Harbor Perspectives in Medicine* 2.1 (2012), a006304.

[19]   A. Escamilla-Ayala et al. "Contribution of the Presenilins in the cell biology, structure and function of g-secretase". In: *Seminars in Cell & Developmental Biology* 105 (2020), pp. 12–26.

[20]   D. V. Jeyaraju et al. "Phosphorylation and cleavage of presenilin-associated rhomboid-like protein (PARL) promotes changes in mitochondrial morphology". In: *Proceedings of the National Academy of Sciences of the United States of America* 103.49 (2006), pp. 18562–18567.

[21]   A. M. Pickrell and R. J. Youle. "The roles of PINK1, parkin, and mitochondrial fidelity in Parkinson's disease". In: *Neuron* 85.2 (2015), pp. 257–273.

[22]   M. Spinazzi and B. de Strooper. "PARL: The mitochondrial rhomboid protease". In: *Seminars in Cell & Developmental Biology* 60 (2016), pp. 19–28.

[23]   J. C. Christianson and Y. Ye. "Cleaning up in the endoplasmic reticulum: ubiquitin in charge". In: *Nature Structural & Molecular Biology* 21.4 (2014), pp. 325–335.

[24]   L. Ellgaard et al. "Co- and Post-Translational Protein Folding in the ER". In: *Traffic (Copenhagen, Denmark)* 17.6 (2016), pp. 615–638.

[25]   T. Ast, S. Michaelis, and M. Schuldiner. "The Protease Ste24 Clears Clogged Translocons". In: *Cell* 164.1-2 (2016), pp. 103–114.

[26]   C. Kayatekin et al. "Translocon Declogger Ste24 Protects against IAPP Oligomer-Induced Proteotoxicity". In: *Cell* 173.1 (2018), 62–73.e9.

[27]   R. B. Rawson et al. "Isolation of cholesterol-requiring mutant Chinese hamster ovary cells with defects in cleavage of sterol regulatory element-binding proteins at site 1". In: *The Journal of biological chemistry* 273.43 (1998), pp. 28261–28269.

[28]   A. C. Nyborg et al. "Intramembrane proteolytic cleavage by human signal peptide peptidase like 3 and malaria signal peptide peptidase". In: *FASEB journal* 20.10 (2006), pp. 1671–1679.

[29]   M. Voss et al. "Shedding of glycan-modifying enzymes by signal peptide peptidase-like 3 (SPPL3) regulates cellular N-glycosylation". In: *The EMBO Journal* 33.24 (2014), pp. 2890–2905.

[30]   X. Li et al. "Structure of a presenilin family intramembrane aspartate protease". In: *Nature* 493.7430 (2013), pp. 56–61.

[31]   Z. Wu et al. "Structural analysis of a rhomboid family intramembrane protease reveals a gating mechanism for substrate entry". In: *Nature Structural & Molecular Biology* 13.12 (2006), pp. 1084–1091.

[32]   R. P. Baker et al. "Enzymatic analysis of a rhomboid intramembrane protease implicates transmembrane helix 5 as the lateral substrate gate". In: *Proceedings of the National Academy of Sciences of the United States of America* 104.20 (2007), pp. 8257–8262.

[33]   K. Strisovsky, H. J. Sharpe, and M. Freeman. "Sequence-specific intramembrane proteolysis: identification of a recognition motif in rhomboid substrates". In: *Molecular Cell* 36.6 (2009), pp. 1048–1059.

[34]   Y. Xue and Y. Ha. "Large lateral movement of transmembrane helix S5 is not required for substrate access to the active site of rhomboid intramembrane protease". In: *The Journal of biological chemistry* 288.23 (2013), pp. 16645–16654.

[35]   Y. Akiyama and S. Maegawa. "Sequence features of substrates required for cleavage by GlpG, an Escherichia coli rhomboid protease". In: *Molecular Microbiology* 64.4 (2007), pp. 1028–1037.

[36]   S. Urban and M. Freeman. "Substrate Specificity of Rhomboid Intramembrane Proteases Is Governed by Helix-Breaking Residues in the Substrate Transmembrane Domain". In: *Molecular Cell* 11.6 (2003), pp. 1425–1434.

[37]   S. M. Moin and S. Urban. *Membrane immersion allows rhomboid proteases to achieve specificity by reading transmembrane segment dynamics.* Vol. 1. 2012.

[38]   P. Zeeman. "XXXII. On the influence of magnetism on the nature of the light emitted by a substance". In: *The London, Edinburgh, and Dublin Philosophical Magazine and Journal of Science* 43.262 (1897), pp. 226–239.

[39]   W. Gerlach and O. Stern. "Der experimentelle Nachweis der Richtungsquantelung im Magnetfeld". In: *Zeitschrift fr Physik* 9.1 (1922), pp. 349–352.

[40]   I. I. Rabi et al. "A New Method of Measuring Nuclear Magnetic Moment". In: *Physical Review* 53.4 (1938), p. 318.

[41]   F. Bloch, W. W. Hansen, and M. Packard. "The Nuclear Induction Experiment". In: *Physical Review* 70.7-8 (1946), pp. 474–485.

[42]   E. M. Purcell, H. C. Torrey, and R. V. Pound. "Resonance Absorption by Nuclear Magnetic Moments in a Solid". In: *Physical Review* 69.1-2 (1946), pp. 37–38.

[43]   W. G. Proctor and F. C. Yu. "The Dependence of a Nuclear Magnetic Resonance Frequency upon Chemical Compound". In: *Physical Review* 77.5 (1950), p. 717.

[44]   R. R. Ernst and W. A. Anderson. "Application of Fourier Transform Spectroscopy to Magnetic Resonance". In: *Review of Scientific Instruments* 37.1 (1966), pp. 93–102.

[45]   D. Marion. "An introduction to biological NMR spectroscopy". In: *Molecular & cellular proteomics : MCP* 12.11 (2013), pp. 3006–3025.

[46] M. Saunders, A. Wishnia, and J. G. Kirkwood. "THE NUCLEAR MAGNETIC RESO-NANCE SPECTRUM OF RIBONUCLEASE 1". In: *Journal of the American Chemical Society* 79.12 (1957), pp. 3289–3290.

[47] D. M. Grant, ed. *Encyclopedia of Nuclear Magnetic Resonance.* Chichester: Wiley, 1996.

[48] L. Müller, A. Kumar, and R. R. Ernst. "Two–dimensional carbon–13 NMR spectroscopy". In: *The Journal of Chemical Physics* 63.12 (1975), pp. 5490–5491.

[49] M. P. Williamson, T. F. Havel, and K. Wüthrich. "Solution conformation of proteinase inhibitor IIA from bull seminal plasma by 1H nuclear magnetic resonance and distance geometry". In: *Journal of Molecular Biology* 182.2 (1985), pp. 295–315.

[50] C. Gayathri et al. "Dipolar magnetic field effects in NMR spectra of liquids". In: *Chemical Physics Letters* 87.2 (1982), pp. 192–196.

[51] J. R. Tolman et al. "Nuclear magnetic dipole interactions in field-oriented proteins: information for structure determination in solution". In: *Proceedings of the National Academy of Sciences of the United States of America* 92.20 (1995), pp. 9279–9283.

[52] K. Pervushin et al. "Attenuated T2 relaxation by mutual cancellation of dipole-dipole coupling and chemical shift anisotropy indicates an avenue to NMR structures of very large biological macromolecules in solution". In: *Proceedings of the National Academy of Sciences of the United States of America* 94.23 (1997), pp. 12366–12371.

[53] A. Bax. "Multidimensional nuclear magnetic resonance methods for protein studies". In: *Current Opinion in Structural Biology* 4.5 (1994), pp. 738–744.

[54] G. Wagner et al. "Spatial structure of rabbit liver metallothionein-2 in solution by NMR". In: *Experientia. Supplementum* 52 (1987), pp. 149–157.

[55] Y. Bertini, ed. *NMR of biomolecules: Towards mechanistic systems biology.* Weinheim: Wiley-Blackwell, 2012.

[56] H. M. Berman et al. "The Protein Data Bank". In: *Nucleic Acids Research* 28.1 (2000), pp. 235–242.

[57] J. Keeler. *Understanding NMR spectroscopy.* 2. ed. Chichester: Wiley, 2010.

[58] J. Cavanagh. *Protein NMR Spectroscopy: Principles and Practice.* 2. Aufl. s.l.: Elsevier professional, 2006. URL: http://gbv.eblib.com/patron/FullRecord.aspx?p=287969.

[59] D. S. Wishart, B. D. Sykes, and F. M. Richards. "The chemical shift index: a fast and simple method for the assignment of protein secondary structure through NMR spectroscopy". In: *Biochemistry* 31.6 (1992), pp. 1647–1651.

[60] G. Cornilescu, F. Delaglio, and A. Bax. "Protein backbone angle restraints from searching a database for chemical shift and sequence homology". In: *Journal of Biomolecular NMR* 13.3 (1999), pp. 289–302.

[61] M. V. Berjanskii and D. S. Wishart. "A simple method to predict protein flexibility using secondary chemical shifts". In: *Journal of the American Chemical Society* 127.43 (2005), pp. 14970–14971.

[62] A. Cavalli et al. "Protein structure determination from NMR chemical shifts". In: *Proceedings of the National Academy of Sciences of the United States of America* 104.23 (2007), pp. 9615–9620.

[63] M. V. Berjanskii and D. S. Wishart. "Unraveling the meaning of chemical shifts in protein NMR". In: *Biochimica et Biophysica Acta - Proteins and Proteomics* 1865.11 Pt B (2017), pp. 1564–1576.

[64] J. L. Markley, D. H. Meadows, and O. Jardetzky. "Nuclear magnetic resonance studies of helix-coil transitions in polyamino acids". In: *Journal of Molecular Biology* 27.1 (1967), pp. 25–40.

[65] J. Yao, H. Dyson, and P. E. Wright. "Chemical shift dispersion and secondary structure prediction in unfolded and partly folded proteins". In: *FEBS Letters* 419.2-3 (1997), pp. 285–289.

[66] D. S. Wishart, B. D. Sykes, and F. M. Richards. "Relationship between nuclear magnetic resonance chemical shift and protein secondary structure". In: *Journal of Molecular Biology* 222.2 (1991), pp. 311–333.

[67] D. C. Dalgarno et al. "Proton-NMR studies of the solution conformations of vitamin-D-induced bovine intestinal calcium-binding protein". In: *European Journal of Biochemistry* 137.3 (1983), pp. 523–529.

[68] K. Wüthrich. *NMR and nucleic acids of proteins.* A Wiley-interscience publication. New York: Wiley, 1986.

[69] R. Richarz and K. Wüthrich. "Carbon-13 NMR chemical shifts of the common amino acid residues measured in aqueous solutions of the linear tetrapeptides H-Gly-Gly-X- L - Ala-OH". In: *Biopolymers* 17.9 (1978), pp. 2133–2141.

[70] D. S. Wishart et al. "1H, 13C and 15N chemical shift referencing in biomolecular NMR". In: *Journal of Biomolecular NMR* 6.2 (1995), pp. 135–140.

[71] E. A. Bienkiewicz and K. J. Lumb. "Random-coil chemical shifts of phosphorylated amino acids". In: *Journal of Biomolecular NMR* 15.3 (1999), pp. 203–206.

[72] Y. Shen et al. "TALOS+: a hybrid method for predicting protein backbone torsion angles from NMR chemical shifts". In: *Journal of Biomolecular NMR* 44.4 (2009), pp. 213–223.

[73] M. P. Williamson. "Chemical Shift Perturbation". In: *Modern Magnetic Resonance.* Ed. by G. A. Webb. Cham: Springer International Publishing, 2018, pp. 995–1012.

[74] M. Karplus. "Vicinal Proton Coupling in Nuclear Magnetic Resonance". In: *Journal of the American Chemical Society* 85.18 (1963), pp. 2870–2871.

[75] Rędzikowski.Adam. *Protein backbone dihedral angles phi, psi, and omega.* 2017. URL: https://commons.wikimedia.org/wiki/File:Protein_backbone_PhiPsiOmega_drawing.svg.

[76] G. Kummerlöwe and B. Luy. "Residual dipolar couplings as a tool in determining the structure of organic molecules". In: *TrAC Trends in Analytical Chemistry* 28.4 (2009), pp. 483–493.

[77] B. Luy and H. Kessler. "Partial Alignment for Structure Determination of Organic Molecules". In: *Modern Magnetic Resonance.* Ed. by G. A. Webb. Dordrecht: Springer Netherlands, 2006, pp. 1279–1285.

[78] N. Tjandra and A. Bax. "Direct measurement of distances and angles in biomolecules by NMR in a dilute liquid crystalline medium". In: *Science* 278.5340 (1997), pp. 1111–1114.

[79] H. J. Sass et al. "Solution NMR of proteins within polyacrylamide gels: diffusional properties and residual alignment by mechanical stress or embedding of oriented purple membranes". In: *Journal of Biomolecular NMR* 18.4 (2000), pp. 303–309.

[80] R. Tycko, F. J. Blanco, and Y. Ishii. "Alignment of Biopolymers in Strained Gels: A New Way To Create Detectable Dipole−Dipole Couplings in High-Resolution Biomolecular NMR". In: *Journal of the American Chemical Society* 122.38 (2000), pp. 9340–9341.

[81] M. R. Hansen, L. Mueller, and A. Pardi. "Tunable alignment of macromolecules by filamentous phage yields dipolar coupling interactions". In: *Nature Structural Biology* 5.12 (1998), pp. 1065–1074.

[82] T. Gloge. "Development of a universal alignment medium for the extraction of RDCs and structure elucidation with tensorial constraints: Dissertation". In: ().

[83] C. Merle et al. "Crosslinked Poly(ethylene oxide) as a Versatile Alignment Medium for the Measurement of Residual Anisotropic NMR Parameters". In: *Angewandte Chemie* 125.39 (2013), pp. 10499–10502.

[84] J. J. Chou, D. A. Case, and A. Bax. "Insights into the mobility of methyl-bearing side chains in proteins from (3)J(CC) and (3)J(CN) couplings". In: *Journal of the American Chemical Society* 125.29 (2003), pp. 8959–8966.

[85] G. M. Clore and C. D. Schwieters. "Amplitudes of protein backbone dynamics and correlated motions in a small alpha/beta protein: correspondence of dipolar coupling and heteronuclear relaxation measurements". In: *Biochemistry* 43.33 (2004), pp. 10678–10691.

[86] J. Meiler et al. "Model-free approach to the dynamic interpretation of residual dipolar couplings in globular proteins". In: *Journal of the American Chemical Society* 123.25 (2001), pp. 6098–6107.

[87] J. R. Tolman et al. "NMR evidence for slow collective motions in cyanometmyoglobin". In: *Nature Structural Biology* 4.4 (1997), pp. 292–297.

[88] N. Tjandra, S. Grzesiek, and A. Bax. "Magnetic Field Dependence of Nitrogen−Proton J Splittings in 15 N-Enriched Human Ubiquitin Resulting from Relaxation Interference and Residual Dipolar Coupling". In: *Journal of the American Chemical Society* 118.26 (1996), pp. 6264–6272.

[89] M. Ottiger and A. Bax. "Determination of Relative N−H N , N−C‛, C a −C‛, and C a −H a Effective Bond Lengths in a Protein by NMR in a Dilute Liquid Crystalline Phase". In: *Journal of the American Chemical Society* 120.47 (1998), pp. 12334–12341.

[90] K. Chen and N. Tjandra. "The Use of Residual Dipolar Coupling in Studying Proteins by NMR". In: *Topics in current chemistry* 326 (2012), pp. 47–67.

[91] G. Wider et al. "Homonuclear two-dimensional 1H NMR of proteins. Experimental procedures". In: *Journal of Magnetic Resonance (1969)* 56.2 (1984), pp. 207–234.

[92] W. P. Aue, E. Bartholdi, and R. R. Ernst. "Two−dimensional spectroscopy. Application to nuclear magnetic resonance". In: *The Journal of Chemical Physics* 64.5 (1976), pp. 2229–2246.

[93] L. Braunschweiler and R. Ernst. "Coherence transfer by isotropic mixing: Application to proton correlation spectroscopy". In: *Journal of Magnetic Resonance (1969)* 53.3 (1983), pp. 521–528.

[94] A. Bax and D. G. Davis. "MLEV-17-based two-dimensional homonuclear magnetization transfer spectroscopy". In: *Journal of Magnetic Resonance (1969)* 65.2 (1985), pp. 355–360.

[95] I. Solomon. "Relaxation Processes in a System of Two Spins". In: *Physical Review* 99.2 (1955), pp. 559–565.

[96] S. Macura and R. R. Ernst. "Elucidation of cross relaxation in liquids by two-dimensional N.M.R. spectroscopy". In: *Molecular Physics* 41.1 (1980), pp. 95–117.

[97] M. Sattler. "Heteronuclear multidimensional NMR experiments for the structure determination of proteins in solution employing pulsed field gradients". In: *Progress in Nuclear Magnetic Resonance Spectroscopy* 34.2 (1999), pp. 93–158.

[98] M. Ikura et al. "Triple-resonance multidimensional NMR study of calmodulin complexed with the binding domain of skeletal muscle myosin light-chain kinase: indication of a conformational change in the central helix". In: *Biochemistry* 30.22 (1991), pp. 5498–5504.

[99] L. E. Kay et al. "Three-dimensional triple-resonance NMR spectroscopy of isotopically enriched proteins". In: *Journal of Magnetic Resonance (1969)* 89.3 (1990), pp. 496–514.

[100] A. Bax and M. Ikura. "An efficient 3D NMR technique for correlating the proton and 15N backbone amide resonances with the alpha-carbon of the preceding residue in uniformly 15N/13C enriched proteins". In: *Journal of Biomolecular NMR* 1.1 (1991), pp. 99–104.

[101] S. Grzesiek and A. Bax. "Improved 3D triple-resonance NMR techniques applied to a 31 kDa protein". In: *Journal of Magnetic Resonance (1969)* 96.2 (1992), pp. 432–440.

[102] B. T. Farmer et al. "A refocused and optimized HNCA: increased sensitivity and resolution in large macromolecules". In: *Journal of Biomolecular NMR* 2.2 (1992), pp. 195–202.

[103] D. R. Muhandiram and L. E. Kay. "Gradient-Enhanced Triple-Resonance Three-Dimensional NMR Experiments with Improved Sensitivity". In: *Journal of magnetic resonance. Series B* 103.3 (1994), pp. 203–216.

[104] S. Grzesiek, J. Anglister, and A. Bax. "Correlation of Backbone Amide and Aliphatic Side-Chain Resonances in 13C/15N-Enriched Proteins by Isotropic Mixing of 13C Magnetization". In: *Journal of magnetic resonance. Series B* 101.1 (1993), pp. 114–119.

[105] S. Grzesiek and A. Bax. "Amino acid type determination in the sequential assignment procedure of uniformly 13C/15N-enriched proteins". In: *Journal of Biomolecular NMR* 3.2 (1993), pp. 185–204.

[106] K. Wüthrich. "Protein structure determination in solution by NMR spectroscopy". In: *Journal of Biological Chemistry* 265.36 (1990), pp. 22059–22062.

[107] D. Marion et al. "Overcoming the overlap problem in the assignment of 1H NMR spectra of larger proteins by use of three-dimensional heteronuclear 1H-15N Hartmann-Hahn-multiple quantum coherence and nuclear Overhauser-multiple quantum coherence spectroscopy: application to interleukin 1 beta". In: *Biochemistry* 28.15 (1989), pp. 6150–6156.

[108] D. Marion et al. "Three-dimensional heteronuclear NMR of nitrogen-15 labeled proteins". In: *Journal of the American Chemical Society* 111.4 (1989), pp. 1515–1517.

[109] E. R. Zuiderweg and S. W. Fesik. "Heteronuclear three-dimensional NMR spectroscopy of the inflammatory protein C5a". In: *Biochemistry* 28.6 (1989), pp. 2387–2391.

[110] S. Kirkpatrick, C. D. Gelatt, and M. P. Vecchi. "Optimization by simulated annealing". In: *Science* 220.4598 (1983), pp. 671–680.

[111] P. J. M. van Laarhoven and E. H. L. Aarts. *Simulated annealing: Theory and applications.* Vol. 37. Mathematics and its applications. Dordrecht: Reidel, 1987.

[112] A. T. Brünger, P. D. Adams, and L. M. Rice. "New applications of simulated annealing in X-ray crystallography and solution NMR". In: *Structure* 5.3 (1997), pp. 325–336.

[113] W. H. Press. *Numerical recipes: The art of scientific computing.* 3. ed. Cambridge: Cambridge Univ. Press, 2007.

[114] W. A. Hendrickson. "Stereochemically restrained refinement of macromolecular structures". In: *Diffraction Methods for Biological Macromolecules Part B.* Vol. 115. Methods in Enzymology. Elsevier, 1985, pp. 252–270.

[115] M. Nilges, J. Kuszewski, and A. T. Brünger. "Sampling Properties of Simulated Annealing and Distance Geometry". In: *Computational Aspects of the Study of Biological Macromolecules by Nuclear Magnetic Resonance Spectroscopy.* Ed. by J. C. Hoch, F. M. Poulsen, and C. Redfield. Boston, MA: Springer US, 1991, pp. 451–455.

[116] M. Nilges. "Ambiguous distance data in the calculation of NMR structures". In: *Folding & design* 2.4 (1997), S53–7.

[117] J. P. Linge et al. "ARIA: automated NOE assignment and NMR structure calculation". In: *Bioinformatics* 19.2 (2003), pp. 315–316.

[118] W. Rieping et al. "ARIA2: automated NOE assignment and data integration in NMR structure calculation". In: *Bioinformatics* 23.3 (2007), pp. 381–382.

[119] M. Nilges. "Calculation of protein structures with ambiguous distance restraints. Automated assignment of ambiguous NOE crosspeaks and disulphide connectivities". In: *Journal of Molecular Biology* 245.5 (1995), pp. 645–660.

[120] C. A. Spronk et al. "Validation of protein structures derived by NMR spectroscopy". In: *Progress in Nuclear Magnetic Resonance Spectroscopy* 45.3-4 (2004), pp. 315–337.

[121] J. P. Linge et al. "Correction of spin diffusion during iterative automated NOE assignment". In: *Journal of Magnetic Resonance (1969)* 167.2 (2004), pp. 334–342.

[122] D. Zhao and O. Jardetzky. "An assessment of the precision and accuracy of protein structures determined by NMR. Dependence on distance errors". In: *Journal of Molecular Biology* 239.5 (1994), pp. 601–607.

[123] W. Kabsch and C. Sander. "Dictionary of protein secondary structure: pattern recognition of hydrogen-bonded and geometrical features". In: *Biopolymers* 22.12 (1983), pp. 2577–2637.

[124] P. Schultze and J. Feigon. "Chirality errors in nucleic acid structures". In: *Nature* 387.6634 (1997), p. 668.

[125] C. A. E. M. Spronk et al. "Improving the quality of protein structures derived by NMR spectroscopy". In: *Journal of Biomolecular NMR* 22.3 (2002), pp. 281–289.

[126] I. R. Kleckner and M. P. Foster. "An introduction to NMR-based approaches for measuring protein dynamics". In: *Biochimica et Biophysica Acta* 1814.8 (2011), pp. 942–968.

[127] J. G. Kempf and J. P. Loria. "Protein Dynamics from Solution NMR". In: *Cell Biochemistry and Biophysics* 37.3 (2003), pp. 187–212.

[128] D. Besghini, M. Mauri, and R. Simonutti. "Time Domain NMR in Polymer Science: From the Laboratory to the Industry". In: *Applied Sciences* 9.9 (2019), p. 1801.

[129] A. Mittermaier and L. E. Kay. "New tools provide new insights in NMR studies of protein dynamics". In: *Science* 312.5771 (2006), pp. 224–228.

[130] T. L. Religa, R. Sprangers, and L. E. Kay. "Dynamic regulation of archaeal proteasome gate opening as studied by TROSY NMR". In: *Science* 328.5974 (2010), pp. 98–102.

[131] Y. Nikolaev and K. Pervushin. "NMR spin state exchange spectroscopy reveals equilibrium of two distinct conformations of leucine zipper GCN4 in solution". In: *Journal of the American Chemical Society* 129.20 (2007), pp. 6461–6469.

[132] V. A. Jarymowycz and M. J. Stone. "Fast time scale dynamics of protein backbones: NMR relaxation methods, applications, and functional consequences". In: *Chemical Reviews* 106.5 (2006), pp. 1624–1671.

[133] T. I. Igumenova, K. K. Frederick, and A. J. Wand. "Characterization of the fast dynamics of protein amino acid side chains using NMR relaxation in solution". In: *Chemical Reviews* 106.5 (2006), pp. 1672–1699.

[134] C. Renner et al. "Practical aspects of the 2D 15N-1h-NOE experiment". In: *Journal of Biomolecular NMR* 23.1 (2002), pp. 23–33.

[135] H. M. McConnell. "Indirect Hyperfine Interactions in the Paramagnetic Resonance Spectra of Aromatic Free Radicals". In: *The Journal of Chemical Physics* 24.4 (1956), pp. 764–766.

[136] E. L. Hahn. "Spin Echoes". In: *Physical Review* 80.4 (1950), pp. 580–594.

[137] S. Meiboom. "Nuclear Magnetic Resonance". In: *Annual review of physical chemistry* 14.1 (1963), pp. 335–358.

[138] H. Y. Carr and E. M. Purcell. "Effects of Diffusion on Free Precession in Nuclear Magnetic Resonance Experiments". In: *Physical Review* 94.3 (1954), pp. 630–638.

[139] A. G. Palmer, C. D. Kroenke, and J. Patrick Loria. "Nuclear Magnetic Resonance Methods for Quantifying Microsecond-to-Millisecond Motions in Biological Macromolecules". In: *Nuclear Magnetic Resonance of Biological Macromolecules - Part B*. Vol. 339. Methods in Enzymology. Elsevier, 2001, pp. 204–238.

[140] M. Kovermann, P. Rogne, and M. Wolf-Watz. "Protein dynamics and function from solution state NMR spectroscopy". In: *Quarterly Reviews of Biophysics* 49 (2016), e6.

[141] R. Ishima and D. A. Torchia. "Extending the range of amide proton relaxation dispersion experiments in proteins using a constant-time relaxation-compensated CPMG approach". In: *Journal of Biomolecular NMR* 25.3 (2003), pp. 243–248.

[142] A. Hvidt and S. O. Nielsen. "Hydrogen Exchange in Proteins". In: *Advances in Protein Chemistry Volume 21*. Vol. 21. Advances in Protein Chemistry. Elsevier, 1966, pp. 287–386.

[143] F. Persson and B. Halle. "How amide hydrogens exchange in native proteins". In: *Proceedings of the National Academy of Sciences of the United States of America* 112.33 (2015), pp. 10383–10388.

[144] L. Konermann, J. Pan, and Y.-H. Liu. "Hydrogen exchange mass spectrometry for studying protein structure and dynamics". In: *Chemical Society Reviews* 40.3 (2011), pp. 1224–1234.

[145] M. Liu et al. "Improved WATERGATE Pulse Sequences for Solvent Suppression in NMR Spectroscopy". In: *Journal of Magnetic Resonance (1969)* 132.1 (1998), pp. 125–129.

[146] J. Jeener et al. "Investigation of exchange processes by two–dimensional NMR spectroscopy". In: *The Journal of Chemical Physics* 71.11 (1979), pp. 4546–4553.

[147] Wagner and Berger. "Gradient-Selected NOESY-A Fourfold Reduction of the Measurement Time for the NOESY Experiment". In: *Journal of magnetic resonance. Series A* 123.1 (1996), pp. 119–121.

[148] M. R. M. Koos et al. "CLIP-COSY: A Clean In-Phase Experiment for the Rapid Acquisition of COSY-type Correlations". In: *Angewandte Chemie (International ed. in English)* 55.27 (2016), pp. 7655–7659.

[149]   L. Kay, P. Keifer, and T. Saarinen. "Pure absorption gradient enhanced heteronuclear single quantum correlation spectroscopy with improved sensitivity". In: *Journal of the American Chemical Society* 114.26 (1992), pp. 10663–10665.

[150]   A. G. Palmer et al. "Sensitivity improvement in proton-detected two-dimensional heteronuclear correlation NMR spectroscopy". In: *Journal of Magnetic Resonance (1969)* 93.1 (1991), pp. 151–170.

[151]   J. Schleucher et al. "A general enhancement scheme in heteronuclear multidimensional NMR employing pulsed field gradients". In: *Journal of Biomolecular NMR* 4.2 (1994), pp. 301–306.

[152]   P. Schanda, H. van Melckebeke, and B. Brutscher. "Speeding up three-dimensional protein NMR experiments to a few minutes". In: *Journal of the American Chemical Society* 128.28 (2006), pp. 9042–9043.

[153]   E. Lescop, P. Schanda, and B. Brutscher. "A set of BEST triple-resonance experiments for time-optimized protein resonance assignment". In: *Journal of Magnetic Resonance (1969)* 187.1 (2007), pp. 163–169.

[154]   W. F. Vranken et al. "The CCPN data model for NMR spectroscopy: development of a software pipeline". In: *Proteins* 59.4 (2005), pp. 687–696.

[155]   A. T. Brunger. "Version 1.2 of the Crystallography and NMR system". In: *Nature Protocols* 2.11 (2007), pp. 2728–2733.

[156]   A. T. Brünger et al. "Crystallography & NMR system: A new software suite for macromolecular structure determination". In: *Acta Crystallographica* 54.Pt 5 (1998), pp. 905–921.

[157]   M. Silber et al. "Altered Hinge Conformations in APP Transmembrane Helix Mutants May Affect Enzyme-Substrate Interactions of g-Secretase". In: *ACS Chemical Neuroscience* 11.24 (2020), pp. 4426–4433.

[158]   C. Moser. "NMR Strukturbestimmung und Lipidinteraktionen von Transmembranhelices". Master's Thesis. Karlsruhe: Karlsruhe Institute of Technology, 2020.

[159]   C. Hein et al. "Hydrophobic supplements in cell-free systems: Designing artificial environments for membrane proteins". In: *Engineering in Life Sciences* 14.4 (2014), pp. 365–379.

[160]   T. Matsuda, S. Watanabe, and T. Kigawa. "Cell-free synthesis system suitable for disulfide-containing proteins". In: *Biochemical and Biophysical Research Communications* 431.2 (2013), pp. 296–301.

[161]   F. Hagn, M. L. Nasr, and G. Wagner. "Assembly of phospholipid nanodiscs of controlled size for structural studies of membrane proteins by NMR". In: *Nature Protocols* 13.1 (2018), pp. 79–98.

[162]   F. Hagn et al. "Optimized phospholipid bilayer nanodiscs facilitate high-resolution structure determination of membrane proteins". In: *Journal of the American Chemical Society* 135.5 (2013), pp. 1919–1925.

[163]   A. Micsonai et al. "BeStSel: a web server for accurate protein secondary structure prediction and fold recognition from the circular dichroism spectra". In: *Nucleic Acids Research* 46.W1 (2018), W315–W322.

[164]   A. Micsonai et al. "Accurate secondary structure prediction and fold recognition for circular dichroism spectroscopy". In: *Proceedings of the National Academy of Sciences of the United States of America* 112.24 (2015), E3095–103.

[165]   the Alzheimer's Association. "2020 Alzheimer's disease facts and figures". In: *Alzheimer's & dementia: the journal of the Alzheimer's Association* (2020).

[166]   N. C. Berchtold and C. W. Cotman. "Evolution in the Conceptualization of Dementia and Alzheimer's Disease: Greco-Roman Period to the 1960s". In: *Neurobiology of Aging* 19.3 (1998), pp. 173–189.

[167]   R. A. Sperling et al. "Toward defining the preclinical stages of Alzheimer's disease: recommendations from the National Institute on Aging-Alzheimer's Association workgroups on diagnostic guidelines for Alzheimer's disease". In: *Alzheimer's & dementia: the journal of the Alzheimer's Association* 7.3 (2011), pp. 280–292.

[168]   M. S. Albert et al. "The diagnosis of mild cognitive impairment due to Alzheimer's disease: recommendations from the National Institute on Aging-Alzheimer's Association workgroups on diagnostic guidelines for Alzheimer's disease". In: *Alzheimer's & dementia: the journal of the Alzheimer's Association* 7.3 (2011), pp. 270–279.

[169]   G. M. McKhann et al. "The diagnosis of dementia due to Alzheimer's disease: recommendations from the National Institute on Aging-Alzheimer's Association workgroups on diagnostic guidelines for Alzheimer's disease". In: *Alzheimer's & dementia: the journal of the Alzheimer's Association* 7.3 (2011), pp. 263–269.

[170]   C. R. Jack et al. "Introduction to the recommendations from the National Institute on Aging-Alzheimer's Association workgroups on diagnostic guidelines for Alzheimer's disease". In: *Alzheimer's & dementia: the journal of the Alzheimer's Association* 7.3 (2011), pp. 257–262.

[171]   L. E. Hebert et al. "Change in risk of Alzheimer disease over time". In: *Neurology* 75.9 (2010), pp. 786–791.

[172]   Alzheimer Europe. *Dementia in Europe Yearbook 2019: Estimating the prevalence of dementia in Europe.* 2019. URL: https://www.alzheimer-europe.org/content/download/195515/1457520/file/FINAL%2005707%20Alzheimer%20Europe%20yearbook%202019.pdf.

[173]   S. L. Murphy et al. "Deaths: Final Data for 2012". In: *National vital statistics reports : from the Centers for Disease Control and Prevention, National Center for Health Statistics, National Vital Statistics System* 63.9 (2015), pp. 1–117.

[174]   R. Mayeux et al. "Risk of dementia in first-degree relatives of patients with Alzheimer's disease and related disorders". In: *Archives of neurology* 48.3 (1991), pp. 269–273.

[175]   R. C. Green et al. "Risk of dementia among white and African American relatives of patients with Alzheimer disease". In: *JAMA* 287.3 (2002), pp. 329–336.

[176] L. A. Farrer. "Effects of Age, Sex, and Ethnicity on the Association Between Apolipoprotein E Genotype and Alzheimer Disease". In: *JAMA* 278.16 (1997), p. 1349.

[177] C. T. Loy et al. "Genetics of dementia". In: *The Lancet* 383.9919 (2014), pp. 828–840.

[178] D. M. Holtzman, J. Herz, and G. Bu. "Apolipoprotein E and apolipoprotein E receptors: normal biology and roles in Alzheimer disease". In: *Cold Spring Harbor Perspectives in Medicine* 2.3 (2012), a006312.

[179] L. Spinney. "Alzheimer's disease: The forgetting gene". In: *Nature* 510.7503 (2014), pp. 26–28.

[180] G. G. Glenner and C. W. Wong. "Alzheimer's disease and Down's syndrome: Sharing of a unique cerebrovascular amyloid fibril protein". In: *Biochemical and Biophysical Research Communications* 122.3 (1984), pp. 1131–1135.

[181] C. L. Masters et al. "Amyloid plaque core protein in Alzheimer disease and Down syndrome". In: *Proceedings of the National Academy of Sciences of the United States of America* 82.12 (1985), pp. 4245–4249.

[182] D. Goldgaber et al. "Characterization and chromosomal localization of a cDNA encoding brain amyloid of Alzheimer's disease". In: *Science* 235.4791 (1987), pp. 877–880.

[183] J. Kang et al. "The precursor of Alzheimer's disease amyloid A4 protein resembles a cell-surface receptor". In: *Nature* 325.6106 (1987), pp. 733–736.

[184] N. K. Robakis et al. "Molecular cloning and characterization of a cDNA encoding the cerebrovascular and the neuritic plaque amyloid peptides". In: *Proceedings of the National Academy of Sciences of the United States of America* 84.12 (1987), pp. 4190–4194.

[185] R. E. Tanzi et al. "Amyloid beta protein gene: cDNA, mRNA distribution, and genetic linkage near the Alzheimer locus". In: *Science* 235.4791 (1987), pp. 880–884.

[186] G. Thinakaran and E. H. Koo. "Amyloid precursor protein trafficking, processing, and function". In: *Journal of Biological Chemistry* 283.44 (2008), pp. 29615–29619.

[187] J. Hardy and D. Allsop. "Amyloid deposition as the central event in the aetiology of Alzheimer's disease". In: *Trends in Pharmacological Sciences* 12 (1991), pp. 383–388.

[188] D. J. Selkoe. "The molecular pathology of Alzheimer's disease". In: *Neuron* 6.4 (1991), pp. 487–498.

[189] J. A. Hardy and G. A. Higgins. "Alzheimer's disease: the amyloid cascade hypothesis". In: *Science* 256.5054 (1992), pp. 184–185.

[190] J. Hardy and D. J. Selkoe. "The amyloid hypothesis of Alzheimer's disease: progress and problems on the road to therapeutics". In: *Science* 297.5580 (2002), pp. 353–356.

[191] L. Bertram and R. E. Tanzi. "Alzheimer's disease: one disorder, too many genes?" In: *Human Molecular Genetics* 13 Spec No 1 (2004), R135–41.

[192] L. M. Bekris et al. "Genetics of Alzheimer disease". In: *Journal of geriatric psychiatry and neurology* 23.4 (2010), pp. 213–227.

[193] C. M. Karch and A. M. Goate. "Alzheimer's disease risk genes and mechanisms of disease pathogenesis". In: *Biological psychiatry* 77.1 (2015), pp. 43–51.

[194] M. Willem et al. "h-Secretase processing of APP inhibits neuronal activity in the hippocampus". In: *Nature* 526.7573 (2015), pp. 443–447.

[195] E. Siemers et al. "Safety, tolerability, and changes in amyloid beta concentrations after administration of a gamma-secretase inhibitor in volunteers". In: *Clinical neuropharmacology* 28.3 (2005), pp. 126–132.

[196] K. W. Gillman et al. "Discovery and Evaluation of BMS-708163, a Potent, Selective and Orally Bioavailable g-Secretase Inhibitor". In: *ACS medicinal chemistry letters* 1.3 (2010), pp. 120–124.

[197] C. C. Shelton et al. "Modulation of gamma-secretase specificity using small molecule allosteric inhibitors". In: *Proceedings of the National Academy of Sciences of the United States of America* 106.48 (2009), pp. 20228–20233.

[198] S. Salloway et al. "Two phase 3 trials of bapineuzumab in mild-to-moderate Alzheimer's disease". In: *The New England journal of medicine* 370.4 (2014), pp. 322–333.

[199] D. J. Selkoe. "Translating cell biology into therapeutic advances in Alzheimer's disease". In: *Nature* 399.6738 Suppl (1999), A23–31.

[200] K. L. Puig and C. K. Combs. "Expression and function of APP and its metabolites outside the central nervous system". In: *Experimental gerontology* 48.7 (2013), pp. 608–611.

[201] P. R. Turner et al. "Roles of amyloid precursor protein and its fragments in regulating neural activity, plasticity and memory". In: *Progress in Neurobiology* 70.1 (2003), pp. 1–32.

[202] C. Priller et al. "Synapse formation and function is modulated by the amyloid precursor protein". In: *Journal of Neuroscience* 26.27 (2006), pp. 7212–7221.

[203] R. van der Kant and L. S. B. Goldstein. "Cellular functions of the amyloid precursor protein from development to dementia". In: *Developmental Cell* 32.4 (2015), pp. 502–515.

[204] E. Bossy-Wetzel, R. Schwarzenbacher, and S. A. Lipton. "Molecular pathways to neurodegeneration". In: *Nature Medicine* 10 Suppl (2004), S2–9.

[205] L. Devi et al. "Accumulation of amyloid precursor protein in the mitochondrial import channels of human Alzheimer's disease brain is associated with mitochondrial dysfunction". In: *The Journal of neuroscience : the official journal of the Society for Neuroscience* 26.35 (2006), pp. 9057–9068.

[206] H. K. Anandatheerthavarada et al. "Mitochondrial targeting and a novel transmembrane arrest of Alzheimer's amyloid precursor protein impairs mitochondrial function in neuronal cells". In: *The Journal of cell biology* 161.1 (2003), pp. 41–54.

[207] E. Gowing et al. "Chemical characterization of A beta 17-42 peptide, a component of diffuse amyloid deposits of Alzheimer disease". In: *Journal of Biological Chemistry* 269.15 (1994), pp. 10987–10990.

[208] J. D. Buxbaum et al. "Evidence that tumor necrosis factor alpha converting enzyme is involved in regulated alpha-secretase cleavage of the Alzheimer amyloid protein precursor". In: *Journal of Biological Chemistry* 273.43 (1998), pp. 27765–27767.

[209] D. J. Stephens and B. M. Austen. "Metabolites of the beta-amyloid precursor protein generated by beta-secretase localise to the trans-Golgi network and late endosome in 293 cells". In: *Journal of Neuroscience Research* 46.2 (1996), pp. 211–225.

[210] B. L. Daugherty and S. A. Green. "Endosomal sorting of amyloid precursor protein-P-selectin chimeras influences secretase processing". In: *Traffic (Copenhagen, Denmark)* 2.12 (2001), pp. 908–916.

[211] D. J. Selkoe. "Alzheimer disease: mechanistic understanding predicts novel therapies". In: *Annals of internal medicine* 140.8 (2004), pp. 627–638.

[212] M. P. Mattson. "Pathways towards and away from Alzheimer's disease". In: *Nature* 430.7000 (2004), pp. 631–639.

[213] W. T. Kimberly et al. "The intracellular domain of the beta-amyloid precursor protein is stabilized by Fe65 and translocates to the nucleus in a notch-like manner". In: *Journal of Biological Chemistry* 276.43 (2001), pp. 40288–40292.

[214] X. Cao and T. C. Südhof. "A transcriptionally correction of transcriptively active complex of APP with Fe65 and histone acetyltransferase Tip60". In: *Science* 293.5527 (2001), pp. 115–120.

[215] R. C. von Rotz et al. "The APP intracellular domain forms nuclear multiprotein complexes and regulates the transcription of its own precursor". In: *Journal of Cell Science* 117.Pt 19 (2004), pp. 4435–4448.

[216] W. Wei et al. "Abeta 17-42 in Alzheimer's disease activates JNK and caspase-8 leading to neuronal apoptosis". In: *Brain: a journal of neurology* 125.Pt 9 (2002), pp. 2036–2043.

[217] A. M. Szczepanik, D. Rampe, and G. E. Ringheim. "Amyloid-beta peptide fragments p3 and p4 induce pro-inflammatory cytokine and chemokine production in vitro and in vivo". In: *Journal of Neurochemistry* 77.1 (2001), pp. 304–317.

[218] A. Hornsten et al. "APL-1, a Caenorhabditis elegans protein related to the human beta-amyloid precursor protein, is essential for viability". In: *Proceedings of the National Academy of Sciences of the United States of America* 104.6 (2007), pp. 1971–1976.

[219] Z.-d. Zhou et al. "The roles of amyloid precursor protein (APP) in neurogenesis: Implications to pathogenesis and therapy of Alzheimer disease". In: *Cell adhesion & migration* 5.4 (2011), pp. 280–292.

[220] S. Ring et al. "The secreted beta-amyloid precursor protein ectodomain APPs alpha is sufficient to rescue the anatomical, behavioral, and electrophysiological abnormalities of APP-deficient mice". In: *The Journal of neuroscience : the official journal of the Society for Neuroscience* 27.29 (2007), pp. 7817–7826.

[221] K. Furukawa et al. "Increased activity-regulating and neuroprotective efficacy of alpha-secretase-derived secreted amyloid precursor protein conferred by a C-terminal heparin-binding domain". In: *Journal of Neurochemistry* 67.5 (1996), pp. 1882–1896.

[222] M. P. Mattson. "Cellular actions of beta-amyloid precursor protein and its soluble and fibrillogenic derivatives". In: *Physiological reviews* 77.4 (1997), pp. 1081–1132.

[223] B. Passer et al. "Generation of an apoptotic intracellular peptide by gamma-secretase cleavage of Alzheimer's amyloid beta protein precursor". In: *Journal of Alzheimer's disease* 2.3-4 (2000), pp. 289–301.

[224] S. Jäger et al. "alpha-secretase mediated conversion of the amyloid precursor protein derived membrane stub C99 to C83 limits Abeta generation". In: *Journal of Neurochemistry* 111.6 (2009), pp. 1369–1382.

[225] I. Hussain et al. "Identification of a novel aspartic protease (Asp 2) as beta-secretase". In: *Molecular and Cellular Neurosciences* 14.6 (1999), pp. 419–427.

[226] S. Sinha et al. "Purification and cloning of amyloid precursor protein beta-secretase from human brain". In: *Nature* 402.6761 (1999), pp. 537–540.

[227] R. Vassar et al. "Beta-secretase cleavage of Alzheimer's amyloid precursor protein by the transmembrane aspartic protease BACE". In: *Science* 286.5440 (1999), pp. 735–741.

[228] R. Yan et al. "Membrane-anchored aspartyl protease with Alzheimer's disease beta-secretase activity". In: *Nature* 402.6761 (1999), pp. 533–537.

[229] A. Weidemann et al. "A novel epsilon-cleavage within the transmembrane domain of the Alzheimer amyloid precursor protein demonstrates homology with Notch processing". In: *Biochemistry* 41.8 (2002), pp. 2825–2835.

[230] J. Berger-Sweeney et al. "Impairments in learning and memory accompanied by neurodegeneration in mice transgenic for the carboxyl-terminus of the amyloid precursor protein". In: *Molecular Brain Research* 66.1-2 (1999), pp. 150–162.

[231] R. L. Neve, A. Kammesheidt, and C. F. Hohmann. "Brain transplants of cells expressing the carboxyl-terminal fragment of the Alzheimer amyloid protein precursor cause specific neuropathology in vivo". In: *Proceedings of the National Academy of Sciences of the United States of America* 89.8 (1992), pp. 3448–3452.

[232] X. Cao and T. C. Südhof. "Dissection of amyloid-beta precursor protein-dependent transcriptional transactivation". In: *Journal of Biological Chemistry* 279.23 (2004), pp. 24601–24611.

[233] T. Ozaki et al. "The intracellular domain of the amyloid precursor protein (AICD) enhances the p53-mediated apoptosis". In: *Biochemical and Biophysical Research Communications* 351.1 (2006), pp. 57–63.

[234] C. Yu et al. "Characterization of a presenilin-mediated amyloid precursor protein carboxyl-terminal fragment gamma. Evidence for distinct mechanisms involved in gamma -secretase processing of the APP and Notch1 transmembrane domains". In: *Journal of Biological Chemistry* 276.47 (2001), pp. 43756–43760.

[235]   T. Sato et al. "Potential link between amyloid beta-protein 42 and C-terminal fragment gamma 49-99 of beta-amyloid precursor protein". In: *The Journal of biological chemistry* 278.27 (2003), pp. 24294–24301.

[236]   S. Yagishita, E. Futai, and S. Ishiura. "In vitro reconstitution of gamma-secretase activity using yeast microsomes". In: *Biochemical and Biophysical Research Communications* 377.1 (2008), pp. 141–145.

[237]   N. Matsumura et al. "g-Secretase associated with lipid rafts: multiple interactive pathways in the stepwise processing of b-carboxyl-terminal fragment". In: *The Journal of biological chemistry* 289.8 (2014), pp. 5109–5121.

[238]   H. S. Nhan, K. Chiang, and E. H. Koo. "The multifaceted nature of amyloid precursor protein and its proteolytic fragments: friends and foes". In: *Acta neuropathologica* 129.1 (2015), pp. 1–19.

[239]   D. M. Walsh et al. "The APP family of proteins: similarities and differences". In: *Biochemical Society transactions* 35.Pt 2 (2007), pp. 416–420.

[240]   D. J. Selkoe and J. Hardy. "The amyloid hypothesis of Alzheimer's disease at 25 years". In: *EMBO Molecular Medicine* 8.6 (2016), pp. 595–608.

[241]   S. Funamoto et al. "Successive cleavage of b-amyloid precursor protein by g-secretase". In: *Seminars in Cell & Developmental Biology* 105 (2020), pp. 64–74.

[242]   D. M. Bolduc et al. "The amyloid-beta forming tripeptide cleavage mechanism of g-secretase". In: *eLife* 5 (2016).

[243]   M. Takami and S. Funamoto. "g-Secretase-Dependent Proteolysis of Transmembrane Domain of Amyloid Precursor Protein: Successive Tri- and Tetrapeptide Release in Amyloid b-Protein Production". In: *International Journal of Alzheimer's Disease* 2012 (2012), p. 591392.

[244]   K. Yanagida et al. "The 28-amino acid form of an APLP1-derived Abeta-like peptide is a surrogate marker for Abeta42 production in the central nervous system". In: *EMBO Molecular Medicine* 1.4 (2009), pp. 223–235.

[245]   E. H. Schroeter, J. A. Kisslinger, and R. Kopan. "Notch-1 signalling requires ligand-induced proteolytic release of intracellular domain". In: *Nature* 393.6683 (1998), pp. 382–386.

[246]   M. Okochi et al. "Secretion of the Notch-1 Abeta-like peptide during Notch signaling". In: *Journal of Biological Chemistry* 281.12 (2006), pp. 7890–7898.

[247]   M. Okochi et al. "Presenilins mediate a dual intramembranous gamma-secretase cleavage of Notch-1". In: *The EMBO Journal* 21.20 (2002), pp. 5408–5416.

[248]   A. Fukumori et al. "Three-amino acid spacing of presenilin endoproteolysis suggests a general stepwise cleavage of gamma-secretase-mediated intramembrane proteolysis". In: *The Journal of neuroscience : the official journal of the Society for Neuroscience* 30.23 (2010), pp. 7853–7862.

[249]   P. J. Barrett et al. "The amyloid precursor protein has a flexible transmembrane domain and binds cholesterol". In: *Science* 336.6085 (2012), pp. 1168–1171.

[250] K. D. Nadezhdin et al. "Structural and Dynamic Study of the Transmembrane Domain of the Amyloid Precursor Protein". In: *Acta Naturae* 3.1 (2011), pp. 69–76.

[251] K. D. Nadezhdin et al. "Dimeric structure of transmembrane domain of amyloid precursor protein in micellar environment". In: *FEBS Letters* 586.12 (2012), pp. 1687–1692.

[252] C.-y. Chen et al. "Signal peptide peptidase functions in ERAD to cleave the unfolded protein response regulator XBP1u". In: *The EMBO Journal* 33.21 (2014), pp. 2492–2506.

[253] W. Chen et al. "Familial Alzheimer's mutations within APPTM increase Ab42 production by enhancing accessibility of e-cleavage site". In: *Nature Communications* 5 (2014), p. 3037.

[254] R. Kopan and M. X. G. Ilagan. "Gamma-secretase: proteasome of the membrane?" In: *Nature reviews. Molecular cell biology* 5.6 (2004), pp. 499–504.

[255] G. Güner and S. F. Lichtenthaler. "The substrate repertoire of g-secretase/presenilin". In: *Seminars in Cell & Developmental Biology* 105 (2020), pp. 27–42.

[256] A. Haapasalo and D. M. Kovacs. "The many substrates of presenilin/g-secretase". In: *Journal of Alzheimer's disease* 25.1 (2011), pp. 3–28.

[257] M. L. Hemming et al. "Proteomic Profiling of g-Secretase Substrates and Mapping of Substrate Requirements". In: *PLoS Biology* 6.10 (2008), pp. 2314–2328.

[258] Y. Tian et al. "An APP inhibitory domain containing the Flemish mutation residue modulates gamma-secretase activity for Abeta production". In: *Nature Structural & Molecular Biology* 17.2 (2010), pp. 151–158.

[259] O. Lazarov et al. "Axonal transport, amyloid precursor protein, kinesin-1, and the processing apparatus: revisited". In: *Journal of Neuroscience* 25.9 (2005), pp. 2386–2395.

[260] A. C. LeBlanc et al. "Role of amyloid precursor protein (APP): study with antisense transfection of human neuroblastoma cells". In: *Journal of Neuroscience Research* 31.4 (1992), pp. 635–645.

[261] E. J. Coulson et al. "Down-regulation of the amyloid protein precursor of Alzheimer's disease by antisense oligonucleotides reduces neuronal adhesion to specific substrata". In: *Brain Research* 770.1-2 (1997), pp. 72–80.

[262] P. Soba et al. "Homo- and heterodimerization of APP family members promotes intercellular adhesion". In: *The EMBO Journal* 24.20 (2005), pp. 3624–3634.

[263] P. Marambaud et al. "A presenilin-1/gamma-secretase cleavage releases the E-cadherin intracellular domain and regulates disassembly of adherens junctions". In: *The EMBO Journal* 21.8 (2002), pp. 1948–1956.

[264] P. Marambaud et al. "A CBP binding transcriptional repressor produced by the PS1/epsilon-cleavage of N-cadherin is inhibited by PS1 FAD mutations". In: *Cell* 114.5 (2003), pp. 635–645.

[265] S. P. Sardi et al. "Presenilin-dependent ErbB4 nuclear signaling regulates the timing of astrogenesis in the developing brain". In: *Cell* 127.1 (2006), pp. 185–197.

[266] H. W. Querfurth and F. M. Laferla. "Alzheimer's disease". In: *The New England journal of medicine* 362.4 (2010), pp. 329–344.

[267] I. Greenwald. "LIN-12/Notch signaling: lessons from worms and flies". In: *Genes & development* 12.12 (1998), pp. 1751–1762.

[268] J. Lewis. "Notch signalling and the control of cell fate choices in vertebrates". In: *Seminars in Cell & Developmental Biology* 9.6 (1998), pp. 583–589.

[269] P. C. Wong et al. "Presenilin 1 is required for Notch1 and DII1 expression in the paraxial mesoderm". In: *Nature* 387.6630 (1997), pp. 288–292.

[270] M. M. Shen. "Cell signaling in growth and development: the 11th Annual CABM Symposium, October 8-9, 1997". In: *Biochimica et Biophysica Acta* 1377.3 (1998), R55–62.

[271] B. de Strooper et al. "A presenilin-1-dependent gamma-secretase-like protease mediates release of Notch intracellular domain". In: *Nature* 398.6727 (1999), pp. 518–522.

[272] G. Struhl and I. Greenwald. "Presenilin is required for activity and nuclear access of Notch in Drosophila". In: *Nature* 398.6727 (1999), pp. 522–525.

[273] R. S. Doody et al. "A phase 3 trial of semagacestat for treatment of Alzheimer's disease". In: *The New England journal of medicine* 369.4 (2013), pp. 341–350.

[274] V. Coric et al. "Targeting Prodromal Alzheimer Disease With Avagacestat: A Randomized Clinical Trial". In: *JAMA neurology* 72.11 (2015), pp. 1324–1333.

[275] I.-M. Shih and T.-L. Wang. "Notch signaling, gamma-secretase inhibitors, and cancer therapy". In: *Cancer research* 67.5 (2007), pp. 1879–1882.

[276] R. A. Habets et al. "Safe targeting of T cell acute lymphoblastic leukemia by pathology-specific NOTCH inhibition". In: *Science translational medicine* 11.494 (2019).

[277] E. R. Andersson and U. Lendahl. "Therapeutic modulation of Notch signalling–are we there yet?" In: *Nature reviews. Drug discovery* 13.5 (2014), pp. 357–378.

[278] D. M. Bolduc et al. "Nicastrin functions to sterically hinder g-secretase-substrate interactions driven by substrate transmembrane domain". In: *Proceedings of the National Academy of Sciences of the United States of America* 113.5 (2016), E509–18.

[279] G. Struhl and A. Adachi. "Requirements for Presenilin-Dependent Cleavage of Notch and Other Transmembrane Proteins". In: *Molecular Cell* 6.3 (2000), pp. 625–636.

[280] S. A. Laurent et al. "g-Secretase directly sheds the survival receptor BCMA from plasma cells". In: *Nature Communications* 6 (2015), p. 7333.

[281] S. Funamoto et al. "Substrate ectodomain is critical for substrate preference and inhibition of g-secretase". In: *Nature Communications* 4 (2013), p. 2529.

[282] Y. Yan et al. "Dimerization of the transmembrane domain of amyloid precursor protein is determined by residues around the g-secretase cleavage sites". In: *Journal of Biological Chemistry* 292.38 (2017), pp. 15826–15837.

[283] A. Weihofen and B. Martoglio. "Intramembrane-cleaving proteases: controlled liberation of proteins and bioactive peptides". In: *Trends in Cell Biology* 13.2 (2003), pp. 71–78.

[284] F. Olsson et al. "Characterization of intermediate steps in amyloid beta (Ab) production under near-native conditions". In: *Journal of Biological Chemistry* 289.3 (2014), pp. 1540–1550.

[285] E. Fischer. "Einfluss der Configuration auf die Wirkung der Enzyme". In: *Berichte der deutschen chemischen Gesellschaft* 27.3 (1894), pp. 2985–2993.

[286] D. E. Koshland. "Application of a Theory of Enzyme Specificity to Protein Synthesis". In: *Proceedings of the National Academy of Sciences of the United States of America* 44.2 (1958), pp. 98–104.

[287] C. J. Tsai, B. Ma, and R. Nussinov. "Folding and binding cascades: shifts in energy landscapes". In: *Proceedings of the National Academy of Sciences of the United States of America* 96.18 (1999), pp. 9970–9972.

[288] H.-X. Zhou and P. A. Bates. "Modeling protein association mechanisms and kinetics". In: *Current opinion in structural biology* 23.6 (2013), pp. 887–893.

[289] D. Langosch et al. "Understanding intramembrane proteolysis: from protein dynamics to reaction kinetics". In: *Trends in Biochemical Sciences* 40.6 (2015), pp. 318–327.

[290] J. D. A. Tyndall, T. Nall, and D. P. Fairlie. "Proteases universally recognize beta strands in their active sites". In: *Chemical Reviews* 105.3 (2005), pp. 973–999.

[291] J. Ye et al. "ER Stress Induces Cleavage of Membrane-Bound ATF6 by the Same Proteases that Process SREBPs". In: *Molecular Cell* 6.6 (2000), pp. 1355–1364.

[292] M. K. Lemberg and B. Martoglio. "Requirements for signal peptide peptidase-catalyzed intramembrane proteolysis". In: *Molecular Cell* 10.4 (2002), pp. 735–744.

[293] T. Sato et al. "A helix-to-coil transition at the epsilon-cut site in the transmembrane dimer of the amyloid precursor protein is required for proteolysis". In: *Proceedings of the National Academy of Sciences of the United States of America* 106.5 (2009), pp. 1421–1426.

[294] D. Langosch and I. T. Arkin. "Interaction and conformational dynamics of membrane-spanning protein helices". In: *Protein science : a publication of the Protein Society* 18.7 (2009), pp. 1343–1358.

[295] G. Grigoryan, D. T. Moore, and W. F. DeGrado. "Transmembrane communication: general principles and lessons from the structure and function of the M2 proton channel, K$^+$ channels, and integrin receptors". In: *Annual Review of Biochemistry* 80 (2011), pp. 211–237.

[296] M. Hong, Y. Zhang, and F. Hu. "Membrane protein structure and dynamics from NMR spectroscopy". In: *Annual review of physical chemistry* 63 (2012), pp. 1–24.

[297] R. P. Riek et al. "Non-alpha-helical elements modulate polytopic membrane protein architecture". In: *Journal of Molecular Biology* 306.2 (2001), pp. 349–362.

[298] Y.-H. Huang and C.-M. Chen. "Statistical analyses and computational prediction of helical kinks in membrane proteins". In: *Journal of computer-aided molecular design* 26.10 (2012), pp. 1171–1185.

[299] S. Quint et al. "Residue-specific side-chain packing determines the backbone dynamics of transmembrane model helices". In: *Biophysical Journal* 99.8 (2010), pp. 2541–2549.

[300] C. Scharnagl et al. "Side-chain to main-chain hydrogen bonding controls the intrinsic backbone dynamics of the amyloid precursor protein transmembrane helix". In: *Biophysical Journal* 106.6 (2014), pp. 1318–1326.

[301] O. Pester et al. "The backbone dynamics of the amyloid precursor protein transmembrane helix provides a rationale for the sequential cleavage mechanism of g-secretase". In: *Journal of the American Chemical Society* 135.4 (2013), pp. 1317–1329.

[302] C. Kaether, C. Haass, and H. Steiner. "Assembly, trafficking and function of gamma-secretase". In: *Neurodegenerative Diseases* 3.4-5 (2006), pp. 275–283.

[303] P. Lu et al. "Three-dimensional structure of human g-secretase". In: *Nature* 512.7513 (2014), pp. 166–170.

[304] R. Zhou et al. "Recognition of the amyloid precursor protein by human g-secretase". In: *Science* 363.6428 (2019).

[305] G. Yang et al. "Structural basis of Notch recognition by human g-secretase". In: *Nature* 565.7738 (2019), pp. 192–197.

[306] L. Serneels et al. "Differential contribution of the three Aph1 genes to gamma-secretase activity in vivo". In: *Proceedings of the National Academy of Sciences of the United States of America* 102.5 (2005), pp. 1719–1724.

[307] R. Sherrington et al. "Cloning of a gene bearing missense mutations in early-onset familial Alzheimer's disease". In: *Nature* 375.6534 (1995), pp. 754–760.

[308] E. Levy-Lahad et al. "A familial Alzheimer's disease locus on chromosome 1". In: *Science* 269.5226 (1995), pp. 970–973.

[309] R. Sannerud et al. "Restricted Location of PSEN2/g-Secretase Determines Substrate Specificity and Generates an Intracellular Ab Pool". In: *Cell* 166.1 (2016), pp. 193–208.

[310] X. Meckler and F. Checler. "Presenilin 1 and Presenilin 2 Target g-Secretase Complexes to Distinct Cellular Compartments". In: *The Journal of biological chemistry* 291.24 (2016), pp. 12821–12837.

[311] X.-C. Bai et al. "An atomic structure of human g-secretase". In: *Nature* 525.7568 (2015), pp. 212–217.

[312] M. S. Wolfe et al. "Are presenilins intramembrane-cleaving proteases? Implications for the molecular mechanism of Alzheimer's disease". In: *Biochemistry* 38.35 (1999), pp. 11223–11230.

[313] M. S. Wolfe et al. "Peptidomimetic probes and molecular modeling suggest that Alzheimer's gamma-secretase is an intramembrane-cleaving aspartyl protease". In: *Biochemistry* 38.15 (1999), pp. 4720–4727.

[314] G. Thinakaran et al. "Endoproteolysis of Presenilin 1 and Accumulation of Processed Derivatives In Vivo". In: *Neuron* 17.1 (1996), pp. 181–190.

[315] M. B. Podlisny et al. "Presenilin proteins undergo heterogeneous endoproteolysis between Thr291 and Ala299 and occur as stable N- and C-terminal fragments in normal and Alzheimer brain tissue". In: *Neurobiology of disease* 3.4 (1997), pp. 325–337.

[316] D. Petit et al. "Extracellular interface between APP and Nicastrin regulates Ab length and response to g-secretase modulators". In: *The EMBO Journal* 38.12 (2019).

[317] S. Prokop et al. "Requirement of PEN-2 for stabilization of the presenilin N-/C-terminal fragment heterodimer within the gamma-secretase complex". In: *Journal of Biological Chemistry* 279.22 (2004), pp. 23255–23261.

[318] X. Zhang, C. J. Yu, and S. S. Sisodia. "The topology of pen-2, a g-secretase subunit, revisited: evidence for a reentrant loop and a single pass transmembrane domain". In: *Molecular Neurodegeneration* 10 (2015), p. 39.

[319] S.-H. Kim and S. S. Sisodia. "Evidence that the "NF" motif in transmembrane domain 4 of presenilin 1 is critical for binding with PEN-2". In: *Journal of Biological Chemistry* 280.51 (2005), pp. 41953–41966.

[320] N. Watanabe et al. "Pen-2 is incorporated into the gamma-secretase complex through binding to transmembrane domain 4 of presenilin 1". In: *Journal of Biological Chemistry* 280.51 (2005), pp. 41967–41975.

[321] A. Fukumori and H. Steiner. "Substrate recruitment of g-secretase and mechanism of clinical presenilin mutations revealed by photoaffinity mapping". In: *The EMBO Journal* 35.15 (2016), pp. 1628–1643.

[322] R. Aguayo-Ortiz et al. "Characterizing the structural ensemble of g-secretase using a multiscale molecular dynamics approach". In: *Chemical science* 8.8 (2017), pp. 5576–5584.

[323] N. Elad et al. "The dynamic conformational landscape of gamma-secretase". In: *Journal of Cell Science* 128.3 (2015), pp. 589–598.

[324] J. Y. Lee et al. "Allosteric Modulation of Intact g-Secretase Structural Dynamics". In: *Biophysical Journal* 113.12 (2017), pp. 2634–2649.

[325] M. Hitzenberger and M. Zacharias. "Structural Modeling of g-Secretase Ab n Complex Formation and Substrate Processing". In: *ACS Chemical Neuroscience* 10.3 (2019), pp. 1826–1840.

[326]   A. Brik and C.-H. Wong. "HIV-1 protease: mechanism and drug discovery". In: *Organic & biomolecular chemistry* 1.1 (2003), pp. 5–14.

[327]   K. Suguna et al. "Structure and refinement at 1.8 A resolution of the aspartic proteinase from Rhizopus chinensis". In: *Journal of Molecular Biology* 196.4 (1987), pp. 877–900.

[328]   B. Dehury, N. Tang, and K. P. Kepp. "Molecular dynamics of C99-bound g-secretase reveal two binding modes with distinct compactness, stability, and active-site retention: implications for Ab production". In: *Biochemical Journal* 476.7 (2019), pp. 1173–1189.

[329]   R. Kong et al. "Molecular dynamics simulation study reveals potential substrate entry path into g-secretase/presenilin-1". In: *Journal of structural biology* 191.2 (2015), pp. 120–129.

[330]   A. K. Somavarapu and K. P. Kepp. "The dynamic mechanism of presenilin-1 function: Sensitive gate dynamics and loop unplugging control protein access". In: *Neurobiology of disease* 89 (2016), pp. 147–156.

[331]   T. Lemmin et al. "Perturbations of the straight transmembrane a-helical structure of the amyloid precursor protein affect its processing by g-secretase". In: *Journal of Biological Chemistry* 289.10 (2014), pp. 6763–6774.

[332]   N. Clemente et al. "Coupled Transmembrane Substrate Docking and Helical Unwinding in Intramembrane Proteolysis of Amyloid Precursor Protein". In: *Scientific Reports* 8.1 (2018), p. 12411.

[333]   M. C. Brown et al. "Unwinding of the Substrate Transmembrane Helix in Intramembrane Proteolysis". In: *Biophysical Journal* 114.7 (2018), pp. 1579–1589.

[334]   F. Kamp et al. "Intramembrane proteolysis of b-amyloid precursor protein by g-secretase is an unusually slow process". In: *Biophysical Journal* 108.5 (2015), pp. 1229–1237.

[335]   S. Bjelic and J. Aqvist. "Catalysis and linear free energy relationships in aspartic proteases". In: *Biochemistry* 45.25 (2006), pp. 7709–7723.

[336]   D. Langosch and H. Steiner. "Substrate processing in intramembrane proteolysis by g-secretase - the role of protein dynamics". In: *Biological Chemistry* 398.4 (2017), pp. 441–453.

[337]   W. P. Esler, C. Das, and M. S. Wolfe. "Probing pockets S2-S4' of the gamma-secretase active site with (hydroxyethyl)urea peptidomimetics". In: *Bioorganic & Medicinal Chemistry Letters* 14.8 (2004), pp. 1935–1938.

[338]   M. Szaruga et al. "Alzheimer's-Causing Mutations Shift Ab Length by Destabilizing g-Secretase-Abn Interactions". In: *Cell* 170.3 (2017), 443–456.e14.

[339]   Alzforum. *Mutations*. URL: https://www.alzforum.org/mutations.

[340]   R. M. Page et al. "Beta-amyloid precursor protein mutants respond to gamma-secretase modulators". In: *The Journal of biological chemistry* 285.23 (2010), pp. 17798–17810.

[341] L. Chávez-Gutiérrez et al. "The mechanism of g-Secretase dysfunction in familial Alzheimer disease". In: *The EMBO Journal* 31.10 (2012), pp. 2261–2274.

[342] M. Dimitrov et al. "Alzheimer's disease mutations in APP but not g-secretase modulators affect epsilon-cleavage-dependent AICD production". In: *Nature Communications* 4 (2013), p. 2246.

[343] M. A. Fernandez et al. "Alzheimer presenilin-1 mutations dramatically reduce trimming of long amyloid b-peptides (Ab) by g-secretase to increase 42-to-40-residue Ab". In: *Journal of Biological Chemistry* 289.45 (2014), pp. 31043–31052.

[344] A. Götz et al. "Modulating Hinge Flexibility in the APP Transmembrane Domain Alters g-Secretase Cleavage". In: *Biophysical Journal* 116.11 (2019), pp. 2103–2120.

[345] E. C. Schulte et al. "Rare variants in b-Amyloid precursor protein (APP) and Parkinson's disease". In: *European Journal of Human Genetics* 23.10 (2015), pp. 1328–1333.

[346] K. Ancolio et al. "Unusual phenotypic alteration of beta amyloid precursor protein (betaAPP) maturation by a new Val-715 – Met betaAPP-770 mutation responsible for probable early-onset Alzheimer's disease". In: *Proceedings of the National Academy of Sciences of the United States of America* 96.7 (1999), pp. 4119–4124.

[347] T.-H. Xu et al. "Alzheimer's disease-associated mutations increase amyloid precursor protein resistance to g-secretase cleavage and the Ab42/Ab40 ratio". In: *Cell Discovery* 2 (2016), p. 16026.

[348] L. Terreni et al. "Novel pathogenic mutation in an Italian patient with familial Alzheimer's disease detected in APP gene". In: *Neurobiology of Aging* 23.S1 (2002), p. 319.

[349] M. Suárez-Calvet et al. "Autosomal-dominant Alzheimer's disease mutations at the same codon of amyloid precursor protein differentially alter Ab production". In: *Journal of Neurochemistry* 128.2 (2014), pp. 330–339.

[350] F. Oestereich et al. "Impact of amyloid precursor protein hydrophilic transmembrane residues on amyloid-beta generation". In: *Biochemistry* 54.17 (2015), pp. 2777–2784.

[351] L.-M. Munter et al. "Aberrant Amyloid Precursor Protein (APP) Processing in Hereditary Forms of Alzheimer Disease Caused by APP Familial Alzheimer Disease Mutations Can Be Rescued by Mutations in the APP GxxxG Motif*". In: *The Journal of biological chemistry* 285.28 (2010), pp. 21636–21643.

[352] S. Kumar-Singh et al. "Nonfibrillar diffuse amyloid deposition due to a gamma(42)-secretase site mutation points to an essential role for N-truncated A beta(42) in Alzheimer's disease". In: *Human Molecular Genetics* 9.18 (2000), pp. 2589–2598.

[353] M. A. Fernandez et al. "Transmembrane Substrate Determinants for g-Secretase Processing of APP CTFb". In: *Biochemistry* 55.40 (2016), pp. 5675–5688.

[354] K. T. O'Neil and W. F. DeGrado. "A thermodynamic scale for the helix-forming tendencies of the commonly occurring amino acids". In: *Science* 250.4981 (1990), pp. 646–651.

[355] S. Weggen and D. Beher. "Molecular consequences of amyloid precursor protein and presenilin mutations causing autosomal-dominant Alzheimer's disease". In: *Alzheimer's research & therapy* 4.2 (2012), p. 9.

[356] A. Götz et al. "Increased H-Bond Stability Relates to Altered e-Cleavage Efficiency and Ab Levels in the I45T Familial Alzheimer's Disease Mutant of APP". In: (2018).

[357] A. Götz et al. "Increased H-Bond Stability Relates to Altered e-Cleavage Efficiency and Ab Levels in the I45T Familial Alzheimer's Disease Mutant of APP". In: *Scientific Reports* 9.1 (2019), p. 5321.

[358] M. Buck. "Trifluoroethanol and colleagues: cosolvents come of age. Recent studies with peptides and proteins". In: *Quarterly Reviews of Biophysics* 31.3 (1998), pp. 297–355.

[359] Y. M. Li et al. "Presenilin 1 is linked with gamma-secretase activity in the detergent solubilized state". In: *Proceedings of the National Academy of Sciences of the United States of America* 97.11 (2000), pp. 6138–6143.

[360] D. S. Wishart. "Interpreting protein chemical shift data". In: *Progress in Nuclear Magnetic Resonance Spectroscopy* 58.1-2 (2011), pp. 62–87.

[361] N. E. Hafsa, D. Arndt, and D. S. Wishart. "CSI 3.0: a web server for identifying secondary and super-secondary structure in proteins using NMR chemical shifts". In: *Nucleic Acids Research* 43.W1 (2015), W370–7.

[362] N. E. Hafsa and D. S. Wishart. "CSI 2.0: a significantly improved version of the Chemical Shift Index". In: *Journal of Biomolecular NMR* 60.2-3 (2014), pp. 131–146.

[363] M. V. Berjanskii and D. S. Wishart. "A simple method to measure protein side-chain mobility using NMR chemical shifts". In: *Journal of the American Chemical Society* 135.39 (2013), pp. 14536–14539.

[364] Y. Shen and A. Bax. "Protein backbone and sidechain torsion angles predicted from NMR chemical shifts using artificial neural networks". In: *Journal of Biomolecular NMR* 56.3 (2013), pp. 227–241.

[365] G. Wagner et al. "Nuclear magnetic resonance identification of "half-turn" and 3(10)-helix secondary structure in rabbit liver metallothionein-2". In: *Journal of Molecular Biology* 187.1 (1986), pp. 131–135.

[366] K. Wüthrich et al. "Protein secondary structure determination by NMR Application with recombinant human cyclophilin: Application with recombinant human cyclophilin". In: *FEBS Letters* 285.2 (1991), pp. 237–247.

[367] S. J. Coales et al. "Expansion of time window for mass spectrometric measurement of amide hydrogen/deuterium exchange reactions". In: *Rapid communications in mass spectrometry : RCM* 24.24 (2010), pp. 3585–3592.

[368] M. Buck, S. E. Radford, and C. M. Dobson. "A partially folded state of hen egg white lysozyme in trifluoroethanol: structural characterization and implications for protein folding". In: *Biochemistry* 32.2 (1993), pp. 669–678.

[369] N. Schönbrunner et al. "Native-like beta-structure in a trifluoroethanol-induced partially folded state of the all-beta-sheet protein tendamistat". In: *Journal of Molecular Biology* 260.3 (1996), pp. 432–445.

[370] Z. Cao et al. "Backbone Hydrogen Bond Strengths Can Vary Widely in Transmembrane Helices". In: *Journal of the American Chemical Society* 139.31 (2017), pp. 10742–10749.

[371] D. S. Wishart and D. A. Case. "Use of Chemical Shifts in Macromolecular Structure Determination". In: *Nuclear Magnetic Resonance of Biological Macromolecules Part A*. Vol. 338. Methods in Enzymology. Elsevier, 2002, pp. 3–34.

[372] J. L. Goodman, M. D. Pagel, and M. J. Stone. "Relationships between protein structure and dynamics from a database of NMR-derived backbone order parameters". In: *Journal of Molecular Biology* 295.4 (2000), pp. 963–978.

[373] L. Dominguez et al. "Structural heterogeneity in transmembrane amyloid precursor protein homodimer is a consequence of environmental selection". In: *Journal of the American Chemical Society* 136.27 (2014), pp. 9619–9626.

[374] S. Choe and S. X. Sun. "The elasticity of alpha-helices". In: *The Journal of Chemical Physics* 122.24 (2005), p. 244912.

[375] E. G. Emberly et al. "Flexibility of alpha-helices: results of a statistical analysis of database protein structures". In: *Journal of Molecular Biology* 327.1 (2003), pp. 229–237.

[376] J. Pleiss and F. Jähnig. "Collective vibrations of an alpha-helix. A molecular dynamics study". In: *Biophysical Journal* 59.4 (1991), pp. 795–804.

[377] D. N. Woolfson and D. H. Williams. "The influence of proline residues on a-helical structure". In: *FEBS Letters* 277.1-2 (1990), pp. 185–188.

[378] D. J. Barlow and J. M. Thornton. "Helix geometry in proteins". In: *Journal of Molecular Biology* 201.3 (1988), pp. 601–619.

[379] G. von Heijne. "Proline kinks in transmembrane a-helices". In: *Journal of Molecular Biology* 218.3 (1991), pp. 499–503.

[380] M. Hitzenberger et al. "The dynamics of g-secretase and its substrates". In: *Seminars in Cell & Developmental Biology* 105 (2020), pp. 86–101.

[381] J. H. C. Orth et al. "Cell-free synthesis and characterization of a novel cytotoxic pierisin-like protein from the cabbage butterfly Pieris rapae". In: *Toxicon : official journal of the International Society on Toxinology* 57.2 (2011), pp. 199–207.

[382] M. Villate, N. Merino, and F. J. Blanco. "Production of meganucleases by cell-free protein synthesis for functional and structural studies". In: *Protein expression and purification* 85.2 (2012), pp. 246–249.

[383] K.-H. Lee et al. "Ribosomal synthesis and in situ isolation of peptide molecules in a cell-free translation system". In: *Protein expression and purification* 71.1 (2010), pp. 16–20.

[384] T. Tsuboi et al. "An efficient approach to the production of vaccines against the malaria parasite". In: *Methods in Molecular Biology* 607 (2010), pp. 73–83.

[385] A. S. Spirin. "High-throughput cell-free systems for synthesis of functionally active proteins". In: *Trends in Biotechnology* 22.10 (2004), pp. 538–545.

[386] V. A. Shirokov et al. "Continuous-exchange protein-synthesizing systems". In: *Methods in Molecular Biology* 375 (2007), pp. 19–55.

[387] F. Junge et al. "Advances in cell-free protein synthesis for the functional and structural analysis of membrane proteins". In: *New Biotechnology* 28.3 (2011), pp. 262–271.

[388] J. J. Wuu and J. R. Swartz. "High yield cell-free production of integral membrane proteins without refolding or detergents". In: *Biochimica et Biophysica Acta* 1778.5 (2008), pp. 1237–1250.

[389] C. Klammt et al. "High level cell-free expression and specific labeling of integral membrane proteins". In: *European Journal of Biochemistry* 271.3 (2004), pp. 568–580.

[390] H. Dong et al. "Glycines: role in a-helical membrane protein structures and a potential indicator of native conformation". In: *Biochemistry* 51.24 (2012), pp. 4779–4789.

[391] M. W. MacArthur and J. M. Thornton. "Influence of proline residues on protein conformation". In: *Journal of Molecular Biology* 218.2 (1991), pp. 397–412.

[392] I. Visiers, B. B. Braunheim, and H. Weinstein. "Prokink: a protocol for numerical evaluation of helix distortions by proline". In: *Protein engineering* 13.9 (2000), pp. 603–606.

[393] F. S. Cordes, J. N. Bright, and M. S. Sansom. "Proline-induced Distortions of Transmembrane Helices". In: *Journal of Molecular Biology* 323.5 (2002), pp. 951–960.

[394] A. Götz and C. Scharnagl. "Dissecting conformational changes in APP's transmembrane domain linked to e-efficiency in familial Alzheimer's disease". In: *PloS One* 13.7 (2018), e0200077.

[395] R. C. Oliver et al. "Dependence of micelle size and shape on detergent alkyl chain length and head group". In: *PloS One* 8.5 (2013), e62488.

[396] C. N. . Pace and J. Martin Scholtz. "A Helix Propensity Scale Based on Experimental Studies of Peptides and Proteins". In: *Biophysical Journal* 75.1 (1998), pp. 422–427.

[397] S. C. Li and C. M. Deber. "Glycine and beta-branched residues support and modulate peptide helicity in membrane environments". In: *FEBS Letters* 311.3 (1992), pp. 217–220.

[398] S. C. Li and C. M. Deber. "A measure of helical propensity for amino acids in membrane environments". In: *Nature Structural Biology* 1.6 (1994), pp. 368–373.

[399] J. A. Baker et al. "Charged residues next to transmembrane regions revisited: "Positive-inside rule" is complemented by the "negative inside depletion/outside enrichment rule"". In: *BMC Biology* 15.1 (2017), p. 66.

[400] H. J. Sharpe, T. J. Stevens, and S. Munro. "A comprehensive comparison of transmembrane domains reveals organelle-specific properties". In: *Cell* 142.1 (2010), pp. 158–169.

[401] S. Ousson et al. "Substrate determinants in the C99 juxtamembrane domains differentially affect g-secretase cleavage specificity and modulator pharmacology". In: *Journal of Neurochemistry* 125.4 (2013), pp. 610–619.

[402] Y. Song et al. "Competition between homodimerization and cholesterol binding to the C99 domain of the amyloid precursor protein". In: *Biochemistry* 52.30 (2013), pp. 5051–5064.

[403] L. Dominguez et al. "Impact of membrane lipid composition on the structure and stability of the transmembrane domain of amyloid precursor protein". In: *Proceedings of the National Academy of Sciences of the United States of America* 113.36 (2016), E5281–7.

[404] A. J. Beel and C. R. Sanders. "Substrate specificity of gamma-secretase and other intramembrane proteases". In: *Cellular and Molecular Life Sciences : CMLS* 65.9 (2008), pp. 1311–1334.

[405] P. Kienlen-Campard et al. "Amyloidogenic processing but not amyloid precursor protein (APP) intracellular C-terminal domain production requires a precisely oriented APP dimer assembled by transmembrane GXXXG motifs". In: *Journal of Biological Chemistry* 283.12 (2008), pp. 7733–7744.

[406] T.-C. Tang et al. "Influence of the familial Alzheimer's disease-associated T43I mutation on the transmembrane structure and g-secretase processing of the C99 peptide". In: *Journal of Biological Chemistry* 294.15 (2019), pp. 5854–5866.

[407] V. Corradi et al. "Emerging Diversity in Lipid-Protein Interactions". In: *Chemical Reviews* 119.9 (2019), pp. 5775–5848.

[408] J. in Jung et al. "Independent relationship between amyloid precursor protein (APP) dimerization and g-secretase processivity". In: *PloS One* 9.10 (2014), e111553.

[409] E. Winkler et al. "Homodimerization Protects the Amyloid Precursor Protein C99 Fragment from Cleavage by g-Secretase". In: *Biochemistry* 54.40 (2015), pp. 6149–6152.

[410] F. Perrin et al. "Dimeric Transmembrane Orientations of APP/C99 Regulate g-Secretase Processing Line Impacting Signaling and Oligomerization". In: *iScience* 23.12 (2020), p. 101887.

[411] W. Chen. "Solution NMR Studies of Transmembrane Domain of Amyloid Precursor Protein and Discovery of an Intramolecular Disulfide Bond between Catalytic Cysteines in an Intein Precursor". Dissertation. Rensselaer Polytechnic Institute, 2012.

[412] K. S. Mineev et al. "Spatial structure and dimer–monomer equilibrium of the ErbB3 transmembrane domain in DPC micelles". In: *Biochimica et Biophysica Acta* 1808.8 (2011), pp. 2081–2088.

[413] M. Wittlich et al. "NMR structure of the transmembrane and cytoplasmic domains of human CD4 in micelles". In: *Biochimica et Biophysica Acta* 1798.2 (2010), pp. 122–127.

[414] C. L. Deatherage et al. "Structural and biochemical differences between the Notch and the amyloid precursor protein transmembrane domains". In: *Science advances* 3.4 (2017), e1602794.

[415] Y. Gu et al. "Distinct intramembrane cleavage of the beta-amyloid precursor protein family resembling gamma-secretase-like cleavage of Notch". In: *Journal of Biological Chemistry* 276.38 (2001), pp. 35235–35238.

[416] H.-J. Lee et al. "Presenilin-dependent gamma-secretase-like intramembrane cleavage of ErbB4". In: *The Journal of biological chemistry* 277.8 (2002), pp. 6318–6323.

[417] L. Tarassishin et al. "Processing of Notch and amyloid precursor protein by gamma-secretase is spatially distinct". In: *Proceedings of the National Academy of Sciences of the United States of America* 101.49 (2004), pp. 17050–17055.

[418] I. Sörensen, R. H. Adams, and A. Gossler. "DLL1-mediated Notch activation regulates endothelial identity in mouse fetal arteries". In: *Blood* 113.22 (2009), pp. 5680–5688.

[419] M. Freeman. "Rhomboid proteases and their biological functions". In: *Annual Review of Genetics* 42 (2008), pp. 191–210.

[420] S. Yogev, E. D. Schejter, and B.-Z. Shilo. "Drosophila EGFR signalling is modulated by differential compartmentalization of Rhomboid intramembrane proteases". In: *The EMBO Journal* 27.8 (2008), pp. 1219–1230.

[421] S. Yogev, E. D. Schejter, and B.-Z. Shilo. "Polarized Secretion of Drosophila EGFR Ligand from Photoreceptor Neurons Is Controlled by ER Localization of the Ligand-Processing Machinery". In: *PLoS Biology* 8.10 (2010).

[422] S. W. Dickey et al. "Proteolysis inside the membrane is a rate-governed reaction not driven by substrate affinity". In: *Cell* 155.6 (2013), pp. 1270–1281.

[423] M. K. Lemberg. "Intramembrane proteolysis in regulated protein trafficking". In: *Traffic (Copenhagen, Denmark)* 12.9 (2011), pp. 1109–1118.

[424] S. Urban and S. W. Dickey. "The rhomboid protease family: a decade of progress on function and mechanism". In: *Genome Biology* 12.10 (2011), p. 231.

[425] E. V. Koonin et al. "The rhomboids: a nearly ubiquitous family of intramembrane serine proteases that probably evolved by multiple ancient horizontal gene transfers". In: *Genome Biology* 4.3 (2003), R19.

[426] S. Urban, J. R. Lee, and M. Freeman. "Drosophila Rhomboid-1 Defines a Family of Putative Intramembrane Serine Proteases". In: *Cell* 107.2 (2001), pp. 173–182.

[427] S. Urban, J. R. Lee, and M. Freeman. "A family of Rhomboid intramembrane proteases activates all Drosophila membrane-tethered EGF ligands". In: *The EMBO Journal* 21.16 (2002), pp. 4277–4286.

[428]   S. Urban and M. S. Wolfe. "Reconstitution of intramembrane proteolysis in vitro reveals that pure rhomboid is sufficient for catalysis and specificity". In: *Proceedings of the National Academy of Sciences of the United States of America* 102.6 (2005), pp. 1883–1888.

[429]   M. K. Lemberg et al. "Mechanism of intramembrane proteolysis investigated with purified rhomboid proteases". In: *The EMBO Journal* 24.3 (2005), pp. 464–472.

[430]   S. Maegawa, K. Ito, and Y. Akiyama. "Proteolytic action of GlpG, a rhomboid protease in the Escherichia coli cytoplasmic membrane". In: *Biochemistry* 44.41 (2005), pp. 13543–13552.

[431]   Y. Wang et al. "The role of L1 loop in the mechanism of rhomboid intramembrane protease GlpG". In: *Journal of Molecular Biology* 374.4 (2007), pp. 1104–1113.

[432]   Y. Xue et al. "Conformational change in rhomboid protease GlpG induced by inhibitor binding to its S' subsites". In: *Biochemistry* 51.18 (2012), pp. 3723–3731.

[433]   S. Maegawa et al. "The intramembrane active site of GlpG, an E. coli rhomboid protease, is accessible to water and hydrolyses an extramembrane peptide bond of substrates". In: *Molecular Microbiology* 64.2 (2007), pp. 435–447.

[434]   S. Cho et al. "Ten catalytic snapshots of rhomboid intramembrane proteolysis from gate opening to peptide release". In: *Nature Structural & Molecular Biology* (2019), pp. 910–918.

[435]   S. Cho, S. W. Dickey, and S. Urban. "Crystal Structures and Inhibition Kinetics Reveal a Two-Stage Catalytic Mechanism with Drug Design Implications for Rhomboid Proteolysis". In: *Molecular Cell* (2016), pp. 329–340.

[436]   M. J. Lemieux et al. "The crystal structure of the rhomboid peptidase from Haemophilus influenzae provides insight into intramembrane proteolysis". In: *Proceedings of the National Academy of Sciences of the United States of America* 104.3 (2007), pp. 750–754.

[437]   C. L. Brooks et al. "Insights into substrate gating in H. influenzae rhomboid". In: *Journal of Molecular Biology* 407.5 (2011), pp. 687–697.

[438]   E. Erez and E. Bibi. "Cleavage of a multispanning membrane protein by an intramembrane serine protease". In: *Biochemistry* 48.51 (2009), pp. 12314–12322.

[439]   C. Wan et al. "Exosome-related multi-pass transmembrane protein TSAP6 is a target of rhomboid protease RHBDD1-induced proteolysis". In: *PloS One* 7.5 (2012), e37452.

[440]   A. Tichá et al. "Sensitive Versatile Fluorogenic Transmembrane Peptide Substrates for Rhomboid Intramembrane Proteases". In: *The Journal of biological chemistry* 292.7 (2017), pp. 2703–2713.

[441]   Y. S. Park, S. E. Choi, and H. C. Koh. "PGAM5 regulates PINK1/Parkin-mediated mitophagy via DRP1 in CCCP-induced mitochondrial dysfunction". In: *Toxicology Letters* (2018), pp. 120–128.

[442]   D. E. Kelley et al. "Dysfunction of mitochondria in human skeletal muscle in type 2 diabetes". In: *Diabetes* 51.10 (2002), pp. 2944–2950.

[443]   K. F. Petersen et al. "Mitochondrial dysfunction in the elderly: possible role in insulin resistance". In: *Science* 300.5622 (2003), pp. 1140–1142.

[444]   D. V. Jeyaraju et al. "Structural and mechanistic basis of Parl activity and regulation". In: *Cell Death and Differentiation* (2011), pp. 1531–1539.

[445]   L. Pellegrini et al. "PAMP and PARL, two novel putative metalloproteases interacting with the COOH-terminus of Presenilin-1 and -2". In: *Journal of Alzheimer's disease* 3.2 (2001), pp. 181–190.

[446]   L. Lysyk et al. "Insights into the catalytic properties of the mitochondrial rhomboid protease PARL". In: *The Journal of biological chemistry* (2021), p. 100383.

[447]   T. Wai et al. "The membrane scaffold SLP2 anchors a proteolytic hub in mitochondria containing PARL and the i-AAA protease YME1L". In: *EMBO Reports* 17.12 (2016), pp. 1844–1856.

[448]   S. Zoll et al. "Substrate binding and specificity of rhomboid intramembrane protease revealed by substrate-peptide complex structures". In: *The EMBO Journal* 33.20 (2014), pp. 2408–2421.

[449]   J. D. Lapek et al. "Quantitative Multiplex Substrate Profiling of Peptidases by Mass Spectrometry". In: *Molecular & cellular proteomics : MCP* 18.5 (2019), pp. 968–981.

[450]   S. Sekine et al. "Rhomboid protease PARL mediates the mitochondrial membrane potential loss-induced cleavage of PGAM5". In: *The Journal of biological chemistry* 287.41 (2012), pp. 34635–34645.

[451]   S. M. Jin et al. "Mitochondrial membrane potential regulates PINK1 import and proteolytic destabilization by PARL". In: *Journal of Cell Biology* 191.5 (2010), pp. 933–942.

[452]   C. Meissner et al. "The mitochondrial intramembrane protease PARL cleaves human Pink1 to regulate Pink1 trafficking". In: *Journal of Neurochemistry* 117.5 (2011), pp. 856–867.

[453]   S. Saita et al. "PARL mediates Smac proteolytic maturation in mitochondria to promote apoptosis". In: *Nature cell biology* 19.4 (2017), pp. 318–328.

[454]   M. Spinazzi et al. "PARL deficiency in mouse causes Complex III defects, coenzyme Q depletion, and Leigh-like syndrome". In: *Proceedings of the National Academy of Sciences of the United States of America* 116.1 (2019), pp. 277–286.

[455]   S. Saita et al. "PARL partitions the lipid transfer protein STARD7 between the cytosol and mitochondria". In: *The EMBO Journal* 37.4 (2018).

[456]   K. Takeda et al. "Mitochondrial phosphoglycerate mutase 5 uses alternate catalytic activity as a protein serine/threonine phosphatase to activate ASK1". In: *Proceedings of the National Academy of Sciences of the United States of America* 106.30 (2009), pp. 12301–12305.

[457]   K. Moriwaki and F. K.-M. Chan. "RIP3: a molecular switch for necrosis and inflammation". In: *Genes & development* 27.15 (2013), pp. 1640–1649.

[458]   M. Zhuang et al. "Substrates of IAP ubiquitin ligases identified with a designed orthogonal E3 ligase, the NEDDylator". In: *Molecular Cell* 49.2 (2013), pp. 273–282.

[459]   H. Wu et al. "The BCL2L1 and PGAM5 axis defines hypoxia-induced receptor-mediated mitophagy". In: *Autophagy* 10.10 (2014), pp. 1712–1725.

[460]   W. Xu et al. "Bax-PGAM5L-Drp1 complex is required for intrinsic apoptosis execution". In: *Oncotarget* 6.30 (2015), pp. 30017–30034.

[461]   L. Liu et al. "Receptor-mediated mitophagy in yeast and mammalian systems". In: *Cell research* 24.7 (2014), pp. 787–795.

[462]   Y. J. Kang et al. "Regulation of NKT cell-mediated immune responses to tumours and liver inflammation by mitochondrial PGAM5-Drp1 signalling". In: *Nature Communications* 6 (2015), p. 8371.

[463]   S.-C. Lo and M. Hannink. "PGAM5 tethers a ternary complex containing Keap1 and Nrf2 to mitochondria". In: *Experimental cell research* 314.8 (2008), pp. 1789–1803.

[464]   C. Brenner et al. "Decoding cell death signals in liver inflammation". In: *Journal of hepatology* 59.3 (2013), pp. 583–594.

[465]   Y. Kanamaru et al. "The phosphorylation-dependent regulation of mitochondrial proteins in stress responses". In: *Journal of signal transduction* 2012 (2012), p. 931215.

[466]   Q. Remijsen et al. "Depletion of RIPK3 or MLKL blocks TNF-driven necroptosis and switches towards a delayed RIPK1 kinase-dependent apoptosis". In: *Cell death & disease* 5 (2014), e1004.

[467]   E. M. Valente et al. "Hereditary early-onset Parkinson's disease caused by mutations in PINK1". In: *Science* 304.5674 (2004), pp. 1158–1160.

[468]   S. Sekine and R. J. Youle. "PINK1 import regulation; a fine system to convey mitochondrial stress to the cytosol". In: *BMC Biology* 16.1 (2018), p. 2.

[469]   E. Deas et al. "PINK1 cleavage at position A103 by the mitochondrial protease PARL". In: *Human Molecular Genetics* (2011), pp. 867–879.

[470]   K. Yamano and R. J. Youle. "PINK1 is degraded through the N-end rule pathway". In: *Autophagy* 9.11 (2013), pp. 1758–1769.

[471]   Y. Matsuda et al. "T cell activation in abnormal perinatal events". In: *Microbiology and immunology* 54.1 (2010), pp. 38–45.

[472]   C. Vives-Bauza et al. "PINK1-dependent recruitment of Parkin to mitochondria in mitophagy". In: *Proceedings of the National Academy of Sciences of the United States of America* 107.1 (2010), pp. 378–383.

[473]   R. K. Dagda et al. "Loss of PINK1 function promotes mitophagy through effects on oxidative stress and mitochondrial fission". In: *Journal of Biological Chemistry* 284.20 (2009), pp. 13843–13855.

[474] S. Geisler et al. "The PINK1/Parkin-mediated mitophagy is compromised by PD-associated mutations". In: *Autophagy* 6.7 (2010), pp. 871–878.

[475] F. Koyano et al. "Ubiquitin is phosphorylated by PINK1 to activate parkin". In: *Nature* 510.7503 (2014), pp. 162–166.

[476] A. Ordureau et al. "Quantitative proteomics reveal a feedforward mechanism for mitochondrial PARKIN translocation and ubiquitin chain synthesis". In: *Molecular Cell* 56.3 (2014), pp. 360–375.

[477] T. Wauer et al. "Mechanism of phospho-ubiquitin-induced PARKIN activation". In: *Nature* 524.7565 (2015), pp. 370–374.

[478] S. A. Sarraf et al. "Landscape of the PARKIN-dependent ubiquitylome in response to mitochondrial depolarization". In: *Nature* 496.7445 (2013), pp. 372–376.

[479] D. Narendra et al. "Parkin is recruited selectively to impaired mitochondria and promotes their autophagy". In: *Journal of Cell Biology* (2008), pp. 795–803.

[480] K. Yamano, N. Matsuda, and K. Tanaka. "The ubiquitin signal and autophagy: an orchestrated dance leading to mitochondrial degradation". In: *EMBO Reports* 17.3 (2016), pp. 300–316.

[481] T. N. Nguyen, B. S. Padman, and M. Lazarou. "Deciphering the Molecular Signals of PINK1/Parkin Mitophagy". In: *Trends in Cell Biology* 26.10 (2016), pp. 733–744.

[482] C. Meissner et al. "Intramembrane protease PARL defines a negative regulator of PINK1- and PARK2/Parkin-dependent mitophagy". In: *Autophagy* 11.9 (2015), pp. 1484–1498.

[483] F. Rodriguez et al. "Structural model for the protein-translocating element of the twin-arginine transport system". In: *Proceedings of the National Academy of Sciences of the United States of America* 110.12 (2013), E1092–101.

[484] Y. Zhang et al. "Structural basis for TatA oligomerization: an NMR study of Escherichia coli TatA dimeric structure". In: *PloS One* 9.8 (2014), e103157.

[485] L. P. Liu and C. M. Deber. "Uncoupling hydrophobicity and helicity in transmembrane segments. Alpha-helical propensities of the amino acids in non-polar environments". In: *Journal of Biological Chemistry* 273.37 (1998), pp. 23645–23648.

[486] A. Chaikuad et al. "Structures of PGAM5 Provide Insight into Active Site Plasticity and Multimeric Assembly". In: *Structure* 25.7 (2017), 1089–1099.e3.

[487] K. Ruiz et al. "Functional role of PGAM5 multimeric assemblies and their polymerization into filaments". In: *Nature Communications* 10.1 (2019), p. 531.

[488] D. Sharma and K. Rajarathnam. "13C NMR chemical shifts can predict disulfide bond formation". In: *Journal of Biomolecular NMR* 18.2 (2000), pp. 165–171.

[489] C. Torres-Arancivia et al. "Identification of an archaeal presenilin-like intramembrane protease". In: *PloS One* 5.9 (2010).

[490] C. P. Ponting et al. "Identification of a novel family of presenilin homologues". In: *Human Molecular Genetics* 11.9 (2002), pp. 1037–1044.

List of Figures

List of Tables

A. Appendix

A.1. List of buffers, media and primers

Plasmid and primers
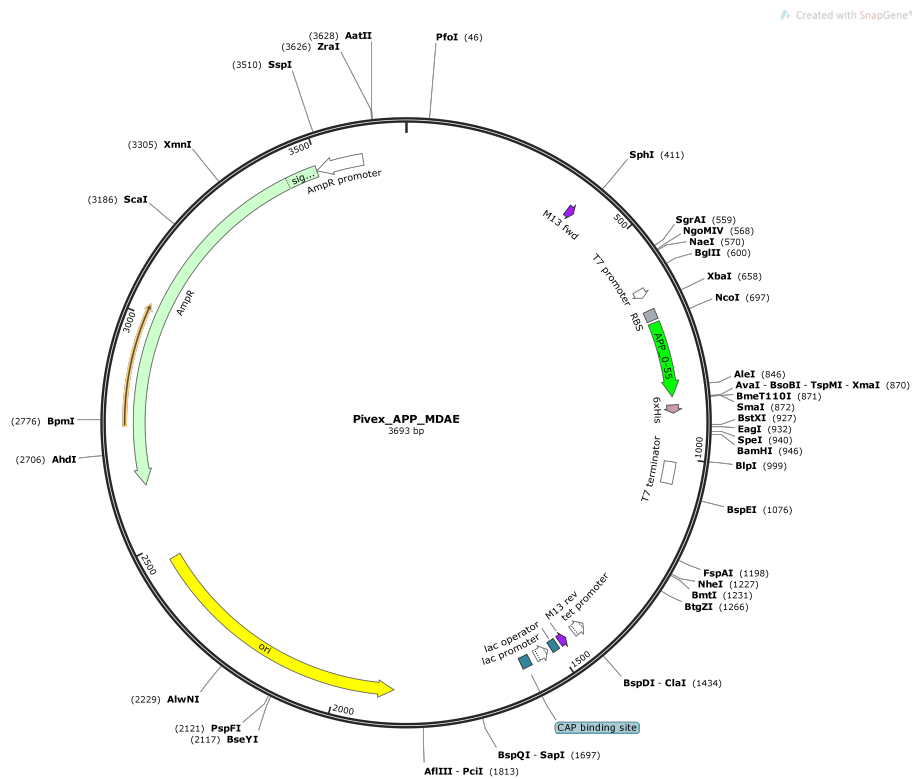
Figure A.1. Pivex 2.3d with APP$_{0-55}$ insert. Empty vector was supplied by Ulrike Krug, Prof. Daniel Huster, Leipzig

Table A.1. Primers used for Pivex2.3d + APP$_{0-55}$

	sequence	enzyme	T_m
FW APP$_{0-55}$	5′ TTTCC<u>ATGG</u>ATGCAGAATTCCGACATGACTCAGGATATG 3′	*NcoI*	68 °C
RV with His-Tag	5′ TTTCC<u>CGGG</u>TTTCTTCTTCAGCATCACCAAGGTGATGACGATC 3′	*SmaI*	68 °C

Standard procedures, buffers and media

Standard PCR mix	
5 μL	10x Polymerase Buffer
1 μL	dNTP-Mix
5 μL	Primer forward (10 pmol/μL)
5 μL	Primer reverse (10 pmol/μL)
0.5 μL	DNA-Template
32.5 μL	ddH2O
0.5 μL	Pfu-Polymerase

Colony PCR mix	
5 μL	10x Polymerase Buffer
1 μL	dNTP-Mix
5 μL	Primer forward (10 pmol/μL)
5 μL	Primer reverse (10 pmol/μL)
	cells picked from agar plate
32.5 μL	ddH2O
0.5 μL	Pfu-Polymerase

Standard PCR protocol

Step	T [°C]	t [s]	
Initial Denat.	95	60	
Denaturation	95	45	
Annealing	58	30	30
Extension	72	60	cycles
Final Extension	72	600	
Soak	4		

Colony PCR protocol

Step	T [°C]	t [s]	
Initial Denat.	95	600	
Denaturation	95	45	
Annealing	58	30	20
Extension	72	60	cycles
Final Extension	72	600	
Soak	4		

Standard digest

	Vector	PCR product
H2O	2 μL	13 μL
CutSmart Buff.	1 μL	5 μL
NcoI	1 μL	1 μL
SmaI	1 μL	1 μL
DNA	5 μL	30 μL

Standard ligation mix

3 μL	Ligase Buffer
10 μL	Vector
17.5 μL	Insert
1 μL	T4 DNA-Ligase

Standard transformation mix

50 μL	competent cells
1 μL	vector
800 μL	SOC

LB medium, 1L

10 g	Tryptone
5 g	Yeast extract
10 g	NaCl

SOC medium, 1L

20 g	Tryptone
5 g	Yeast extract
0.5 g	NaCl
2.5 mL	KOH 1 M

50x TAE-buffer

50 mM	EDTA
2 M	Tris
1 M	Acetic acid

S30 extract buffer, pH 8.2

10 mM	Tris-acetate
14 mM	magnesium acetate
60 mM	potassium acetate
adjust pH with KOH	

Tris-buffer, pH 8

50 mM	Tris-HCl
100 mM	NaCl

NMR-buffer pH 5

1 mM	Acetic acid-d4
10%	D_2O
90%	H_2O

CF wash buffer, pH 8

20 mM	Tris
100 mM	NaCl

MSP-buffer, pH 7.5

20 mM	Tris
100 mM	NaCl
0.5 mM	EDTA

MSP-cholate buffer, pH 7.5

20 mM	Tris
100 mM	NaCl
0.5 mM	EDTA
100 mM	Cholat

Cell-free solutions

<div align="center">

CF stock solutions

</div>

Hepes buffer (pH 8.4)	2.5 M	Hepes in H_2O
$Mg(OAc)_2$	2 M	$Mg(OAc)_2$ in H_2O
KOAc	4 M	
PEG 8000	40 % m/V	
NaN3	10 % m/V	
Folinic acid	20 mg/mL	Folinic acid calcium salt hydrate
DTT	500 mM	
NTP	75 x	0.36 M ATP, 0.24 M GTP, 0.24 M UTP, 0.24 CTP
Complete	50 x	1 tablet in 1 ml H_2O
Phosphoenolpyruvate (PEP)	1 M	
Acetyl Phosphate (AcP)	1 M	
amino acid-mix	4 mM	
S30C buffer	1 x	S30 buffer + 0.5 mM DTT
Pyruvate kinase (PK)	2.4 mg/mL	
tRNA	40 mg/mL	
T7RNA-Polymerase	200 U/μL	
RiboLock	40 U/μL	Thermo Scientifi™RiboLock RNase Inhibitor
vector	xxx μg/mL	Pivex2.3d carrying the respective gene sequence
S30-extract	100 %	P- or R-extract

NTP mix	
0.36 M	ATP
0.24 M	GTP
0.24 M	UTP
0.24	CTP

Amino acid stock solutions

	concentration	solvent
Ala	100 mM	H_2O
Cys	100 mM	Hepes buffer, 100 mM
Asp	100 mM	Hepes buffer, 100 mM
Phe	100 mM	Hepes buffer, 100 mM
Gly	100 mM	H_2O
His	100 mM	H_2O
Ile	100 mM	H_2O
Lys	100 mM	H_2O
Leu	100 mM	H_2O
Met	100 mM	H_2O
Asn	100 mM	Hepes buffer, 100 mM
Pro	100 mM	H_2O
Gln	100 mM	Hepes buffer, 100 mM
Arg	100 mM	H_2O
Ser	100 mM	H_2O
Thr	100 mM	H_2O
Val	100 mM	H_2O
Trp	50 mM	Hepes buffer, 100 mM
Tyr	20 mM	Hepes buffer, 100 mM

Cell-free protocols

TNR12 D-CF 10.02.20 12:1

Compound	Stock Concentration		Final Concentration					14 mM			16 mM			18 mM				Mastermische		
								MM (µL)	FM (µL)	RM (µL)	MM (µL)	FM (µL)	RM (µL)	MM (µL)	FM (µL)	RM (µL)		MM (µL)	FM (µL)	RM (µL)
ddH2O																				
HEPES (pH 8.4)	2510	mM	100.00	mM				78			78			78				233		
Mg(OAc)2	2021	mM	5.63	mM	7.628	9.628		5			7			9				-		
KOAc	4002	mM	94.78	mM	94.78	94.78		46			46			46				139		
PEG 8000	40.03	% m/V	2.00	% m/V				97			97			97				292		
NaN3	10.25	% m/V	0.05	% m/V				10			10			10				29		
Folinic acid	20.00	mg/mL	0.10	mg/mL				10			10			10				29		
DTT	515	mM	2.00	mM				8			8			8				23		
NTP	75.00	x	1.00	x				26			26			26				78		
Complete	50.00	x	1.00	x				39			39			39				117		
PEP	1016	mM	20.00	mM				38			38			38				115		
AcP	1000	mM	20.00	mM				39			39			39				117		
aa-Mix	4.00	mM	1.00	mM				244	244		244	244		244	244			731	731	
Brij-95	2.00	% m/V	0.20	% m/V				195			195			195				-		
Mastermix									788	36		790	36		792	36			1797	106
S30 C buffer	1.00	x	0.35	x					630			630			630				1890	
PK	2.40	mg/mL	0.04	mg/mL						3			3			3				8
tRNA	40.00	mg/mL	0.50	mg/mL						1.9			1.9			1.9				6
T7RNAP	200.00	U/µL	6.00	U/µL						5			5			5				14
RiboLock	40.00	U/µL	0.30	U/µL						1.1			1.1			1.1				3
DNA	1305.00	µg/mL	26.00	µg/mL						3			3			3				9
S30-Extract	100.00	mM	40.00	mM						60			60			60				180
ND (MSP-buffer)	100.00	mM	0.80	mM																0
ddH2O									138	41		136	41		134	41			408	124
			Total (µL)					835	1800	150	837	1800	150	839	1800	150		1903		

Mg2+	14	mM
K+	280	mM
Plasmid	1305	µg/mL

16	mM
18	mM

P-Extrakt, Nov 18

Pivex+TNR12 31.10.19

	14 mM	16 mM	18 mM
Cond.	30°C 100 rpm	30°C 100 rpm	30°C 100 rpm
Start	14:00	14:00	14:00
End	10:00	10:00	10:00

AA Mix ges   0.5 mL

AA	Stock c.		Final c.		AA µL	Für alle 3
Ala	8.0	mM	2.00	mM	39	117
Arg	12.0	mM	3.00	mM	59	176
Asn	0.0	mM	0.00	mM	0	0
Asp	6.0	mM	1.50	mM	29	88
Cys	8.0	mM	2.00	mM	39	117
Gln	1.0	mM	0.25	mM	5	15
Glu	6.0	mM	1.50	mM	29	88
Gly	8.0	mM	2.00	mM	39	117
His	4.0	mM	1.00	mM	20	59
Ile	2.0	mM	0.50	mM	10	29
Leu	8.0	mM	2.00	mM	39	117
Lys	1.0	mM	0.25	mM	5	15
Met	2.0	mM	0.50	mM	10	29
Phe	3.0	mM	0.75	mM	15	44
Pro	6.0	mM	1.50	mM	29	88
Ser	6.0	mM	1.50	mM	29	88
Thr	3.0	mM	0.75	mM	15	44
Trp	4.0	mM	1.00	mM	39	117
Tyr	0.0	mM	0.00	mM	0	0
Val	2.0	mM	0.50	mM	10	29
H2O					29	88
			Total (µL)		488	1463

MW: 12,233 Da
Monoisotop 12,226 Da
Ext: 17,000 M-1cm-1

TNR12 P-CF 24.02.20 17:1

Compound	Stock Concentration	Final Concentration				14 mM MM (µL)	14 mM FM (µL)	14 mM RM (µL)	16 mM MM (µL)	16 mM FM (µL)	16 mM RM (µL)	18 mM MM (µL)	18 mM FM (µL)	18 mM RM (µL)	Mastermische MM (µL)	Mastermische FM (µL)	Mastermische RM (µL)
ddH2O																	
HEPES (pH 8.4)	2510 mM	100.00 mM				108			108			108			323		
Mg(OAc)2	2021 mM	5.63 mM	7.628	9.628		8			10			13			31		
KOAc	4002 mM	94.78 mM	94.78	94.78		64			64			64			192		
PEG 8000	40.03 % m/V	2.00 % m/V				135			135			135			405		
NaN3	10.25 % m/V	0.05 % m/V				13			13			13			40		
Folinic acid	20.00 mg/mL	0.10 mg/mL				14			14			14			41		
DTT	515 mM	2.00 mM				10			10			10			31		
NTP	75.00 x	1.00 x				36			36			36			108		
Complete	50.00 x	1.00 x				54			54			54			162		
PEP	1016 mM	20.00 mM				53			53			53			159		
AcP	1000 mM	20.00 mM				54			54			54			162		
aa-Mix	4.00 mM	1.00 mM				338	338		338	338		338	338		1013	1013	
Brij-98	2.00 % m/V	0.20 % m/V				/			/			/			-		
Mastermix							837	49		839	49		842	50		2517	148
S30 C buffer	1.00 x	0.35 x					893			893			893			2678	
PK	2.40 mg/mL	0.04 mg/mL						3			3			3			8
tRNA	40.00 mg/mL	0.50 mg/mL						1.9			1.9			1.9			6
T7RNAP	200.00 U/µL	6.00 U/µL						5			5			5			14
RiboLock	40.00 U/µL	0.30 U/µL						1.1			1.1			1.1			3
DNA	1305.00 µg/mL	26.00 µg/mL						3			3			3			9
S30-Extract	100.00 %	40.00 %						60			60			60			180
ND (MSP-buffer)	mM	mM															
ddH2O						483		28	481		28	478		28		1443	83
Total (µL)						886	2550	150	888	2550	150	891	2550	150	2665		

Mg2+	14	mM
K+	280	mM
Plasmid	1305	µg/mL

16	mM
18	mM

P-Extrakt, Nov 18	
Pivex+TNR12 31.10.19	

	14 mM	16 mM	18 mM
Cond.	110 rpm, 34 °C	110 rpm, 34 °C	110 rpm, 34 °C
Start	14:40	14:40	14:40
End	10:40	10:40	10:40

AA Mix ges   0.7 mL

AA	Stock c.		Final c.		AA µL	Für alle 3
Ala	8.0	mM	2.00	mM	54	162
Arg	12.0	mM	3.00	mM	81	243
Asn	0.0	mM	0.00	mM	0	0
Asp	6.0	mM	1.50	mM	41	122
Cys	8.0	mM	2.00	mM	54	162
Gln	1.0	mM	0.25	mM	7	20
Glu	6.0	mM	1.50	mM	41	122
Gly	8.0	mM	2.00	mM	54	162
His	4.0	mM	1.00	mM	27	81
Ile	2.0	mM	0.50	mM	14	41
Leu	8.0	mM	2.00	mM	54	162
Lys	1.0	mM	0.25	mM	7	20
Met	2.0	mM	0.50	mM	14	41
Phe	3.0	mM	0.75	mM	20	61
Pro	6.0	mM	1.50	mM	41	122
Ser	6.0	mM	1.50	mM	41	122
Thr	3.0	mM	0.75	mM	20	61
Trp	4.0	mM	1.00	mM	54	162
Tyr	0.0	mM	0.00	mM	0	0
Val	2.0	mM	0.50	mM	14	41
H2O					40	122
Total (µL)					675	2025

MW: 12,233 Da
Monoisotop: 12,226 Da
Ext: 17,000 M-1cm-1

	TNR12 in ND(DMPC) 25.11.19			FM:RM 12:1	

Compound	Stock Concentration		Final Concentration		MM (µL)	FM (µL)	RM (µL)
ddH2O							
HEPES (pH 8.4)	2510	mM	100.00	mM	337		
Mg(OAc)2	2021	mM	5.63	mM	24		
KOAc	4002	mM	94.78	mM	200		
PEG 8000	40.03	% m/V	2.00	% m/V	422		
NaN3	10.25	% m/V	0.05	% m/V	41		
Folinic acid	20.00	mg/mL	0.10	mg/mL	42		
DTT	515	mM	2.00	mM	33		
NTP	75.00	x	1.00	x	113		
Complete	50.00	x	1.00	x	169		
PEP	1016	mM	20.00	mM	166		
AcP	1000	mM	20.00	mM	169		
aa-Mix	4.00	mM	1.00	mM	1056	1056	
Mastermix						2618	154
S30 C buffer	1.00	x	0.35	x		2730	
PK	2.40	mg/mL	0.04	mg/mL			11
tRNA	40.00	mg/mL	0.50	mg/mL			8.1
T7RNAP	200.00	U/µL	6.00	U/µL			20
RiboLock	40.00	U/µL	0.30	U/µL			4.9
DNA	1305.00	µg/mL	26.00	µg/mL			13
S30-Extract	100.00	%	40.00	%			260
ND (MSP-buffer)	0.35	mM	0.05	mM			93
ddH2O						1396	87
			Total (µL)		2772	7800	650

AA	Stock Conc.		Final Conc.		AA Mix V	
Ala	8.0	mM	2.00	mM	176	µL
Arg	12.0	mM	3.00	mM	264	µL
Asn	0.0	mM	0.00	mM	0	µL
Asp	6.0	mM	1.50	mM	132	µL
Cys	8.0	mM	2.00	mM	176	µL
Gln	1.0	mM	0.25	mM	22	µL
Glu	6.0	mM	1.50	mM	132	µL
Gly	8.0	mM	2.00	mM	176	µL
His	4.0	mM	1.00	mM	88	µL
Ile	2.0	mM	0.50	mM	44	µL
Leu	8.0	mM	2.00	mM	176	µL
Lys	1.0	mM	0.25	mM	22	µL
Met	2.0	mM	0.50	mM	44	µL
Phe	3.0	mM	0.75	mM	66	µL
Pro	6.0	mM	1.50	mM	132	µL
Ser	6.0	mM	1.50	mM	132	µL
Thr	3.0	mM	0.75	mM	66	µL
Trp	4.0	mM	1.00	mM	176	µL
Tyr	0.0	mM	0.00	mM	0	µL
Val	2.0	mM	0.50	mM	44	µL
H2O					132	µL
			Total (µL)		2200	µL

Mg2+	14	mM
K+	280	mM
Plasmid	1305	µg/mL

P-Extrakt, Nov 18

Pivex+TNR12, 31.10.19

Cond.

Start

End

AA Mix ges | 2.2 | mL

A.2. Resonance Assignments

APP WT in TFE/H$_2$O

Table A.2. APP WT TMD in TFE/H$_2$O, pH 7

		H	N	HA	HB	CA	CB
26	Ser	7.8	119.26	4.42	3.97,3.83	57.94	63.2
27	Asn	8.2	119.29	4.8	2.92,2.92	52.55	37.26
28	Lys	8.08	120.65	4.11	1.89,1.89	58.25	31.53
29	Gly	8.26	105.18	3.85,3.85	-	45.88	-
30	Ala	7.66	122.92	4.22	1.5	53.76	17.22
31	Ile	7.51	116.95	3.91	2.03	63.22	37.28
32	Ile	7.9	119.89	3.84	1.94	64.09	36.96
33	Gly	7.94	105.26	3.84,3.82	-	46.4	-
34	Leu	7.88	121.99	4.24	2.01,1.64	57.01	41.4
35	Met	8.24	119.67	4.27	2.36,2.18	57.96	31.9
36	Val	8.63	118.84	3.81	2.17	65.34	31.31
37	Gly	8.15	106.44	3.90,3.90	-	46.35	-
38	Gly	7.9	106.01	3.93,3.94	-	46.3	-
39	Val	7.74	121.7	3.85	2.37	65.39	31.04
40	Val	8.2	123.56	3.6	2.33	66.87	30.88
41	Ile	8.15	118.64	3.75	1.93	64.18	36.96
42	Ala	7.89	119.89	4.05	1.54	54.96	16.99
43	Thr	7.94	112.49	3.9	4.56	66.74	68.33
44	Val	8.27	121.19	3.64	2.35	67.38	31.04
45	Ile	8.48	123.52	3.64	2.11	65.71	36.87
46	Val	8.22	119.71	3.64	2.28	66.47	30.88
47	Ile	8.56	117.96	3.7	1.98	64.78	36.95
48	Thr	8.16	116.1	3.84	4.55	67.29	68.02
49	Leu	8.49	121.71	4.11	1.52,2.12	57.97	41.03
50	Val	8.62	120.04	3.61	2.33	66.58	30.88
51	Met	8.55	118.76	4.2	2.43,2.11	58.03	31.05
52	Leu	8.53	119.68	4.14	1.57,2.01	57.13	41.39
53	Lys	8.2	119.29	4.13	2.00,2.07	57.66	31.38
54	Lys	8.24	118.61	4.19	1.95,2.00	57.21	31.73
55	Lys	8.02	119.19	4.24	1.95,1.95	56.12	32.03

APP G38L TMD in TFE/H$_2$O

Table A.3. APP G38L TMD in TFE/H$_2$O, pH 7

		H	N	HA	HB	CA	CB
26	Ser	7.79	119.15	4.4	3.83,3.96	58	63.14
27	Asn	-	-	4.79	2.92,2.92	-	37.16
28	Lys	8.04	119.08	4.12	-	58.15	-
29	Gly	8.24	105.04	3.85,3.85	-	45.82	-
30	Ala	7.65	122.86	4.23	1.5	53.68	17.26
31	Ile	7.5	117.16	3.95	2.03	63.02	37.36
32	Ile	7.84	120.13	3.84	1.93	63.98	37.02
33	Gly	7.9	104.6	3.82,3.82	-	46.29	-
34	Leu	7.77	122.71	4.27	1.89,1.81	57.12	41.37
35	Met	8.12	118.2	4.25	2.17,2.33	58.02	31.58
36	Val	8.45	118.12	3.72	2.14	65.83	31.11
37	Gly	7.86	105.6	3.81,3.89	-	46.53	-
38	Leu	7.94	119.93	4.22	2.02,1.64	57.42	41.09
39	Val	7.86	119.4	3.75	2.38	65.8	30.91
40	Val	8.39	123.61	3.61	2.34	67.08	30.86
41	Ile	8.21	119.28	3.74	1.98	64.51	37.05
42	Ala	8.24	120.2	4.05	1.55	54.94	16.95
43	Thr	8	112.8	3.9	4.58	66.76	68.3
44	Val	8.34	121.44	3.64	2.36	67.38	30.86
45	Ile	8.53	123.63	3.64	2.12	65.77	36.87
46	Val	8.22	119.77	3.64	2.28	66.49	30.84
47	Ile	8.58	118.07	3.7	1.98	64.8	37.05
48	Thr	8.18	116.13	3.84	4.55	67.27	68.02
49	Leu	8.5	121.73	4.11	1.52,2.12	57.95	41.02
50	Val	8.63	120.12	3.61	2.34	66.56	30.86
51	Met	-	-	-	-	-	-
51	Met	8.56	118.8	4.2	2.11,2.43	58.04	31
52	Leu	8.54	119.72	4.14	2.01,1.57	57.18	41.35
53	Lys	8.2	119.28	4.13	2.00,2.07	57.65	-
54	Lys	8.25	118.57	4.18	1.96,1.99	57.25	-
55	Lys	8.01	119.08	4.22	1.95,1.95	56.19	32.02

APP G38P TMD in TFE/H$_2$O

Table A.4. APP G38P TMD in TFE/H$_2$O, pH 7

		H	N	HA	HB	CA	CB
26	Ser	7.77	119.08	4.39	3.83,3.96	58.02	63.14
27	Asn	-	-	4.79	2.91,2.91	52.41	37.12
28	Lys	8.02	119.04	4.12	1.86,1.89	58	31.57
29	Gly	8.21	105.06	3.85,3.85	-	45.74	-
30	Ala	7.63	122.75	4.23	1.49	53.53	17.31
31	Ile	7.48	116.81	3.94	2.02	62.95	37.41
32	Ile	7.81	119.73	3.86	1.93	63.79	37.1
33	Gly	7.93	105.65	3.84,3.84	-	46.21	-
34	Leu	7.77	120.24	4.29	1.97,1.64	56.38	41.61
35	Met	7.96	116.56	4.44	2.30,2.16	56.72	32.45
36	Val	8.11	118.59	4.25	2.27	62.61	32.04
37	Gly	7.92	108.51	3.94,4.19	-	47.22	-
38	Pro	-	-	4.27	2.40,1.87	65.05	31.24
39	Val	7.42	116.05	3.8	2.31	64.95	31.19
40	Val	8.02	123.77	3.61	2.3	66.57	30.9
41	Ile	8.13	114.28	3.7	1.87	64.15	36.93
42	Ala	7.87	119.47	4.05	1.54	54.96	16.97
43	Thr	7.86	112.37	3.89	4.55	66.78	68.35
44	Val	8.25	121.11	3.63	-	67.38	30.88
44	Val	-	-	-	2.34	-	-
45	Ile	8.45	123.61	3.63	2.11	65.71	36.88
46	Val	8.25	119.79	3.64	2.27	66.44	30.89
47	Ile	8.56	118.02	3.7	1.98	64.79	36.99
48	Thr	8.16	116.13	3.84	4.55	67.3	68.04
49	Leu	8.5	121.71	4.11	2.12,1.52	58	41.05
50	Val	8.63	120.11	3.61	2.33	66.57	30.88
51	Met	8.56	118.74	4.2	2.11,2.43	58.06	31.04
52	Leu	8.54	119.7	4.14	2.02,1.57	57.19	41.37
53	Lys	8.21	119.34	4.12	1.99,2.07	57.71	31.34
54	Lys	8.25	118.53	4.18	2.00,1.96	57.24	31.74
55	Lys	8	-	4.22	1.95,1.95	56.21	32.03

APP V44M TMD in TFE/H$_2$O

Table A.5. APP V44M TMD in TFE/H$_2$O, pH 7

		H	N	HA	HB	CA	CB
26	Ser	7.76	119.05	4.4	3.84,3.97	58.02	63.15
27	Asn	8.16	-	4.8	2.92,2.92	52.48	37.1
28	Lys	8.03	120.61	4.11	1.89,1.89	58.27	31.56
29	Gly	8.23	104.92	3.85,3.85	-	45.88	-
30	Ala	7.64	122.88	4.23	1.5	53.75	17.19
31	Ile	7.49	116.9	3.91	2.03	63.22	37.28
32	Ile	7.88	119.98	3.85	1.94	64.11	36.98
33	Gly	7.93	105.18	3.85,3.82	-	46.42	-
34	Leu	7.88	122.11	4.25	2.01,1.65	57.02	41.38
35	Met	8.24	119.76	4.26	2.37,2.19	58.02	31.89
36	Val	8.64	119	3.8	2.17	65.45	31.27
37	Gly	8.16	106.41	3.84,3.89	-	46.39	-
38	Gly	7.9	105.97	3.94,3.94	-	46.37	-
39	Val	7.76	121.86	3.85	2.38	65.51	31.13
40	Val	8.27	124.15	3.59	2.35	66.89	30.91
41	Ile	8.21	119.31	3.8	1.96	64.39	36.99
42	Ala	8.03	120.23	4.06	1.55	55.09	16.95
43	Thr	8.08	112.42	3.89	4.51	66.71	68.32
44	Met	8.27	119.94	4.21	2.15,2.41	58.26	31.14
45	Ile	8.51	123.35	3.66	2.15	65.57	37.04
46	Val	8.17	120.17	3.63	2.29	67.35	30.89
47	Ile	8.56	117.67	3.7	1.97	64.84	36.99
48	Thr	7.98	116.1	3.85	4.56	67.28	68.05
49	Leu	8.48	121.65	4.11	2.13,1.52	57.98	41
50	Val	8.63	120.04	3.61	2.33	66.56	30.91
51	Met	8.54	118.79	4.21	2.43,2.11	58.05	31.05
52	Leu	8.54	119.68	4.14	1.56,2.01	57.16	41.37
53	Lys	8.2	119.31	4.13	1.99,2.08	57.65	31.32
54	Lys	8.24	118.59	4.18	1.96,2.00	57.22	31.72
55	Lys	8	119.08	4.23	1.95,1.95	56.18	32.02

APP I45T TMD in TFE/H$_2$O

Table A.6. APP I45T TMD in TFE/H$_2$O, pH 7

		H	N	HA	HB	CA	CB
26	Ser	7.78	119.06	4.4	3.97,3.84	58.03	63.13
27	Asn	8.16	-	4.8	2.92,2.92	52.46	37.11
28	Lys	8.03	-	4.11	1.88,1.88	58.25	31.54
29	Gly	8.24	104.92	3.85,3.85	-	45.88	-
30	Ala	7.64	122.88	4.23	1.5	53.74	17.2
31	Ile	7.49	116.96	3.91	2.03	63.22	37.28
32	Ile	7.88	120	3.85	1.94	64.09	36.98
33	Gly	7.93	105.18	3.85,3.85	-	46.42	-
34	Leu	7.88	122.17	4.25	1.64,2.01	57.03	41.37
35	Met	8.24	119.83	4.26	2.19,2.37	58.04	31.87
36	Val	8.65	119.12	3.78	2.17	65.57	31.24
37	Gly	8.17	106.34	3.83,3.90	-	46.44	-
38	Gly	7.92	106.22	3.96,3.92	-	46.43	-
39	Val	7.79	122.22	3.83	2.41	65.74	31.02
40	Val	8.37	124.6	3.6	2.36	67.18	30.87
41	Ile	8.38	118.5	3.76	1.95	64.29	36.98
42	Ala	8.38	124.85	4.09	1.58	55.36	16.97
43	Thr	8.17	114.25	3.9	4.52	67.1	68.18
44	Val	8.74	119.52	3.68	2.18	66.1	31.07
45	Thr	8.29	119.47	3.86	4.55	67.59	67.92
46	Val	8.2	121.72	3.67	2.28	67.24	30.93
47	Ile	8.4	118.11	3.67	1.94	64.97	37.11
48	Thr	8.11	115.43	3.85	4.51	67.26	68.33
49	Leu	8.29	121.64	4.11	1.56,2.08	58.01	41.11
50	Val	8.59	119.75	3.61	2.33	66.59	30.85
51	Met	8.52	118.67	4.2	2.43,2.11	58.05	31.02
52	Leu	8.54	119.66	4.14	2.02,1.57	57.16	41.36
53	Lys	8.22	119.26	4.13	1.99,2.08	57.64	31.29
54	Lys	8.25	118.51	4.19	1.96,2.00	57.24	31.7
55	Lys	8	119.04	4.23	1.95,1.95	56.21	32.02

APP WT in DPC

Table A.7. APP WT in DPC, pH 5, 320 K

		H	N	HA	HB	C	CA	CB
1	Asp	-	-	-	-	-	54.61	38.9
2	Ala	8.35	138.41	4.3	1.38	116.4	52.74	19.39
3	Glu	8.25	137.9	4.24	2.25,1.96	118.33	56.69	30.04
4	Phe	8.09	139.14	4.73	3.08	117.05	57.75	39.24
5	Arg	7.97	135.1	4.29	1.71,1.82	116.56	56.22	31.01
6	His	-	-	-	3.28,3.18	-	55.49	29.2
7	Asp	8.37	135.26	4.7	2.74	115.14	54.33	41.29
8	Ser	8.32	130.22	4.44	3.92	117.1	59.04	64.11
9	Gly	8.46	124.3	3.96,3.96	-	116.01	45.68	-
10	Tyr	8.09	134.13	4.69	3.05	-	58.8	39.04
11	Glu	8.32	135.65	4.33	1.96,2.12	-	56.9	30.28
12	Val	8	131.05	4.02	2	-	62.94	32.68
13	His							
14	His							
15	Gln	8.17	136.94	4.33	1.95	-	56.98	29.42
16	Lys	8.31	139.23	4.29	1.88	117.36	57.67	33.03
17	Leu	8.17	139.63	4.31	1.64	118.02	56.59	42.32
18	Val	7.8	132.12	3.92	2.07	118.15	64.17	32.27
19	Phe	7.97	138.87	4.49	3.08	117.34	58.97	39.24
20	Phe	7.92	137.08	4.47	3.18	117.32	59.07	39.39
21	Ala	8.14	135.52	4.11	1.47	116.84	53.94	19.14
22	Glu	8.14	135.31	4.21	2.11	119.09	57.57	29.46
23	Asp	8.13	132.99	4.66	2.76	117.8	54.92	40.33
24	Val	7.89	131.81	4.02	2.16	117.69	63.71	32.18
25	Gly	8.22	126.7	3.96,3.96	-	117.44	46.12	-
26	Ser	7.98	128.27	4.5	3.99	115.25	58.8	64.06
27	Asn	8.27	134.34	4.87	2.87	115.47	53.76	39.22
28	Lys	8.46	140.02	4.25	1.91	116.41	59.06	32.64
29	Gly	8.57	125.6	4.05,3.89	-	118.51	47.33	-
30	Ala	8.03	141.39	4.21	1.52	116.02	54.96	18.8
31	Ile	7.81	134.97	3.86	2.07	119.74	64.38	37.76
32	Ile	8.14	138.14	3.79	2.04	118.4	65.2	37.38
33	Gly	8.44	125.33	3.83,3.83	-	118.84	47.93	-
34	Leu	8.21	134.89	4.08	1.64	115.74	58.38	42.32
35	Met	8.18	131.25	4.1	1.94,2.22	119.39	59.61	33.1
36	Val	8.6	131.8	3.54	2.32	118.62	67.2	31.24
37	Gly	8.69	124.83	3.70,3.70	-	118.91	47.67	-
38	Gly	8.72	126.94	3.78,3.78	-	115.92	47.64	-
39	Val	8.21	139.48	3.64	2.29	115.39	67.19	31.4
40	Val	8.5	141.02	3.51	2.41	119.9	68.05	28.51

Table A.8. APP WT in DPC, pH 5, 320 K , part 2

41	Ile	8.45	137.38	3.6	1.98	118.21	65.47	37.32
42	Ala	8.57	134.6	3.91	1.45	118.33	55.97	18.1
43	Thr	8.16	132.73	3.7	4.16	119.59	68.57	71.27
44	Val	8.25	138.99	3.56	2.31	117.22	67.39	31.41
45	Ile	8.44	140.7	3.6	2.13	119.96	66.51	37.4
46	Val	8.46	137.84	3.58	2.22	117.99	68.19	31.45
47	Ile	8.61	136.5	3.62	1.98	118.62	65.93	37.76
48	Thr	8.19	135.43	3.74	4.35	118.58	68.72	67.82
49	Leu	8.36	138.92	4.05	1.56,2.07	117.12	58.59	41.99
50	Val	8.4	136.53	3.66	2.33	120.17	66.84	31.66
51	Met	8.42	136.34	4.28	2.34,2.19	119.31	58.28	32.16
52	Leu	8.3	136.62	4.24	1.64,1.96	119.57	56.9	42.3
53	Lys	7.85	135.99	4.28	2	119.31	57.01	32.68
54	Lys	7.94	138.17	4.37	-	117.98	56.3	30.55
55	Lys	8.05	136.05	4.71	1.85	117.02	54.65	32.58
56	Pro	-	-	-	-	-	63.52	29.6
57	Gly	8.51	123.13	4.04,4.04	-	118.47	45.45	-
58	Gly	8.33	127.32	4.04,4.04	-	115.85	45.49	-

PGAM5 WT TMD in TFE/H$_2$O

Table A.9. PGAM5 WT TMD in TFE/H$_2$O, pH 5

		H	N	HA	HB	CA	CB
2	Ala	7.81	128.87	4.17	1.38	53.41	16.93
3	Phe	7.31	113.92	4.45	3.13,3.19	58.08	37.67
4	Arg	7.41	118.89	3.98	1.79,1.84	58.33	28.93
5	Gln	7.89	117.74	4.13	2.16	58.12	27.66
6	Ala	7.76	121.41	4.12	1.53	53.46	16.73
7	Leu	7.86	117.37	4.14	1.64,1.82	57.27	41.07
8	Gln	7.83	117.62	4.07	2.22	58.23	27.77
9	Leu	8.03	119.46	4.15	1.63,1.91	57.26	41
10	Ala	8.16	122.21	4.14	1.55	54.29	16.96
11	Ala	8.29	120.1	4.14	1.57	54.29	16.94
12	Cys	8.09	115.01	4.29	3.14,2.99	61.35	26.05
13	Gly	8.2	108.11	3.95	-	45.51	-
14	Leu	8.09	122.19	4.29	1.84,1.65	56.27	41.35
15	Ala	8.14	122.11	4.22	1.51	53.44	17.05
16	Gly	8.19	105.19	3.95	-	45.51	-
17	Gly	8.17	108.18	4.01	-	45.46	-
18	Ser	8	115.26	4.28	3.96,4.02	60.2	62.47
19	Ala	7.89	123.96	4.11	1.49	54.35	16.88
20	Ala	7.69	118.33	4.16	1.55	54.22	16.96
21	Val	7.73	118.66	3.7	2.24	65.53	31.15
22	Leu	7.83	120.67	4.13	1.66,1.71	57.37	40.99
23	Phe	8.46	116.66	4.35	3.22,3.21	59.79	37.91
24	Ser	8.02	113.96	4.19	4.03,4.12	61.02	62.43
25	Ala	8.03	123.95	4.18	1.55	54.04	16.96
26	Val	7.9	116.04	3.83	2.17	64.02	31.44
27	Ala	7.94	121.78	4.12	1.34	54.35	17.74
28	Val	7.66	114.8	3.98	2.21	63.07	31.45
29	Gly	7.97	108.89	3.92,3.92	-	44.67	-
30	Lys	7.66	120.06	4.61	1.86	53.79	31.59
31	Pro	-	-	4.4	1.91,2.29	62.86	30.93
32	Arg	7.82	119.02	4.39	1.92,1.79	54.93	30.31
33	Ala	7.84	123.68	4.34	1.41	51.84	17.95
34	Gly	7.99	106.64	3.87,4.03	-	44.46	-
35	Gly	8	107.21	3.95,3.95	-	44.64	-
36	Asp	7.95	117.81	6.89	2.88	52.84	-

PGAM5 C12L TMD in TFE/H$_2$O

Table A.10. PGAM5 C12L TMD in TFE/H$_2$O, pH 5

		H	HA	HB	CA	CB
2	Ala	-	4.07	1.63	51.88	18.18
3	Phe	7.66	4.51	3.22,3.22	59.57	38.32
4	Arg	8.33	3.98	1.91,1.84	58.59	29.12
5	Gln	7.95	4.11	2.20,2.07	58.64	27.48
6	Ala	7.65	4.09	1.48	54.46	16.91
7	Leu	7.83	4.07	1.57,1.68	57.03	41.09
8	Gln	7.8	4.04	2.15,2.23	58.32	27.94
9	Leu	7.97	4.15	1.58,1.88	57.22	41.04
10	Ala	8.11	4.12	1.53	53.55	16.63
11	Ala	8.15	4.09	1.53	54.46	16.94
12	Leu	8.06	4.29	1.86,1.65	56.37	41.44
13	Gly	8.17	3.91,3.91	-	45.85	-
14	Leu	8	4.18	1.65,1.91	56.84	41.42
15	Ala	8.17	4.22	1.51	53.6	17.2
16	Gly	8.25	3.96	-	45.54	-
17	Gly	8.17	3.97	-	45.54	-
18	Ser	8.01	4.29	4.03,3.96	60.28	62.54
19	Ala	7.93	4.09	1.47	54.46	16.91
20	Ala	7.69	4.14	1.53	54.45	16.94
21	Val	7.68	3.7	2.22	65.6	31.25
22	Leu	7.79	4.12	1.63,1.68	57.48	41.09
23	Phe	8.41	4.35	3.2	59.84	37.98
24	Ser	7.99	4.19	4.12,4.02	61.04	62.54
25	Ala	8	4.19	1.53	54.09	17.34
26	Val	7.87	3.84	2.16	64.06	31.56
27	Ala	7.94	4.1	1.33	54.42	17.8
28	Val	7.63	4	2.21	63.05	31.57
29	Gly	7.94	3.93,3.93	-	44.75	-
30	Lys	7.69	4.62	1.84,1.86	53.9	31.75
31	Pro	-	4.42	1.91,2.29	62.95	30.98
32	Arg	7.92	4.41	1.79,1.92	55.08	30.4
33	Ala	7.98	4.35	1.41	51.99	18.05
34	Gly	8.06	4.03,3.89	-	44.57	-
35	Gly	8	3.96,3.96	-	44.51	-
36	Asp	7.78	4.51	2.72,2.68	54.21	40.89

PGAM5 C12S TMD in TFE/H$_2$O

Table A.11. PGAM5 C12S TMD in TFE/H$_2$O, pH 5

		H	N	HA	HB	CA	CB
2	Ala	7.84	128.94	4.17	1.37	53.33	16.86
3	Phe	7.39	114.36	4.44	3.13,3.18	58.08	37.55
4	Arg	7.47	118.87	3.96	1.82,1.82	58.31	28.84
5	Gln	7.89	117.61	4.12	2.15,2.15	58.07	27.55
6	Ala	7.77	121.56	4.11	1.51	53.39	16.63
7	Leu	7.9	117.76	4.12	1.79,1.63	57.09	40.97
8	Gln	7.85	117.3	4.02	2.24	58.23	27.57
9	Leu	8.11	120.82	4.11	1.91,1.64	57.09	40.91
10	Ala	8.29	122.97	4.13	1.54	54.35	16.64
11	Ala	8.52	119.82	4.14	1.52	54.31	16.88
12	Ser	7.98	112.28	4.28	4.07	60.32	62.59
13	Gly	7.98	109.48	3.99	-	45.33	-
14	Leu	7.98	121.92	4.28	1.63,1.82	56.15	41.26
15	Ala	8.1	121.68	4.22	1.47	53.29	17.05
16	Gly	8.1	105.2	3.95	-	45.32	-
17	Gly	8.12	108.01	3.95,4.00	-	45.33	-
18	Ser	7.98	115.12	4.28	3.95,4.02	60.08	62.37
19	Ala	7.91	124	4.09	1.47	54.47	16.8
20	Ala	7.68	118.3	4.14	1.52	53.87	16.88
21	Val	7.68	118.3	3.69	2.22	65.42	31.08
22	Leu	7.77	120.57	4.11	1.69,1.63	57.3	40.92
23	Phe	8.4	116.61	4.34	3.2	59.7	37.83
24	Ser	7.99	113.86	4.19	4.02,4.11	60.91	62.34
25	Ala	7.99	123.84	4.18	1.53	53.93	17.15
26	Val	7.86	115.93	3.83	2.16	63.93	31.38
27	Ala	7.92	121.85	4.11	1.33	54.37	17.67
28	Val	7.62	114.67	3.98	2.2	62.97	31.37
29	Gly	7.96	109	3.92,3.92	-	44.57	-
30	Lys	7.65	120.22	4.62	1.84,1.84	53.69	31.52
31	Pro	-	-	4.41	1.90,2.28	62.77	30.84
32	Arg	7.9	119.33	4.39	1.91,1.78	54.84	30.24
33	Ala	7.94	124	4.34	1.4	51.76	17.89
34	Gly	8.07	106.74	4.03,3.87	-	44.37	-
35	Gly	8.05	107.6	3.94,3.94	-	44.56	-
36	Asp	8.1	119.26	4.64	2.69,2.69	52.85	40.09

PGAM5 G17L TMD in TFE/H₂O

Table A.12. PGAM5 G17L TMD in TFE/H$_2$O, pH 5

		H	N	HA	HB	CA	CB
2	Ala	7.83	128.94	4.16	1.37	53.35	16.85
3	Phe	7.35	114.17	4.45	3.18,3.13	58	37.57
4	Arg	7.43	118.88	3.97	1.83,1.78	58.26	28.85
5	Gln	7.89	117.78	4.12	2.15	58.06	27.58
6	Ala	7.77	121.46	4.1	1.52	53.45	16.7
7	Leu	7.87	117.5	4.14	1.63,1.80	57.04	41.05
8	Gln	7.83	117.71	4.07	2.2	58.17	27.69
9	Leu	8.04	119.54	4.14	1.62,1.91	57.25	40.95
10	Ala	8.16	122.31	4.13	1.54	54.32	17.18
11	Ala	8.3	120.21	4.14	1.57	54.32	16.81
12	Cys	8.12	115.27	4.28	2.99,3.14	61.51	25.91
13	Gly	8.23	108.61	3.95,3.95	-	45.75	-
14	Leu	8.18	122.31	4.27	1.68,1.82	56.74	41.04
15	Ala	8.22	122.94	4.14	1.53	54.32	16.7
16	Gly	8.07	105.06	3.91,3.91	-	45.83	-
17	Leu	8.05	122.88	4.27	1.77,1.81	56.9	41.38
18	Ser	8.16	113.02	4.13	3.95,4.08	61.21	62.17
19	Ala	7.79	123.23	4.11	1.52	54.39	16.7
20	Ala	7.79	119.89	4.17	1.59	54.01	16.72
21	Val	8.27	119.88	3.66	2.23	65.95	31.06
22	Leu	8.03	120.96	4.12	1.74,1.67	57.53	40.97
23	Phe	8.55	117.04	4.32	3.23	60.03	37.91
24	Ser	8.11	114.01	4.17	4.13,4.03	61.09	62.28
25	Ala	8.06	124	4.17	1.54	54.46	17.18
26	Val	7.93	116.18	3.82	2.16	64.03	31.14
27	Ala	7.97	121.83	4.1	1.3	54.38	17.65
28	Val	7.62	114.65	3.98	2.2	63.01	31.37
29	Gly	7.96	109	3.91,3.91	-	44.57	-
30	Lys	7.66	120.21	4.62	1.85	53.73	31.51
31	Pro	-	-	4.4	2.28,1.90	62.8	30.86
32	Arg	7.89	119.33	4.39	1.78,1.92	54.84	30.23
33	Ala	7.93	124.02	4.34	1.4	51.76	17.9
34	Gly	8.06	106.73	3.88,4.03	-	44.4	-
35	Gly	8.05	107.62	3.94,3.94	-	44.57	-
36	Asp	8.11	119.36	4.64	2.68	52.86	40.16

PGAM5 S18L TMD in TFE/H₂O

Table A.13. PGAM5 S18L TMD in TFE/H$_2$O, pH 5

		H	HA	HB	CA	CB
2	Ala	7.83	4.11	1.67	51.81	18.06
3	Phe	7.64	4.52	3.22	59.61	38.11
4	Arg	8.32	3.97	1.92,1.84	58.53	29.13
5	Gln	7.92	4.11	2.07,2.20	58.62	27.48
6	Ala	7.64	4.08	1.47	54.49	16.84
7	Leu	7.83	4.07	1.64,1.58	57.01	41.1
8	Gln	7.79	4.04	2.22,2.16	58.3	27.86
9	Leu	7.98	4.14	1.59,1.87	57.32	41.09
10	Ala	8.11	4.13	1.52	54.27	16.77
11	Ala	8.29	4.13	1.54	54.27	17.06
12	Cys	8.02	4.31	2.98,3.12	61.15	26.22
13	Gly	8.14	3.95,3.95	-	45.61	-
14	Leu	8.03	4.28	1.67,1.80	56.41	41.49
15	Ala	8.01	4.19	1.49	54.43	17.22
16	Gly	8.02	3.94	-	45.53	-
17	Gly	8.01	3.94	-	45.53	-
18	Leu	7.96	4.18	1.71	56.89	41.26
19	Ala	7.96	3.99	1.48	54.81	16.84
20	Ala	7.54	4.17	1.55	54.07	17.06
21	Val	7.75	3.69	2.32	65.77	31.26
22	Leu	8.2	4.1	1.74,1.51	57.5	40.96
23	Phe	8.49	4.34	3.22	60	38.34
24	Ser	7.98	4.17	4.12,4.04	61.15	62.49
25	Ala	8.01	4.19	1.53	53.55	17.34
26	Val	7.83	3.84	2.15	63.99	31.5
27	Ala	7.93	4.11	1.3	53.52	17.8
28	Val	7.64	4	2.2	63	31.59
29	Gly	7.92	3.93,3.93	-	44.69	-
30	Lys	7.7	4.62	1.84	53.94	31.75
31	Pro	-	4.42	1.92,2.28	62.95	31.01
32	Arg	7.94	4.4	1.92,1.79	55.12	30.37
33	Ala	7.99	4.34	1.41	52.02	18.07
34	Gly	8.08	3.90,4.03	-	44.57	-
35	Gly	8.01	3.96,3.96	-	44.51	-
36	Asp	7.79	4.51	2.71	54.14	40.79

A.3. Structure Statistics

Structure statistics of APP WT TMD and four single point mutants.

All values refer to the ensemble of 20 structures with the lowest energy from 400 calculated structures.

	WT	G38L	G38P	V44M	I45T
Total restraints used	416	406	452	378	356
unambigous NOE restraints	371	376	395	352	324
Intraresidue	161	168	210	153	134
Sequential ($|i-j|=1$)	108	100	103	94	97
Medium range ($1 < |i-j| < 4$)	88	89	66	86	73
Long range ($|i-j| \geq 4$)	14	19	16	19	20
Ambiguous NOE restraints	45	30	57	26	27
Backbone dihedral angle restraints	52	52	52	54	50
Statistics for structure calculations					
RMSD of bonds (A)	0.001 +/- 0.00007	0.001 +/- 0.00008	0.001 +/- 0.00006	0.001 +/- 0.00015	0.001 +/- 0.00005
RMSD of bond angles (°)	0.257 +/- 0.005	0.290 +/- 0.009	0.279 +/- 0.007	0.259 +/- 0.006	0.260 +/- 0.003
RMSD of improper torsions (°)	0.140 +/- 0.012	0.170 +/- 0.018	0.174 +/- 0.013	0.133 +/- 0.007	0.139 +/- 0.009
Final Energies (kcal mol^{-1})					
E_{total}	-1001 +/- 42	-1048 +/- 28	-1011 +/- 28	-1041 +/- 22	-1028 +/- 32
E_{bonds}	0.448 +/- 0.064	0.747 +/- 0.092	0.633 +/- 0.063	0.546 +/- 0.158	0.450 +/- 0.048
E_{angles}	8.85 +/- 0.35	11.56 +/- 0.711	10.6 +/- 0.5	8.98 +/- 0.247	8.88 +/- 0.24
$E_{impropers}$	0.616 +/- 0.107	0.936 +/- 0.200	0.973 +/- 0.146	0.555 +/- 0.062	0.598 +/- 0.074
E_{dihed}	121.5 +/- 1.2	134.5 +/- 2.4	124.0 +/- 1.0	122.9 +/- 2.0	122.5 +/- 1.50
E_{vdW}	-229.6 +/- 3.2	-232.8 +/- 2.9	-235.4 +/- 2.8	-227.8 +/- 3.5	-226.3 +/- 3.0
E_{NOE}	-902.8 +/- 42.3	-962.9 +/- 26.8	-912.2 +/- 28.2	-945.9 +/- 22.0	-934.4 +/- 32.5
Coordinate precision (A)					
RMSD of backbone (N,CA,C,O) of all residues	2.10 +/- 0.69	1.84 +/- 0.54	1.76 +/- 0.62	2.23 +/- 0.65	2.09 +/- 0.76
RMSD of all heavy atoms of all residues	2.53 +/- 0.66	2.16 +/- 0.56	2.12 +/- 0.70	2.57 +/- 0.72	2.40 +/- 0.74
RMSD of backbone (N,CA,C,O) of ordered residues (29:54)	1.43 +/- 0.48	1.31 +/- 0.39	1.44 +/- 0.55	1.77 +/- 0.59	1.40 +/- 0.54
RMSD of all heavy atoms of ordered residues (29:54)	1.65 +/- 0.47	1.53 +/- 0.39	1.79 +/- 0.64	2.09 +/- 0.61	1.61 +/- 0.47

Structure statistics of PGAM5 WT TMD and four single point mutants.

All values refer to the ensemble of 20 structures with the lowest energy from 400 calculated structures.

	WT	C12L	C12S	G17L	S18L
Total restraints used	269	279	261	274	229
unambigous NOE restraints	269	279	261	274	229
Intraresidue	106	107	124	127	89
Sequential ($|i-j|=1$)	85	87	87	93	81
Medium range ($1 < |i-j| < 4$)	61	66	47	40	50
Long range ($|i-j| \geq 4$)	17	19	3	17	9
Ambiguous NOE restraints	0	0	0	0	0
Backbone dihedral angle restraints					
Statistics for structure calculations					
RMSD of bonds (A)	0.001+/- 0.00007	0.001 +/- 0.00007	0.001 +/- 0.00006	0.001 +/- 0.0001	0.001 +/- 0.00005
RMSD of bond angles (°)	0.253 +/- 0.005	0.260 +/- 0.005	0.252 +/- 0.004	0.285 +/- 0.011	0.260 +/- 0.003
RMSD of improper torsions (°)	0.108 +/- 0.007	0.098 +/- 0.007	0.102 +/- 0.007	0.146 +/- 0.02	0.98 +/- 0.006
Final Energies (kcal mol^{-1})					
E_{total}	-1044 +/- 30	1057 +/- 24	-1034 +/- 30	-1058 +/- 22	-1039 +/- 27
E_{bonds}	0.369 +/- 0.064	0.360 +/- 0.059	0.403 +/- 0.056	0.566 +/- 0.121	0.340 +/- 0.040
E_{angles}	8.35 +/- 0.33	8.98 +/- 0.32	8.24 +/- 0.26	10.90 +/- 0.89	8.95 +/- 0.24
$E_{impropers}$	0.432 +/- 0.057	0.362 +/- 0.055	0.387 +/- 0.053	0.823 +/- 0.287	0.367 +/- 0.047
E_{dihed}	134.0 +/- 0.98	134.2 +/- 0.81	133.3 +/- 0.82	140.2 +/- 1.78	134.0 +/- 0.89
E_{vdW}	-207.6 +/- 4.3	-203.22 +/- 4.28	-195.96 +/- 3.2	-210.1 +/- 2.7	-199.2 +/- 3.26
E_{NOE}	-980.1 +/- 28.7	-988.25 +/- 25.5	-981.0 +/- 29.5	-1001 +/- 22	-983.69 +/- 27.9
Coordinate precision (A)					
RMSD of backbone (N,CA,C,O) of all residues	3.06	4.47	4.20	4.35	3.07
RMSD of all heavy atoms of all residues	3.56	5.11	5.05	5.05	3.56
RMSD of backbone (N,CA,C,O) of ordered residues (3:28)	2.18	2.30	2.95	3.42	2.67
RMSD of all heavy atoms of ordered residues (3:28)	2.67	2.96	4.0	2.37	2.12

B. Danksagung